

Evaluation of full-scale laboratory models of geosynthetic reinforced pavement systems
by Macgregor L Fogelsong

A thesis submitted in partial fulfillment of the requirements for the degree of Master of Science in Civil Engineering
Montana State University
© Copyright by Macgregor L Fogelsong (1998)

Abstract:
Geogrids and geotextiles have been used for more than 16 years as reinforcement in the base course layer of flexible pavements. Benefits from reinforcement include a possible reduction in the required thickness of the base course layer and an increase in the design life of the pavement.

Currently, mechanisms of reinforcement are not well understood and a quantitative evaluation of geosynthetic reinforcement effects on rutting behavior in flexible pavements is difficult.

21 full-scale laboratory models of flexible pavements systems were constructed and cyclically loaded. Both control (unreinforced) and reinforced sections were constructed and tested. Major variables included geosynthetic type, subgrade stiffness, base course thickness, and location of reinforcement.

Geogrid and geotextile reinforcement of the base layer over a soft clay subgrade showed improved rutting performance over comparable unreinforced sections. No significant performance differences were seen when a stiff silty-sand subgrade was used. Changes in major variables such as subgrade type, geosynthetic type, and base layer thickness resulted in significant performance differences. Geosynthetic reinforcement of the base layer appears to be a viable technology for improving rutting performance of flexible pavements over soft subgrades.

EVALUATION OF FULL-SCALE LABORATORY MODELS OF GEOSYNTHETIC REINFORCED PAVEMENT SYSTEMS

by

Macgregor L. Fogelsong

A thesis submitted in partial fulfillment
of the requirements for the degree

of

Master of Science

in

Civil Engineering

MONTANA STATE UNIVERSITY-BOZEMAN
Bozeman, Montana

December 1998

© COPYRIGHT

by

Macgregor Leroy Fogelsong

1998

All Rights Reserved

N378
F6869

APPROVAL

of a thesis submitted by

Macgregor L. Fogelsong

This thesis has been read by each member of the thesis committee and has been found to be satisfactory regarding content, English usage, format, citations, bibliographic style, and consistency, and is ready for submission to the College of Graduate Studies.

Dr. Steven W. Perkins — (Signature) — 12-17-98 (Date)

Approved for the Department of Civil Engineering

Dr. Donald Rabern — (Signature) — 12/17/98 (Date)

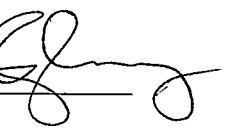
Approved for the College of Graduate Studies

Dr. Joe Fedock — (Signature) — 12/17/98 (Date)

STATEMENT OF PERMISSION TO USE

In presenting this thesis in partial fulfillment of the requirements for a master's degree at Montana State University-Bozeman, I agree that the Library shall make it available to borrowers under the rules of the Library.

If I have indicated my intention to copyright this thesis by including a copyright notice page, copying is allowable for scholarly purposes, consistent with "fair use" as prescribed in the U.S. Copyright law. Requests for permission for extended quotation from or reproduction of this thesis in whole or in parts may be granted only by the copyright holder.

Signature 

Date 12/17/98

TABLE OF CONTENTS

	Page
1. INTRODUCTION	1
Background	1
Scope of Work	2
2. REVIEW OF THE LITERATURE	4
Introduction	4
Geosynthetic Functions	5
Filtration and Drainage Functions	6
Separation Function	6
Reinforcement Functions	8
Previous Experimental Work	12
Geogrid Reinforcement	12
Study Involving Geotextiles	23
Mixed Studies (Geogrids & Geotextiles)	25
Conclusions	30
3. EXPERIMENTAL METHODS	32
Introduction	32
Laboratory Test Facility	33
Test Box and Loading Apparatus	33
Instrumentation	36
Asphalt Concrete Instrumentation	37
Geosynthetic Instrumentation	40
Base Course and Subgrade Instrumentation	41
General Instrumentation	43
Pavement Layer Materials	46
Asphalt Concrete	46
Base Course	46
Subgrade Materials	47
Geosynthetics	48
Test Section Construction	50

TABLE OF CONTENTS-Continued

Page

Instrument Calibration 55
Instrument Installation 56
In-Situ Instrument Locations 61
Pavement Loading 63
As-Constructed Test Section Properties 64
Statistical Comparison of Test Section Properties 72
Instrument Measurement Repeatability 78
Construction and Loading of PCS1 79
Illustrations of Repeatability 80

4. DISCUSSION OF RESULTS 89
Introduction 89
Clay Section Behavior 90
Rutting Behavior 90
Lateral Base Restraint Mechanism 95
Improved Vertical Stress Distribution on Subgrade 101
Lateral Spreading on Top of Subgrade 103
Vertical Strain in Subgrade 104
Effect of Additional Base Material 105
Silty-Sand Subgrade Section Behavior 106
Rutting Behavior 106
Lateral Base Restraint Mechanism 107
Soil/Geosynthetic Compatibility 108
Subgrade Effects 109

5. COMPARISON OF SINGLE-PULSE TEST RESULTS TO LINEAR ELASTIC THEORY 147
Introduction 147
KENLAYER Computer Program 148
Model Geometry and Determination of Pavement Layer Elastic Moduli 148
Comparison of Model Output to Section PCS1 152
Surface Deflections/AC Strain 153
Stress Predictions 155
Strain Predictions 156
Stress and Strain Beneath Load Centerline 157
Subgrade Strain Criterion Analysis 158

TABLE OF CONTENTS-Continued

Page

Rut Development Predictions Using Empirical Relations..... 161

6. CONCLUSIONS AND RECOMMENDATIONS..... 182
Summary..... 182
Shear Resisting Interface Mechanism..... 184
Modeling Developments..... 188
Recommendations for Further Research..... 189

BIBLIOGRAPHY..... 190

APPENDIX A..... 197

LIST OF TABLES

Page

Table 2.1. Test section data from Haas et al. (1998) (from Perkins & Ismeik (1997a)).....19

Table 2.2. Test section data from Brandon et al. (1995).....28

Table 3.1. Geosynthetic material parameters.....49

Table 3.2. Reinforcement placement for all test sections.....51

Table 3.3. CBR results showing time variation for subgrades of sections SSS1-4.....65

Table 3.4. As-constructed subgrade properties.....66

Table 3.5. As-constructed base course properties.....67

Table 3.6. Coefficients of variation for base course and subgrade construction.....70

Table 3.7. As-constructed asphalt concrete properties.....71

Table 3.8. One-way analysis of variance (ANOVA) for asphalt concrete voids in the SSS series tests.....73

Table 3.9. One-way analysis of variance (ANOVA) for asphalt concrete voids in the CS series tests.....74

Table 3.10. Post hoc comparison of mean voids for the SSS series of test sections.....74

Table 3.11. Post hoc comparison of mean voids for the CS series of tests sections.....75

Table 3.12. Average load applied for all test sections completed.....78

LIST OF TABLES-Continued

Page

Table 4.1. Dynamic load induced in the geosynthetic. 100

Table 5.1. Summary of model input parameters. 152

Table 5.2. Empirical constants "x" and "y" and rut depth proposed by various agencies. 160

Table 5.3. Comparison of empirical failure models (rutting) to CS2 and CS8. 160

Table 5.4. Comparison of experimental plastic strain parameters to parameters from Li et al. (1996). 165

Table A1. Sensor locations for test section SSS1. 198

Table A2. Sensor locations for test section SSS2. 200

Table A3. Sensor locations for test section SSS3. 202

Table A4. Sensor locations for test section SSS4. 204

Table A5. Sensor locations for test section SSS5. 206

Table A6. Sensor locations for test section SSS6. 208

Table A7. Sensor locations for test section SSS7. 210

Table A8. Sensor locations for test section SSS8. 212

Table A9. Sensor locations for test section SSS9. 214

Table A10. Sensor locations for test section PCS1 216

Table A11. Sensor locations for test section CS1 218

Table A12. Sensor locations for test section CS2. 220

Table A13. Sensor locations for test section CS3 222

LIST OF TABLES-Continued

Page

Table A14. Sensor locations for test section CS5.....223

Table A15. Sensor locations for test section CS6.....225

Table A16. Sensor locations for test section CS7.....227

Table A17. Sensor locations for test section CS8.....229

Table A18. Sensor locations for test section CS9.....231

Table A19. Sensor locations for test section CS10.....233

Table A20. Sensor locations for test section CS11.....235

LIST OF FIGURES

Page

Figure 2.1. Illustration of mixing of the base and subgrade, where addition of geosynthetic would be beneficial as a separator 7

Figure 2.2. Illustration of the tensioned membrane effect 9

Figure 2.3. Shear surface alteration resulting in an increased bearing capacity 10

Figure 2.4. Illustration of the lateral restraint concept 11

Figure 2.5. TBR versus base thickness for geogrid A and B (Collin et al. 1996) 16

Figure 2.6. TBR versus rut depth based on results from Webster (1992) (from Perkins & Ismeik (1997a)). 17

Figure 2.7. TBR versus rut depth from results of Haas et al. (1988) (from Perkins & Ismeik (1997a)) 20

Figure 2.8. TBR versus rut depth from results of Miura (1990) (from Perkins & Ismeik (1997a)) 22

Figure 3.1. Isometric view of the test box and loading apparatus. 34

Figure 3.2. Schematic of apparatus components and pavement layers. Note: Load not shown in center of box to illustrate movement capabilities. 35

Figure 3.3. Overall picture of the pavement test facility 36

Figure 3.4. Closeup of the 305 mm diameter load plate, load cell (top), and surface LVDT's resting on the pavement surface 37

LIST OF FIGURES-Continued

Page

Figure 3.5. Typical plot of permanent surface deformation after 5 load cycles for test section CS1 38

Figure 3.6. Asphalt concrete strain gage 39

Figure 3.7. Different components of the Dynatest H-type PAST (Dynatest, 1991) 40

Figure 3.8. Large geotextile foil strain gage (top) and smaller geogrid foil strain gage (bottom) 41

Figure 3.9. Dynatest SOil Pressure Transducer (SOPT) (Dynatest, 1991) 42

Figure 3.10. Typical stress cell 43

Figure 3.11. Typical LVDT from RDP Electronics (Pottstown, PA) 44

Figure 3.12. A view of the amplifiers used for all instruments and the corresponding onscreen output from Labview 45

Figure 3.13. Grain size distribution of cold-mix aggregate, hot-mix aggregate, base course, and silty-sand subgrade 47

Figure 3.14. Laboratory test CBR versus water content for the clay subgrade 49

Figure 3.15. Skid steer loader used for all soil mixing and lift placement 52

Figure 3.16. Vibratory plate compactor used for compaction of silty-sand subgrade, base course, and asphalt concrete 53

Figure 3.17. Troxler model 3411-B nuclear densometer 54

Figure 3.18. Dynamic cone penetrometer used for CBR determinations of pavement layer materials 54

Figure 3.19. Upright "jumping-jack" compactor used for compaction of clay subgrade 55

LIST OF FIGURES-Continued

Page

Figure 3.20. Theoretical stress and strain measurements for an element of soil inside a test section 62

Figure 3.21. Input load pulse and corresponding load cell measurement 64

Figure 3.22. Dry density and water content versus depth from section SSS9 excavation 69

Figure 3.23. Peak vertical strain versus distance in the base layer for two soil strain sensors (LVDT's) from section PCS1 at two different positions (Z=300 mm) 81

Figure 3.24. Vertical strain versus radial distance from the load application from section PCS1 in the top of the subgrade (Z=450 mm) 82

Figure 3.25. Illustration of radial strain measures from two soil strain sensors in the top of the subgrade from section PCS1 (Z=415 mm) 83

Figure 3.26. Vertical stress distribution in the base layer from two stress cells from section PCS1 (Z=300 mm) 83

Figure 3.27. Vertical stress distribution in the subgrade from two stress cells from section PCS1 (Z=675 mm) 84

Figure 3.28. Permanent rut development for test sections CS2 and CS8 85

Figure 3.29. Long-term measures of radial strain in the base at a radial distance of 200 mm from the load centerline from test sections CS2 and CS8 (Z=325 mm) 85

Figure 3.30. Long-term dynamic vertical stress in the top of the subgrade from test sections CS2 and CS8 (R=0 mm, Z=450 mm) 86

Figure 3.31. Permanent radial strain in the base (R=150 mm, Z=215 mm) (SSS1, SSS4) 87

LIST OF FIGURES-Continued

Page

Figure 3.32. Dynamic vertical stress versus cycle number in subgrade (R=0 mm, Z=350 mm) (SSS1, SSS4) 87

Figure 3.33. Permanent vertical strain versus cycle number in subgrade (R=60 mm, Z=575 mm) (SSS1, SSS4) 88

Figure 4.1. Permanent surface deformation versus cycle number for less than 80,000 cycles (CS2-CS11) 111

Figure 4.2. Permanent surface deformation versus cycle number for all cycles (CS2-CS11) 111

Figure 4.3. Permanent surface deformation versus cycle number (CS9, CS10) 112

Figure 4.4. TBR for sections CS5, 6, 7, 9, and 11 relative to CS2 112

Figure 4.5. TRB for section CS10 relative to CS9 113

Figure 4.6. Permanent surface deformation bowls at cycle 1 (CS2-CS11) 113

Figure 4.7. Permanent surface deformation bowls at cycle 40,000 (CS2-CS11) 114

Figure 4.8. Permanent surface deformation bowls at cycle 1 (CS9-CS10) 114

Figure 4.9. Permanent surface deformation bowls at cycle 125,000. (CS9-CS10) 115

Figure 4.10. Surface dynamic deformation bowls at cycle 1 (CS2-CS11) 115

Figure 4.11. Dynamic surface deformation bowls at a permanent rut depth of 12.5 mm (CS2-CS11) 116

Figure 4.12. Dynamic surface deformation versus cycle number (CS2-CS11) 116

Figure 4.13. Dynamic surface deformation versus cycle number (CS9, CS10) 117

LIST OF FIGURES-Continued

Page

Figure 4.14. Permanent radial strain in base of sections CS2-CS11. (R=100, Z=325mm) 117

Figure 4.15. Permanent radial strain in base of sections CS2-CS11. (R=200, Z=325mm) 118

Figure 4.16. Permanent radial strain in the base versus radial distance at cycle 1 of sections CS2-CS11 (Z=325mm) 118

Figure 4.17. Permanent radial strain in the base versus radial distance at cycle 40,000 of sections CS2-CS11 (Z=325mm) 119

Figure 4.18. Permanent radial strain versus cycle number in the base of sections CS9-CS10 (R=100mm, Z=400mm) 119

Figure 4.19. Permanent radial strain versus cycle number in the base of sections CS9-CS10 (R=200mm, Z=400mm) 120

Figure 4.20. Permanent radial strain versus radial distance in the base of sections CS9-CS10 at cycle 125,000 (Z=400mm) 120

Figure 4.21. Dynamic radial strain in base of sections CS2-CS11 (R=100, Z=325mm) 121

Figure 4.22. Permanent radial strain (M) in the geosynthetics of sections CS5-CS11 (R=15 mm) 121

Figure 4.23. Permanent radial strain (XM) in the geosynthetics of sections CS5-CS11 (R=20 mm) 122

Figure 4.24. Permanent radial strain in the geosynthetic (M) versus radial distance of sections CS5-CS11 at cycle 7,500. 122

Figure 4.25. Dynamic radial strain (M) in the geosynthetics of sections CS5-CS11 (R=15mm) 123

Figure 4.26. Dynamic radial strain (XM) in the geosynthetics of sections CS5-CS11 (R=20mm) 123

LIST OF FIGURES-Continued

Page

Figure 4.27. Dynamic radial strain in the geosynthetic (M) vesus radial distance of sections CS5-CS11 at cycle 1. 124

Figure 4.28. Dynamic radial strain in the geosynthetic (M) versus radial distance of sections CS5-CS11 at cycle 7,500. 124

Figure 4.29. Permanent vertical strain versus cycle number in the base beneath the load centerline (R=65mm) (CS2-CS11) 125

Figure 4.30. Dynamic vertical stress versus cycle number in the subgrade of sections CS2-CS11 (R=0, Z=450 mm) 125

Figure 4.31. Dynamic vertical stress versus cycle number in the subgrade of sections CS2-CS11 (R=0, Z=625 mm) 126

Figure 4.32. Dynamic vertical stress versus cycle number in the subgrade of sections CS2-CS11 (R=0, Z=775 mm) 126

Figure 4.33. Dynamic vertical stress versus cycle number in the subgrade of sections CS2-CS11 (R=0, Z=1075 mm) 127

Figure 4.34. Dynamic vertical stress versus cycle number in the subgrade of sections CS9-CS10 (R=200, Z=525 mm) 127

Figure 4.35. Dynamic vertical stress in the subgrade versus radial distance of sections CS2-CS11 at cycle 1. 128

Figure 4.36. Dynamic vertical stress in the subgrade versus radial distance of sections CS2-CS11 at cycle 40,000. 128

Figure 4.37. Permanent radial strain in the subgrade versus radial distance of sections CS2-CS11 at cycle 40,000. 129

Figure 4.38. Permanent radial strain versus radial distance in the subgrade of sections CS9-CS10 at cycle 125,000. (Z=490 mm) 129

Figure 4.39. Permanent radial strain versus cycle number in the subgrade of sections CS9-CS10 (R=150mm, Z=490mm) 130

LIST OF FIGURES-Continued

Page

Figure 4.40. Permanent radial strain in the subgrade versus radial distance of sections CS2-CS11 at cycle 1. 130

Figure 4.41. Dynamic radial stress versus cycle number in the subgrade of sections CS9-CS10 (R=250, Z=525mm) 131

Figure 4.42. Permanent vertical strain versus cycle number in the subgrade of sections CS2-CS11 (R=65, Z=450 mm)....131

Figure 4.43. Permanent vertical strain versus cycle number in the subgrade of sections CS2-CS11 (R=65, Z=625 mm)....132

Figure 4.44. Permanent vertical strain versus cycle number in the subgrade of sections CS2-CS11 (R=65, Z=775 mm)....132

Figure 4.45. Permanent vertical strain versus cycle number in the subgrade of sections CS2-CS11 (R=65, Z=1075 mm)....133

Figure 4.46. Permanent vertical strain versus cycle number in the subgrade of sections CS9-CS10 (R=65, Z=525 mm)....133

Figure 4.47. Permanent radial strain in the base versus radial distance of sections CS2, CS8, and CS9 at cycle 1. 134

Figure 4.48. Permanent radial strain in the base versus radial distance of sections CS2, CS8, and CS9 at cycle 40,000. 134

Figure 4.49. Dynamic vertical stress in the subgrade versus radial distance of sections CS2 and CS9 at cycle 1....135

Figure 4.50. Dynamic vertical stress in the subgrade versus radial distance of sections CS2 and CS9 at cycle 40,000....135

Figure 4.51. Permanent radial strain in the subgrade versus radial distance of sections CS2, CS8, and CS9 at cycle 1....136

Figure 4.52. Permanent radial strain in the subgrade versus radial distance of sections CS2, CS8, and CS9 at cycle 40,000....136

LIST OF FIGURES-Continued

Page

Figure 4.53. Permanent vertical strain versus cycle number in the subgrade of sections CS2, CS8, and CS9 (R=65) 137

Figure 4.54. Permanent surface deformation versus cycle number for sections SSS1-4 137

Figure 4.55. Permanent radial strain vs. cycle in the bottom of asphalt layer at R=0 (SSS1-4) 138

Figure 4.56. Permanent radial strain in the base (R=150, Z=215 mm) (SSS1-4) 138

Figure 4.57. Permanent radial strain in the base (R=300, Z=215 mm) (SSS1-4) 139

Figure 4.58. Permanent radial strain in the base versus radial distance at cycle 500,000.(Z=160 mm) (SSS1-4) 139

Figure 4.59. Permanent vertical strain versus cycle number in the base beneath the load centerline. (R=60 mm) (Z=160 mm) (SSS1-4) 140

Figure 4.60. Permanent radial strain (M) in the geosynthetics (R=15 mm) 140

Figure 4.61. Permanent radial strain (XM) in the geosynthetics (R=23 mm) 141

Figure 4.62. Distribution of peak radial strain in the geogrid and base course aggregate in section SSS5 at 5000 load cycles. 141

Figure 4.63. Distribution of permanent tangential strain in the geogrid and base course aggregate in section SSS5 at 5000 load cycles. 142

Figure 4.64. Distribution of permanent radial strain in the geotextile and base course aggregate in section SSS8 at 5000 load cycles. 142

Figure 4.65. Distribution of permanent tangential strain in the geotextile and base course aggregate in section SSS8 at 5000 load cycles. 143

LIST OF FIGURES-Continued

Page

Figure 4.66. Distribution of peak radial strain in the geogrid and base course aggregate in section SSS2 at 5000 load cycles. 143

Figure 4.67. Dynamic vertical stress versus cycle number in the subgrade (R=0, Z=350 mm) (SSS1-4)....144

Figure 4.68. Dynamic vertical stress versus radial distance in the subgrade at cycle 500,000. (Z=350 mm) (SSS1-4) 144

Figure 4.69. Permanent vertical strain versus cycle number in the subgrade (R=60 mm) (Z=350 mm) 145

Figure 4.70. Permanent vertical strain versus cycle number in the subgrade (R=60 mm) (Z=575 mm) (SSS1-4) 145

Figure 4.71. Permanent vertical strain versus cycle number in the subgrade (R=60 mm) (Z=825 mm) (SSS1-4) 146

Figure 4.72. Permanent vertical strain versus cycle number in the subgrade. (R=60 mm) (Z=1075 mm) (SSS1-4) 146

Figure 5.1. Model geometry illustrating response levels corresponding to instrument depths....149

Figure 5.2. Peak elastic asphalt concrete surface deflection....167

Figure 5.3. Peak elastic radial strain versus radial distance in the AC (Z=67 mm)....167

Figure 5.4. Peak elastic radial stress versus radial distance in the base (Z=225 mm)....168

Figure 5.5. Peak elastic tangential stress versus radial distance in the base (Z=300 mm)....168

Figure 5.6. Peak elastic radial stress versus radial distance in the base. (Z=300 mm)....169

LIST OF FIGURES-Continued

Page

Figure 5.7. Peak elastic vertical stress versus radial distance in the base (Z=300 mm) 169

Figure 5.8. Peak elastic tangential stress versus distance in the subgrade (Z=450 mm) 170

Figure 5.9. Peak elastic radial stress versus radial distance in the subgrade (Z=450 mm) 170

Figure 5.10. Peak elastic vertical stress versus radial distance in the subgrade (Z=450 mm) 171

Figure 5.11. Peak tangential stress versus distance in the subgrade (Z=675 mm) 171

Figure 5.12. Peak elastic radial stress versus radial distance in the subgrade (Z=675 mm) 172

Figure 5.13. Peak elastic vertical stress versus radial distance in the subgrade (Z=675 mm) 172

Figure 5.14. Peak elastic tangential stress versus distance in the subgrade (Z=675 mm) 173

Figure 5.15. Peak elastic radial strain versus radial distance in the base (Z=225 mm) 174

Figure 5.16. Peak elastic tangential strain versus radial distance in the base (Z=355 mm) 174

Figure 5.17. Peak elastic radial strain versus radial distance in the base (Z=355 mm) 175

Figure 5.18. Peak elastic vertical strain versus radial distance in the base (Z=300 mm) 175

Figure 5.19. Peak elastic tangential strain versus radial distance in the base (Z=355 mm) 176

LIST OF FIGURES-Continued

Page

Figure 5.20. Peak elastic radial strain versus radial distance in the subgrade (Z=415mm) 177

Figure 5.21. Peak elastic vertical strain versus radial distance in the subgrade (Z=450 mm) 177

Figure 5.22. Peak elastic tangential strain versus distance in the subgrade (Z=415 mm) 178

Figure 5.23. Peak elastic radial strain versus radial distance in the subgrade (Z=675 mm) 178

Figure 5.24. Peak elastic vertical strain versus radial distance in the subgrade (Z=675 mm) 179

Figure 5.25. Peak elastic vertical stress versus depth at R=0 mm 179

Figure 5.26. Peak elastic radial stress versus depth at R=0 mm 180

Figure 5.27. Peak elastic radial strain versus depth at R=0 mm 180

Figure 5.28. Peak elastic vertical strain versus depth at R=0 mm 181

Figure 5.29. First cycle plastic strain parameter "A" as a function of the deviator stress/static stress ratio 181

ABSTRACT

Geogrids and geotextiles have been used for more than 16 years as reinforcement in the base course layer of flexible pavements. Benefits from reinforcement include a possible reduction in the required thickness of the base course layer and an increase in the design life of the pavement.

Currently, mechanisms of reinforcement are not well understood and a quantitative evaluation of geosynthetic reinforcement effects on rutting behavior in flexible pavements is difficult.

21 full-scale laboratory models of flexible pavements systems were constructed and cyclically loaded. Both control (unreinforced) and reinforced sections were constructed and tested. Major variables included geosynthetic type, subgrade stiffness, base course thickness, and location of reinforcement.

Geogrid and geotextile reinforcement of the base layer over a soft clay subgrade showed improved rutting performance over comparable unreinforced sections. No significant performance differences were seen when a stiff silty-sand subgrade was used. Changes in major variables such as subgrade type, geosynthetic type, and base layer thickness resulted in significant performance differences. Geosynthetic reinforcement of the base layer appears to be a viable technology for improving rutting performance of flexible pavements over soft subgrades.

CHAPTER ONE

INTRODUCTION

Background

Geogrids and geotextiles have been used for more than 16 years as reinforcement in the base course layer of flexible pavements. Geotextiles were first used in unpaved haul roads in the late 1970's (Steward, et al. 1977), while geogrids were first studied in the late 1980's for reinforcement purposes (Haas et al. 1988; Barksdale et al. 1989). Use of these materials in the base course layer for reinforcement purposes is attractive from an economic point of view. Incorporating reinforcement into the base layer can benefit the roadway in two ways. The first benefit of reinforcement involves a possible reduction in the required thickness of the base layer. This alternative is attractive where thick base course layers may be needed over soft subgrades, or where gravel sources may be scarce. The second benefit exists when the reinforcement increases the design life of a pavement. This benefit is achieved through slower permanent rut development associated with geosynthetic reinforcement in the pavement system.

Specifically, the Montana Department of Transportation is interested in the use of the technology where low subgrade support values and thick base course layers are required, primarily in the eastern part of the state. In this area, quality aggregate sources

are scarce and haul costs of quality material are high. The intention of this research project is to provide data that for an interpretation of mechanisms by which geosynthetics increase pavement performance, and to provide a data base that will be used in developing a comprehensive Finite Element Model (FEM) of the reinforced pavement system. In the future, this model will be able to predict pavement response for different pavement layer properties as well as benefits from the inclusion of geogrids and geotextiles. Eventually, a design tool for geosynthetic reinforced pavements will be developed using test section data and FEM results.

Scope of Work

The goal of this research was to evaluate the effects of geosynthetic reinforcement on the performance of laboratory-scale flexible pavement systems. This work was broken into five main tasks that coincide with five chapter divisions of this thesis. The tasks are listed and summarized below. It is noted that this thesis will neither include the finite element modeling work, nor the resulting design tool described above. These are future tasks in the overall research project that will be reported by others at a future date.

- Task 1: Conduct a thorough review of the literature to gain background information necessary for the successful implementation of a research program.

- Task 2: Design, build, and load laboratory-scale flexible pavement test sections incorporating informative variables such as geosynthetic type, subgrade strength, and base course thickness.
- Task 3: Synthesize results obtained from the experimental test sections and interpret the results pertaining to improvements in pavement performance.
- Task 4: Compare the stress/strain response of unreinforced test sections to layered linear elastic theory and to other published performance prediction models. This task should facilitate FEM development by exposing weaknesses in simpler modeling methods.
- Task 5: Conclude experimental results and comment on further research needed for the development of an accurate finite model and an effective design tool.

CHAPTER TWO

REVIEW OF THE LITERATURE

Introduction

The purpose of this chapter is to provide a review of concepts involved with geosynthetic reinforcement and to highlight experimental studies performed to date in this area of research. This chapter focuses mainly on laboratory-scale experiments using stationary cyclic loads or moving wheel loads in indoor test-track facilities, and on full-scale field studies involving vehicular traffic. The previous experimental work is critiqued with close attention given to important variables such as section layer thickness, pavement layer stiffness, geosynthetic type and stiffness, and geosynthetic placement within the section. Experimental results of numerous studies are summarized and critiqued. Benefits of reinforcement are at times described by the Traffic Benefit Ratio (TBR), defined as the ratio of the number of load cycles of a reinforced section to an identical unreinforced section necessary to achieve a particular rut depth. Unless noted, a 25 mm permanent surface deformation is used for TBR comparisons.

This chapter is divided into a review of geosynthetic functions and reinforcement mechanisms, and a review of previous experimental studies. At the conclusion of this chapter, an effort is made to combine the knowledge gained from previous experimental

results into a basis for the experimental program used in this research. The literature review will provide a basis for understanding previous problems encountered in this area of research and will illustrate important variables that will be incorporated into this thesis.

Geosynthetic Functions

In order to quantify pavement behavior and response for unreinforced and geosynthetic reinforced situations, it is first necessary to understand the mechanisms thought to be responsible for reinforcement benefits and to understand other functions provided by geosynthetics. It is known that several mechanisms may contribute to improved performance, rather than a single mechanism. It is also known that different functions may occur between geotextile reinforced sections versus geogrid sections. The following sections will provide a deeper understanding of several main mechanisms believed to increase the performance of geosynthetic-reinforced roadways. These sections will also show why some reinforcement mechanisms do not account for reinforcement benefits in flexible pavement systems where rut depths are generally less than 25 mm.

Geotextiles and geogrids have several functions when used in roadways. Generally, four functions are used in describing the role of geosynthetics in roadways. These functions include separation, reinforcement, filtration, and drainage. Filtration and drainage will be described in general here, with specific descriptions of reinforcement and separation given hereafter.

Filtration and Drainage Functions

Filtration and drainage functions can be considered to be similar. Filtration is defined as the ability of a geosynthetic to filter fines from the subgrade when water flows from the subgrade upward to the base. This water flow usually stems from excess pore water pressure development from either loading by traffic or freeze/thaw conditions. The purpose of the geosynthetic in this function is to filter the fines that would migrate into the base layer due to the flow of water. This condition could reduce the thickness of the subgrade and/or reduce the strength of the base layer, leading to a higher rut development rate than would otherwise be present without the geosynthetic.

The drainage function refers to a geosynthetic's ability to drain water from the pavement layer materials to the edge of the pavement. Drainage water can originate from the base layer (water intrusion laterally or from the AC surface) or from the subgrade layer, provided that excess pore water pressures are developed. Excess water in a pavement can lead to a reduction in effective stresses in the subgrade, causing increased rutting of that layer. The function of the geosynthetic then, is to provide a mechanism to route the water to the edge of the pavement, reducing the chance of rutting.

Separation Function

The main difference between a soil separation function and a reinforcement function is that the latter provides a mechanical improvement of the soil. The separation function defines a geosynthetic's ability to maintain physical separation between the base and subgrade layers of a flexible pavement system. Separation prevents mixing of the

base and subgrade materials. Mixing is usually caused by construction techniques, which may push aggregate from the base into the subgrade. Another cause of mixing is from post-construction, cyclic loading due to traffic. Cyclic loading from traffic causes the subgrade fines to be squeezed into the aggregate of the base layer. Once the base is contaminated with these fines, frictional characteristics between aggregate particles are reduced. The reduction in frictional characteristics of the base reduces the strength and stiffness of the layer and promotes rutting. Rutting is promoted from a loss of support by the base leading to a more critical state of stress on the usually weaker subgrade layer. Potential benefits of geotextiles combine the separation and reinforcement functions. The separator can reduce intermixing while the reinforcement increases load carrying capacity. Figure 2.1 illustrates the situation where a geosynthetic would be beneficial as a separator in preventing mixing of the base and subgrade layers.

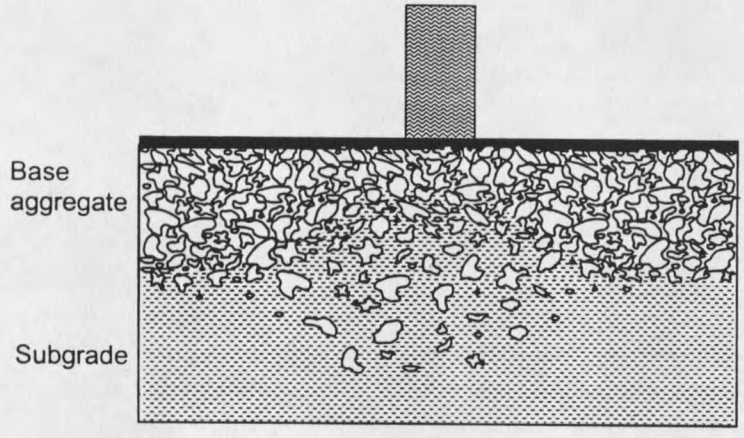


Figure 2.1. Illustration of mixing of the base and subgrade, where addition of geosynthetic would be beneficial as a separator.

Reinforcement Functions

Two main reinforcement mechanisms are thought to be accountable for increasing the capacity of a geosynthetic reinforced roadway: the tensioned membrane mechanism, and the lateral restraint mechanism. Most reinforcement functions fall under these two categories. Many times, reinforcement effects are combined with one of the functions described previously. For example, reinforcement could be combined with a drainage or filtration function. It is often difficult to distinguish analytically or quantitatively between the rutting behavior of a pavement and the function(s) responsible for the behavior.

The tensioned membrane reinforcement mechanism requires locally applied loading and significant deformation of the pavement layers. Significant deformation is required to develop enough tension in the geosynthetic material to provide a net uplifting force. This level of deformation (usually much greater than 25 mm of rut), is not tolerable in flexible pavement systems, in contrast to unpaved or haul roads where this function may be more significant, as the large rut depths required by the mechanism are tolerable. In general, a stress reduction is achieved on the underlying soil beneath the applied load due to the uplift force provided by the tensioned membrane effect (Figure 2.2). Stress reduction provided by the geosynthetic leads to a less critical state of stress, which reduces the amount of rutting on the subgrade.

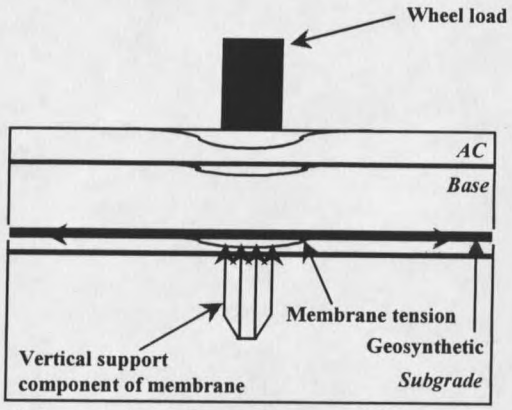


Figure 2.2. Illustration of the tensioned membrane effect.

Sometimes included in the tensioned membrane reinforcement concept is an increased bearing capacity function. The increased bearing capacity function essentially resists lateral displacement of the foundation soil (subgrade in this case) by restraining the lateral thrust in the fill (base layer). This function essentially alters the failure shear surface and forces a less critical failure surface to develop, usually above the level of the geosynthetic. This shear failure alteration is shown in Figure 2.3. Unfortunately for flexible pavement systems, the increased bearing capacity concept implies that the shear surface alteration is provided when the system is on the verge of failure or significant rut has developed, which as mentioned previously, cannot be tolerated by a flexible pavement system.

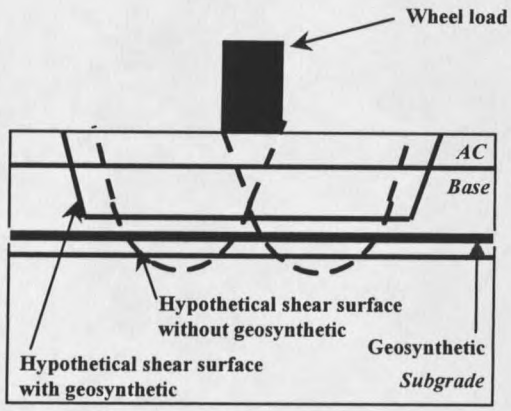


Figure 2.3. Shear surface alteration resulting in an increased bearing capacity.

The second and most probable reinforcement mechanism believed to account for increased performance of geosynthetic reinforced flexible pavements is that of lateral restraint. Lateral restraint is induced by frictional interaction (through direct friction or interlock in the case of geogrids) of the geosynthetic and surrounding soil. For this mechanism to be present, adequate friction must develop between the geosynthetic and the soil. In the case of geogrids, interlock of particles through the aperature of the grid provides adequate frictional resistance. For geotextiles, either direct frictional resistance between the soil and the material must be sufficient, or the reinforcement material must deform slightly into the subgrade soil to provide a dimpled effect (only in the case of low strength soils), resulting in satisfactory frictional characteristics.

Vertical, cyclic loading induces lateral spreading of the base course, which in turn induces tension in the geosynthetic. Load is transmitted from the surrounding soil into the geosynthetic. As the tension increases in the geosynthetic, the material confines the base material and increases the mean stress in the layer. With an increase in mean stress,

the base becomes "stiffer" and limits the shear failure mode. Another benefit of the base becoming "stiffer", is that load spreading characteristics of the base layer are improved. As load is spread more evenly across the subgrade, a less critical state of stress is developed, reducing rutting.

Additionally, the lateral restraint provided by the geosynthetic reduces the lateral spreading of the base aggregate, thereby reducing the subsequent vertical deformation, which would have normally occurred without the geosynthetic reinforcement being present. The mechanism also reduces the shear stress on the top of the subgrade, and spreads the load over the subgrade. The reduction in shear stress and lateral spreading reduces the net vertical strain experienced by the subgrade. The lateral restraint mechanism is believed to occur with small vertical deformations in the pavement system, which makes it ideal for flexible pavement applications. Figure 2.4 illustrates the lateral restraint concept.

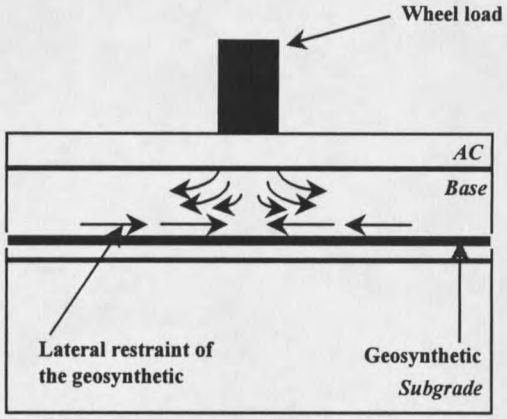


Figure 2.4. Illustration of the lateral restraint concept.

Previous Experimental Work

This section provides an examination of previous experimental work. This research includes experiments performed at the laboratory scale involving stationary, cyclic loads and field-scale experiments involving vehicular traffic. Also provided is a description of test sections including critical design parameters such as section thickness, geosynthetic location, geosynthetic type, subgrade strength, and loading conditions. Previous experimental work is critiqued if it is believed that the methods affected the outcome of the study significantly. Results, whether showing improvement or not, are also contrasted with other findings to provide a basis for the research performed as part of this study. The previous experimental work will be divided into three categories: 1) studies involving geogrid reinforcement, 2) studies involving geotextile reinforcement, and 3) mixed studies involving both geogrids and geotextiles.

Geogrid Reinforcement

The effect of geogrid reinforcement in model track tests was studied by Moghaddas-Nejad & Small (1996). The loading carriage provided a 210 kPa (30 psi) load over a 24.5 cm^2 contact area. The wearing course consisted of a cold-mix (proprietary Pavefix) which had a maximum aggregate size of 5 mm. This material was chosen as to be a prototype of ¼ scale of real asphalt concrete aggregate. Base course material was an A-1-a or SP uniform fine gravel. D_{10} and D_{60} were 2.0 and 4.0 mm respectively. A-3 silica sand was used for the subgrade material. A Tensar SS2 geogrid was used for reinforcement (aperatures of 40 mm and 28 mm in the longitudinal and

transverse directions). Thicknesses of the asphalt concrete, base, and subgrade were 20 mm, 40 mm, and 2000 mm respectively. Measurements were taken at the top of the asphalt layer (surface deformation), the top of the base course, and the top of the subgrade in only the vertical direction with LVDT's. The geogrid was not instrumented.

The authors showed that a geogrid placed in the middle of the base provided the best performance (70% reduction in surface deformation) for single-track and multiple-track tests with respect to surface deformation. This configuration also provided the smallest base course vertical displacement. Single-track loading was defined as a single unique path along which the wheel load traveled. The multiple-track tests included a sequence of nine random paths along which the wheel could travel, spaced 25 mm apart. The authors tried to disprove the tensioned membrane mechanism and showed that the maximum vertical geogrid deformation was less than 2mm, which they believed was insufficient to mobilize the membrane effect. They also showed that improvement of reinforced sections was substantial even at the point of only 100 load applications, where surface deformation was approximately 2-3 mm. Improvement over a small number of load cycles implies that the reinforcement was engaged immediately, rather than after large deformations as the tensioned membrane theory requires. The authors stated lateral confinement and interlocking with the base layer reduced the vertical displacement of the base layer, and acted as a "slab" in spreading the load to the subgrade. As the geogrid aperature size and stiffness was much larger than the aggregate size in the base layer of the proposed scaled down model, results in this study (with respect to improvement TBR ratios) may have been magnified somewhat due to scale effects.

A full-scale laboratory test on geosynthetic reinforcement of paved roads was conducted by Cancelli et al. (1996). A 1.8 m x 0.9 m x 0.9 m box was filled with 450 mm of Ticino siliceous sand, 300 mm of crushed limestone base with a maximum particle size of 30 mm, and 75 mm of asphalt concrete. The box was divided into two halves to construct and load both a control and a reinforced section at the same time. A 5 or 10 Hz load of 570 kPa was applied to the pavement surface through a 300 mm diameter plate, similar to that described in Haas (1986). Tests were constructed at subgrade California Bearing Ratio's (CBR) ranging from 1-18. Pavement sections were loaded to rather high deformations, up to 150 mm (2 inch). Several different types of geosynthetics were used in this research, which included multilayer biaxially oriented polypropylene geogrids, punched, biaxially-oriented polypropylene geogrids, biaxially oriented polypropylene geogrids manufactured by extrusion and orientation processing, polyester woven geogrid, and a slit film woven polypropylene geotextile.

Cancelli, et al. (1996) found that a punching shear failure near the edge of the load plate occurred in the AC layer in most tests. Reinforced sections exhibited less of the shear failure phenomena due primarily to better load spreading by the geogrid shown by permanent rut geometry across the pavement surface. Approximate traffic benefit ratios (at 25 mm rut depth) ranged from 1.53 (Amoco 6070) to 6.2 (Tenax LBO301) for a subgrade CBR of 3.0. Traffic benefit ratios (25 mm rut) ranged from 10-100 for several geogrids for a subgrade CBR=1.0. In addition, they found that improvement defined by TBR's increased for increasing rut depths, usually over 25 mm. The authors also showed that a geogrid reinforced section with a 300 mm base course performed slightly better in

terms of permanent deformation than an unreinforced section with a 400 mm base course. Results such as this provide promise for the use of the reinforcement technology where gravel is costly or scarce.

Another large loading facility was designed at the University of Alaska (Collin et al., 1996). The test facility consisted of a box 1.2 m deep, 2.4 m wide and 14.6 m long. A 20 kN load was applied by a rolling tire in one direction, and 9 kN in the opposite direction (180^0). Four tests involving stiff geogrids (Tensar BX-1100, 'Geogrid A' and Tensar BX-1200, 'Geogrid B') were constructed. Two tests involved placing the geogrid at the subgrade/base course interface and a third involved two geogrids placed at the interface and within the base course. The final section was an unreinforced control section. Asphalt thickness was 50 mm, base course thickness was 150-460 mm, and the subgrade was 200-500 mm in thickness. Average subgrade CBR was 1.9.

The authors found that the stiffer BX-1200 (5% secant modulus=320 kN/m MD) performed better than a less stiff BX-1100 (5% secant modulus=211 kN/m). They found the stiffer geogrid to be more sensitive to base thickness. TBR ratios obtained from this research ranged from 1.8-10 for 175-300 mm base courses constructed on subgrade CBR's of 3.0. A maximum TBR of 10.0 was obtained from the BX-1200 geogrid with a 250 mm base, as shown in Figure 2.5. The authors obtained TBR's similar to those of Haas (1985) (TBR=2.7-3.0 for geogrid A) and Webster (1992) (TBR=4.7 for geogrid B).

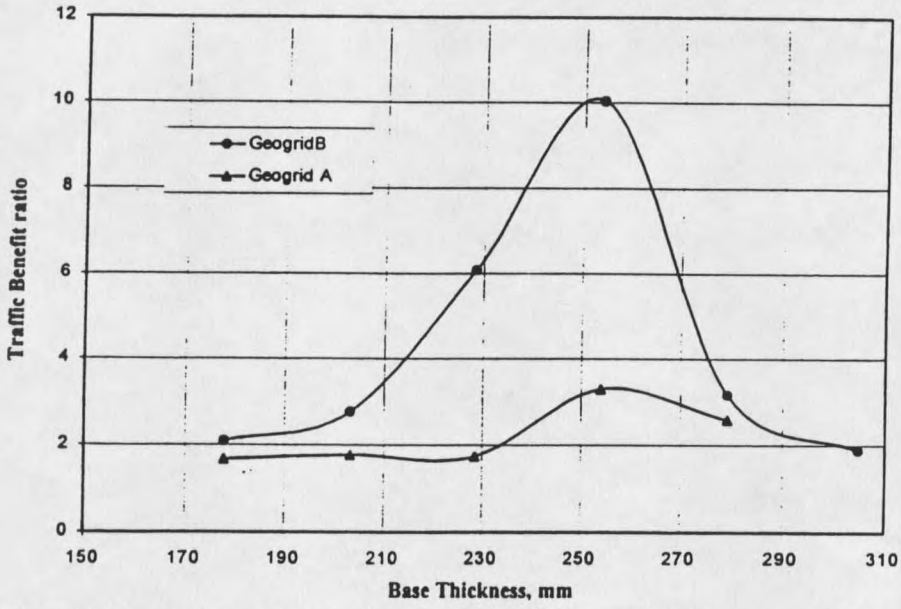


Figure 2.5 TBR versus base thickness for geogrid A and B (Collin et al. 1996).

Webster (1992) investigated the use of geogrids in reinforcing base courses for flexible pavements for light aircraft in full-scale field test sections. Webster investigated the importance of geogrid stiffness using a Tensar BX-1100 and BX-1200 geogrid. The subgrade consisted of a heavy clay (CH) material. CBR strengths of 3 and 8 were tested to be representative of low and high strength subgrades. A crushed limestone base course was used containing 12.3 % fines, which was considered to be low quality. All tests utilized a 50 mm AC surface, with maximum aggregate size of 12.7 mm and minimum Marshall Stability of 1500 lbs. It was noted that asphalt thickness varied from 56 mm to 66 mm thick, and averaged 61 mm thick. The geogrids specimens were not instrumented.

Webster did not observe any mixing between the base and subgrade. A TBR of 23 (at a permanent deformation of 25 mm) was obtained with the Tensar BX-1200 geogrid, corresponding to a base thickness of 152 mm and a CBR of 8. Initial elastic pavement deformations of reinforced versus unreinforced sections showed virtually no differences, implying that long-term effects such as the geogrid strength and creep properties may have influenced long-term deformation behavior.

Of interesting note from this study is that the maximum TBR values (based on 25 mm rut depth) were obtained with thin bases (150 mm to 200 mm). Figure 2.6 below summarizes several sections of varying base thickness with respect to TBR. In all cases, the geogrid was placed at the subgrade-base interface. Webster also found that the stiffer Tensar BX-1200 geogrid provided the best performance.

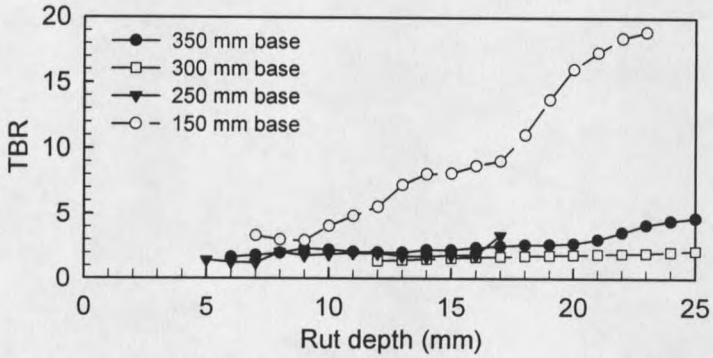


Figure 2.6. TBR versus rut depth based on results from Webster (1992) (from Perkins & Ismeik (1997a)).

Haas et al. (1988) utilized a 4.6 m x 1.8 m x 0.9 m box for an experimental test section. Loading was applied through a 300 mm diameter steel plate at a pressure of 550 kPa (80 psi). Loading frequency was 8 Hz. Dial gages were placed on the asphalt surface to measure surface deflections. Geogrids were instrumented with foil strain gages. Pressure cells were placed at the top of the subgrade in selected test sections.

Test variables included depth of reinforcement placement within the base course, base course thickness, and subgrade strength. Subgrade CBR strengths ranged from <1 to 8.0. A beach sand subgrade was used for all experiments, with some sections containing peat to yield low CBR values. Various CBR values were obtained by varying the water content. A Tensar BX-1100 geogrid was used for all tests.

Haas et al. (1988) concluded that geogrids may provide a TBR of up to 3.0 when properly located within the base course. The authors suggested that the optimal geogrid placement is at the bottom of thinner base courses and tending toward mid-base for thicker sections. Analysis of vertical stress induced on the top of the subgrade, strain in the geogrid, and surface deflection data showed that the load distribution characteristics of reinforced sections were quite different from unreinforced sections. Haas et al. (1988) also recommended placing the geogrid in a zone of moderate tensile strain (0.05-0.2% dynamic strain) and that permanent strain should not exceed 1-2%. It is the opinion of the author of this paper that this recommendation was made in order to prevent extensive plastic deformations of the geogrid from contributing to excess lateral deformation of the base layer. Excessive lateral deformations would lead to larger vertical deformations,

which are not desirable. In this case, a stiffer geogrid should be used which resists permanent strains better.

Table 2.1 gives section data for selected test sections from Haas et al. (1988). Figure 2.7 illustrates the TBR (for increasing rut depths) versus rut depth for the sections listed in Table 2.1. It is noted that the best results were obtained with the weakest subgrade conditions and placement of the geogrid at the mid-base position. Results with the same subgrade conditions but thinner base and placement of the geogrid at the base/subgrade interface provided the lowest TBR values. The differences between these two sets of sections implies that section thickness design and placement of the geogrid in a strain region as to not over strain the geogrid is very important. TBR values obtained from the stronger subgrade (sections 1 and 3) were high, which indicates there may be some validity to the use of geogrid reinforcement in cases of stiffer subgrades. Differences between TBR values between sections 11,12 and 15,16 may not be significant enough to determine effects of geogrid placement and/or reinforcement effects between subgrade strength differences.

Table 2.1 Test Section data from Haas et al. (1988) (from Perkins & Ismeik (1997a)).

Section	Geosynthetic Position	AC thickness (mm)	Base thickness (mm)	Subgrade CBR
1	Unreinforced	100	200	8
3	Middle of base	100	200	8
5	Unreinforced	75	300	1
6	Middle of base	75	300	1
11	Unreinforced	75	200	3.5
12	Bottom of base	75	200	3.5
15	Unreinforced	75	200	1
16	Bottom of base	75	200	1

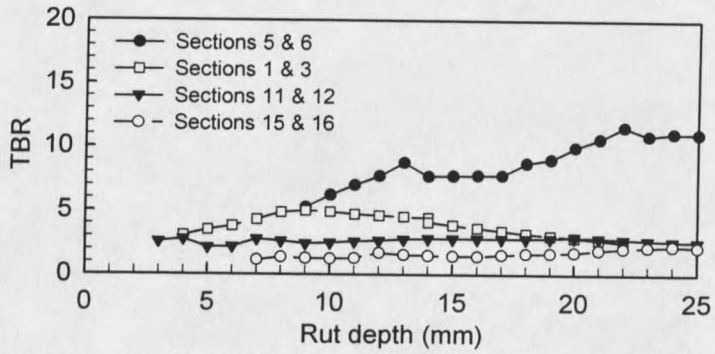


Figure 2.7. TBR versus rut depth from results of Haas et al. (1988) (from Perkins & Ismeik (1997a)).

As a summary, Haas (1988), suggested that a geosynthetic should provide appropriate interlock and should possess the following mechanical properties:

1) High tensile modulus to resist stretching under the load;
2) Dimensional stability to resist radial stresses without deforming, warping, or stretching;
3) Elastic response under dynamic loading (i.e small permanent strain development);
4) Resistance to plastic strain with repeated load applications;
5) Inertness and durability

Miura et al. (1990) conducted studies at both model and full-scale investigating the effects of geogrid reinforcement on soft clay subgrades (CBR=4-6). Materials investigated were Tensar BX-1200, and BX-1300 geogrids. Model tests were constructed in a box measuring 150 cm x 150 cm x 100 cm in depth. Model tests incorporated section thicknesses of 5 cm of asphalt, 35 cm of base, and 60 cm subgrade. Asphalt surface deformation was monitored via dial gages, and vertical pressure cells

were installed in the subgrade. Geogrid reinforcement was instrumented with strain gages. The model tests showed the BX-1200 geogrid to be most effective in reducing vertical surface deformation. Optimal placement for the grid was at the top of the subgrade, between the subgrade and base layers. The TBR's obtained at a deformation of 5 mm was 2.0-2.4 for the BX-1200 placed at the top of the subgrade and the subbase respectively. Interlocking and the tensioned membrane effect were noted for mechanisms responsible for behavior, but the authors believed placement in the field would not be appropriate to engage the tensioned membrane effect. Overall, not much difference was seen with placement depth.

Field tests by Miura (1990), incorporated section thicknesses of 5 cm, 15 cm, 20 cm (asphalt, base, and subbase) and a very large thickness of subgrade. The base course thickness was reduced by 5 cm for reinforced sections. From long-term results (6 months), it was concluded that the addition of a one-layer geogrid (BX-1200) was equivalent to 10 cm of base course. Figure 2.8 below shows section 4 (CBR=6, reinforced with Tensar BX-1300 geogrid, 20 cm base) and section 6 (CBR=4, reinforced with Tensar BX-1200 geogrid, 20 cm base) described by TBR versus depth. Fairly high TBR values were obtained with the two reinforced sections (TBR 5-17) with the sections performing relatively equal at higher rut depths. It is noted that the TBR decreases with increasing rut depth, which is contrary to the findings of both Haas et al. (1988), and Webster (1992). Both of those studies indicated increasing TBR with increasing rut depth. Apparently, some of the operating mechanisms or load distribution characteristics of the test sections are different between Miura (1990) and the other studies. The only

difference noticed was that Miura (1990) used a sub-base making the test sections a four-layer system. The four-layer system may have changed the load distribution characteristics of the section to cause the opposite trend of decreasing TBR with increasing rut depth.

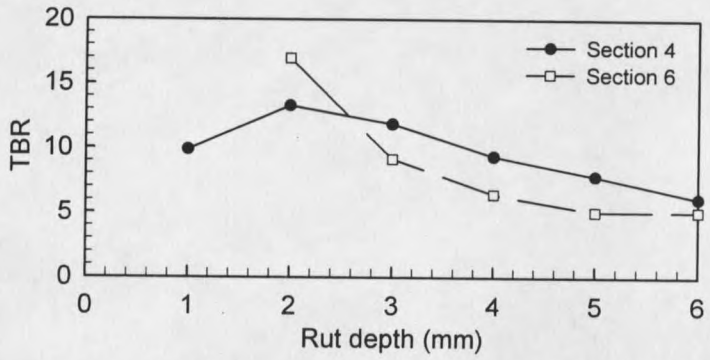


Figure 2.8. TBR versus rut depth from results of Miura (1990) (from Perkins & Ismeik (1997a)).

Kinney et al. (1998) and Kinney & Schuler (1998) developed an experimental program similar to earlier programs (Collin et al. 1996) using a moving cart providing a 550 kPa (80 psi) tire pressure to 61 mm of asphalt concrete. Subgrade soil was an alluvial sand and gravel mixed with additional silt and water to provide a CBR of on the order of 1.0. Variables in the study were base course thickness, tire pressure, and geogrid type. The two geogrids utilized (Tensar BX-1100 and BX-1200) had modulus values of 197 kN/m and 270 kN/m respectively. The BX-1100 geogrid had 39% open area (aperatures) while the BX-1200 had 70% open area.

Experimental results showed geogrid reinforcement improved rut behavior for base course thicknesses up to 400 mm thick. For thicker bases, reinforcement provided

no additional improvement. As expected, lower tire pressure (225 kPa versus 550 kPa) provided slightly higher TBR values and less rutting when compared to the control. For a tire pressure of 550 kPa (80 psi), the BX-1100 provided a TBR from 6-10 for a 200 mm thick base, a TBR of 4.5 for a 280 mm base, and a TBR of approximately 2.0 with a 360 mm thick base. Response was fairly linear between those three points. For the same conditions, the BX-1200 geogrid had a much steeper TBR versus base course depth curve, indicating that the stiffer material had a better benefit for the same base course thickness. For a 250 mm thick base course, the BX-1200 provided a TBR of 10, a TBR of 7.5 for a 280 mm base, and a TBR of 2 for a 360 mm base. The TBR versus depth of base was nonlinear for the stiffer BX-1200 geogrid. Additionally, deflection basins (rut depth versus distance from the applied load) showed mixed results between the control, BX-1100 geogrid, and BX-1200 geogrid for a thick 360 mm base course. Deflection profiles for thinner (235 mm base) showed the stiffer BX-1200 to have a smaller peak deflection and less-steep sides to the basin, than the BX-1100 and the control. These experimental results seem to indicate a stiffer geogrid may provide a longer pavement life or significant savings of gravel when used in thinner bases. It remains to be seen whether economic implications will negate the better performance of the stiffer geogrid.

Study Involving Geotextiles

A study by Halliday & Potter (1984), concluded that the incorporation of a woven polyester geotextile (ultimate strength 83 kN/m) at the base course/subgrade interface of

both a macadam (bitumen reinforced) surfaced and granite base course (unsurfaced) did little to improve the permanent deformation of the pavement. The authors constructed laboratory-scale sections on a low-strength subgrade (CBR=2.5). Loading was provided by rolling lorries on a test track and sections were loaded to approximately 75,000 standard axle loads. Measurements were taken of subgrade vertical stress, vertical strain, and transverse strain. Longitudinal and transverse strains were measured in the base course. Macadam surface thicknesses evaluated were 160 mm and 220 mm. Granite base course thickness was 300 mm. Asphalt surface thickness was variable due to variations in optical level measurements.

It was noted in all experimental measurements that results were clearly correlated to the thickness of the asphalt concrete layer, which had a variation in thickness throughout the sections. It was also noted that longitudinal and transverse strains at the bottom of the layer were unaffected by the inclusion of a geotextile which may provide insight into a geotextile providing poor lateral confinement due to shear interaction with the base course particles. Transient vertical stress and strain in the subgrade soil was also unaffected by the geotextile. The authors did note, however, that construction was easier with the geotextile, which provided a separation function between reinforced and unreinforced sections. 70 mm of contamination from the subgrade into the base course was seen in the control sections, which may be a function of construction techniques and/or loading conditions. This mixing was attributed to compaction. Additional material was needed in the control sections to provide the same total thickness due to the 70 mm of mixing.

Mixed Studies (Geogrids and Geotextiles)

Large-scale laboratory experiments, involving both geotextiles and geogrids were carried out by Barksdale (1989). A 4.9 m x 2.4 m linear test track utilized a 7 kN wheel load moving at 4.8 kilometers per hour. Up to 70,000 loads were applied to the pavement surface. Contact pressures were between 462 kPa (67 psi) and 504 kPa (73 psi).

With very weak sections (CBR< 3.0), inclusion of a stiff geotextile at the bottom of the base course reduced the amount of surface rut by 44% compared to a control section. Barksdale also found that a major portion of the total deformation occurred within the aggregate base. Permanent deformation in the subgrade was small compared to that in the base course. The author illustrated a trend of large permanent vertical strain at the top of the base course decreasing rapidly with depth towards the subgrade. Barksdale found a decrease of permanent strain in the top of the subgrade but an increase in vertical strain in the top of the base course, when comparing the reinforced section to control sections. Another interesting point related to reinforcement effects on the subgrade, showed that only the top 150-180 mm of the subgrade were affected (i.e. differences in stress and strain in the material).

With respect to geosynthetic placement within the base, a geotextile (750 kN/m, at 5% strain) placed at the subgrade/base interface had a 57% reduction in the permanent deformation in the subgrade but only a 3% reduction in the base. A geotextile placed in the middle of the base reduced permanent base deformation by 31% and permanent subgrade deformation by only 14%. A geogrid placed at the interface did not decrease permanent deformation in the base (measurements showed a 5% increase), and showed a

52% improvement in permanent subgrade deformation. He found a geogrid of less stiffness (300 kN/m at 5% strain) compared to a geotextile (stiffness=750 kN/m at 5% strain) placed at mid-base performed better (6.6 mm rut with the textile compared to 4.6 mm rut with the geogrid) than the geotextile.

For a typical pavement section designed for 2,000,000 ESALs (AC thickness 165 mm, base thickness =165 mm, subgrade modulus=24,000 kPa), Barksdale et al. (1989) showed from analytical model predictions little or no improvement in stress/strain distributions and rutting with the inclusion of a geosynthetic.

In summary, Barksdale et al. (1989) recommended minimum stiffnesses for a geogrid of 260 kN/m and 700 kN/m for a geotextile (5% strain secant moduli) to be used with subgrades of CBR< 3.0, and recommended placement of the reinforcement at the base/subgrade interface. Barksdale et al. (1989) also stated that little improvement was seen for an AC thickness greater than 65 mm based on his evaluation of the design 2,000,000 ESAL experimental tests. The stated reason for geosynthetic improvement of pavements was that the presence of a geosynthetic caused a small increase in confining stress and reduction in vertical stress in the base and in the upper 150-180 mm of the subgrade. This statement may imply that the lateral restraint mechanism was involved in improvement. The lateral restraint may have increased the stiffness of the base and may also be the reason for a decrease in vertical stress on the subgrade. Without further quantitative analysis, the determination of the lateral restraint mechanism being solely responsible for improvement is difficult at best.

Al-Qadi et al. (1994) conducted laboratory studies of geosynthetic reinforced pavements in a test box measuring 3.1 x 1.8 x 2.1 m deep. Subgrade material was a Yatesville silty-sand with a CBR strength of 4.0. 70 mm of AC surfacing was placed over 150 mm of basecourse. Amoco 2002 and 2016 geotextiles (5% strain 8.9 kN/m and 10.3 kN/m respectively) as well as a Tensar BX-1200 biaxial geogrid (5% strain 10.3 kN/m) were used for reinforcement. All materials were placed at the base/subgrade interface. A 550 kPa presure was applied at a rate of 0.5 Hz through a stationary steel plate 30 cm in diameter. Loading was commenced until 25 mm of rut depth was obtained.

The control sections deformed 12.5 mm after only 25 cycles which may imply that the control sections were underdesigned. The two geotextiles performed better than the geogrid section (TBR's of 6,7 and 3 respectively). The authors attributed this to mixing of the subgrade/base. The geotextile sections failed (25 mm of rut) after about 1200-1400 cycles which also implies that those sections were underdesigned.

Another field-scale series of reinforced flexible pavements was constructed by Brandon et al. (1995). Nine experimental sections were constructed over a sandy-silt (ML) material with an approximate CBR of 7. The AC thickness was 89 mm and base thicknesses ranged from 100-200 mm. Pressure cells, gypsum blocks (moisture content), and soil strain gages were placed in the base and subgrade layers. AC strain gages were placed in the asphalt layer. Core samples taken from the AC layer of the sections ranged from 78 mm to 99 mm thick. Table 2.2 gives section data for the nine 15 meter long test sections. Three sections had missing thickness data for cut cores (sections 2,6, and 8),

which were geotextile, geogrid, and geotextile reinforced sections respectively. Survey measurement of section 8 indicated a maximum AC thickness of 128 mm.

Table 2.2 Test section data from Brandon et al. (1995).

Section	Geosynthetic	AC thickness (mm)[a]	Base thickness (mm)
1	Unreinforced	77.7	102
2	Geotextile	N/A	102
3	Geogrid	99.0	102
4	Unreinforced	97.8	152
5	Geotextile	90.7	152
6	Geogrid	N/A	152
7	Unreinforced	88.9	203
8	Geotextile	N/A	203
9	Geogrid	85.6	203

[a] Thickness reported from AC cores.
N/A = Not Available

Brandon et al. (1996) presented results from the field-scale experiments. Strain gages were placed on the bottom side of the geotextile and geogrid specimens. Survivability ranged from 6% on the geotextile specimens to 28% for the geogrid foil strain gages over the first eight months. Strain gage results were presented in Bhutta et al. (1998). Strain results were few in number (one geotextile gage and one geogrid gage) and were presented for the perpendicular direction of traffic.

Rut depth versus time measurements were also presented in Bhutta et al. (1998). Results are a bit difficult to interpret for the first year, due to missing data for the first two to three months of operation. By November 1997 (testing commenced August 1994), the control section with 100 mm of base performed very poorly with respect to the corresponding reinforced sections. The textile performed a bit better (by 4 mm) than the

geogrid reinforced section. For the thicker 150 mm base, sections 4-6 and 7-9 were performing about the same.

By November 1997, the geogrid reinforced (section 6) had performed the best, while the geotextile reinforced (section 8) performed a bit worse. Interestingly, one of the control sections (either 4 or 9) performed better than any sections from December 1994 to approximately May 1996, and then began to accelerate rut depth. Measurements for these two control sections are not shown past October 1996. It is also difficult to determine how the variations in AC thickness shown in Table 2.2 affected outcomes of the experimental sections.

Appea et al. (1998) reported results from the experimental program of Brandon et al. (1995) investigating the use of FWD results to predict the separation/contamination function of geotextiles and geogrids. A modulus back calculation program MODULUS was used in conjunction with KENLAYER and ELSYM5 to obtain a transition layer near the subgrade/base interface which was interpreted to be contaminated from cyclic moving wheel loads. The authors stated that geotextiles in the sections provide the separation function while geogrids partially provide that function. Between experimental section 1 (control) and experimental section 3 (geogrid), it appeared that the development of the transition layer (contamination), started lower with the geogrid (0 mm for the geogrid versus 13 mm for the control section), but increased at a faster rate than the control section. This difference occurred up to a period of one year where afterwards the two sections were approximately equal. From this point on, both sections appeared to have

no mixing occurring, which may be due to increasing subgrade strength due to moisture loss or consolidation.

Conclusions

From the previous experimental studies, the promise of geosynthetics for reinforcement of the base layer remains promising (Moghaddas-Nejad & Small, 1996; Cancelli et al., 1996; Collin et al., 1996; Webster, 1992; Miura, 1990; and Kinney et al., 1998). Other studies (Halliday & Potter, 1984; Barksdale, 1989; and Brandon et al., 1995) have shown mixed results. These mixed results may be based on construction techniques or may be based on material parameters such as subgrade strength. However, the experimental studies have indicated that results are very dependent on the following: layer thickness (particularly the base layer), layer stiffness (particularly the subgrade), geosynthetic type, and geosynthetic placement within the base layer. It also appears from the literature that the mechanisms at work are not well understood because they are not easily quantified. Many efforts (Moghaddas-Nejad & Small, 1996; Cancelli et al., 1996; Collin et al., 1996; Webster, 1992; Kinney et al., 1998; and Brandon et al., 1995), have instrumented the AC surface and the top of the subgrade layers, but with a limited number of instruments that could not describe the stress/strain behavior in light of reinforcement. Instrumenting the geosynthetic with strain gages is another way to more accurately describe the mechanisms involved. In addition, construction quality control must be maintained to high standards for research attempts.

From the previous studies, it appears that geosynthetics are well suited for reinforcement in conditions of soft subgrades (CBR<8.0), and that both geogrids and geotextiles have merits in certain situations. Stiffer materials appear to function better (higher lateral restraint), but the benefits may be offset by the additional costs of stronger materials. Reinforcement also appears to function best when placed at the subgrade/base interface or in the bottom half of the base. It remains to be seen if placement within the base is feasible for construction with thin bases. Additionally, the reinforcement potential is maximized with thin (100-150 mm) to medium thin base courses (300-375 mm).

The research at Montana State University will try to address some of the main variables discussed previously, with an attempt to accurately describe, in a mechanistic way, the behavior of reinforced sections with both geogrids and geotextiles. The research will also attempt to describe reinforcement benefits in a strong subgrade material (CBR=15-20). Chapter 3 presents the experimental apparatus and techniques used in constructing the test sections.

CHAPTER THREE

EXPERIMENTAL METHODS

Introduction

This chapter provides information on the procedures used in constructing, instrumenting, and testing the experimental pavement sections. A total of 21 sections were completed to provide a large database of information that could be used to describe the reinforcement effects of incorporating a geosynthetic into the base course layer of a flexible pavement system. Nine sections were constructed using a silty-sand subgrade and twelve sections were constructed using a clay subgrade. One of the twelve clay sections was termed a "preliminary" section, which contained limited instrumentation designed to provide information on instrument response. Terminology used for naming sections in this report is as follows: 1) Silty-Sand Subgrade tests are termed "SSS", 2) Clay Subgrade tests are termed "CS", and 3) The Preliminary Clay Subgrade test was termed "PCS". Test sections are then numbered in the order performed.

Test section variables studied and implemented into the experimental program consisted of subgrade type, geosynthetic type, location within the base course, and base course layer thickness. Construction of the 21 test sections included in this report began in December, 1996 and terminated in November, 1998.

Laboratory Test Facility

Test Box and Loading Apparatus

A test box was constructed having inside dimensions of 2 meters in width and length and 1.5 meters in height. Walls consisted of 150 mm thick reinforced concrete. The bottom was left open to allow for any drainage that may occur from the subgrade. The front wall is removable in order to facilitate removal for excavation of the test sections. The front wall is attached by large 25 mm diameter bolt and nut assemblies. The box was constructed with reinforced concrete in order to minimize lateral movement when the dynamic 40 kN load was applied to the pavement surface. Figures 3.1 and 3.2 show an isometric view and front view schematics of the test box and loading apparatus.

I-beams were set into the concrete and served as a base for the loading frame. The I-beams also allowed the load-frame to be moved such that the load could be applied at various locations across the pavement surface. The usefulness of a movable load is discussed later. The loading apparatus consists of two I-beams set perpendicular to the I-beams set into the concrete walls of the box.

The load actuator is placed between the two I-beams. The loading assembly consists of an air-operated actuator with a 305 mm bore connected to a 50 mm diameter steel rod. This steel rod is approximately 300 mm long and is rounded at its bottom end. The rounded portion of the loading rod fits into a cup welded on the load plate. This "ball and joint" connection provides some flexibility of rotation between the load plate and the loading rod.

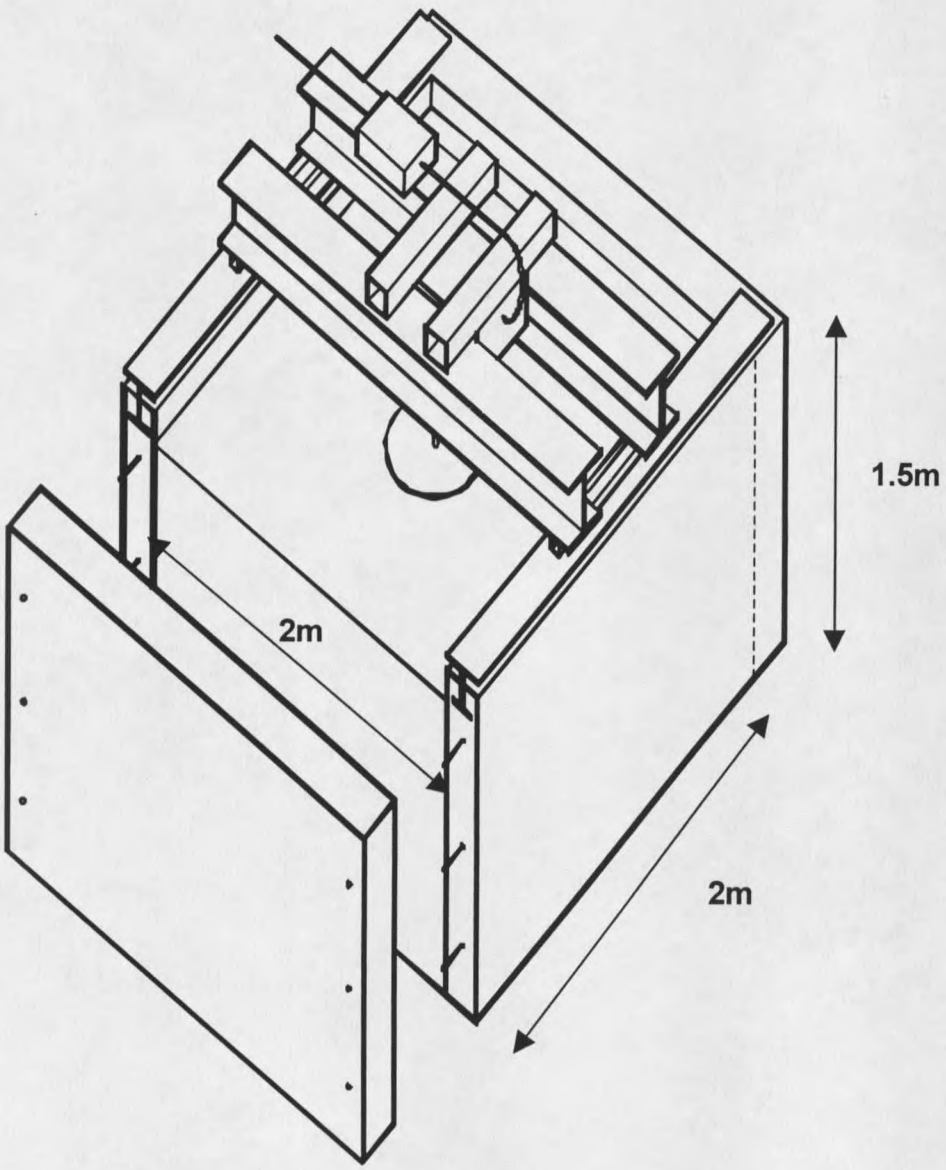


Figure 3.1. Isometric view of the test box and loading apparatus.

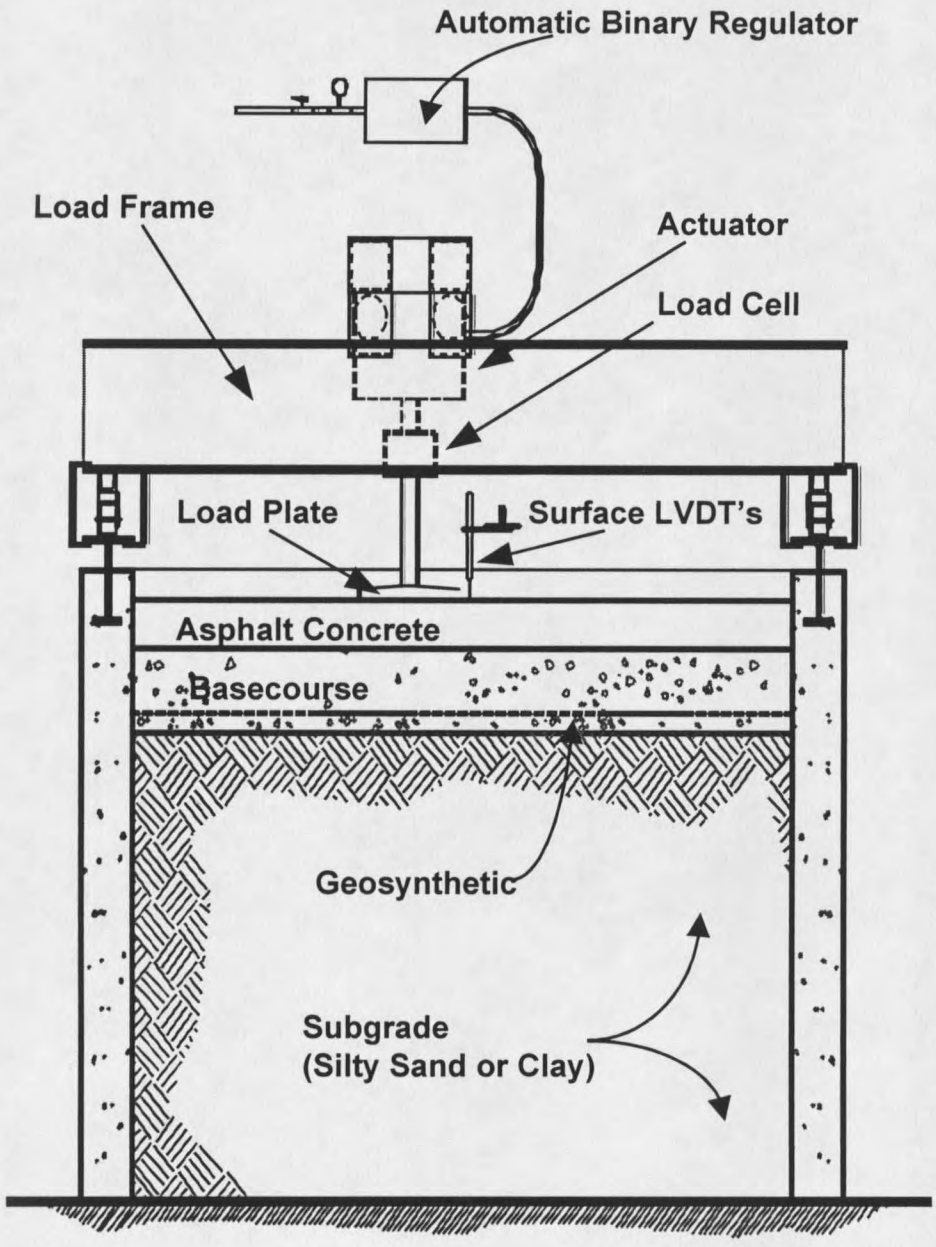


Figure 3.2. Schematic of apparatus components and pavement layers. Note: Load not shown in center of box to illustrate movement capabilites.

A circular, 305 mm diameter load plate with a thickness of 25 mm was machined out of steel. A 4 mm thick, waffled butyl-rubber pad was placed beneath the load plate in order to provide a uniform pressure and avoid stress concentrations along the plate's perimeter. Figures 3.3 and 3.4 show pictures of the test box and the load plate resting on the pavement surface.

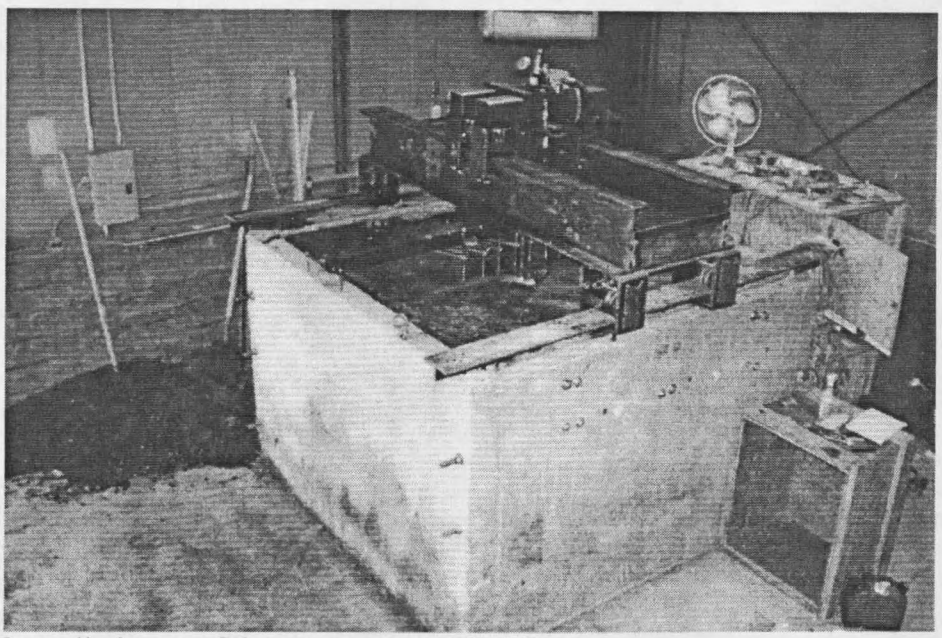


Figure 3.3. Overall picture of the pavement test facility.

Instrumentation

Instrumentation used in the test sections allows for examination of reinforcement mechanisms occurring during dynamic loading and a mechanistic interpretation of pavement response. Results solely based on asphalt concrete surface deformation (rut) are not sufficient and are more valuable when combined with experimental results that describe individual material layer behavior inside the test section.

The test sections contained as many as 100 instruments measuring stress, strain, temperature, and moisture content. Instrumentation has been categorized into instruments measuring asphalt surface deflection, tensile strain in the asphalt concrete, stress and strain in the base course and subgrade, strain on the geosynthetic, and general instrumentation measuring water content and temperature of the pavement system. The next five sections will describe the different categories of instrumentation used in the test sections.

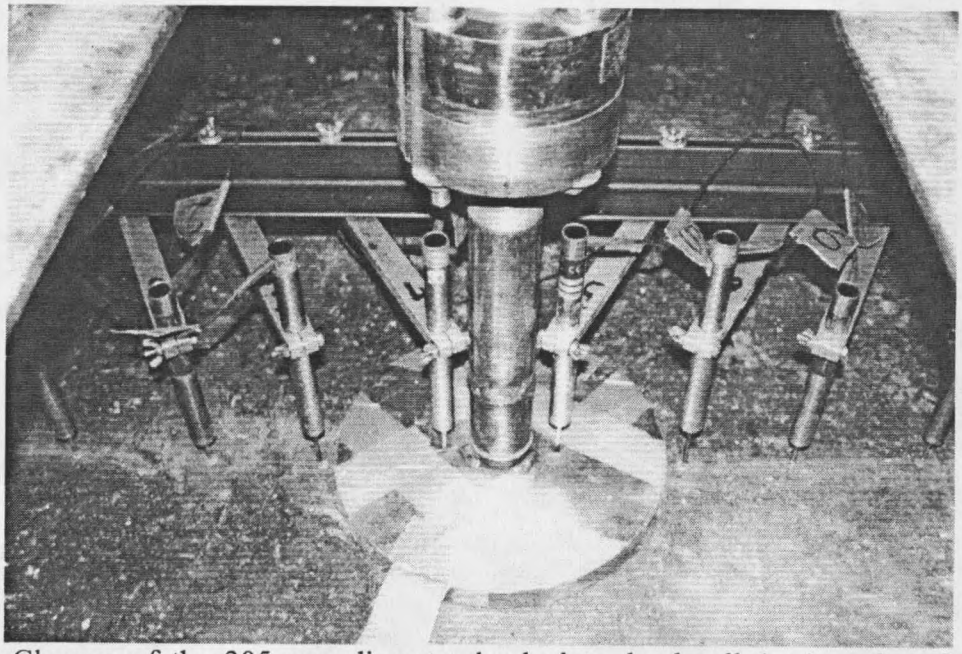


Figure 3.4. Closeup of the 305 mm diameter load plate, load cell (top), and surface LVDT's resting on the pavement surface.

Asphalt Concrete Instrumentation. Linear variable differential transducers (LVDT's) were placed vertically on the asphalt concrete surface to measure surface deflection during loading. These gages are manufactured by RDP Electronics (Pottstown, PA). Two different gages were used with ranges of 25 mm and 50 mm. The

LVDT's with the greatest range were placed closest to the center of the load plate where the largest surface deformations occurred. The other gages were placed at increasing radial distances (100 mm spacings) from the load centerline. These instruments are shown in their respective orientation on the asphalt surface in Figure 3.4. The surface LVDT's provide a smooth asphalt surface deflection bowl (asphalt deflection across the pavement surface) for a given load pulse and an accumulation of permanent deformation with load cycle number. A typical deflection bowl is presented in Figure 3.5.

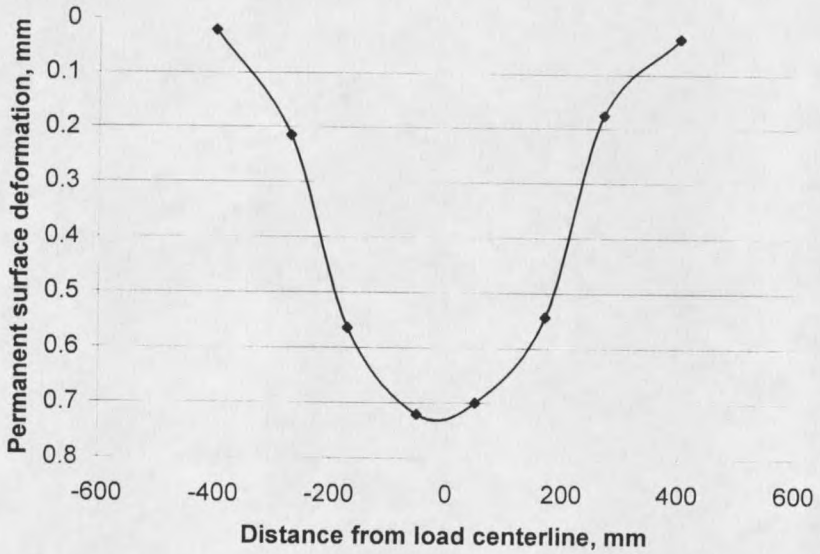


Figure 3.5. Typical plot of permanent surface deformation after 5 load cycles for test section CS1.

H-type, PAST (PAvement Strain Transducer) asphalt strain gages manufactured by Dynatest, Inc. (Ojai, CA), were used to measure tensile strain in the bottom of the asphalt concrete. The gages measure 135 mm in length and 70 mm in width and are shown in Figure 3.6. These gages have a range of approximately 1500 microstrain

(0.15%). The inside of the gage consists of a strain gage embedded in a strip of glass-fiber reinforced epoxy that has a high flexibility and relatively low strength. A multi-layer coating protects the gage from chemical effects. The average elastic modulus of the cell body is 2.2 MPa, resulting in a low "strain force" of 0.11 N/microstrain. Hence, material surrounding the gage is not highly influenced by installation of the strain gage. Fatigue life of the gage is theoretically estimated at 1 x 10^6 cycles. Figure 3.7 illustrates the various coatings and components of the AC strain gage.

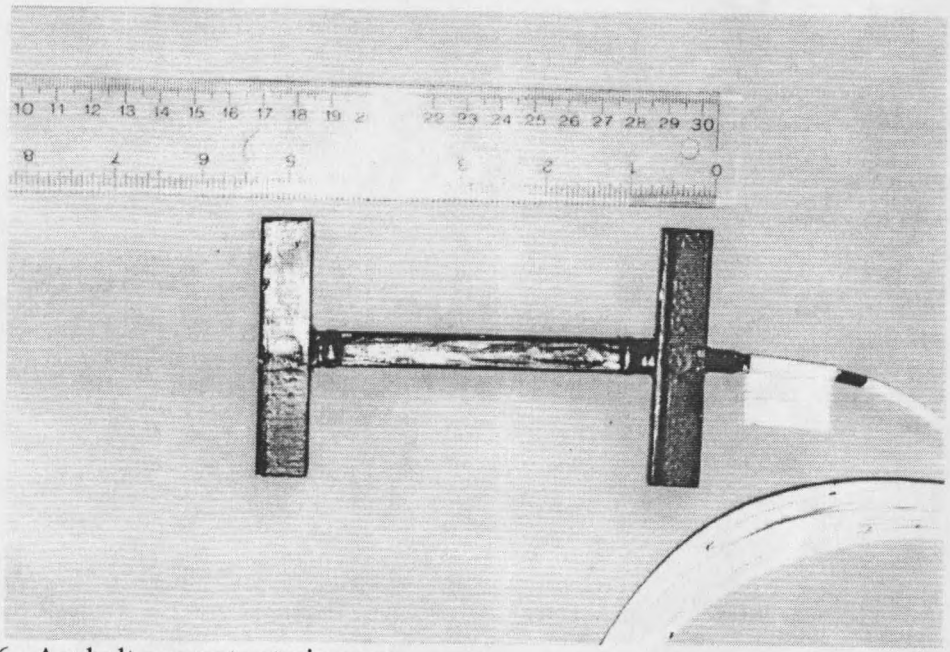


Figure 3.6. Asphalt concrete strain gage.

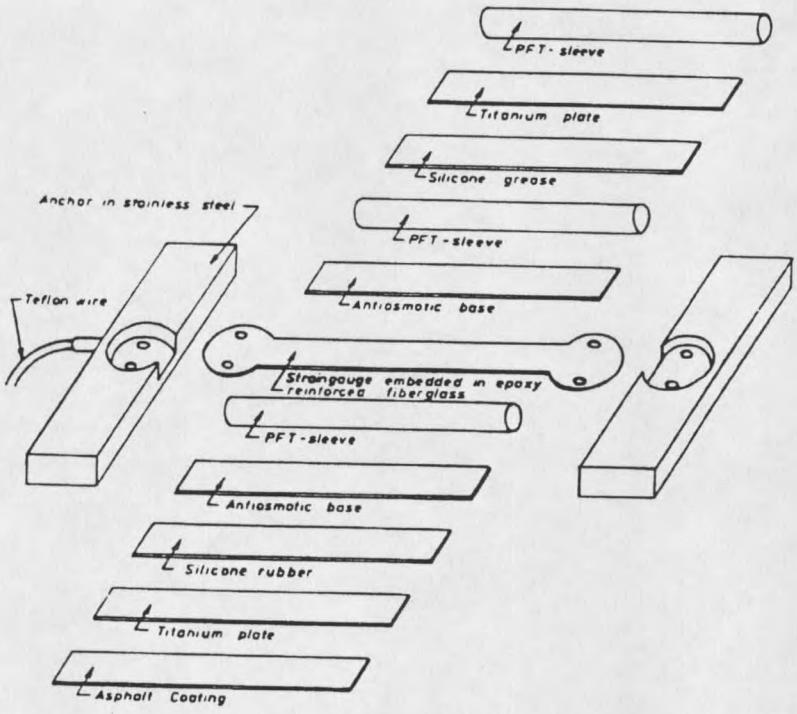


Figure 3.7. Different components of the Dynatest H-type PAST (Dynatest, 1991).

Geosynthetic Instrumentation. Foil strain gages were mounted to geogrid and geotextile samples in order to quantify in-situ strain behavior during pavement loading. Measuring strain on the geosynthetic provides another means of quantifying mechanisms associated with geosynthetic reinforcement. Small, 18 mm long strain gages (Micromeasurements Group, Inc., model EP-080500GB-120) were used for the geogrid specimens. These gages have a range of approximately 20% strain, and a fatigue life of approximately 10,000 cycles under 0.1% dynamic strain. 110 mm long foil strain gages (Micromeasurements Group, Inc., model EP-08-40CBY-120) were attached to geotextile specimens. These gages also have a range of approximately 20% strain, but only 10% of the range was utilized for greater sensitivity. Figure 3.8 shows the two foil strain gages

used in this study. Attachment of the foil strain gages to geosynthetic samples is discussed later in this chapter under the section "Test Section Construction".

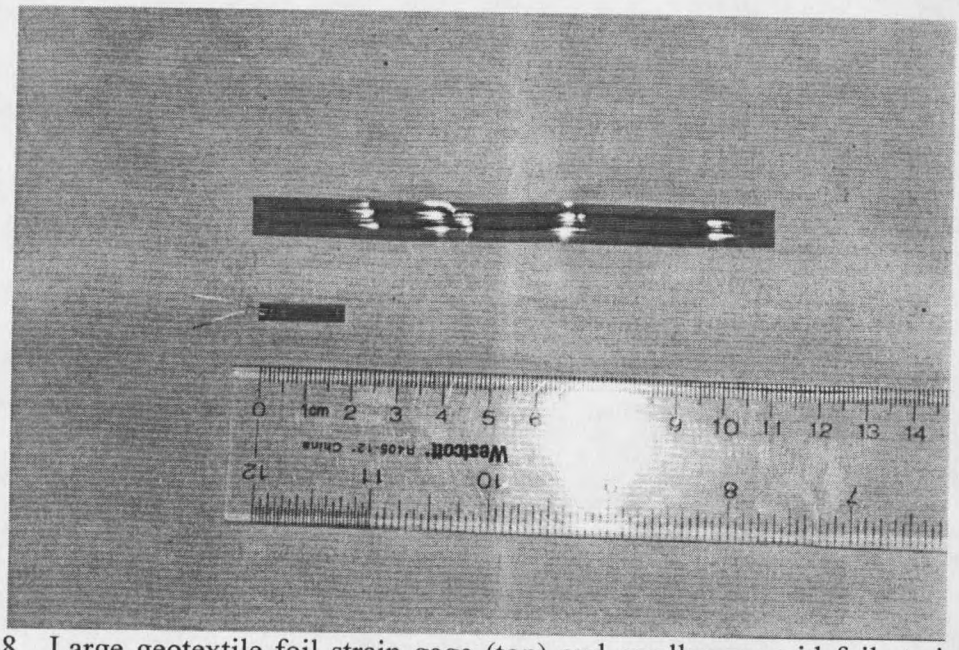


Figure 3.8. Large geotextile foil strain gage (top) and smaller geogrid foil strain gage (bottom).

Base Course and Subgrade Instrumentation. Stress cells were placed in both the base course and the subgrade in order to quantify the dynamic stress behavior of the system. The stress cells were obtained from Dynatest, Inc., (Ojai, CA). The cell utilizes a thin membrane (0.5 mm thick) that covers a layer of fluid. Fluid pressure is measured by a pressure transducer (fully-bridged strain gage) inside the cell. The cells are coated with epoxy and sand to insure proper bonding to soil materials. Fatigue life is listed at 3 X 10^6 cycles. Two types of stress cells were utilized in the test sections having different operating ranges. Type A stress cells were placed in both the base course and subgrade having a range of 10-200 kPa. Type B stress cells having a maximum range of 800 kPa,

were placed in a horizontal orientation (measuring vertical stress) in the base course directly beneath the load plate. The type B cells were placed directly beneath the load because of higher pressures expected. A typical stress cell is pictured in Figures 3.9 and 3.10.

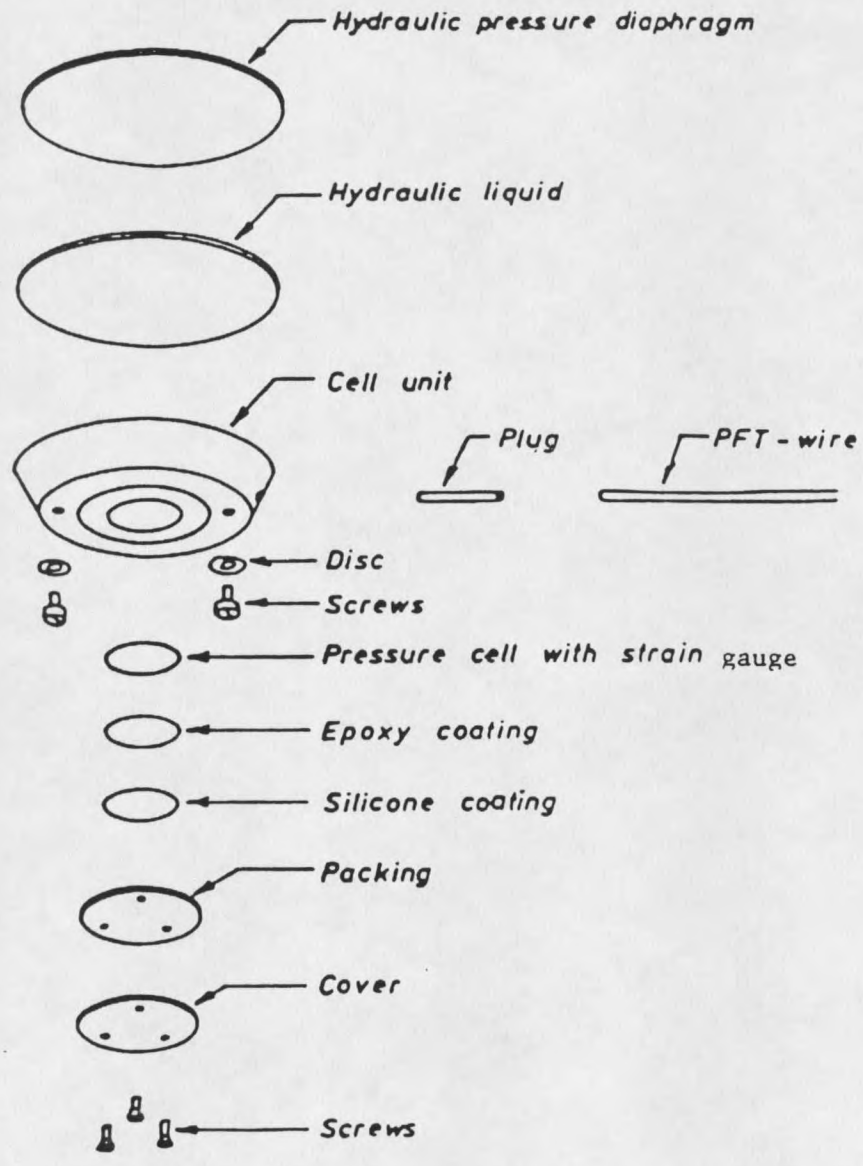


Figure 3.9. Dynatest SOil Pressure Transducer (SOPT) (Dynatest, 1991).

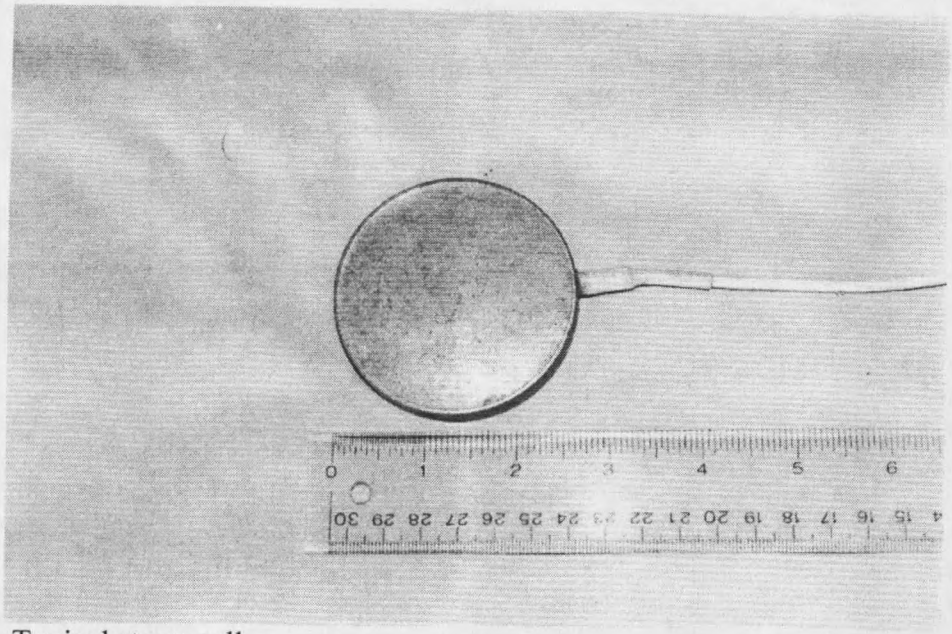


Figure 3.10. Typical stress cell.

Strain in both the base and subgrade was measured by alternating current (AC) LVDT's fitted with steel end plates measuring 50 mm x 15 mm x 5 mm in thickness. The LVDT's (model D5/400W) were obtained from RDP Electronics (Pottstown, PA). The gages have a nominal gage length of 70-80 mm, which corresponds to a 0.2-10% strain range depending on the electronic amplification used for the sensor. A typical LVDT used in test sections is shown in Figure 3.11.

General Instrumentation. Temperature probes from RDP Electronics (Pottstown, PA), were used in certain tests to correct stress cell readings for temperature variations. It was noticed that some stress cells drifted by as much as 2-5 kPa when a temperature variation of 8.3 degrees Celsius occurred. The temperature probes allowed the stress variations due to temperature to be corrected, especially in the summer test sections

where diurnal temperature variations in pavements layers were as much as 4 degrees Celsius.

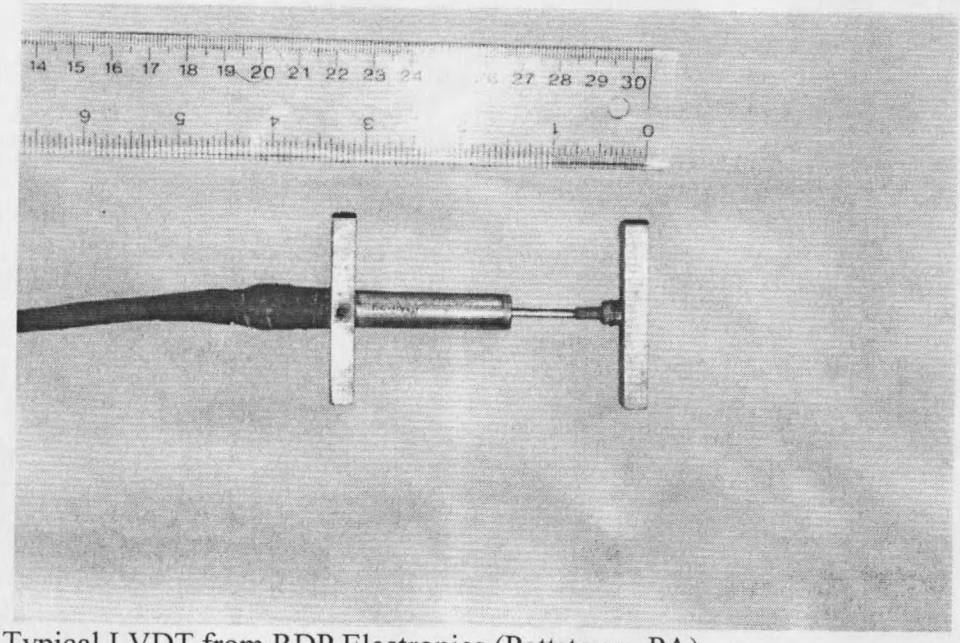


Figure 3.11. Typical LVDT from RDP Electronics (Pottstown, PA).

Moisture content probes (time domain reflectometry) were used for certain test sections, but were found to give erratic readings when compared to moisture contents (oven drying) taken during construction and excavation of the test sections. Thus, the probes were eliminated from the experimental program after the silt subgrade sections were completed.

The data acquisition system consisted of several groups of amplifiers (RDP model 611) connected to a laptop computer running Labview Software marketed by National Instruments. Instruments were connected to the amplifiers, which supplied excitation voltage to the sensors through 7-pin DIN connectors. Return signals from the instruments were amplified and sent to the software program. The software saved

specific full-cycle (instrument response during one cycle of load application) information for a particular load pulse for all instruments, as well as long-term peak and minimum responses for each instrument to a data file. Labview also allowed specific control over load-pulse duration and frequency, which will be discussed in more detail in the "Pavement Loading" section in this chapter. The software provided onscreen, real-time viewing of data generated by any of the instruments in a test section. As many as four instruments could be viewed at any one time on the screen. A typical view of the amplifiers and the Labview on-screen display and real-time graphs is shown in Figure 3.12.

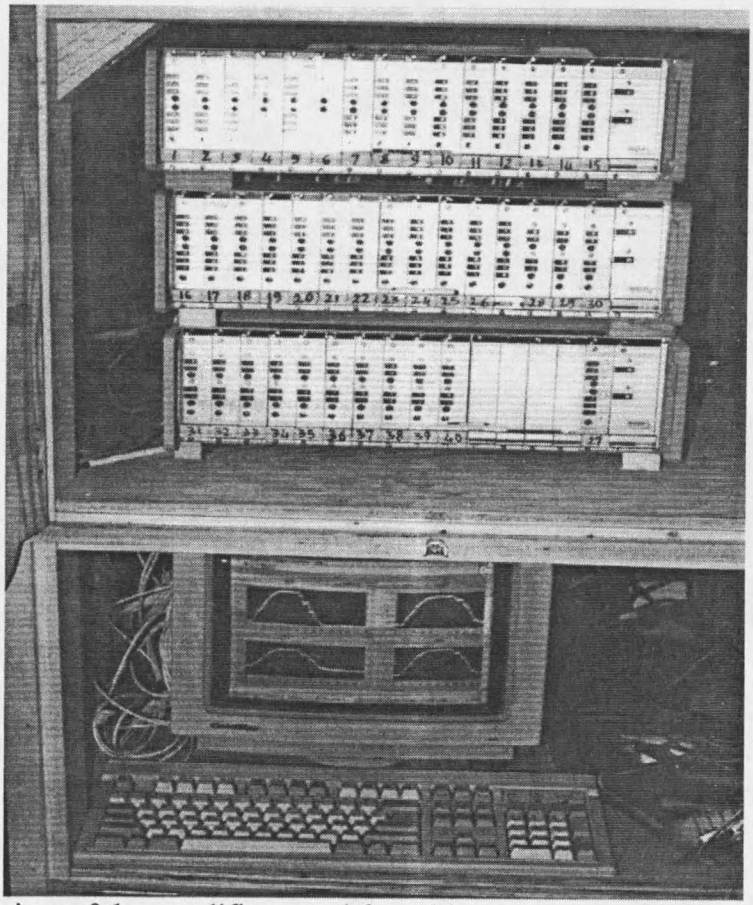


Figure 3.12. A view of the amplifiers used for all instruments and the corresponding on-screen output from Labview.

Pavement Layer Materials

Asphalt Concrete

Hot-mix asphalt concrete was used for silty-sand subgrade sections (SSS) 1-4, for clay subgrade sections (CS) 1-11, and PCS1. The aggregate gradation met the Montana Department of Transportation specifications for a Grade A mix design. Asphalt cement used was PG 58-28 and asphalt content was approximately six percent. The hot-mix was delivered via truck from a local batch plant in approximately 2700 kg (3-ton) loads. Mix in excess of that needed for the test section was ordered in order for the batch to remain hot while placement occurred.

Cold-mix asphalt concrete (MC-800 asphalt cement) was utilized for sections labeled SSS5 through SSS9. Cold-mix was used because of the unavailability of the hot-mix plants during winter months. Particle size distributions for both the hot-mix and cold-mix are shown in Figure 3.13. Specific properties of the AC in each test section are given later in the section "As-Constructed Test Section Properties" in this chapter.

Base Course

A crushed-stone base course meeting the Montana Department of Transportation specifications for Type A, grade 3 was used for all experimental test sections. The base course particle size distribution is shown in Figure 3.7, where it is seen that 100% passes the 19 mm sieve. The material is classified as an A-1-a or a GW. Modified Proctor tests resulted in a maximum dry unit weight of 21.5 kN/m^3 at an optimum moisture content of 7.2%. This material was typically compacted at a water content of 6.3% and to a dry unit

weight of 21 kN/m^3. Specific test section details with respect to individual layer densities and water contents are given in the section "As-Constructed Test Section Properties".

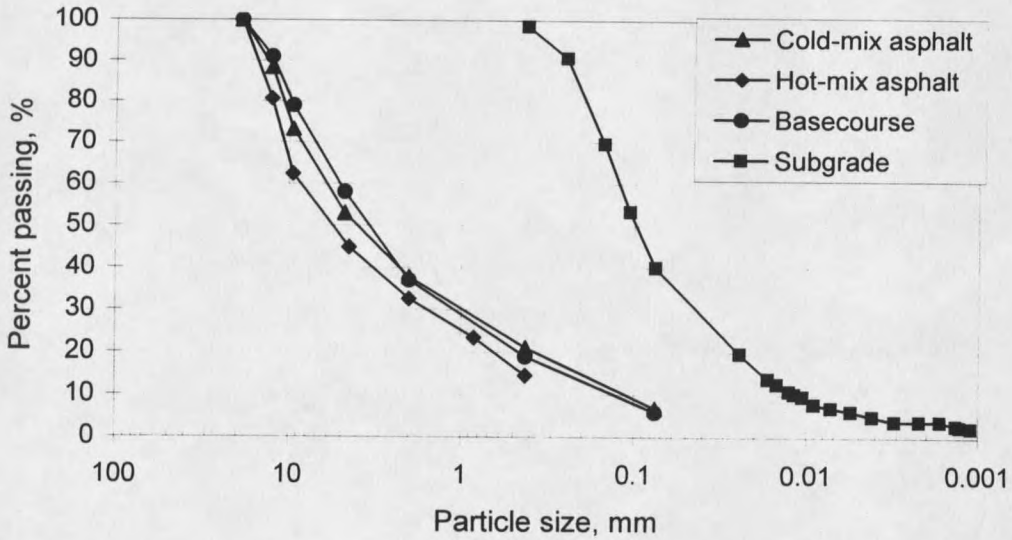


Figure 3.13. Grain size distribution of cold-mix aggregate, hot-mix aggregate, base course, and silty-sand subgrade.

Subgrade Materials

Two different subgrade types were utilized in this study in order to provide information on the influence of subgrade strength on reinforcement benefit. A silty-sand was used for a "strong" subgrade, while a native clay was used for the "weak" subgrade.

The stronger subgrade (approximate CBR=15 at a moisture content of 14%) consisted of fines trapped from the baghouse of a local batch hot-mix plant. The material is classified as a SM or A-4, with 40% fines and a liquid limit of 18%. Modified Proctor tests indicate the A-4 material has a maximum dry unit weight of 18.2 kN/m^3 occurring at a moisture content of 11.5%. This material was typically compacted at a water content of

14.8% and a dry unit weight of 17.5 kN/m^3. Specific test section details with respect to individual layer densities and water contents are given later.

The weaker subgrade consisted of a CH or A7-(6) clay, having a liquid limit of 100% and a plastic limit of 40%. 100% of the clay material passed the #200 sieve. Modified Proctor analyses indicate a maximum dry unit weight of 16.0 kN/m^3 occurring at an optimum moisture content of 20.0%. Typically, the clay was compacted at a water content of 45% in order to obtain CBR values of approximately 1.5, to simulate spring thaw or very weak subgrade conditions in the field. Figure 3.14 shows the CBR variation (from unsoaked laboratory tests) with water content, which was used to obtain a test section design water content. It is also noted that only a relatively small change in CBR results between a water content range of 43-46%. Typical compaction values obtained from the test sections yielded a dry density of 11.5 kN/m^3 at a corresponding moisture content of 45%. Individual section densities and water contents for the clay subgrade series tests are summarized later.

Geosynthetics

Three geosynthetics were used in this study. A Tensar BX-1100 geogrid, a Tensar BX-1200 geogrid, and an Amoco 2006 woven geotextile were used for reinforced test sections. Table 3.1 shows the material properties for these three materials, where these properties are based on manufacturer's data as noted in the table.

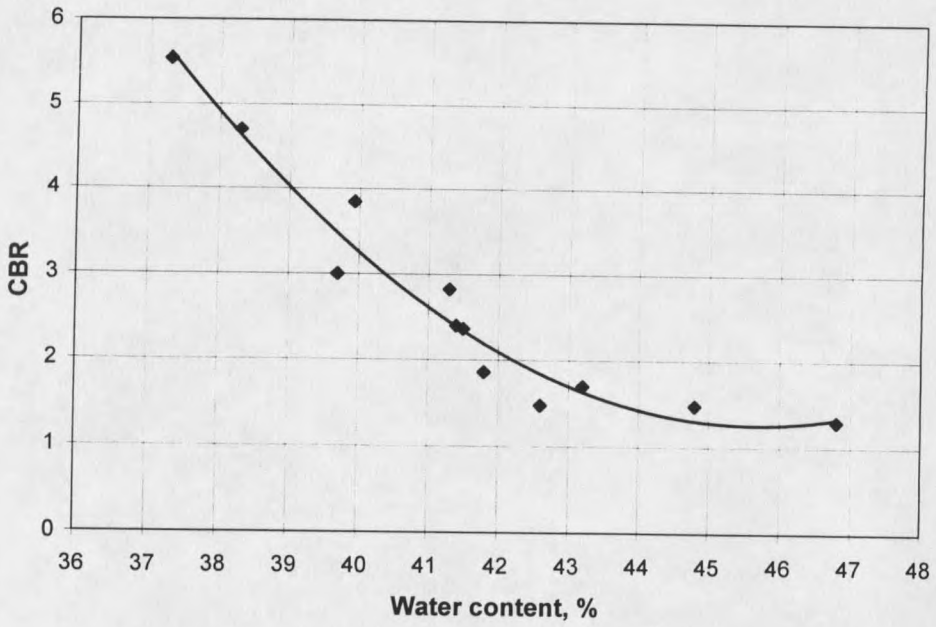


Figure 3.14. Laboratory test CBR versus water content for the clay subgrade.

Table 3.1 Geosynthetic material parameters.

	Geogrid: Tensar BX-1100	Geogrid: Tensar BX-1200	Geotextile: Amoco 2006
Material	Polypropylene	Polypropylene	Polypropylene
Structure	Punched Drawn, Biaxial	Punched Drawn, Biaxial	Woven
Mass/Unit Area (g/m^2)	215[1]	309[1]	250[3]
Aperature Size (mm)			
Machine Direction	25[1]	25[1]	None
Cross-Machine Direction	33[1]	33[1]	
Wide-Width Tensile Strength (at 5% Strain, kN/m)			
Machine Direction	9[1]	11[1]	10[3]
Cross-Machine Direction	13[1]	20[1]	22[3]
Ultimate Wide-Width Tensile Strength			
Machine Direction	13[1]	19[1]	31[2]
Cross-Machine Direction	20[1]	31[1]	31[2]

[1] (GFR, 1994)
[2] (GFR, 1997)
[3] (AMOCO, 1996)

Test Section Construction

This section describes the details associated with the construction of all experimental test sections. The section progresses with subgrade, base course, and asphalt placement procedures and then describes the calibration and installation of each instrument type. Major variables other than subgrade type included in this study were geosynthetic type (geogrid or geotextile) and depth of placement in the base course. Base course thickness was a variable for the CS series of test sections. Asphalt concrete thickness was not a variable in this study for any of the sections completed. Table 3.2 provides details on design test section layer thickness, subgrade type, geosynthetic type used, and placement position of the geosynthetic.

The silty-sand subgrades were constructed in approximate 100 mm lifts and measured with a standard auto-level and Philadelphia rod. Ten lifts were needed to reach the desired thickness of 1150 mm. Soil was mixed with a small skid-steer loader (Figure 3.15) and water was added via a sprinkling bucket. Water content determinations were made during the mixing process until the desired water content of 14.8% was achieved. The soil was dumped into the test box with the skid steer loader and spread level by hand. A vibratory plate compactor (Figure 3.16) was used to compact each layer. Approximately two to three passes with the compactor yielded the desired density. Densities were measured with a Troxler Model 3411-B nuclear densometer (Figure 3.17) and verified for the first test section by sand-cone tests. Five density measurements were taken for each layer to verify uniformity.

Table 3.2. Reinforcement placement for all test sections.

Section	Subgrade Type	Geosynthetic	Position
SSS1[a]	Silty-sand	Control	N/A
SSS2[a]	Silty-sand	Geogrid	BX-1100, 40 mm above base/subgrade interface
SSS3[a]	Silty-sand	Geotextile	Amoco 2006, 40 mm above base/subgrade interface
SSS4[a]	Silty-sand	Control	N/A
SSS5[a]	Silty-sand	Geogrid	BX-1100, base/subgrade interface
SSS6[a]	Silty-sand	Control	N/A
SSS7[a]	Silty-sand	Control	N/A
SSS8[a]	Silty-sand	Geotextile	Amoco 2006, base/subgrade interface
SSS9[a]	Silty-sand	Geogrid	BX-1100, base/subgrade interface
PCS1[b]	Clay	Control	N/A
CS1[b]	Clay	Geogrid	BX-1100, base/subgrade interface
CS2[b]	Clay	Control	N/A
CS3[b]	Clay	Geogrid	BX-1100, 100 mm above base/subgrade interface
CS5[b]	Clay	Geogrid	BX-1200, base/subgrade interface
CS6[b]	Clay	Geotextile	Amoco 2006, base/subgrade interface
CS7[b]	Clay	Geogrid	BX-1100, 100 mm above base/subgrade interface
CS8[b]	Clay	Control	N/A
CS9[c]	Clay	Control	N/A
CS10[c]	Clay	Geogrid	BX-1100, base/subgrade interface
CS11[b]	Clay	Geogrid	BX-1100, base/subgrade interface

Note: AC thickness is 75 mm for all sections.
[a] Base course thickness is 200 mm.
[b] Base course thickness is 300 mm.
[c] Base course thickness is 375 mm.
N/A = Not applicable

Typically, when construction reached the point where instruments were to be installed, the soil was excavated immediately surrounding the area of the instrument, to the proposed level with a hand trowel and the instrument placed. Details of installation of each instrument type are discussed later. A dynamic cone penetrometer (Figure 3.18) was used for determination of subgrade strength. The dynamic penetration index (DPI) was correlated to CBR using correlations from Minnesota Road Research (1993).

The clay subgrades were constructed in 75 mm lifts and compacted with a "jumping jack" trench compactor (Figure 3.19). The lift thickness of 75 mm was determined through trial and error so as to yield a uniform density in the layer without large void spaces. Thickness was measured with the same auto-level as with the silt subgrade. The clay material was also mixed with the skid-steer loader. Many more water contents were taken for the clay subgrades than for the silt in order to verify uniform moisture distribution. Reported water contents in the "As-Constructed Test Section Properties" section are the average of approximately 30 water content samples. Generally, 3 samples were taken from each compacted layer and averaged for the ten layers. Five density measurements were taken for each lift with the nuclear densometer and verified through sand-cone tests. Densities reported in the "As-Constructed Test Section Properties" section are an average of the approximately 50 measurements taken for each section (five measurements per layer X 10 layers).



Figure 3.15. Skid steer loader used for all soil mixing and lift placement.

The base course material was mixed with the skid steer loader and placed in 100 mm lifts. For the SSS series tests, the base course was placed in two lifts, and was placed in three to four lifts for the CS series tests. Compaction was achieved with the vibratory plate compactor, shown in Figure 3.16. Densities were taken with the same nuclear densometer and verified with sand-cone tests. Layer surfaces were roughened with a rake prior to a subsequent lift placement or prior to geosynthetic placement in order to provide layer bonding.

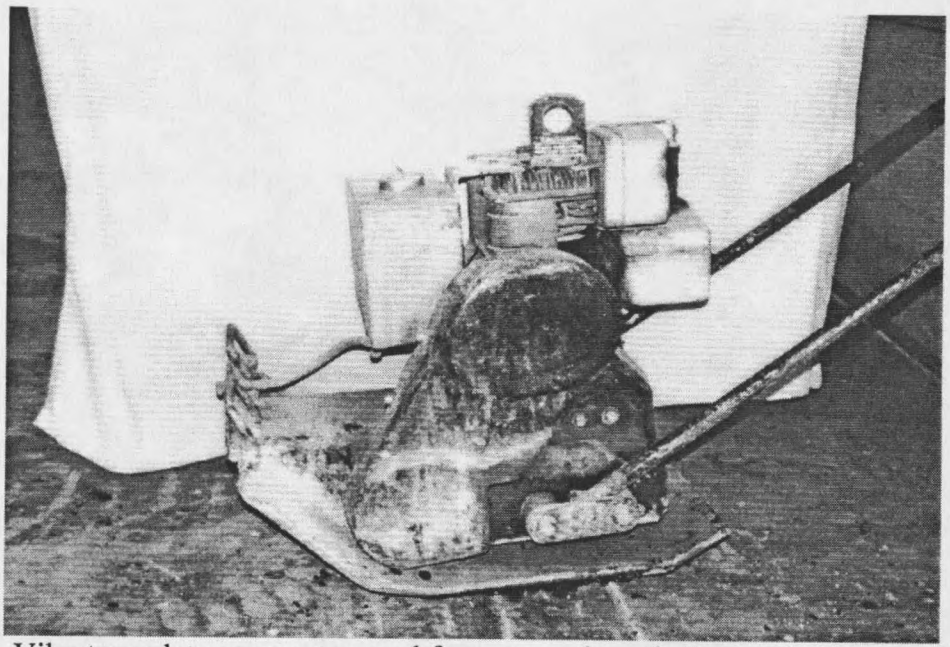


Figure 3.16. Vibratory plate compactor used for compaction of silty-sand subgrade, base course, and asphalt concrete.

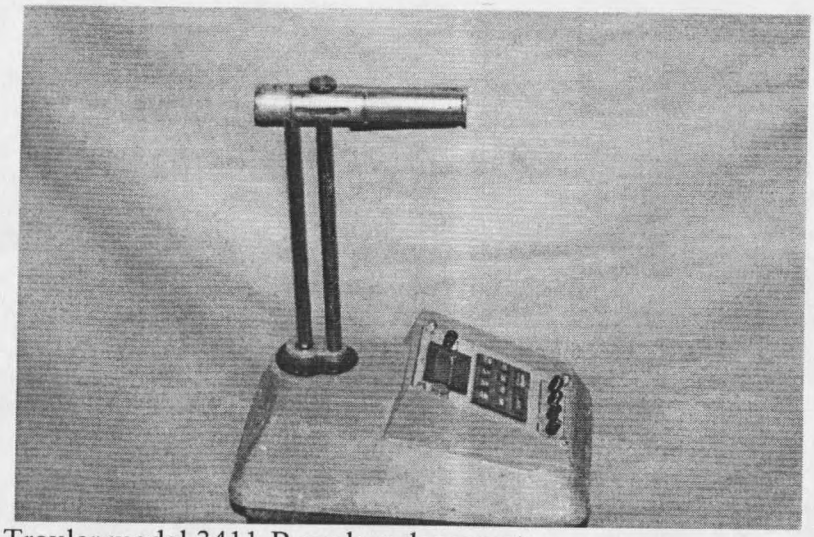


Figure 3.17. Troxler model 3411-B nuclear densometer.

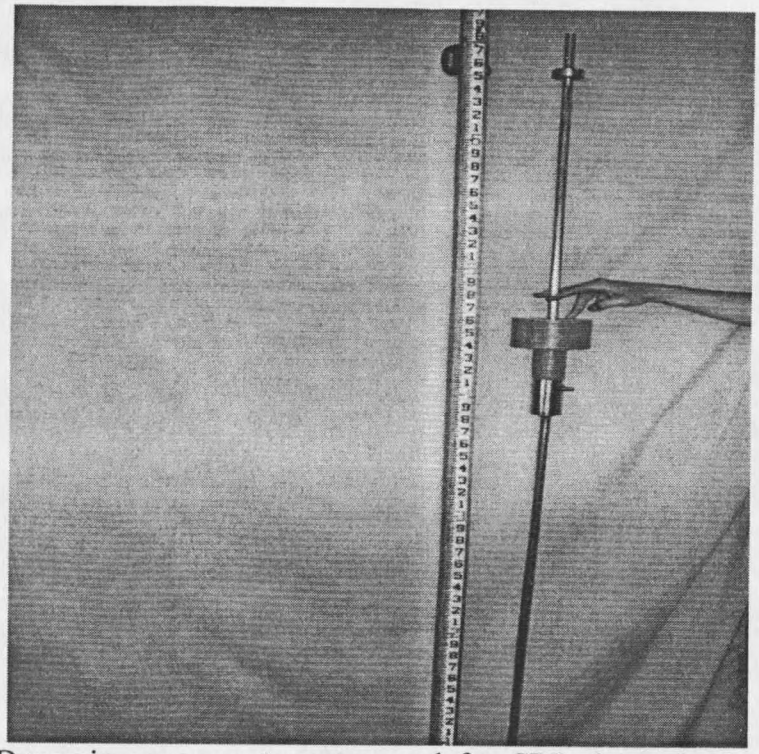


Figure 3.18. Dynamic cone penetrometer used for CBR determinations of pavement layer materials.

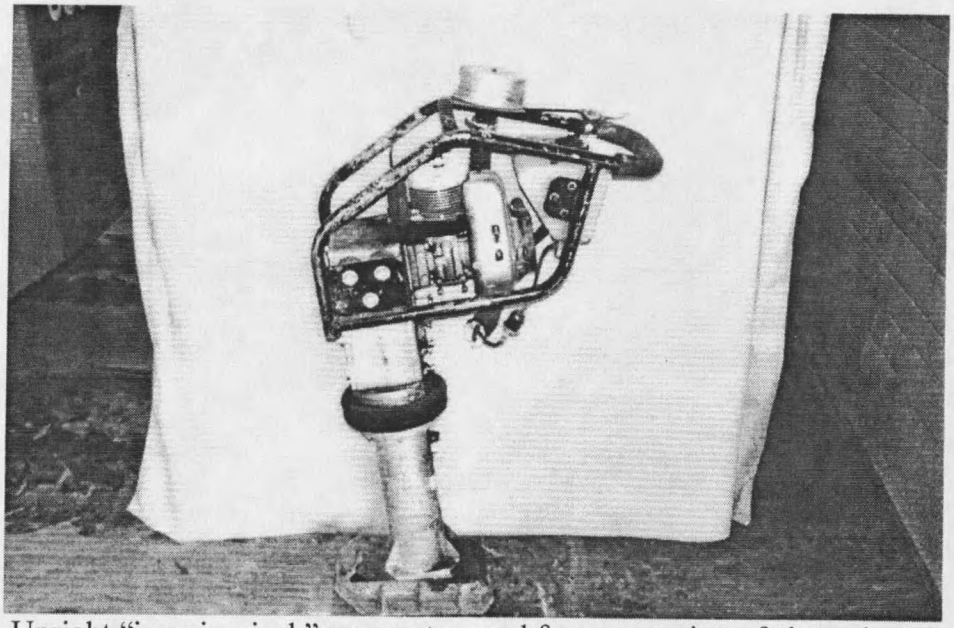


Figure 3.19. Upright "jumping-jack" compactor used for compaction of clay subgrade.

The asphalt concrete layer was placed in two lifts corresponding to a total 75 mm thickness with the vibratory plate compactor. Hot-mix was typically placed at 250 degrees Fahrenheit. In-place densities were taken with the nuclear gage and from drilled cores. These cores were taken from outside the loaded area after testing for a section was completed. The asphalt layer was allowed to cure for one day prior to loading for all sections.

Instrument Calibration

Instruments that required calibration included the LVDT's (both surface and in-situ LVDT's), and the temperature probes. The stress cells and H-type asphalt concrete strain gages were calibrated by Dynatest at the factory. The only calibration necessary was the application of proper scale factors that convert voltage changes given by an

instrument to engineering values such as stress or strain. These scale factors were input into the Labview software. The H-type strain gages had similar factors applied in the software.

Calibration for both the surface and in-situ LVDT's involved mounting the LVDT in a rigid frame, to which a micrometer was attached. Known displacements were applied to the LVDT and changes in voltage were recorded. Once a series of ten readings was obtained, voltage versus displacement was plotted. The slope of the regression or best fit line was the scale factor used in the software measured in mm/volt. A gage length for the in-situ LVDT's was defined as the inside distance between the end plates corresponding to when the sensor was placed in the soil. Strain was defined as the change in length between the two end plates divided by the original gage length. When the scale factor was divided by the gage length, results were converted to percent strain. Soil strains were measured in-situ, while absolute displacements were measured on the asphalt concrete surface.

Instrument Installation

This section describes the installation procedures used for all of the test section instruments. Included are a description of installation procedures for the in-situ LVDT's, soil pressure cells, geosynthetic foil gages, the asphalt strain gages, and the surface LVDT's, respectively.

A template was used for each level of sensors placed in the section. Use of the template allowed precise placement of the sensors from layer to layer, and kept the center

point of the box constant throughout all tests. The template had small holes drilled at the locations of the instruments whereby small nails were pushed through into the soil below. The template was then removed and a chalk line was snapped for X and Y coordinates. Perpendicular lines were then snapped at each instrument location.

For the LVDT's measuring vertical strain, round holes approximately 65 mm in diameter were excavated with a small hand trowel to a predetermined depth which was then verified with the auto-level. The LVDT was placed vertically into the hole and small amounts of soil were dumped and compacted with a metal rod around the instrument. Near the top of the hole, the top portion (the core) of the LVDT was adjusted up or down and voltage monitored, so as to achieve sufficient travel during the test. Voltages were monitored via a voltmeter during instrument installation. Instruments were then covered and the surface soil was hand compacted.

Horizontal LVDT's measuring radial and tangential strain were placed in the same way except that a small bubble level approximately 25 mm by 10 mm was used to level the instrument before compacting around the instrument. The core of the LVDT was initially placed to be in the middle of its range. Compaction then proceeded by hand up to the top of the soil surface. Gains (electronic amplification of the LVDT signal) were set to give a range appropriate for the sensor location in the section.

Stress cells were placed in the same way as the LVDT's with the use of a template. Holes approximately 80 mm in diameter were excavated to a predetermined depth, and were measured with the auto-level. For stress cells measuring vertical stress in the subgrade, the bottom of the hole was flattened with a 75 mm diameter "puck" the

same size as the stress cell. This flattening of the bottom of the hole provided a level base for the stress cell. The stress cell was then placed into the hole with the active face in the upward position and the small bubble level was placed on the instrument. The instrument was adjusted until level and soil backfilled and compacted in small increments over the sensor. Stress cells measuring radial and tangential stresses were placed in the same manner except for their orientation.

Stress cells placed in the base course utilized a 4-5 mm layer of sand placed on either side of the instrument to eliminate stress concentrations caused by large gravel particles. For stress cells measuring vertical stress, the sand was pluviated onto the active face of the cell after leveling to the desired thickness and backfilled as described previously. Stress cells measuring radial and tangential stresses were placed in a vertical orientation in the excavated hole. Two pieces of cardboard equal to the size of the instrument were placed on the active and passive faces of the cell. Soil was compacted around the cell/cardboard configuration until the top of the stress cell was just visible. The two cardboard pieces were then removed leaving a 3-4 mm thick void around the cell. This void was filled with fine sand to prevent inclusion of large rock particles from the base course from damaging the active face of the stress cell. Compaction then proceeded above the instrument. Wires from all instruments were placed in 25 mm deep channels and routed out of the box to the data acquisition software to prevent disruption from compaction of subsequent lifts by the vibratory plate and "jumping-jack" compactors.

Foil strain gages were installed on both the geogrid and geotextile samples. A summary of the procedures and materials used in attaching the foil gages is given here, but for more detailed information on gage and epoxy types, refer to the Micromeasurements (MM) Handbook (1996). Gages were installed in a ½ Wheatstone Bridge configuration, described in detail in the handbook, in order to provide temperature compensation and to reduce errors in strain readings due to bending of the geosynthetic. Foil gage preparation and attachment procedures for geogrid and geotextile samples are given in Cuelho (1998). Included in Cuelho (1998), is a description of the environmental protection used for geotextile and geogrid specimens placed in the soil.

Geogrid and geotextile installation techniques depended on if the material was placed inside the base course, or at the base/subgrade interface. Placing the geogrid inside the base course involved raking a thin layer of gravel beneath the geogrid. A small amount of fine sand was placed beneath each gage before the geosynthetic was installed. The geosynthetic was then installed and a small amount of sand was placed over each gage for protection from large particles. Gravel was then spread by hand over the geosynthetic starting at the center of the box and proceeding outward toward the edges of the test box. Placement of the gravel in this way allowed the geogrid to remain somewhat in tension, and to eliminate any slack or folds in the geosynthetic. The gravel was then compacted over the top of the geosynthetic with the vibratory plate compactor. Readings of each foil gage were taken with each subsequent lift placement of base course in order to determine if compaction induced strains were significant. Placement strains varied, but usually showed the geosynthetic to remain in tension. It is noted that the

strains due to compaction were usually quite small, on the order of 0.002-0.01% strain. Strains of this magnitude were much smaller than the strains observed during loading, which were on the order of 0.1-3.0%. Installation of the geotextile or geogrid at the base course/subgrade interface proceeded in the same manner as for placement inside the base course, except that the fine sand was only added on top of the geosynthetic gages.

Asphalt strain gages were placed 5-10 mm from the bottom of the asphalt concrete in order to observe tensile strains. A thin layer (5-10 mm) of asphalt concrete was placed in the desired location of the sensor. All particles larger than the #4 sieve were removed and the layer was compacted using a rubber mallet. The gage was then placed on top of the material, leveled, and more AC was added around the gage. Again, large particles were removed in the vicinity of the gage. Compaction proceeded over the top of the instrument. Asphalt concrete was placed around the instrument and compacted with the vibratory plate compactor. Asphalt concrete gages for certain sections were placed in several configurations beneath the load plate, which will be discussed in the instrument location section.

Eight LVDT's, measuring surface deflection of the asphalt, were placed in a rigid frame separate from the loading apparatus. Roofing nails were driven into the asphalt while it was still warm for the tips of the LVDT's to rest on. Two instruments were placed through 5 mm diameter holes drilled through the load plate and waffled rubber pad to measure deflection directly under the plate. Three instruments were spaced on either side of the plate, with the array of instruments spanning approximately one meter. The LVDT's are shown clearly in their orientation in Figure 3.4.

In-Situ Instrument Locations

This section is provided to give an understanding of where the instruments were placed in each section. Typical instrument layer locations for a section series are given here, and detailed section instrument locations are given in Appendix A.

Instruments were located in the experimental sections where stresses and strains were thought to be most critical (from a mechanistic point of view). Locations identified as critical to describing reinforcement mechanisms and benefits were: 1) areas directly beneath, and in the vicinity of the load plate, 2) locations on and near the geosynthetic (in the base layer) for reinforced sections, 3) the bottom of the AC layer, and 4) the top of the subgrade. Instruments were also placed to provide a description of the response of a given layer with radial distance from the load centerline.

Generally, the instruments were concentrated in the base layer and in the top 100 mm of the subgrade. Stress and strain instruments were placed to provide measurements in three directions at varying radial distances from the load centerline. Instruments were positioned to provide measurements in vertical, radial, and tangential directions. Several instruments measuring the same quantity were placed at varying radial distances from the load centerline in order to provide distributions across the section for a given depth. For instance, three to four vertical LVDT's (measuring vertical strain, ε_v) were placed at a given depth in the base to provide a profile of vertical strain versus radial distance. The same was done for radial LVDT's (measuring radial strain, ε_r), tangential LVDT's (measuring strain in the circumferential direction, ε_θ), vertical stress cells (measuring vertical stress, σ_v), radial stress cells (measuring radial stress, σ_r), and tangential stress

cells (measuring stress in the circumferential direction, σ_θ). Foil gages were located on the geosynthetic specimens in both the machine and cross-machine directions to provide measurements of radial and circumferential strain. Figure 3.20 illustrates the direction and types of measurements for a theoretical element of soil inside a test section. The purpose of the figure is to illustrate what was measured inside the test section without showing all instruments. The figure is not meant to imply that all six measures were made at the same point since only a single sensor could be placed at one location.

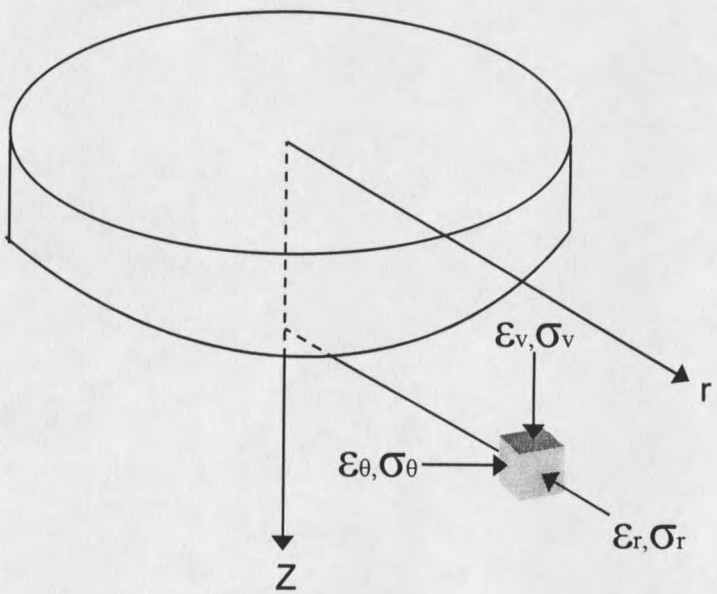


Figure 3.20. Theoretical stress and strain measurements for an element of soil inside a test section

In addition to the two levels of instruments mentioned previously, AC strain gages were installed to measure radial and tangential strain in the bottom of the AC. Additionally, three levels of vertical stress cells and vertically oriented LVDT's were installed directly beneath the load center at increasing depths in the subgrade. These

instruments were intended to provide an understanding of vertical stress and strain transmitted through the subgrade under the load center. It was believed that benefits of reinforcement would be illustrated to the greatest extent in the base layer and in the top of the subgrade.

Pavement Loading

Labview software was used to control the loading of the pavement system. The software allowed for precise control of air pressure input to the actuator, which caused the solenoids in the ABR™ valve to open or close to produce the desired pulse shape and duration. The input air pressure to the actuator was divided into 15 different fractions, ramped up to eventually reach the 550 kPa maximum pressure exerted on the pavement surface. Figure 3.21 below shows an input pulse of 0.8 seconds total duration consisting of a 0.3 second linear rise to 550 kPa, a flat top of 0.2 second duration and a 0.3 second linear pressure reduction. Also shown is a typical response from the load cell, where the load has been divided by the plate area, to yield a pavement pressure.

A 0.5 second rest period was input into the software between pulses in order for the data acquisition system to keep up with the pulse generation. Therefore, including the rest time between successive pulses, loading was performed at a constant 0.67 hertz.

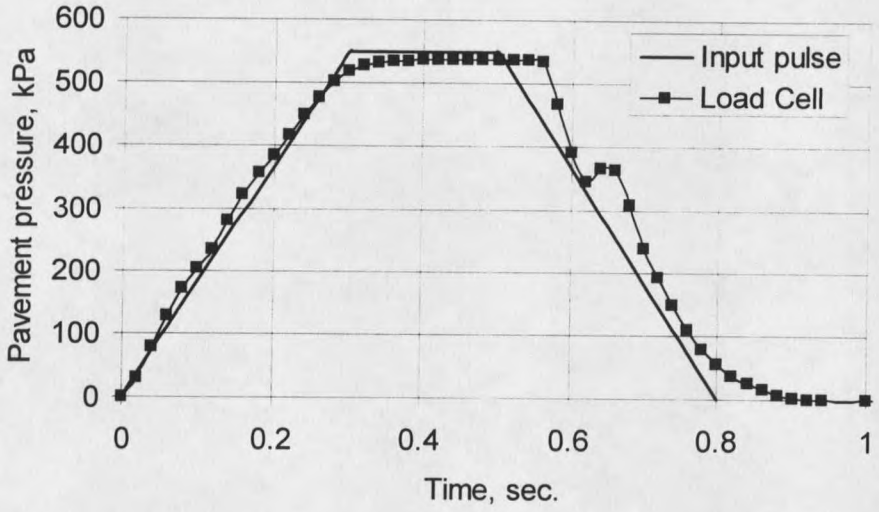


Figure 3.21. Input load pulse and corresponding load cell measurement.

As-Constructed Test Section Properties

This section provides a brief summary of the constructed pavement layer properties and major variables investigated. Variables other than subgrade type included geosynthetic type (geogrid or geotextile) and depth of placement in the basecourse. Test sections SSS1-4 involved varying the geosynthetic type and placement within the basecourse involving constant subgrade, asphalt and basecourse thickness and strengths. Again, hot-mix asphalt concrete was used for these sections. Asphalt concrete thickness was not a variable in this study for any of the sections completed. Sections SSS1-4 involved excavation of the entire section and rebuilding the subgrade. Sections SSS5-9 involved re-using the subgrade starting from section SSS4 and also used cold-mix asphalt concrete due to the unavailability of hot-mix. The subgrades of sections SSS5-9 were not

excavated and reconstructed due to time limitations. Reinforcement placement within the SSS sections was described in Table 3.2.

As-constructed layer properties of the silty-sand subgrade test sections are shown in Tables 3.3-3.7, which describe the subgrade, base course, and AC properties. During the construction of the first several silty-sand subgrade test sections, it was observed that CBR values during construction differed from those taken during excavation of the test section. Water content was also observed to have decreased with the most noticable differences being in the upper portion of the subgrade. Increases in CBR were believed to be due to drainage of water from the material. To ensure that the subgrade strength was the same at the start of loading, DCP tests were performed immediately prior to application of load. These tests were performed by drilling a hole through the AC surface well outside the load footprint and inserting the DCP through this hole. Table 3.3 shows values of CBR's determined from the DCP measurements for three time periods for test sections SSS1-SSS4. The CBR values reported in Table 3.4 correspond to the pre-test condition.

Table 3.3. CBR results showing time variation for subgrades of sections SSS1-4.

Section	During Construction	Pre-test	Excavation
SSS1	N/A	N/A	15.3
SSS2	5.0	N/A	18.0
SSS3	5.0	15.6	18.6
SSS4	14.8	17.3	18.2

Table 3.4. As-constructed subgrade properties.

Section	Thickness (mm)	Construction			Excavation	
		Water Content (%)	Dry Density (kN/m^3)	Pretest CBR	Water Content (%)	Dry Density (kN/m^3)
SSS1	1128	14.7	17.0	14.0[d]	14.8	17.1
SSS2	1131	14.9	17.0	15.0[d]	13.2	17.3
SSS3	1147	14.8	17.1	15.5[d]	14.0	17.0
SSS4	1145	14.8	17.1	16.0[d]	11.7	N/A
SSS5	1145[a]	12.6[b]	N/A	20.5[d]	11.3[b]	N/A
SSS6	1145[a]	N/A	N/A	20.2[d]	N/A	N/A
SSS7	1145[a]	11.4[b]	18.3[c]	21.7[d]	11.4[b]	18.3[c]
SSS8	1145[a]	12.5[b]	18.0[c]	22.9[d]	12.5[b]	18.0[c]
SSS9	1145[a]	N/A	18.0[c]	24.0[d]	10.9[b]	17.7
PCS1	1045	43.6	11.6	1.5[e]	42.4	11.6
CS1	1045	44.8	11.5	1.5[e]	43.4	11.7
CS2	1045	44.8	11.4	1.5[e]	43.9	11.6
CS3	1045	44.9	11.5	1.5[e]	44.1	11.8
CS5	1045	44.9	11.4	1.5[e]	43.3	11.4
CS6	1045	44.4	11.1	1.5[e]	44.6	11.4
CS7	1045	44.2	11.4	1.5[e]	44.7	11.4
CS8	1045	44.8	11.5	1.5[e]	44.5	11.5
CS9	970	44.9	11.4	1.5[e]	44.6	11.3
CS10	970	44.9	11.3	1.5[e]	44.7	11.2
CS11	1045	45.1	11.4	1.5[e]	43.7	11.5

[a] Subgrade from SSS4 was re-used for these tests
[b] Measurements taken 60 mm below top of subgrade
[c] Measurements taken at base/subgrade interface
[d] Defined by the DCP test
[e] Defined from laboratory CBR tests at corresponding in-situ water content
N/A = Not Available

As the subgrades of sections SSS5-9 were re-used from section SSS4, the overall subgrade CBR (as defined by the DCP tests) increased slightly from 16 to 24 between the sections due to further drying of the subgrade as noted in Table 3.4. It is also noted that the DCP tests were taken outside of the area beneath the load plate. Areas directly beneath the load plate were not tested due to vertical stress cells in the center of the

section. Therefore, DCP readings had to be taken 200-300 mm away from the load center.

Table 3.5. As-constructed base course properties.

	Construction			Excavation
Section	Thickness (mm)	Water Content (%)	Dry Density (kN/m^3)	Water Content (%)
SSS1	210	7.6	20.6	5.7
SSS2	205	7.4	20.7	6.1
SSS3	200	7.1	20.8	5.5
SSS4	200	6.4	21.1	4.6
SSS5	200	6.3	20.2	5.2
SSS6	200	6.2	20.5	5.3
SSS7	200	6.3	20.5	5.0
SSS8	200	6.4	20.9	5.1
SSS9	200	6.0	20.9	5.1
PCS1	300	6.2	20.9	5.6
CS1	300	6.1	20.7	5.8
CS2	300	6.3	20.6	6.4
CS3	300	6.3	20.3	6.5
CS5	300	6.2	20.6	5.8
CS6	300	5.8	21.0	5.8
CS7	300	5.5	20.6	5.9
CS8	300	6.9	20.7	6.1
CS9	375	6.4	20.9	6.8
CS10	375	6.7	20.5	6.2
CS11	300	6.3	20.5	6.6

It is also noted that the subgrade water content from section SSS5 to SSS9 decreased slightly from 14.8% in section SSS4 to about 10.9% in section SSS9. Dry densities measured at the top of the subgrade also increased from section SSS4. This may have resulted from water loss to lower areas of the subgrade and/or densification due to cyclic loading of several sections. Water contents listed in Table 3.4 for the subgrade of sections SSS1-SSS4 are an average of approximately 30 samples (10 lifts x 3 samples

per lift). Dry densities are an average of 50 tests (10 lifts x 5 tests per lift). Three samples were taken for each lift of base for three lifts. For sections SSS5-SSS9, water contents reported are for the top 60 mm of subgrade, as the material was not removed. Densities for the subgrade reported in Table 3.4 also reflect the top 60 mm of the subgrade.

Excavation results from section SSS9 showed that the low water contents existed in only the upper 100 mm of the subgrade. Figure 3.22 shows the excavation results of section SSS9 with respect to dry density and water content plotted versus depth within the section. Dry densities remained fairly constant with depth while water content ranged from about 11% from 300 mm beneath the subgrade/base interface to 17% near the bottom of the section. These results confirm that some drainage may have occurred throughout sections SSS1-SSS9.

As-constructed properties for the clay subgrade sections are listed in Tables 3.4-3.7, which report the subgrade, base course, and AC properties respectively. Water contents for the subgrade are an average of approximately 40 samples (10 lifts x 4 samples per lift). Water contents listed in the base are an average of 16 samples (4 lifts x 4 samples per lift). Densities shown are an average of approximately 50 readings for the subgrade and 20 for the base. Subgrade CBR results listed in Table 3.4 were estimated from the constructed water content and dry density and from the use of Figure 3.14, which was based on laboratory CBR test results. These were verified through the DCP test for each lift. Reinforcement placement for the clay subgrade series of tests was included previously in Table 3.2.

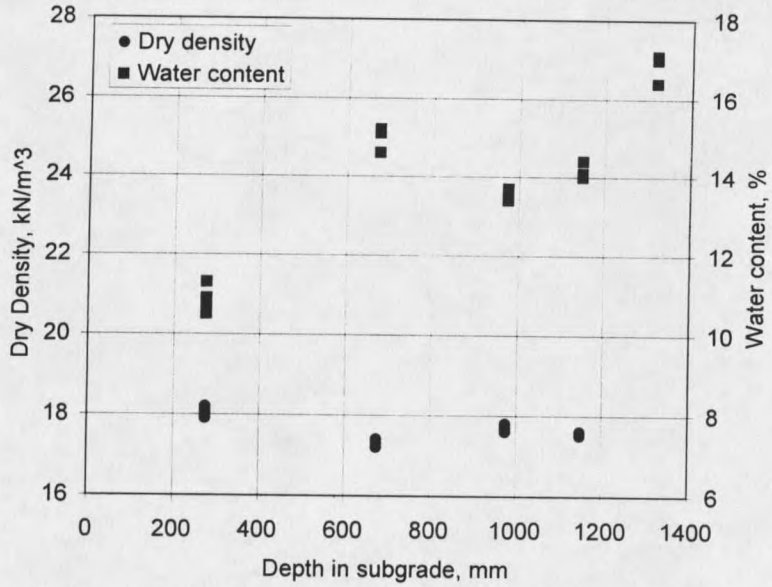


Figure 3.22. Dry density and water content versus depth from section SSS9 excavation.

Quality control of lift dry density and water content was excellent for both the SSS and CS series of tests. Coefficients of variation (CV) for dry density and water content of the basecourse and subgrade are given in Table 3.6. It is noted that both water content and density remained consistent throughout the test sections, with the exception of CS6 and CS7 base water contents which had an average water content of 5.8 and 5.5% respectively, and had a higher coefficient of variation throughout the base layer. Additionally, coefficients of variation were calculated between sections for the SSS and CS series tests for subgrade water content, subgrade dry density, and base course dry density. For the SSS series the CV's were 0.6%, 0.3%, and 1.0% for the subgrade water content, subgrade dry density, and base course dry density. The CS series exhibited CV's of 1.2%, 1.1%, and 1.0% for the same measures. These CV statistics indicate that

virtually no differences existed between test sections in terms of subgrade and base course construction. This point will be reiterated later.

As-constructed asphalt concrete mix properties from experimental sections SSS1-CS10 are shown in Table 3.7. The number of samples analyzed for each measure is given in parentheses. The coefficient of variation is listed for each test section for properties such as thickness, density, and air voids content. Test sections are discussed with respect to asphalt properties and the performance of each section later in the "Statistical Comparison of Test Section Properties" section.

Table 3.6. Coefficients of variation for base course and subgrade construction.

	Basecourse		Subgrade	
Section	Dry Density CV (%)	Water Content CV (%)	Dry Density CV (%)	Water Content CV (%)
SSS1	0.7	3.7	1.1	0.8
SSS2	0.6	3.7	1.1	0.8
SSS3	0.6	4.5	0.9	0.7
SSS4	1.9	5.6	1.2	1.4
SSS5	0.9	1.1	N/A[a]	N/A[a]
SSS6	1.4	1.1	N/A[a]	N/A[a]
SSS7	0.6	1.1	N/A[a]	N/A[a]
SSS8	1.9	1.1	N/A[a]	N/A[a]
SSS9	1.5	0.0	N/A[a]	N/A[a]
PCS1	1.2	5.4	1.7	3.7
CS1	2.6	3.2	0.4	1.3
CS2	1.2	9.0	1.9	0.6
CS3	1.5	6.9	1.8	2.1
CS5	2.9	3.2	1.5	1.1
CS6	2.3	17.2	1.6	1.6
CS7	1.8	15.5	1.8	2.8
CS8	1.8	3.2	1.3	2.6
CS9	1.6	5.6	1.4	1.6
CS10	1.5	8.6	1.4	3.1
CS11	2.0	4.5	1.6	0.9

[a] Subgrade was reused from SSS4

Table 3.7. As-constructed asphalt concrete properties.

Section	Thickness (mm)[a]	Coeff. Var. (%)	Density (kN/m^3) (cores)	Coeff. Var. (%)	Air Voids (%)	Coeff Var. (%)	Asphalt Cement (%)	Marshall Stability		Rice Specific Gravity[b]
								Stability (lbs.)	Flow	
SSS1	78.4 (9)	10.8	23.0 (9)	1.4	4.1 (9)	33.0	5.4	2956 (4)	17	2.442
SSS2	79.1 (10)	5.6	22.6 (10)	1.9	6.3 (10)	24.8	5.7	2043 (4)	18	2.460
SSS3	77.0 (9)	3.2	22.4 (9)	3.2	6.7 (9)	30.0	6.2	1372 (4)	17	2.424
SSS4	77.5 (10)	2.7	22.8 (10)	1.1	4.4 (10)	24.9	6.1	2125 (4)	17	2.425
SSS5	75[c]	N/A	N/A	N/A	N/A	N/A	4.7	4716 (3)[e]	10[e]	2.513
SSS6	75[c]	N/A	N/A	N/A	N/A	N/A	4.7	5400 (3)[e]	10[e]	2.495
SSS7	75[c]	N/A	22.1[d]	N/A	N/A	N/A	5.3	4933 (3)[e]	8[e]	2.514
SSS8	75[c]	N/A	21.5[d]	N/A	N/A	N/A	5.9	6970 (3)[e]	10[e]	2.491
SSS9	75[c]	N/A	21.9[d]	N/A	N/A	N/A	5.1	4630 (3)[e]	9[e]	2.528
PCS1	75.0	N/A	N/A	N/A	N/A	N/A	N/A	N/A	N/A	N/A
CS1	77.7 (10)	3.8	22.5 (3)	0.9	7.4 (3)	10.9	6.8	1840 (3)	15	2.478
CS2	78.4 (10)	2.3	23.1 (6)	0.4	3.3 (6)	12.6	6.8	2013 (6)	26	2.437
CS3	80.3 (9)	2.6	21.9 (5)	2.1	7.9 (4)	7.6	6.6	1440 (5)	17	2.442
CS5	76.2 (10)	3.0	22.6 (6)	2.1	5.6 (6)	35.6	6.1	2292 (6)	13	2.433
CS6	75.3 (10)	1.4	23.3 (6)	0.2	3.1 (6)	10.3	6.6	2471 (6)	18	2.444
CS7	75.6 (10)	2.6	22.9 (6)	1.6	4.3 (6)	34.2	6.6	1979 (6)	16	2.444
CS8	76.3 (10)	2.7	23.1 (6)	0.7	3.3 (6)	17.9	6.1	2527 (6)	15	N/A
CS9	79.0 (10)	3.7	22.7 (6)	2.0	5.2 (6)	35.5	6.3	2167 (6)	14	N/A
CS10	75.1 (10)	1.6	22.9 (6)	1.0	4.3 (6)	22.0	6.5	2190 (6)	13	2.443
CS11	77.4 (10)	4.6	23.4 (6)	0.4	1.9 (6)	17.8	6.0	2480 (6)	20	2.429

Note: The number of samples is listed next to the measured quantity in parentheses(), N/A= Not Available

[a] Average thickness of 100 mm and 150 mm diameter cores

[b] Test performed on one bulk sample

[c] Cold-mix sections in which cores were not possible

[d] In-place densities measured by nuclear densometer

[e] Re-compacted Marshall's from bulk sample

Statistical Comparison of Test Section Properties

As discussed previously, the coefficients of variation for three measures of construction which include subgrade water content, subgrade dry density, and base course dry density were compiled for all test sections including both the SSS and CS series of sections. It has been shown that the coefficients of variation for the three measures from the SSS series of tests were below 1.0%. The coefficient of variations for the same three measures from the CS series were all less than or equal to 1.2%. Thus, it was concluded that no significant differences existed between sections in a given series in terms of subgrade and base course physical properties.

A statistical comparison of the asphalt concrete for all of the test sections completed (including both silty-sand subgrade sections and clay subgrade section) is useful when used in combination with performance characteristics described in Chapter 4 "Discussion of Results". A one-way analysis of variance (ANOVA) with asphalt concrete thickness, air voids, and density as the dependent variables and "test section" as the grouping factor was performed for both the SSS and CS series of test sections. This analysis was performed to establish if significant differences exist between the various test sections in terms of the three asphalt properties mentioned previously.

Tables 3.8 and 3.9 give the details from the ANOVA analysis of voids for both series of test sections. Once it was established that significant differences exist between the test sections from the ANOVA analysis, multiple comparisons of means were performed to determine which specific test sections were significantly different. Two methods of comparing means were used which offered two levels of conservatism. The

LSD (least significant difference) method involved performing all the possible pair-wise Student t-tests. A level of significance is established for each t-test (5% in this case), so the experiment-wise level of significance becomes inflated. The second method, the Tukey procedure, protects an established experiment-wise level of significance (5% in this case). Therefore, the Tukey procedure provides a lower overall probability of incorrectly stating that significant differences exist between test sections. Tables 3.10 and 3.11 give details from both methods in regards to determination of significantly different sections. The silty-sand subgrade sections were analyzed separately from the clay subgrade sections. Significantly different sections are noted with an asterisk with each respective method.

Table 3.8. One-way analysis of variance (ANOVA) for asphalt concrete voids in the SSS series tests.

Source of Variance	Degrees of Freedom	Sum of Squares	Mean Square	F Value	Pr > F
Between Test Sections	3	50.086	16.695	7.082	0.001
Within Test Section	34	80.157	2.358		
Total	37	130.243			

Pr > F: probability of finding an F value larger than that calculated, assuming that all the test sections belong to the same population. This is also the probability of being incorrect if one states that significant differences exist between test sections.

If (Pr > F) is less than 0.05, one can state confidently that significant differences exist between the various test sections in terms of their asphalt concrete air void contents.

Table 3.9. One-way analysis of variance (ANOVA) for asphalt concrete voids in the CS series tests.

Source of Variance	Degrees of Freedom	Sum of Squares	Mean Square	F Value	Pr > F
Between Test Sections	9	188.350	20.928	13.972	0.000
Within Test Section	46	68.900	1.498		
Total	55	257.250			

Pr > F: probability of finding an F value larger than that calculated, assuming that all the test sections belong to the same population. This is also the probability of being incorrect if one states that significant differences exist between test sections.

If (Pr > F) is less than 0.05, one can state confidently that significant differences exist between the various test sections in terms of their asphalt concrete air void contents.

Table 3.10. Post hoc comparison of mean voids for the SSS series of test sections.

SSS(I)	SSS(J)	Mean Difference (I-J)	Standard Error	Pr > Difference	
				LSD	Tukey
1	2	-2.2078	0.705	0.004*	0.018*
1	3	-2.6000	0.724	0.001*	0.005*
1	4	-0.2278	0.705	0.749	0.988
2	3	-0.3922	0.705	0.582	0.944
2	4	1.9800	0.687	0.007*	0.033*
3	4	2.3722	0.705	0.002*	0.010*

Pr > Difference: probability of finding a larger difference than that calculated, assuming that the two test sections belong to the same population. This is also the probability of being incorrect if one states that the two test sections are significantly different.

If (Pr > Difference) is less than 0.05, one can state confidently that a significant difference exists between the two test sections in terms of their asphalt concrete air void contents.

* Test sections I and J are deemed significantly different [(Pr > Difference) is less than 0.05].

Table 3.11. Post hoc comparison of mean voids for the CS series of test sections.

CS(I)	CS(J)	Mean Difference (I-J)	Standard Error	Pr > Difference	
				LSD	Tukey
1	2	4.1167	0.865	0.000*	0.001*
1	3	-1.1667	0.894	0.198	0.947
1	5	1.8500	0.865	0.038*	0.512
1	6	4.3500	0.865	0.000*	0.000*
1	7	3.1000	0.865	0.001*	0.025*
1	8	4.1000	0.865	0.000*	0.001*
1	9	2.2333	0.865	0.013*	0.256
1	10	3.1167	0.865	0.001*	0.024*
1	11	5.5000	0.865	0.000*	0.000*
2	3	-5.2833	0.865	0.000*	0.000*
2	5	-2.2667	0.707	0.002*	0.067
2	6	0.2333	0.707	0.743	1.000
2	7	-1.0167	0.707	0.157	0.908
2	8	-0.0167	0.707	0.981	1.000
2	9	-1.8833	0.707	0.011*	0.218
2	10	-1.0000	0.707	0.164	0.916
2	11	1.3833	0.707	0.056	0.631
3	5	3.0167	0.894	0.000*	0.006*
3	6	5.5167	0.741	0.000*	0.000*
3	7	4.2667	0.741	0.000*	0.000*
3	8	5.2667	0.741	0.000*	0.000*
3	9	3.4000	0.741	0.000*	0.001*
3	10	4.2833	0.741	0.000*	0.000*
3	11	6.6667	0.741	0.000*	0.000*
5	6	2.5000	0.707	0.001*	0.029*
5	7	1.2500	0.707	0.084	0.750
5	8	2.2500	0.707	0.003*	0.070
5	9	0.3833	0.707	0.590	1.000
5	10	1.2667	0.707	0.080*	0.736
5	11	3.6500	0.707	0.000*	0.000*
6	7	-1.2500	0.707	0.084	0.750
6	8	-0.2500	0.707	0.725	1.000
6	9	-2.1167	0.707	0.004*	0.109
6	10	-1.2333	0.707	0.088	0.764
6	11	1.1500	0.707	0.110	0.828
7	8	1.0000	0.707	0.164	0.916
7	9	-0.8667	0.707	0.226	0.964
7	10	0.01667	0.707	0.981	1.000

7	11	2.4000	0.707	0.001*	0.041*
8	9	-1.8667	0.707	0.011*	0.228
8	10	-0.9833	0.707	0.171	0.924
8	11	1.4000	0.707	0.054	0.616
9	10	0.8833	0.707	0.218	0.960
9	11	3.2667	0.707	0.000*	0.001*
10	11	2.3833	0.707	0.002*	0.044*

Pr > Difference: probability of finding a larger difference than that calculated, assuming that the two test sections belong to the same population. This is also the probability of being incorrect if one states that the two test sections are significantly different.

If (Pr > Difference) is less than 0.05, one can state confidently that a significant difference exists between the two test sections in terms of their asphalt concrete air void contents.

* Test sections I and J are deemed significantly different [(Pr > Difference) is less than 0.05].

From these statistical analyses (ANOVA and post hoc comparison of means in Tables 3.8-3.11) it is shown that some significant differences exist between certain test sections, with respect to AC air voids. These significant differences in asphalt voids should be expected to cause certain differences in performances between these sections. The analysis has shown test sections SSS1 and SSS4 to be significantly different from SSS2 and SSS3. Sections SSS1 and SSS4 are similar, while sections SSS2 and SSS3 are similar. In addition, sections CS1 and CS3 have been shown to be significantly different from all other CS sections, in terms of asphalt voids content.

The statistical analysis (ANOVA and post hoc comparison of means) was also performed with asphalt thickness and asphalt density for both the SSS and CS series of tests. The analysis showed sections SSS1-SSS4 were not significantly different in terms of thickness measurements. Statistical comparisons of density between SSS1-SSS4

reinforced the idea presented earlier that SSS2 and SSS3 were significantly different from SSS1 and SSS4.

Analysis of AC thickness and density did not alter conclusions made previously with respect to section comparisons. Statistical thickness analysis showed sections CS2 (the thickest AC layer at 78 mm) and CS7 (the thinnest AC layer at 75 mm) to be significantly different. CS7 will be shown in Chapter 4 to perform much better than CS2, such that small differences in AC thickness were ruled out in the effect on overall rutting behavior. Additionally, sections CS2 and CS8 were not shown to be significantly different, even though a 2 mm thickness difference existed. Statistical comparisons of density illustrated the same trends as found with air voids comparisons discussed previously, that sections CS1 and CS3 were significantly different from the rest of the CS series sections in terms of voids and density. This should be intuitive, however, as air voids and density are closely related. Thus, from the previous discussion, the air voids in the AC were considered most representative of asphalt performance.

Loading pressure was also considered as a statistical measure of quality between all of the test sections completed. Average load pressure and corresponding standard deviation is presented for all test sections in Table 3.12. This table shows excellent consistency between the load applied to all sections. Section PCS1 exhibits a higher standard deviation than the other sections, but this section was not analyzed for long-term performance. Analysis of section PCS1 is described later in this chapter.

Table 3.12. Average load applied for all test sections completed.

Section	Average Load (kPa)	Standard Deviation (kPa)	Section	Average Load (kPa)	Standard Deviation (kPa)
SSS1	549	12	CS1	547	10
SSS2	551	5	CS2	549	4
SSS3	550	10	CS3	548	3
SSS4	554	7	CS5	549	5
SSS5	549	3	CS6	548	5
SSS6	552	8	CS7	548	3
SSS7	548	4	CS8	549	3
SSS8	550	5	CS9	547	4
SSS9	545	14	CS10	549	4
PCS1	542	34	CS11	549	6

Instrument Measurement Repeatability

As mentioned in the introduction to this chapter, a preliminary clay section termed PCS1 was constructed in order to provide insight on the performance of an unreinforced clay section and to provide information on instrument response and repeatability. This section will describe the instrumentation used with PCS1, the loading of the section, and a discussion of instrument repeatability. The plots of instrument response given in this section are not intended for comparison of sections, but are primarily used to show instrument repeatability and trends in stress and strain distributions. Additional instrument response plots will be provided in Chapter 5 where they will be compared to the linear elastic model Kenlayer.

Construction and Loading of PCS1

Construction of PCS1 was similar to other clay sections, except that fewer instruments were installed. Section layer thickness was the same as clay sections CS1-CS8. Orientation of the instruments was such that on average, two instruments were placed in each layer (mainly the base and the top of the subgrade) measuring the same property. For example, two instruments were placed at the same level in the base measuring radial strain. Two instruments were placed in each level measuring vertical stress, vertical strain, radial stress, and radial strain. Some tangential measurements were also made in each layer. Additionally, measurements of vertical stress and strain were made deeper in the subgrade in the center of the box.

With so few instruments in each layer, distributions of stress and strain were not possible unless the load was moved. With this section, the load was moved in two directions from the center of the box in 100 mm increments. For example, the load began at one side of the box and was moved in 100 mm increments to the other side. This was repeated for the other two sides of the box, resulting in a total of 41 response points. At each point, three load pulses were applied to the pavement surface. In this way, a plot of strain or stress for a given sensor from each load point could be made.

Some instrument locations in the preliminary section were duplicated (two instruments of the same type were placed at the same radial distances from the load) to see how repeatable a given response was for a duplicate instrument location in the section. Essentially, if the measurements were repeatable, a direct measure of the homogeneity and construction reliability could be obtained. It was noted that many of

the instruments were very repeatable and increased the confidence of the quality control of the section construction. Furthermore, findings of repeatability meant that instruments did not have to be duplicated in an experiment to provide reliable data. Reducing duplicates in the instrumentation saved analysis and construction time.

Illustrations of Repeatability

This section will provide several examples of repeatability of measurements discussed previously from both the PCS1 section and sections CS2 and CS8 (unreinforced controls). Examples from PCS1 primarily look at several instrument responses versus the horizontal distance from the load center. Examples of repeatability from sections CS2 and CS8 look at long-term measurements (instrument responses over many cycles of load). This section will proceed with examples of strain measurements from PCS1 and then stress measurements. Finally, several examples will be illustrated from CS2 and CS8. When applicable, additional examples of measurement repeatability for sections CS2 and CS8 will be illustrated in the "Discussion of Results" in Chapter 4.

Figure 3.23 illustrates the first example of agreement between two LVDTs placed at the same depth in the base layer. These two instruments add confidence to vertical strain measurements in the base course.

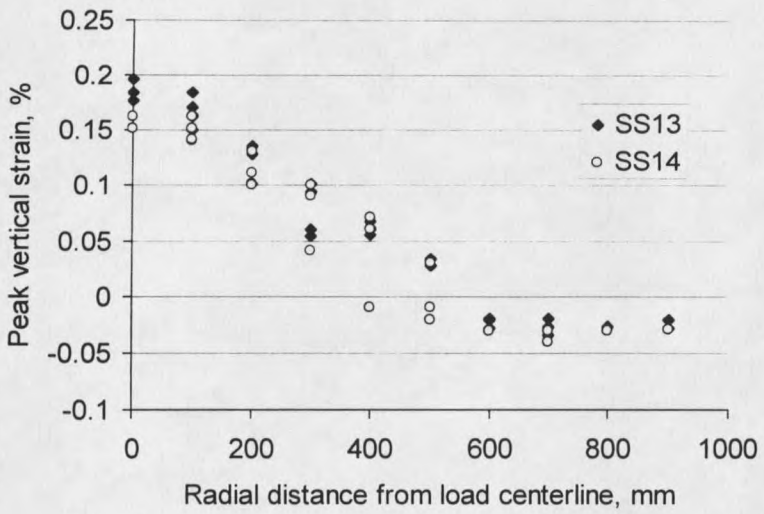


Figure 3.23 Peak vertical strain versus distance in the base layer for two soil strain sensors (LVDT's) from section PCS1 at two different positions (Z=300 mm).

Figure 3.24 illustrates the repeatable measurement of vertical strain in the top of the subgrade for two soil strain sensors from section PCS1. It is noted that this measure is a critical measure contributing to the performance of all sections, especially the clay subgrade sections, where the weak subgrade is susceptible to significant rutting. Thus, repeatable measurements for vertical strain in the top of the subgrade will solidify comparison of results in Chapter 4.

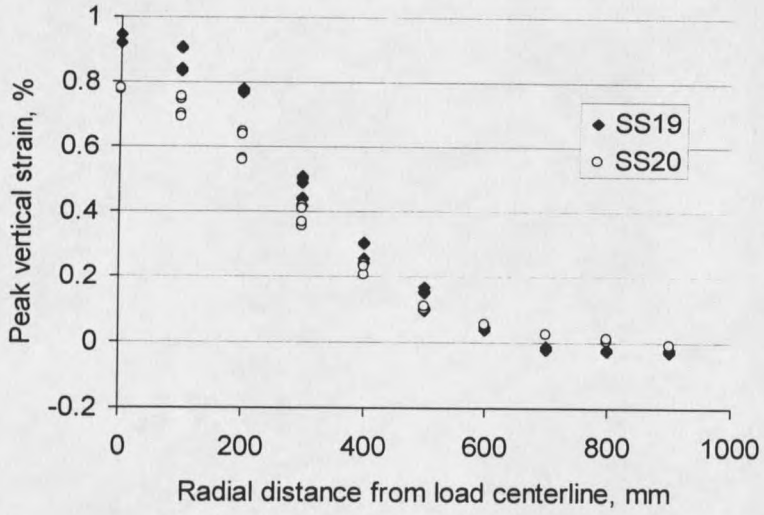


Figure 3.24 Vertical strain versus radial distance from the load application from section PCS1 in the top of the subgrade (Z=450 mm).

Another critical measure for which repeatable measures are necessary is the measure of radial soil strain in the top of the subgrade layer. Quality strain measurements in the top of the subgrade are necessary for an accurate determination of shear behavior which will be described in detail in Chapter 4. Figure 3.25 illustrates reasonable agreement between two radial soil strain sensors in the top of the subgrade layer.

Stress measures from PCS1 were also found to be consistent, in both the base and subgrade layers. Figure 3.26 shows a distribution of vertical stress in the base layer from two stress cells from section PCS1. Figure 3.27 illustrates the distribution of vertical stress in the subgrade from section PCS1. Excellent agreement between instruments is shown in both Figures 3.26 and 3.27.

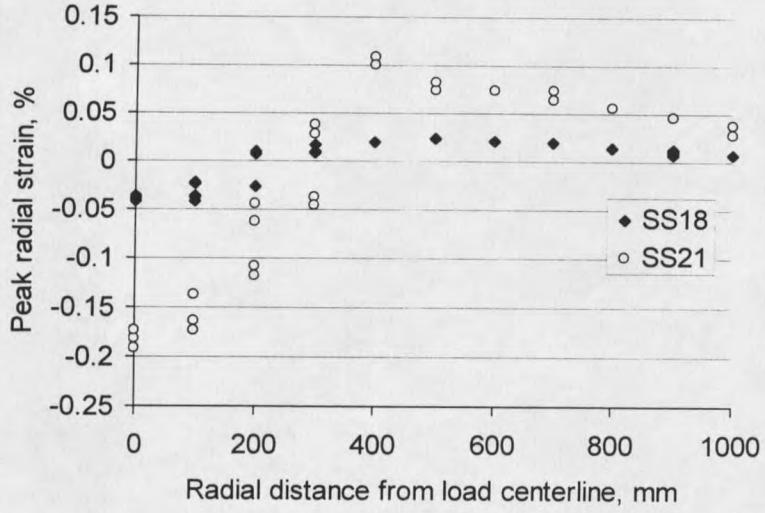


Figure 3.25 Illustration of radial strain measures from two soil strain sensors in the top of the subgrade from section PCS1 (Z=415 mm).

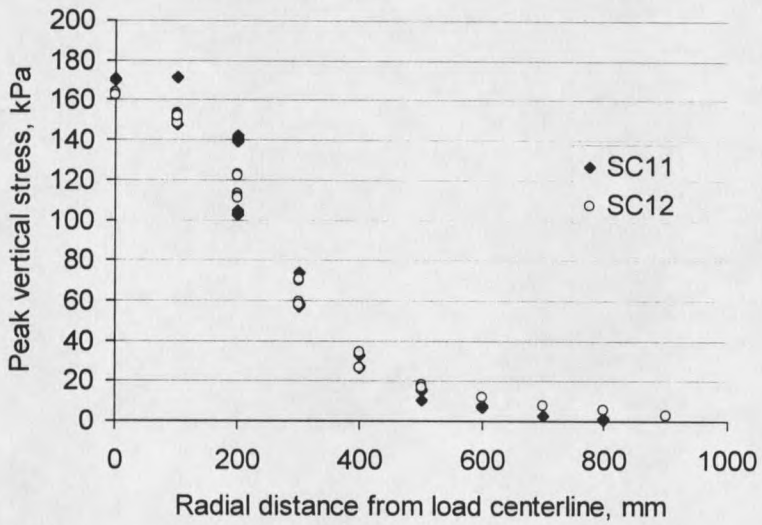


Figure 3.26 Vertical stress distribution in the base layer from two stress cells from section PCS1 (Z=300 mm).

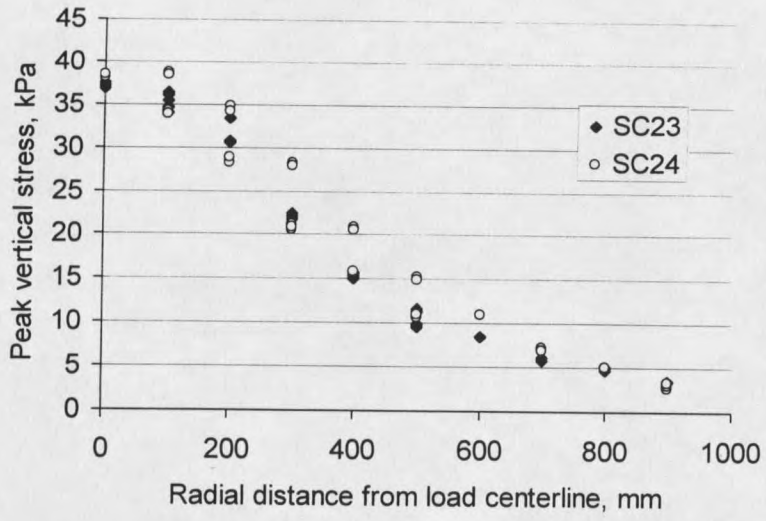


Figure 3.27 Vertical stress distribution in the subgrade from two stress cells from section PCS1 (Z=675 mm).

The following three figures present information from long-term measurements from test sections CS2 and CS8. Figure 3.28 illustrates the permanent rut development of both sections, exhibiting excellent agreement. It is noted that both sections "failed" (defined as 25 mm of permanent rut) at approximately 40,000 cycles of load. Figure 3.29 illustrates another key measure, permanent radial soil strain in the base layer, which will be used in Chapter 4 extensively to characterize differences between reinforced and unreinforced test sections. Permanent strain measures from the two instruments are repeatable. The final example of repeatable measurements is demonstrated in Figure 3.30, which presents a look at the peak dynamic vertical stress directly beneath the load center in the top of the subgrade over a large number of cycles of load. Again, excellent

agreement is obtained from the two stress cells in Figure 3.30. Where applicable, additional examples of repeatability will be given in Chapter 4 "Discussion of Results".

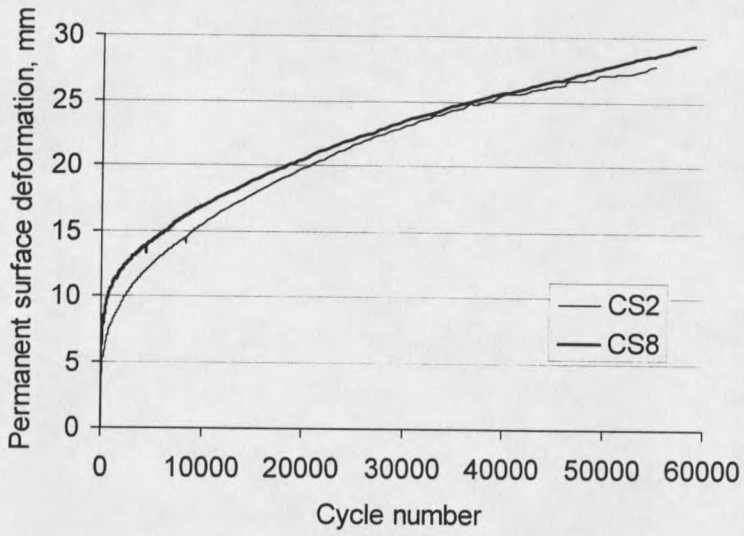


Figure 3.28 Permanent rut development for test sections CS2 and CS8.

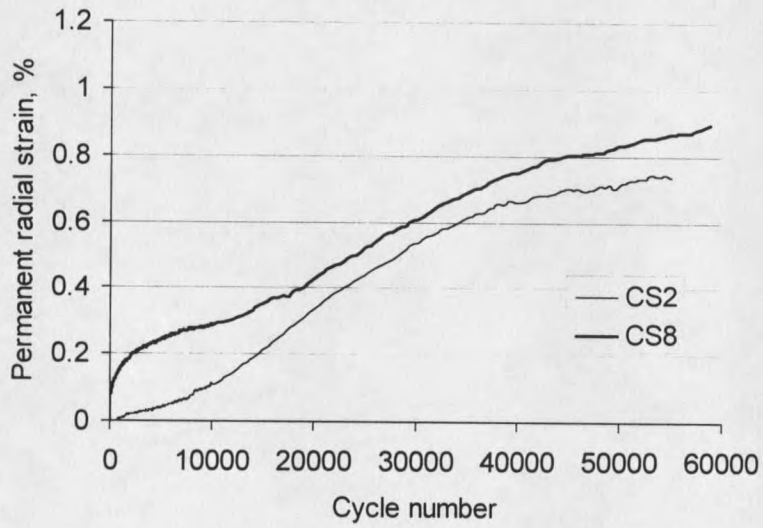


Figure 3.29 Long-term measures of radial strain in the base at a radial distance of 200 mm from the load centerline from test sections CS2 and CS8 (Z=325 mm).

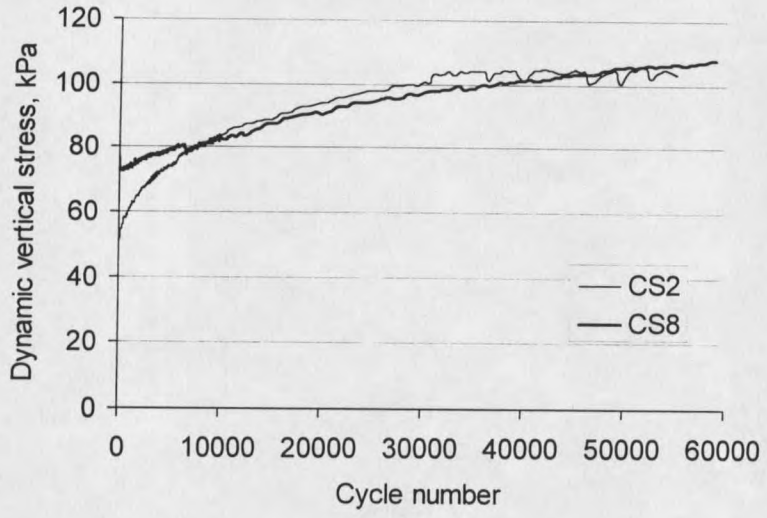


Figure 3.30 Long-term dynamic vertical stress in the top of the subgrade from test sections CS2 and CS8 (R=0 mm, Z=450 mm).

The two control sections SSS1 and SSS4 constructed with the silty-sand subgrade also exhibit excellent repeatability of long-term measurements. Long-term behavior of three critical measures is shown in Figures 3.31-3.33. These measures will be shown in Chapter 4 to be strong indicators of permanent rut development. Figure 3.31 illustrates consistency in the permanent radial strain measurement in the base layer between the two sections. Figure 3.32 illustrates agreement between the dynamic vertical stress transmitted to the top of the subgrade. Figure 3.33 shows repeatability of vertical strain measurements in the subgrade layer, another critical measure in evaluating reinforcement benefits.

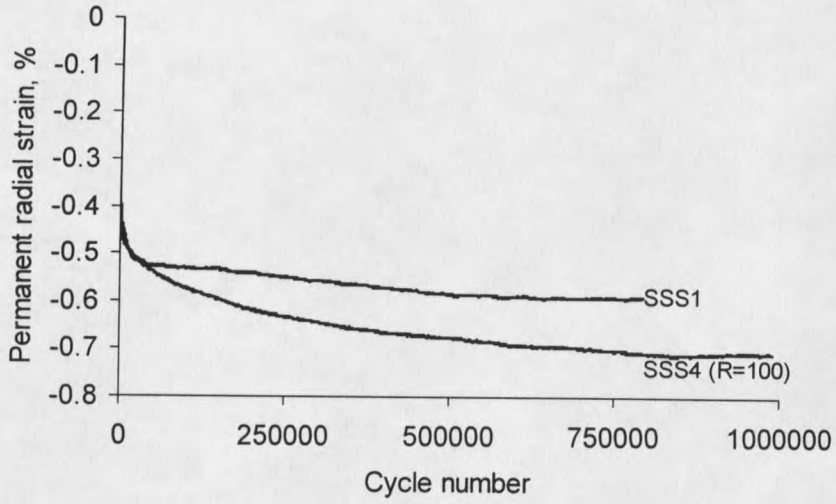


Figure 3.31. Permanent radial strain in the base (R=150 mm, Z=215 mm) (SSS1, SSS4).

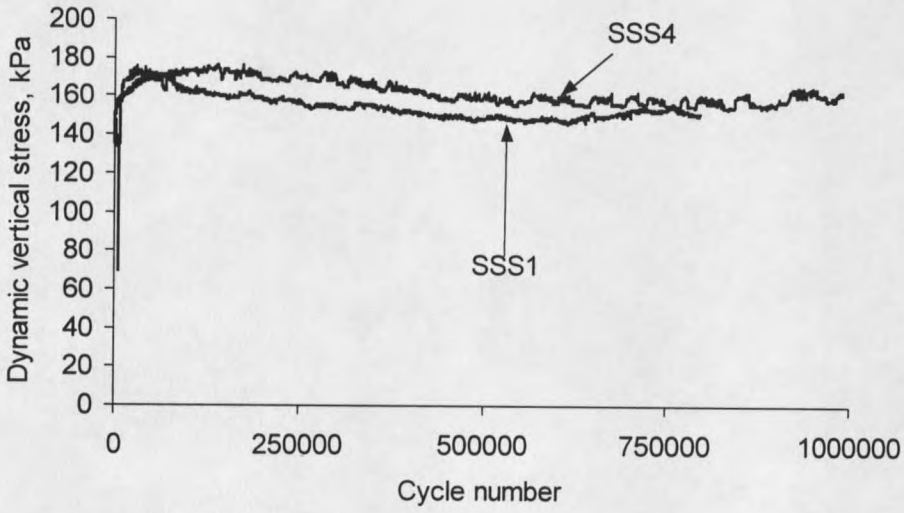


Figure 3.32. Dynamic vertical stress versus cycle number in the subgrade (R=0, Z=350mm) (SSS1, SSS4).

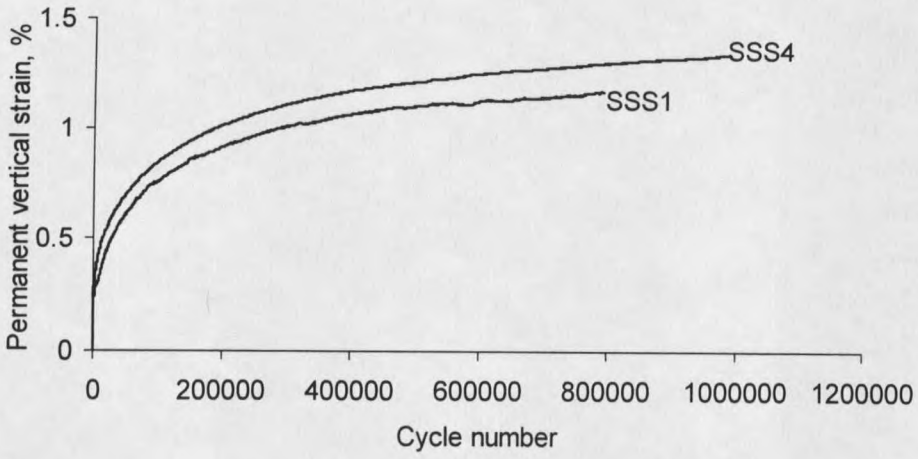


Figure 3.33. Permanent vertical strain versus cycle number in the subgrade (R=60 mm, Z=575 mm) (SSS1, SSS4).

CHAPTER FOUR

DISCUSSION OF RESULTS

Introduction

The purpose of this chapter is to provide a critical examination of the experimental results obtained from the clay subgrade and the silty-sand subgrade test sections. An emphasis is placed on the performance of the reinforced sections, through a detailed analysis of the mechanisms that account for improvements in permanent rut development in reinforced test sections. In this thesis, various mechanisms that account for this improvement are collectively referred to as the mechanism of a shear-resisting interface. Improvements in surface rutting performance will also be described in terms of the Traffic Benefit Ratio (TBR). The Traffic Benefit Ratio is defined as the ratio of the number of load cycles of a reinforced section to an identical unreinforced section necessary to achieve a particular rut depth. Analysis of the shear resisting interface mechanism will focus on test section data that support the beneficial effects of the mechanism. Effects of this mechanism that will be supported with experimental data include: 1) a reduction of lateral strain in the base layer, 2) a reduction of vertical strain in the base layer, 3) tensile strain development in the geosynthetics, 4) improved vertical stress distribution on the subgrade, 5) reduced lateral spreading of the subgrade, and 6) a

reduction in vertical strain in the subgrade. Additionally, the effects of an additional 75 mm of base course material will be incorporated into the discussion. An attempt will be made to point out that dynamic results from the first cycle of loading are not necessarily a good correlation to long-term performance when viewed in terms of several measures. The chapter will proceed with a discussion of the clay subgrade (CS) sections and end with a discussion of the performance of the silty-sand subgrade (SSS) sections. It is noted that sections CS1 and CS3 were not incorporated into the following performance analysis because of significantly different asphalt properties shown in Chapter 3 that led to pavement system behavior that could not be compared to other sections. It was argued in Chapter 3 that the asphalt properties accounted for the poor performance of the two sections, and hence were not used in the following analyses.

Clay Section Behavior

Rutting Behavior

This section provides an examination of the overall performance of the clay subgrade sections with respect to surface deformation (rut). Figures 4.1 and 4.2 illustrate the average permanent surface deformation as measured by the two LVDT's placed through the two holes in the load plate. It is noted that all figures in this chapter are contained at the end of the chapter. These two figures convey the same information, but look at short-term (under 80,000 cycles of load) and long-term (over 80,000 cycles of load) behavior. These figures show that the duplicated control sections CS2 and CS8

appear to be repeatable with respect to permanent surface deformation, and also illustrates failure for both sections (25 mm of rut) at approximately 40,000 cycles of load. With respect to performance, CS7 (BX-1100 geogrid placed 100 mm up from subgrade/base interface) performed slightly better (2 mm less rut over 350,000 cycles) than CS5 (BX-1200 geogrid placed at subgrade/base interface). In light of this small difference in performance between CS5 and CS7, it is worthwhile to look at some of the asphalt statistics presented in Chapter 3. The voids percentage in CS5 was somewhat higher than CS7, which may indicate that the section had a lower quality asphalt layer. Thus, based on surface deformations alone, it is difficult to determine if placement of the less-stiff BX-1100 geogrid 100 mm up into the base resulted in better performance than the more-stiff BX-1200 geogrid being placed at the subgrade/base interface, or whether asphalt properties accounted for the difference in behavior. CS11 (BX-1100 geogrid placed at subgrade/base interface) performed better than the geotextile section CS6 when both materials were placed at the interface. From the asphalt statistics presented in Chapter 3, asphalt properties between sections CS2, CS6, CS8, and CS11 were not statistically different. Additionally, for the first 7 mm of deformation, CS6 performed similarly to the control sections. It is also noted that the initial behavior (through 5 mm of deformation) of the geogrid reinforced sections (CS5, CS7, CS11) was very similar.

Figure 4.3 illustrates the permanent rut development for the thicker base course (375 mm thick) sections CS9 and CS10. Improvement was seen for the reinforced section over the control section. Figures 4.4 and 4.5 present TBR's for the thinner base sections (CS2-CS11) and the thicker base sections (CS9, CS10).

The reinforced section with the thicker base (CS10) exhibited a peak TBR between 12 and 14, while the thinner reinforced sections exhibited peak TBR's between 8 and 56. This may imply that more rutting is needed to mobilize the reinforcement, or that the effects of reinforcement diminish as the base thickness increases over some threshold. More rutting would imply a progression of shear flow in the base that was necessary before the base aggregate began to interact with the geogrid and does not imply that higher deformations were needed to mobilize a membrane type reinforcement function. This may also imply that moving the geogrid up higher in the base would have provided better performance in this situation.

Figure 4.4 illustrates the performance of the reinforced sections (including CS9 involving a thicker base course) with respect to the Traffic Benefit Ratio (TBR). The TBR values were obtained using the control section CS2 as a reference, and are calculated for increasing rut depths. Figure 4.5 illustrates the TBR of section CS10, using CS9 as a reference, with similar rut calculations. Figure 4.4 shows that the reinforced sections exhibit TBR's which, in general, increase with an increase in rut depth. This implies that reinforcement is increasing the performance of the sections while rut depths are developing. Maximum TBR's were obtained with CS7 and CS5, with peak TBR values of 56 and 42 respectively. CS6, the geotextile reinforced section, also exhibited a significant increase in TBR with an increase in rut depth, but exhibited a smaller TBR than the geogrid reinforced sections. A peak TBR of approximately 8 was reached after 23 mm of rut with the geotextile section. CS9 (control section with thicker base) is compared to CS2 in terms of TBR to illustrate the benefits of an additional 75

mm of base material. It is also shown in Figure 4.4 that the addition of 75 mm of base results in a peak TBR of 3.2, which occurs at a rut depth of 25 mm. All reinforced sections provide a higher TBR than the addition of 75 mm of base material, indicating that each reinforcement product is equivalent to at least 75 mm of base aggregate. The geotextile section provided an initially lower TBR than the added 75 mm of base up to approximately 5 mm of rut, where after the geotextile section performed better (in terms of TBR) than the additional base material.

To further understand reinforcement benefits in terms of surface deformation, it is necessary to look at a profile of the rut from directly beneath the load center extending laterally outward from the load center on two sides. Figures 4.6, 4.7, 4.8, and 4.9 show a profile of the rut or permanent deflection bowl for initial stages of loading (cycle 1) and later stages of loading (40,000 cycles and 125,000 cycles). Figure 4.6 illustrates that initial pavement deformation is rapid, but is also very different between the reinforced sections and the control sections. A distinct difference is also seen between the geogrid reinforced sections and the geotextile reinforced section. This difference between the geogrid and geotextile reinforced sections may indicate that geogrid reinforcement is engaged during early stages of loading while geotextile benefits are more delayed. First-cycle load comparisons of CS9 and CS10 in Figure 4.8 show that the reinforced section exhibited a higher level of deformation. This is consistent with earlier comments suggesting that more base aggregate shear flow was necessary to mobilize the reinforcement and that optimal performance may have been observed by moving the geogrid up into the base layer.

After 40,000 cycles of load, Figure 4.7 shows a distinct difference between the control sections and the reinforced sections. Repeatability, showing quality in construction, is again shown in the rut profile for the two control sections. Long-term analysis at 125,000 cycles of load (Figure 4.9) for the thicker base sections also illustrates a shallower deflection bowl for the reinforced section, indicating an overall stiffer section.

Figures 4.10 and 4.11 present results for the dynamic (elastic) surface deformation for early (cycle 1) and late stages of loading (12.5 mm permanent deformation). It is shown in Figure 4.10 that a relationship may exist for early cycles of load that correlate dynamic behavior to expected long-term behavior. The figure shows that the geogrid reinforced sections are somewhat clustered separately from the control sections, and that the geotextile section is more similar to the control sections. Exact correlation of this first-cycle dynamic response to eventual long-term rut development does not, however, exist. The dynamic (elastic) response presented in Figure 4.11 shows that the overall stiffness of the reinforced sections is less than that of the controls. It appears from the figure that the geotextile section was somewhat less-stiff than the other reinforced sections which may have had an effect on overall pavement performance. A similar investigation of the thicker base course sections CS9 and CS10 showed the reinforced section to be stiffer than the unreinforced section.

Additional examples of dynamic behavior that provides a link to long-term behavior is illustrated in Figures 4.12 and 4.13. Again, although not exact, Figure 4.12 shows a grouping of the reinforced sections and a grouping of the control sections.

Dynamic surface deformation would not be able to account for long-term rutting differences between CS5, CS7, and CS11. Figure 4.13 shows that the geogrid section CS10 exhibited a smaller dynamic surface deformation than the unreinforced control CS9.

Despite significant differences in the asphalt surface deformation measures just described, the results from the asphalt strain gages placed within the asphalt layer did not yield significant differences between the sections in terms of tensile strains. At this time, it is not clear if these results are a product of poor instrument function, instrument placement techniques, or that fatigue cracking potential (described by significant strains in the AC layer) was relatively unaffected by the inclusion of reinforcement or lack thereof.

Lateral Base Restraint Mechanism

This section will provide information to support the concept that the lateral base restraint mechanism is in part responsible for the improved performance (with respect to permanent surface deformation) of the reinforced sections. The section will begin with a discussion of results that directly illustrate the mechanism itself, and then proceed with a discussion of other effects/mechanisms that account for improved performance of reinforced sections. General effects of the lateral restraint mechanism were discussed previously in Chapter 2.

Figures 4.14 and 4.15 provide information on the lateral strain developed in the base layer between unreinforced and reinforced sections (300 mm thick base). These two

figures give lateral strain developed in the base at a depth of 325 mm at a radius of 100 mm and 200 mm from the load centerline, respectively. Lateral strain in the base is measured approximately 50 mm above the reinforcement for sections CS5, CS6, and CS11. For section CS7, the lateral base strain is measured approximately 50 mm below the reinforcement. It is shown in Figure 4.14 that all sections develop tensile strains at a radius of 100 mm, with the controls CS2 and CS8 exhibiting considerably more strain than the reinforced sections. Adequate shear-interaction is apparently developed between the soil and geosynthetics in all reinforced sections, although CS6 initially exhibits higher lateral strain comparable to the control sections for about 7-8 load cycles. At 200 mm from the load centerline, Figure 4.15 illustrates that the control sections CS2 and CS8 are in compression, while the reinforced sections are in tension. Reinforced sections are closely grouped in this figure. Between Figures 4.14 and 4.15, it is also shown that a strong gradient exists between the tensile region of soil and the compressive region of soil in the control sections. This gradient indicates that material is moving significantly outward away from the load. The figures also show that the reinforced sections do not tend toward compression at a 200 mm radius from the load, but remain tensile. Smaller tensile strains for the reinforced sections seems to imply restraint. Furthermore, CS2 and CS8 in Figure 4.15 demonstrate repeatability of lateral strain measurements in the base layer.

Figures 4.16 and 4.17 further illustrate the lateral restraint mechanism in reinforced sections (300 mm thick base). These two figures present a distribution of permanent radial strain in the base for the first load cycle and for 40,000 cycles of load.

It is noted that even after one cycle of load that a distinct difference between the reinforced sections and the control sections exist, illustrating that mechanisms of reinforcement are immediate. After 40,000 cycles of load (Figure 4.17), the reinforced sections exhibit very small lateral strains which remain mostly tensile even out to 400 mm beyond the load center. Reinforced sections are grouped closely in this figure, but differences in lateral strain correlate well with overall performance (rut development). It is difficult to determine if this correlation is significant.

Figures 4.18, 4.19, and 4.20 illustrate that the lateral restraint mechanism is also occurring in the 375 mm thick base course section (CS10). At a radii of 100 mm and 200 mm (Figures 4.18, 4.19) from the load center, considerably less lateral strain is exhibited by the reinforced section, with both sections showing extensional strains out to 200 mm. A distribution of the lateral strain is shown in Figure 4.20 for 125,000 cycles of load. Figure 4.20 shows that the control section CS9 had a steep slope and went from tension to compression over a relatively short distance (approximately 150 mm). This sharp change from tension to compression (and large magnitude of strain compared to CS10) substantiates that material is moving laterally outward in this section. The reinforced section exhibited much less change, as shown by the flat profile, resulting from lateral restraint.

Figure 4.21 also shows an improvement in dynamic radial strains. It is inferred that CS5 would be closer to the other reinforced sections if the AC quality was better as discussed previously. Otherwise, the dynamic strains appear to also reasonably correlate

to the order of performance of the sections, indicating that the level of lateral restraint may determine the long-term rutting potential of the section.

A manifestation of lateral base restraint is development of significant tensile strain in the geosynthetics, a requirement of the mechanism. Figures 4.22 and 4.23 show significant development of strains directly beneath the load in the machine and cross-machine directions of the geosynthetics. Long-term development of strain does not necessarily correlate well with long-term performance of the sections. Figure 4.24 also illustrates a distribution of permanent strain in the geosynthetics in the machine direction after 7500 cycles of load. This load cycle level was chosen since after this level, foil gages became inoperable. Again, significant permanent strain is developed in the materials. Permanent strain is accumulated, however under nearly constant dynamic strain. Figures 4.25 and 4.26 show relatively constant dynamic strain under cyclic loading. Additionally, Figures 4.27 and 4.28 show distributions of dynamic strain in the radial direction of the reinforcement for one cycle of load and after 7500 cycles of load. It is apparent from Figure 4.27 that strain is induced immediately in the geosynthetic indicating that reinforcement is immediate. Combining the information in Figures 4.27 and 4.28, it is shown that the dynamic strain remains essentially of the same magnitude over 7500 cycles over the distance of geosynthetic engaged. One additional point gained from Figure 4.27 is that poor correlation exists between the first cycle induced strain in the geosynthetics and the long-term performance differences between the reinforced sections.

Two reasons may describe the accumulation of permanent strain under constant dynamic strain conditions. Creep in the geosynthetic material may be one reason for the phenomena described. Another reason may be due to the accumulation of permanent or plastic strain in the base course material under cyclic loading conditions. Accumulation of cyclic induced strain in the granular material may cause increased plastic strain development in the geosynthetics under constant dynamic strain.

From the dynamic strain results in Figures 4.25 and 4.26, it can be shown that significant load is developed in the geosynthetic. Dynamic moduli were obtained for the BX-1100 geogrid and the 2006 geotextile from rapid loading, uniaxial tension tests from Cuelho (1998). These tests have not been performed to-date on the stiffer, BX-1200 geogrid. These dynamic moduli were multiplied by the dynamic strain exhibited by the two materials directly beneath the load in both the machine direction and the cross-machine direction, assuming a material thickness of 1 mm to yield a line load developed in the material. Table 4.1 summarizes the dynamic moduli for the materials, dynamic strain from Figures 4.25 and 4.26, and the resulting line loads developed in the two materials. Dynamic strain in the two directions is obtained at a radius of 15 mm in the machine direction (65 mm radius for CS6) and a radius of 20 mm in the cross- machine direction (65 mm for CS6). It is shown that line loads of up to 2.6 kN/m are developed in section CS11 (geogrid placed at the interface) and that loads up to 1.4 kN/m were developed in the geotextile. Development of significant loads shown in Table 4.1 indicate that significant load is being transferred from the soil to the geosynthetic, a

requirement of the lateral restraint mechanism, and the shear resisting interface mechanism.

Table 4.1. Dynamic load induced in the geosynthetics.

Section	Direction	Dynamic Moduli (kPa)	Dynamic Strain (%)	Dynamic Load (kN/m)
CS7	MD	600,000	0.3	1.8
	XMD	645,000	0.2	1.3
CS11	MD	600,000	0.43	2.6
	XMD	645,000	0.35	2.3
CS6	MD	239,000	0.15	0.4
	XMD	960,000	0.15	1.4

With a reduction of lateral strain in the base layer discussed previously, it is expected that vertical strain in the base layer should also be reduced. Figure 4.29 shows a distinct reduction in the vertical strain in the base layer beneath the load. Additionally, with the exception of CS5, the reinforced sections are grouped closely, indicating that although greater differences existed with lateral strains, the impact on the differences in vertical base strain is much less significant. It is noted that section CS6 is not much different from other sections and that base movement is apparently not the cause of the decreased performance.

Finally, as theoretically proposed in Chapter 2, the measurements of vertical, radial, and circumferential stress in the base layer did not yield any outstanding differences between the reinforced and unreinforced sections. Thus, the lateral restraint theory discussed in Chapter 2 could not be substantiated from the analysis of stress in the base layer. These inconsistent results may be due to any of three reasons: 1) instruments

were not consistent in measuring stress in large particle granular materials, 2) stress cell placement in the base was inconsistent, or 3) the lateral restraint mechanism does not significantly alter the measurable stress distributions in the base layer. Additionally, the stress cells may not have been spaced close enough to measure an increase in mean stress for the base layer. Essentially, an increase in mean stress in the base layer may have only occurred over a finite area that was missed due to inappropriate instrument spacing. This spacing of instruments may have also given a false impression of the radial stress distribution. An improved vertical stress distribution in the base may be difficult to ascertain given the sharp fluctuations that may be occurring due to the soil being restrained in the lateral direction, which may cause upward arching of the base aggregate in the area of the most geosynthetic/soil interaction.

Improved Vertical Stress Distribution on Subgrade

Another beneficial effect of the shear resisting interface mechanism is an improvement in the magnitude and distribution of vertical stress transmitted to the top of the subgrade. Figures 4.30-4.33 show a reduction of dynamic vertical stress directly beneath the load center through the depth of the subgrade (i.e. from a depth of 450 mm to a depth of 1075 mm). The reinforced sections exhibit a significant reduction in the dynamic vertical stress applied to the subgrade. Also shown in Figures 4.30 and 4.31 is that the geotextile section transmits a greater dynamic vertical stress than the other geogrid reinforced sections, particularly in the top of the subgrade. The geogrid sections appear to perform about equal for depths up to 775 mm. After that depth, performance is

approximately the same. It also appears from these figures that the majority of the vertical stress improvement is seen in the top of the subgrade (i.e. at a depth of 450 mm). Benefits or differences between the reinforced sections and the controls diminish slowly after a depth of 450 mm. This long-term benefit of a reduction in vertical stress is again shown in Figure 4.34, where it is seen that a significant reduction of vertical stress is gained from the reinforced section CS10 in comparison to CS9, the control section. This implies that the effect is also present in a thicker base course situation, at least at one finite distance of 200 mm from the load center. Due to limited data associated with instrument failure, a distribution of vertical stress was not available for the thicker base course sections CS9 and CS10.

Figure 4.35 shows a distribution of vertical stress across the top of the subgrade after one cycle of load has been applied for sections CS2, CS5, CS6, CS7, and CS11. It is noted that several of the reinforced sections perform worse (higher vertical stress transmitted to the subgrade) than the control section CS2. Thus, correlating this first-cycle information to long-term performance of the sections would be invalid. Figure 4.36 shows a distribution of vertical stress across the top of the subgrade after 40,000 cycles of load have been applied for sections CS2, CS5, CS6, CS7, and CS11. It is seen that the reinforced sections perform better (lower vertical stress applied) than the control section. Additionally, it is noted that the geotextile section exhibits a higher vertical stress directly beneath the load (R=0 mm) than the geogrid sections. In this figure, one must assume that a radial distance of 400 mm that the reinforced sections are providing a dynamic vertical stress equal to or less than that of CS2. It is also shown from this figure that the

slope of the vertical stress versus distance curve is much flatter for the reinforced sections, thereby indicating that less dynamic vertical stress is being applied to the top of the subgrade over the distances indicated by the figure. Less vertical stress is transmitted not only beneath the load center, but also out beyond the loaded area, indicating that the load is being spread more efficiently by the reinforced sections.

Lateral Spreading on Top of Subgrade

Lateral spreading on top of the subgrade is undesirable from a rutting point of view. Lateral spreading results from lateral strain directly transmitted through the base subgrade interface. If the shear resisting interface mechanism is functioning, then less spreading of the subgrade should result. Reinforcement appears to reduce the amount of lateral strain in the top of the subgrade in much the same pattern as seen in the bottom of the base layer. Figures 4.37 and 4.38 show an improved distribution of lateral strain for reinforced sections for the 300 mm and 375 mm base thickness respectively. It is noted that the magnitude of strain is significantly lower in Figure 4.38 presumably due to the addition of 75 mm of base material. The rate of development of lateral strain is also reduced by reinforcement as illustrated by Figure 4.39, which illustrates a dramatic reduction of lateral strain in the reinforced section CS10 over time. Additionally, it appears from the results that the effect of reinforcement is immediate as shown in Figure 4.40, where the reinforced sections exhibit a flat distribution of strain having a smaller magnitude than the control sections. Figure 4.39 again shows that the benefit of the reinforcement increases over time. This effect may also be a reason for the increasing

TBR curves with increasing rut depth presented previously. Finally, a plot of dynamic radial stress for sections CS9 and CS10 (Figure 4.41) illustrates that the radial stress at a radius of 250 mm from the load center is significantly reduced in the reinforced section CS10. Indicated is a reduction in "shoving" of the subgrade material outward leading to less rut development. Lateral spreading was only shown in the top of the subgrade due to the lack of radial strain measurements below this level. It is also assumed that no significant lateral spreading would exist below the top of the subgrade.

Vertical Strain in Subgrade

The two previous effects of improved vertical stress distribution and improved lateral spreading on top of the subgrade should lead to less vertical strain in the subgrade. Figures 4.42-4.45 show a dramatic difference in the top of the subgrade (Figure 4.42), with effects diminishing deeper in the subgrade (Figures 4.43-4.45). These figures present vertical strain measures directly beneath the load. In Figure 4.42 it is shown that the rate of development of vertical strain (a direct measure of rut for the subgrade) is significantly less for the reinforced sections. This effect appears to be immediate, with rates of development of vertical strain being lower for the reinforced sections compared to the controls. A reasonable correlation is shown between the development of vertical strain in the subgrade for the reinforced sections and the overall performance (accumulation of permanent surface rut) discussed previously in Figures 4.1 and 4.2. Additionally, Figure 4.42 shows that the geotextile reinforced section accumulated vertical strain much faster than the other reinforced sections during the first 20,000 cycles

of load. At this time, it is not clear why the vertical strain from the geotextile section is higher than the other sections when lateral strains in the base are equivalent. Figure 4.46 also shows a reduction in vertical strain for the thick base sections CS9 and CS10, although the vertical strain reduction in this figure is not as dramatic as in the thinner base sections.

Effect of Additional Base Material

The effect of 75 mm additional base is described by comparing the control sections with the thinner 300 mm base (CS2 and CS8) to the thicker 375 mm base control section CS9. It is noted that in the following figures that due to the different thickness of base, that the depth of the instruments is different between the sections. The measures are common with respect to the distance above or below the base/subgrade interface (i.e. vertical strain in the subgrade is measured at the same point in the top of the subgrade for the three sections). Figures 4.47 and 4.48 show that an additional 75 mm of base has the effect of reducing lateral strain in the base layer similar to the effects of adding reinforcement. It is also shown that this effect of reduction of lateral strain, even without reinforcement present, is apparent immediately at cycle 1 (Figure 4.47).

The 375 mm base exhibits a better load distribution on the top of the subgrade in terms of applied dynamic vertical stress, shown in Figures 4.49 and 4.50. A similar effect is shown with a reduction in radial or lateral strain in the top of the subgrade for section CS9 in Figures 4.51 and 4.52. The net effect of the addition of 75 mm of base is shown in Figure 4.53, where accumulation of vertical strain in the top of the subgrade is

dramatically reduced in section CS9. Additionally, the rate of development of vertical strain is fairly linear for section CS9 as opposed to what appears to be log-based development for sections CS2 and CS8. This effect is very similar to the effect of reinforcement discussed previously in Figure 4.42 with the reinforced thinner base sections.

Interestingly, in terms of total performance (development of permanent surface deformation) the reinforced sections with the 300 mm thick base performed better than the unreinforced 375 mm thick base section. It appears that geosynthetic reinforcement was providing a greater contribution to overall performance (rut depth development) than the addition of 75 mm of base. In summary, combining the information given above, the reinforcement has a comparable structural effect as adding additional base material.

Silty-Sand Subgrade Section Behavior

Rutting Behavior

As illustrated in Chapter 3 from the statistical comparisons of asphalt concrete voids content, sections SSS1 and SSS4 (unreinforced control sections) are statistically different from sections SSS2 and SSS3 (geogrid and geotextile reinforced), while each group is statistically comparable amongst themselves. Thus, direct comparisons are difficult between the controls and the reinforced sections. Comparisons between the sections will be made however, in a modeling effort, which is an extension of this research, but beyond the scope of this report. Modeling will be able to incorporate

differences in asphalt properties and equivalent sections may be modeled to gain a better understanding of the reinforcement benefits. Additionally, sections SSS5-SSS9, which used cold-mix as the surfacing material, did not yield significant performance results due to the fact that the cold-mix material was not consistent with respect to stiffness. Specific in-place properties such as air voids could not be determined due to the inability to obtain drilled cores from the soft cold-mix material as discussed in Chapter 3. However, sections SSS5-SSS9 will be used to illustrate some compatibility issues between the geosynthetics and the surrounding soil in following sections.

Figure 4.54 illustrates the permanent rutting performance of the four sections SSS1-SSS4. Unfortunately, the performance differences between groups of sections is most likely due to AC property differences. Additionally illustrating this difference between the groups of sections is Figure 4.55, which shows significantly higher radial strain developed in sections SSS2 and SSS3, than in sections SSS1 and SSS4, mostly likely due to a less-stiff AC material. Between SSS2 and SSS3 in Figure 4.54, the geogrid section appears to perform slightly better than the geotextile section, although not significantly better. Figure 4.54 demonstrates repeatability between the construction of SSS1 and SSS4, which are identical control sections.

Lateral Base Restraint Mechanism

Figure 4.56 and 4.57 shows a greater amount of lateral spreading of the base in the geotextile reinforced section than in the geogrid reinforced section. Also illustrated in Figure 4.56 is the repeatability of the two control sections, SSS1 and SSS4. Figure 4.58

illustrates a distribution of lateral strain in the base after 500,000 cycles of load. It is shown that the geogrid reinforced section has a better attenuation of radial strain across the section than does the geotextile reinforced section. These three figures indicate that the higher AC stiffness in sections SSS1 and SSS4 exhibits similar results to when reinforcement is added, showing that AC properties are very important.

A result of the reduced lateral spreading in the base layer is a reduction of vertical strain in the base layer. Figure 4.59 illustrates a reduction in vertical strain directly beneath the load center for the geogrid reinforced section compared with the geotextile reinforced section. Another result of lateral restraint occurs with an examination of the strains developed in the geosynthetics. Figures 4.60 and 4.61 illustrate that tensile strain is again developed on the geosynthetics, a necessary requirement of lateral restraint, as discussed previously with the treatment of the clay subgrade sections. It is noted that these strains are in the machine and cross-machine directions directly beneath the load center. Magnitudes cannot be compared due to differences in asphalt type (i.e. hot-mix versus cold-mix sections) that are plotted on the same figures. However, the magnitudes of the radial strain in these figures are much less than the strain exhibited in the geosynthetics in the clay subgrade sections, indicating that subgrade strength is another important variable with respect to reinforcement benefit.

Soil/Geosynthetic Compatibility. This section will demonstrate from cold-mix and hot-mix sections SSS2, SSS5, and SSS8 that compatibility exists between the geosynthetic and the surrounding base aggregate. This condition of compatibility is necessary to engage the geosynthetic in order for the lateral restraint function to occur.

Figures 4.62 and 4.63 show the distribution of permanent radial and tangential strain in the soil and the geogrid in section SSS5. It is shown from these two figures that the distribution of strain in the geogrid follows the distribution of strain in the soil very well, indicating compatibility. Figures 4.64 and 4.65 show a similar distribution of strain for the geotextile reinforced section SSS8. It is noted on both figures that the profile of permanent strain in the geotextile is somewhat "flat" in regards to the corresponding soil strain. The "flat" profile may indicate some slip is occurring between the soil and geosynthetic. Figure 4.66 shows another geogrid section SSS2 develops slightly larger differences between the geogrid and the surrounding soil compared to section SSS5. Reasons for this difference may include the fact the subgrade was weaker in section SSS2, and after 5000 cycles of load the total pavement deformation was much higher for section SSS2 than section SSS5. From the figures presented however, the geogrid sections appear to develop the best bond with the soil as compared to the geotextile section. This difference may not be significant though, and is difficult to substantiate with so few sections.

Subgrade Effects

Figures 4.67 and 4.68 describe the long-term dynamic vertical stress observed at the top of the subgrade, and a distribution of the dynamic vertical stress across the top of the subgrade. Both figures show very little difference between the two reinforced sections in terms of applied vertical stress on top of the subgrade. Again, sections SSS1 and SSS4 show a reduction in the applied vertical stress due to the stiffer AC properties.

An examination of the radial strain (indicative of lateral spreading) also yielded no conclusive differences between the two reinforced sections.

Figures 4.69-4.72 illustrate the vertical strain development over many cycles through the depth of the subgrade. These figures show little consistency between the two reinforced sections. Figures 4.69 and 4.72 show the geogrid section performing better, while Figure 4.70 shows the geotextile section performing better in terms of vertical strain development. Consistently, sections SSS1 and SSS4 perform much better in terms of vertical strain progression in these figures, presumably again due to better AC stiffness.

From the data presented in this section, it appears that there is little effect of reinforcement type on the silty-sand subgrade, given the subgrade strength used and the magnitude of the applied load. It does appear however, that reinforcement is occurring, as exhibited through reductions in lateral spreading in the base and reductions in vertical strain in the base. It appears that overall rut depth may have been related to these base course effects, but unfortunately, the control sections are not directly comparable. Thus, it must be assumed that the reinforcement effects are minor.

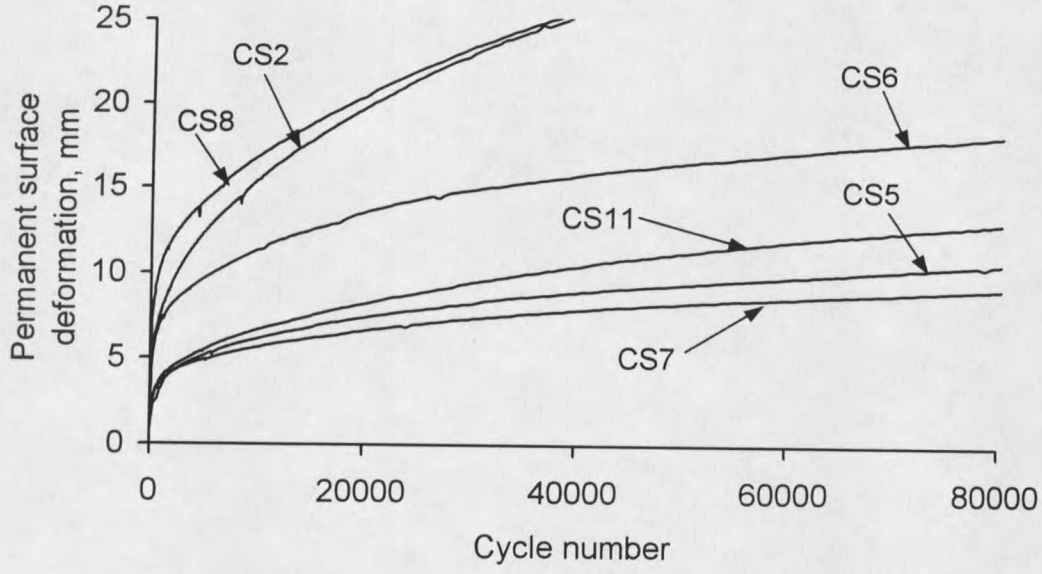


Figure 4.1 Permanent surface deformation versus cycle number for less than 80000 cycles (CS2-CS11).

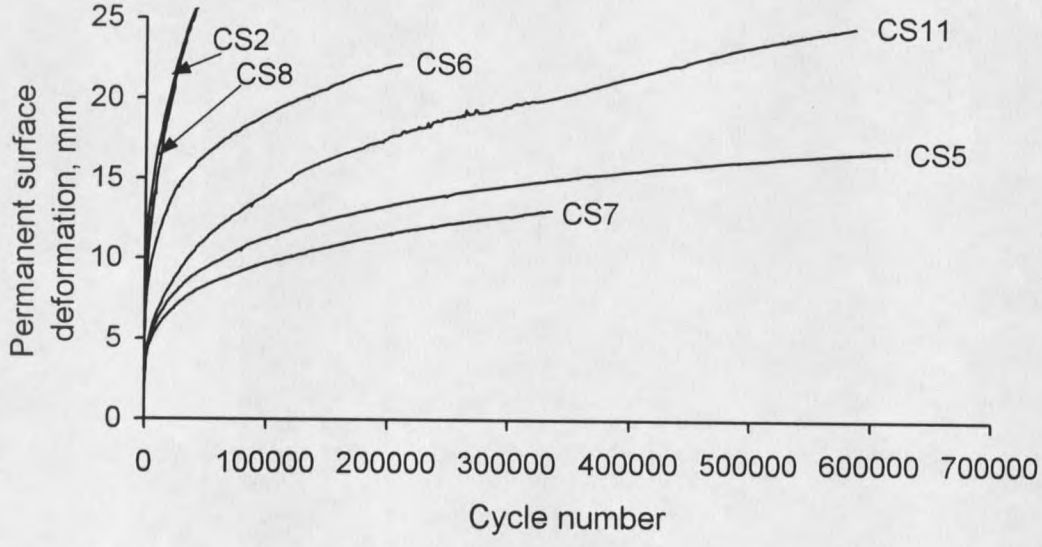


Figure 4.2 Permanent surface deformation versus cycle number for all cycles (CS2-CS11).

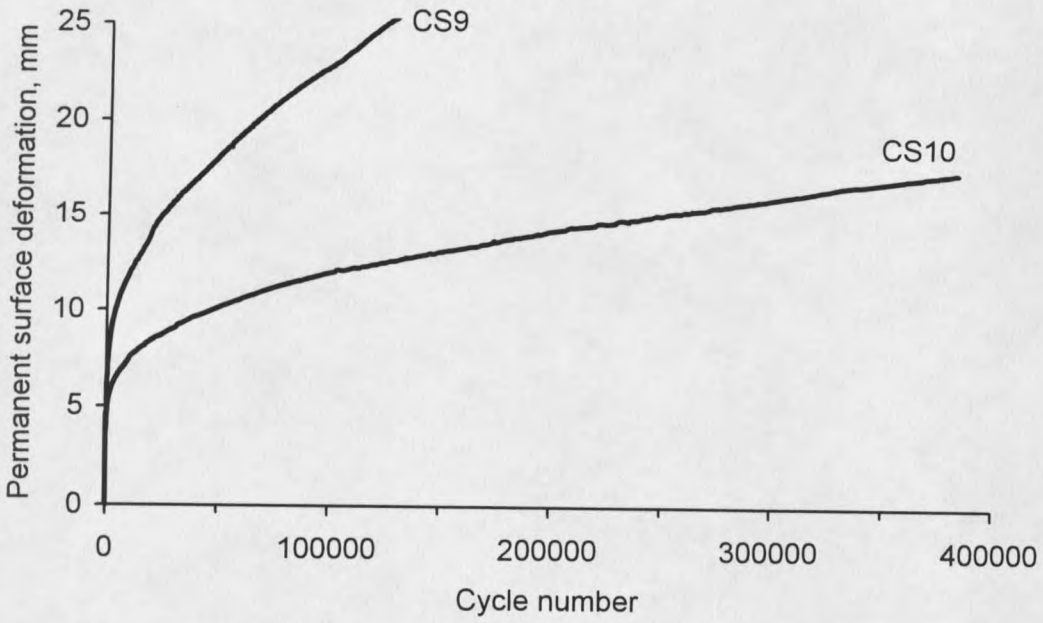


Figure 4.3 Permanent surface deformation versus cycle number (CS9,CS10).

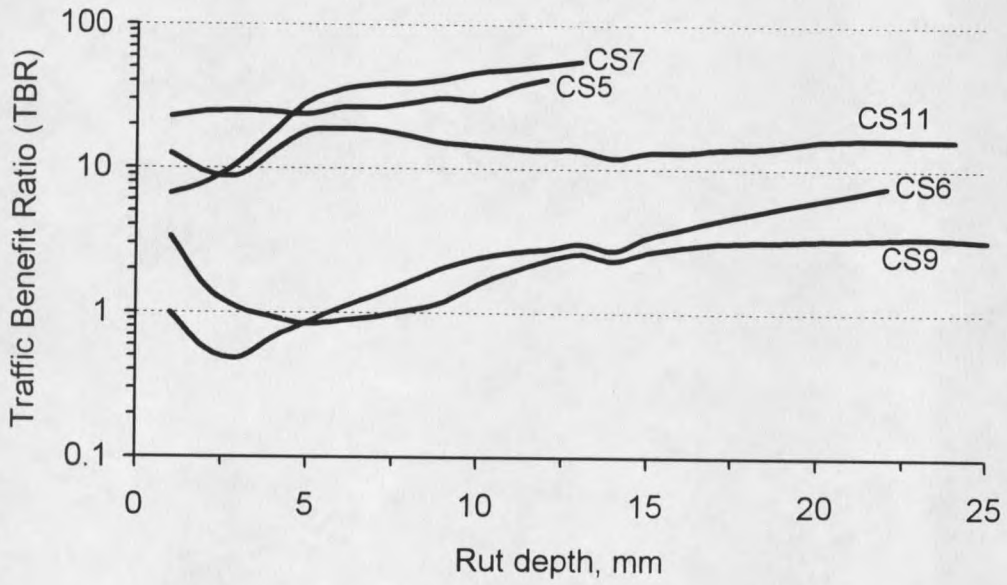


Figure 4.4 TBR for sections CS5,6,7,9, and 11 relative to CS2.

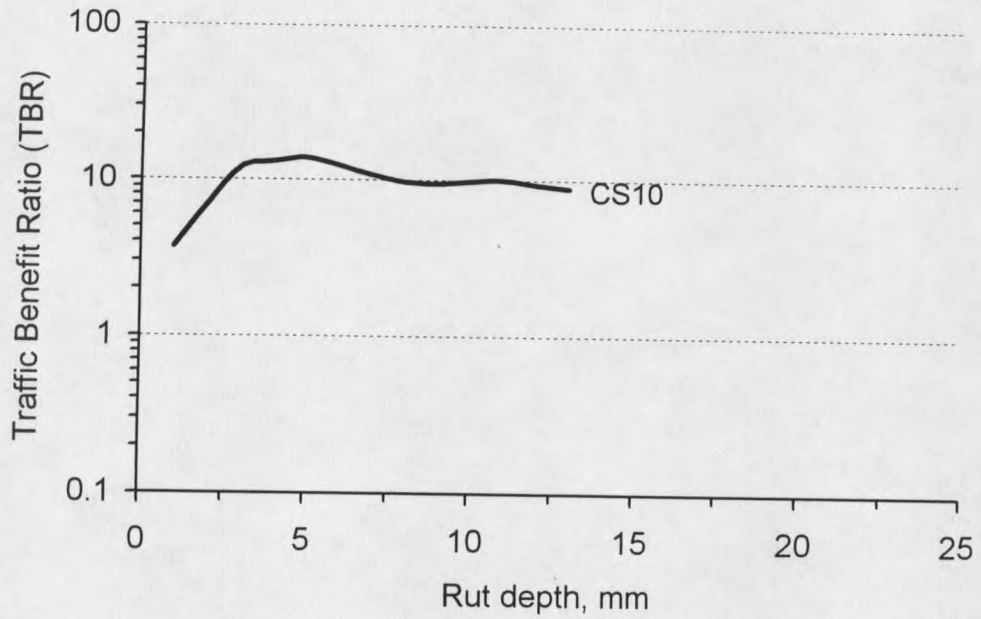


Figure 4.5 TBR for section CS10 relative to CS9.

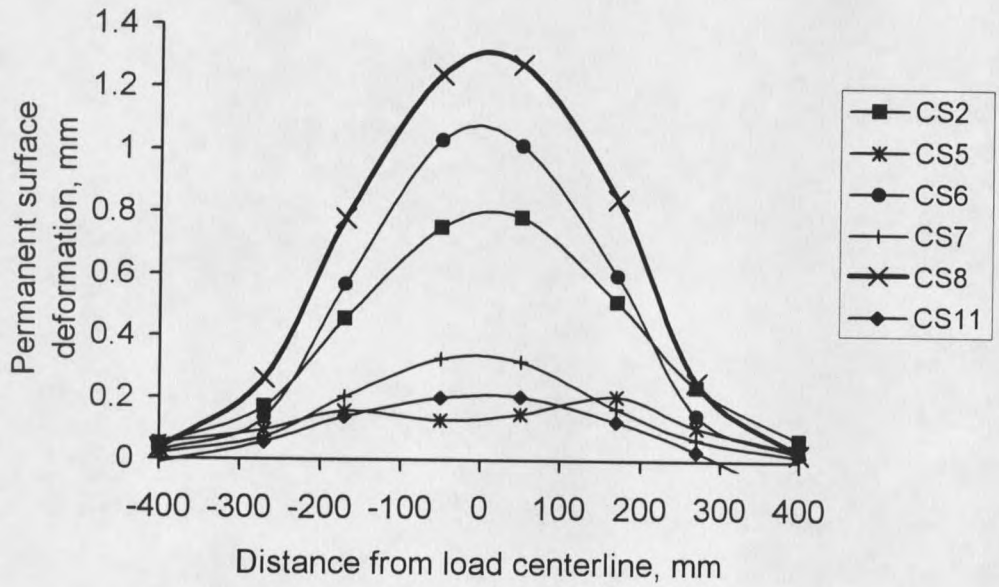


Figure 4.6 Permanent surface deformation bowls at cycle 1 (CS2-CS11).

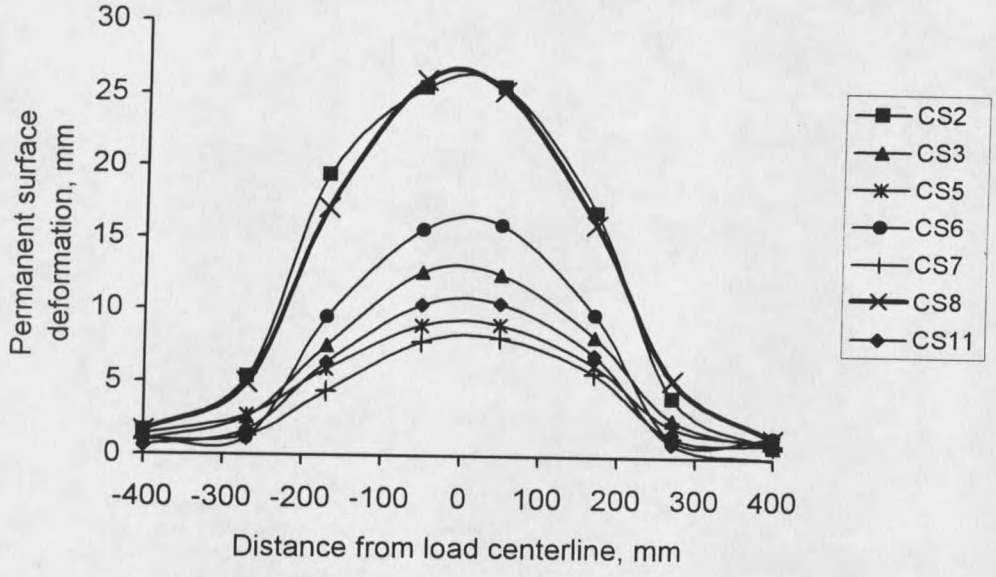


Figure 4.7 Permanent surface deformation bowls at cycle 40,000 (CS2-CS11).

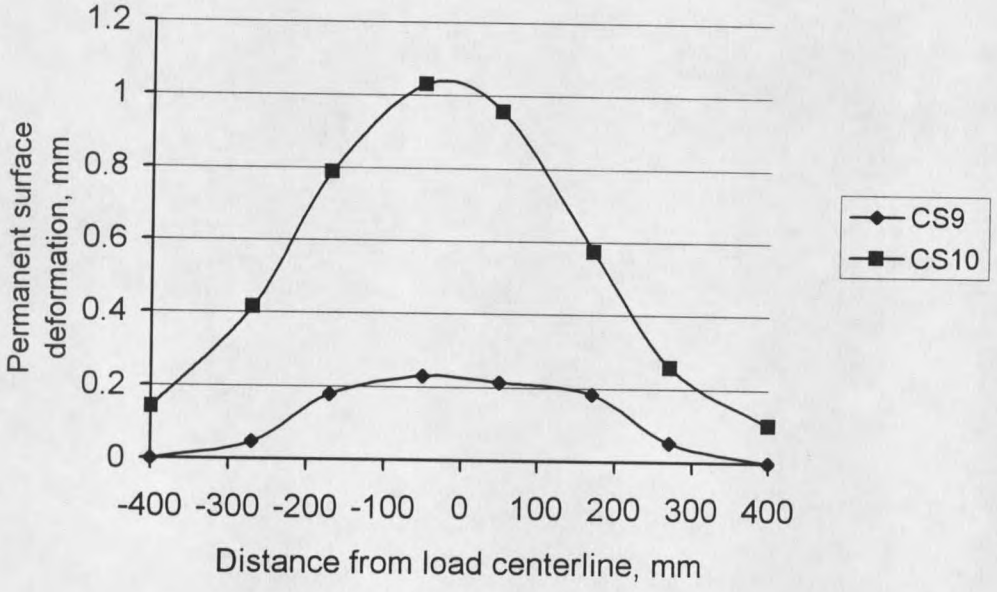


Figure 4.8 Permanent surface deformation bowls at cycle 1 (CS9-CS10).

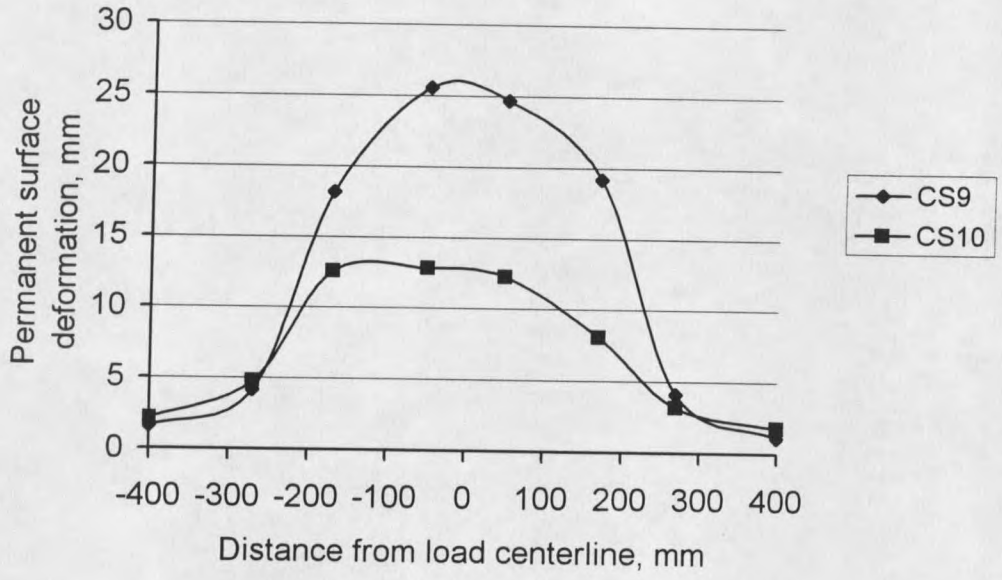


Figure 4.9 Permanent surface deformation bowls at cycle 125000 (CS9-CS10).

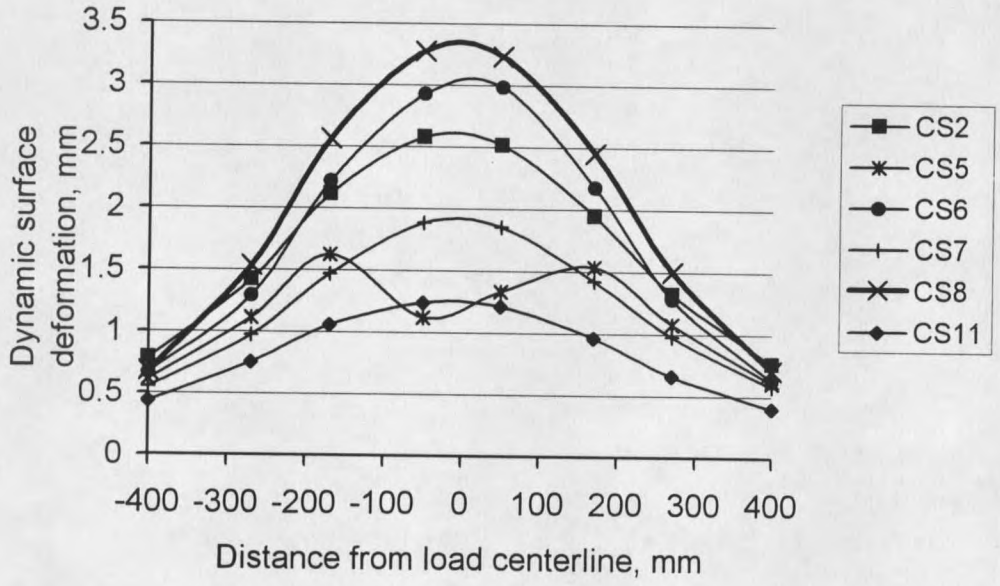


Figure 4.10 Surface dynamic deformation bowls at cycle 1 (CS2-CS11).

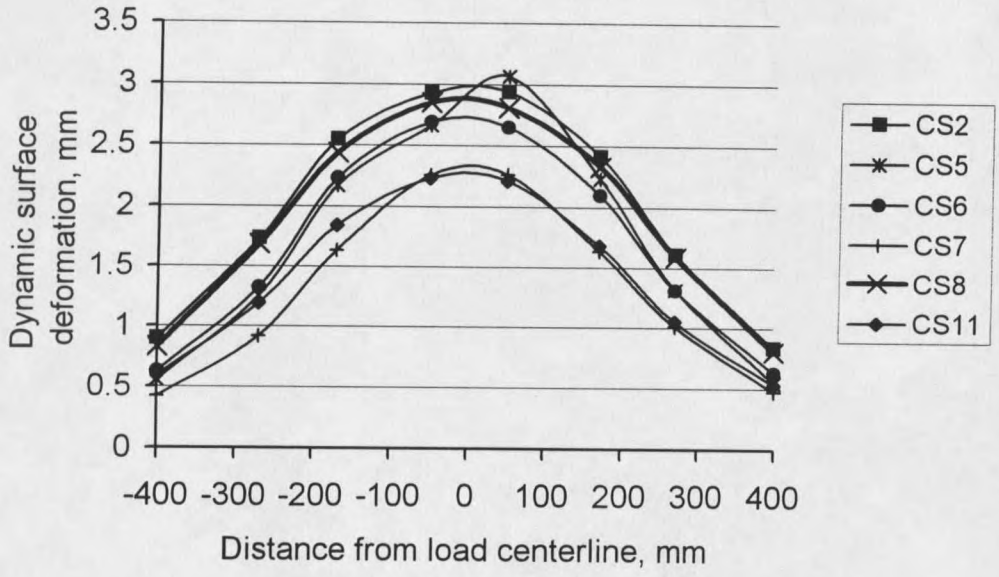


Figure 4.11 Dynamic surface deformation bowls at a permanent rut depth of 12.5 mm. (CS2-CS11).

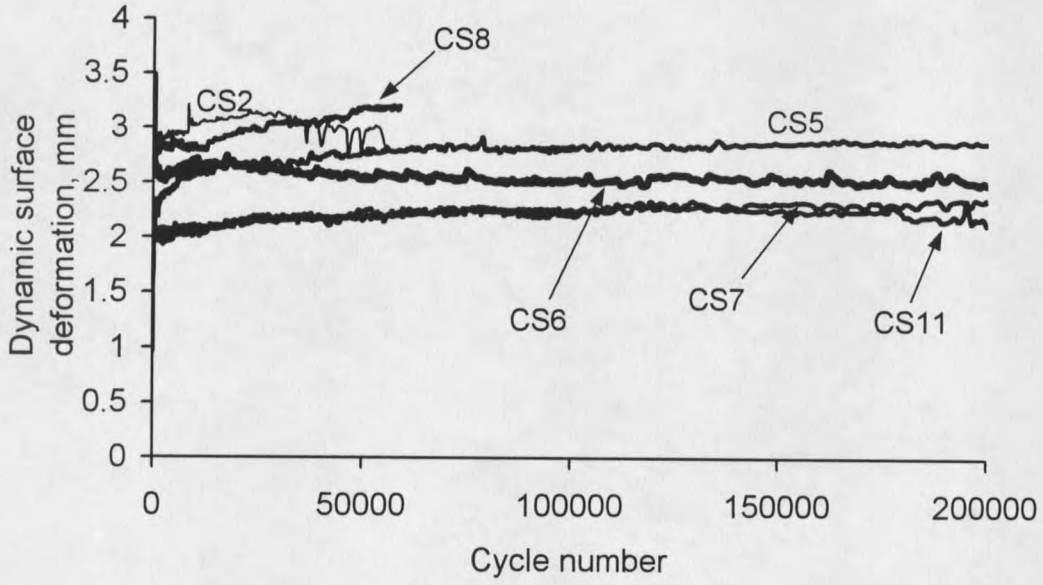


Figure 4.12 Dynamic surface deformation versus cycle number (CS2-CS11).

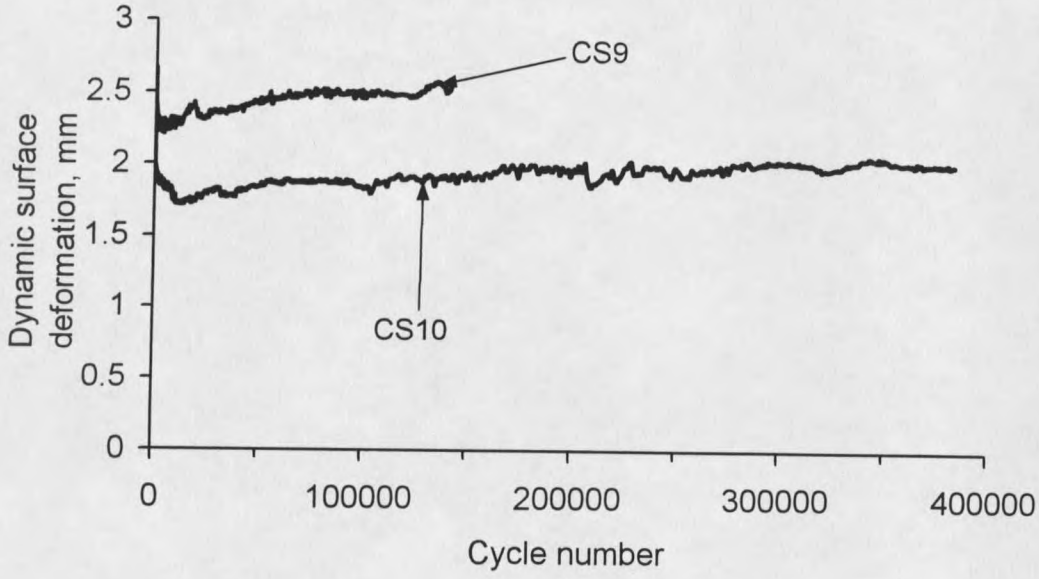


Figure 4.13 Dynamic surface deformation versus cycle number (CS9, CS10).

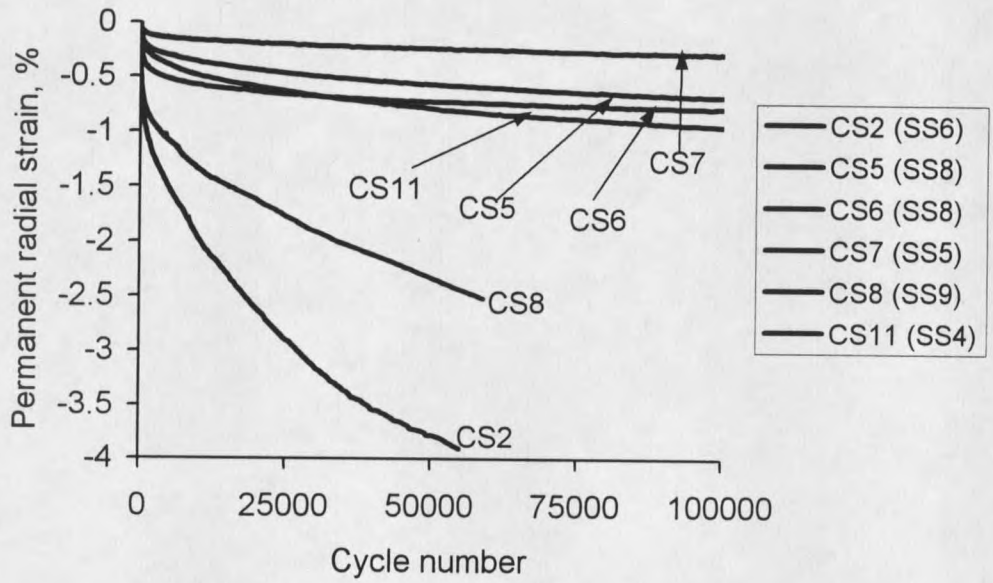


Figure 4.14 Permanent radial strain in base of sections CS2-CS11 (R=100, Z=325mm).

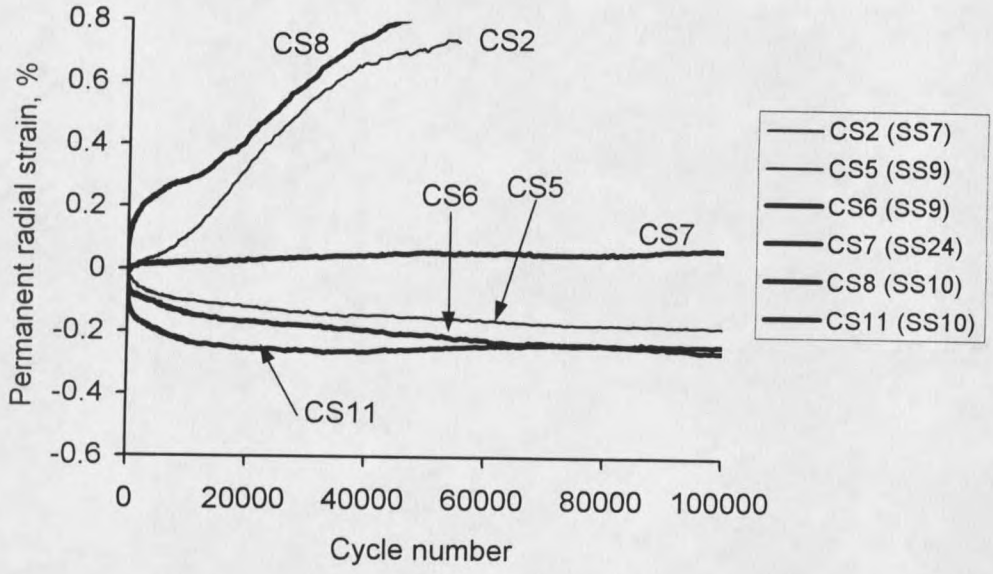


Figure 4.15 Permanent radial strain in base of sections CS2-CS11 (R=200, Z=325 mm).

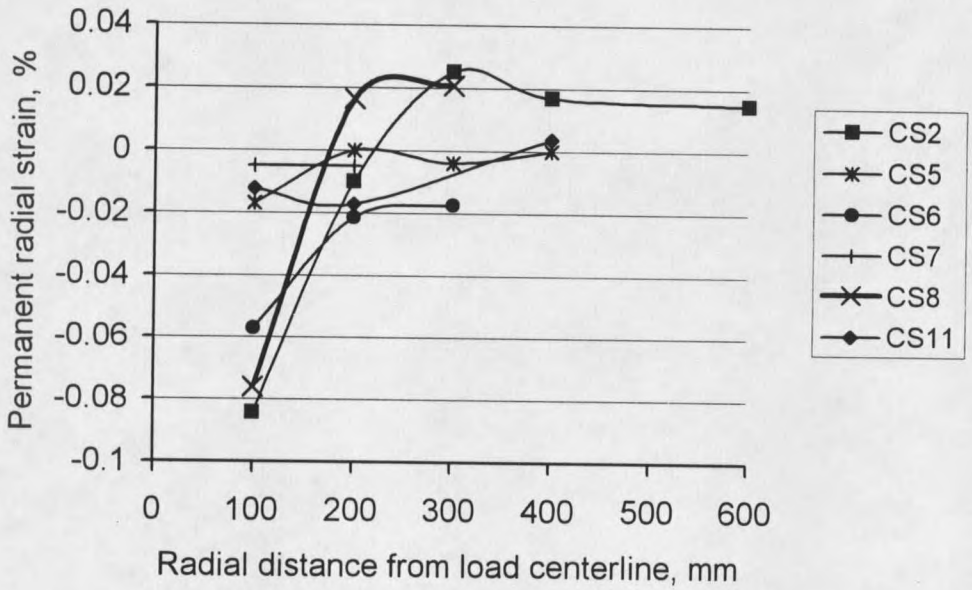


Figure 4.16 Permanent radial strain in the base versus radial distance at cycle 1 of sections CS2-CS11 (Z=325mm).

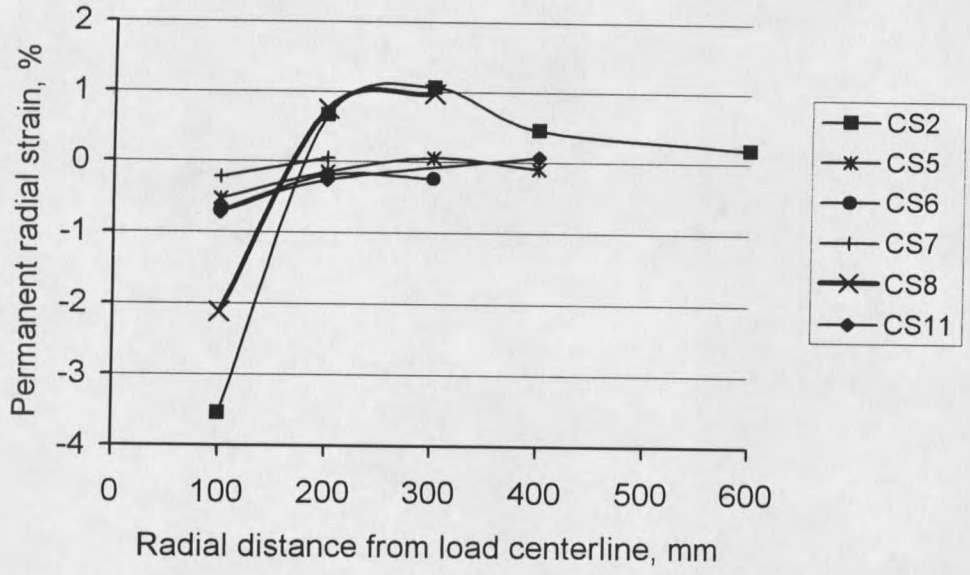


Figure 4.17 Permanent radial strain in the base versus radial distance at cycle 40000 of sections CS2-CS11 (Z=325mm).

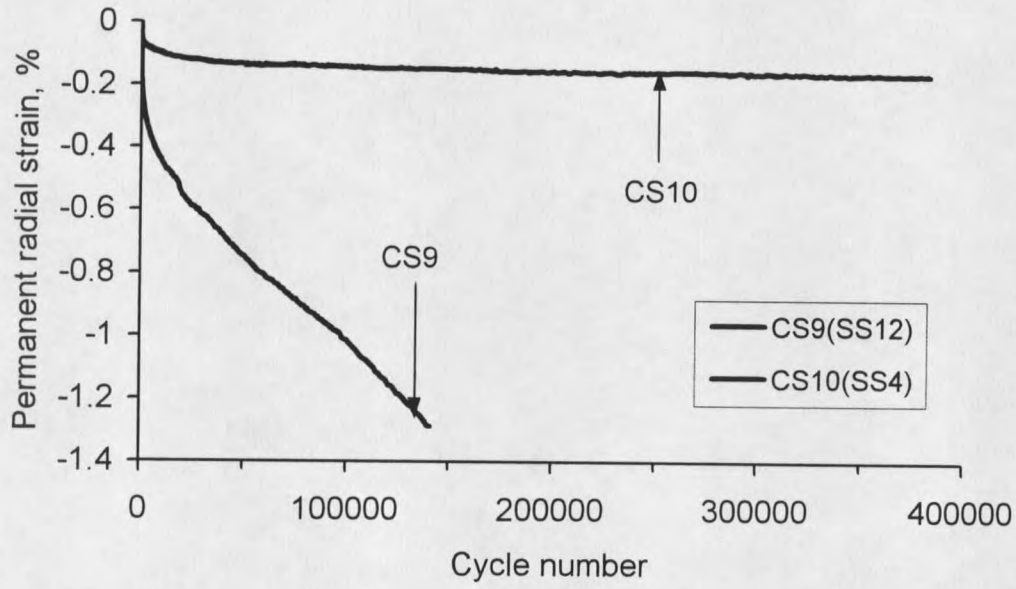


Figure 4.18 Permanent radial strain versus cycle number in the base of sections CS9-CS10 (R=100mm, Z=400mm).

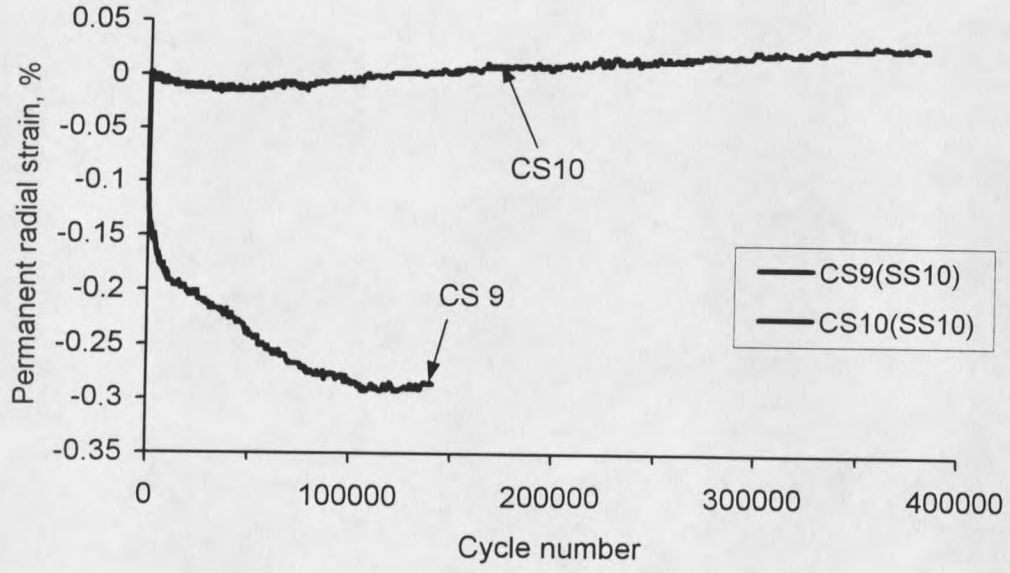


Figure 4.19 Permanent radial strain versus cycle number in the base of sections CS9-CS10 (R=200mm, Z=400mm).

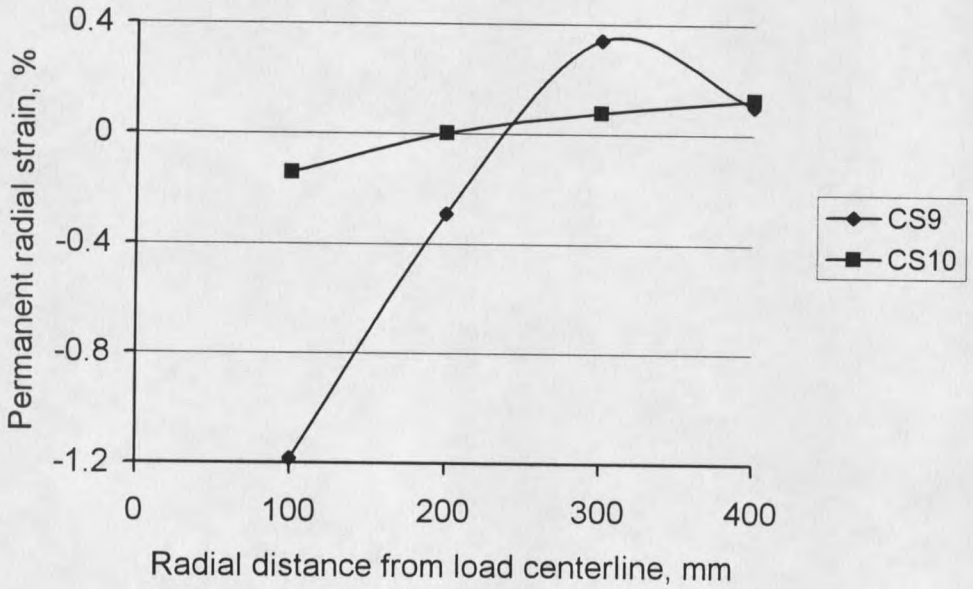


Figure 4.20 Permanent radial strain versus radial distance in the base of sections CS9-CS10 at cycle 125000 (Z=400 mm).

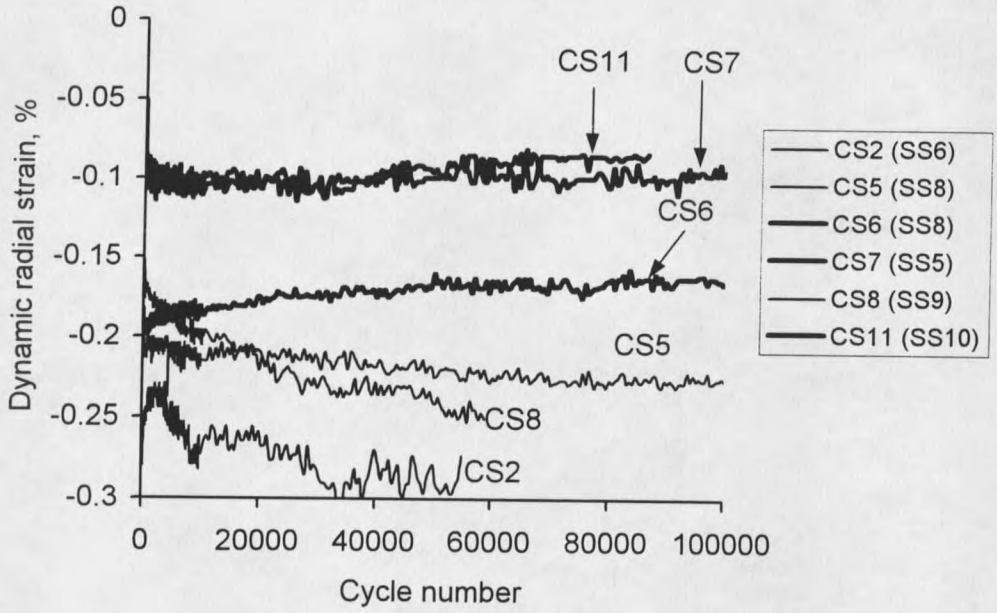


Figure 4.21 Dynamic radial strain in base of sections CS2-CS11 (R=100, Z=325mm).

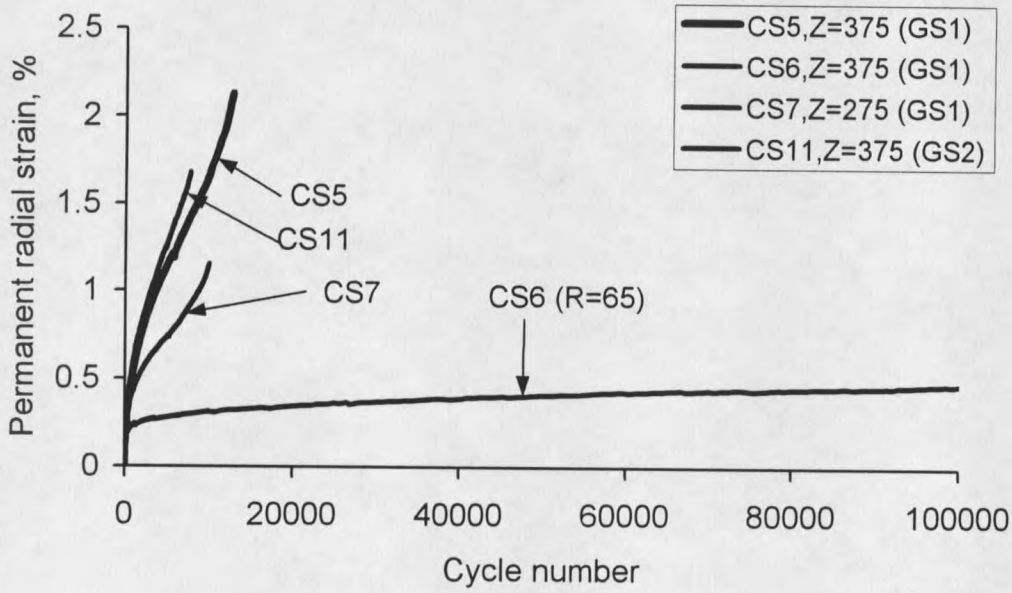


Figure 4.22 Permanent radial strain (M) in the geosynthetics of sections CS5-CS11 (R=15 mm).

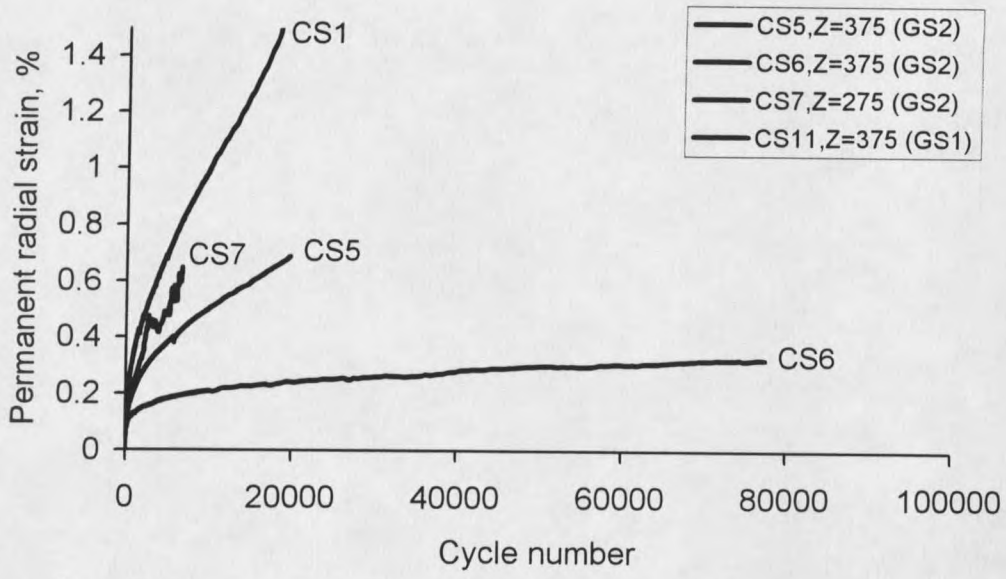


Figure 4.23 Permanent radial strain (XM) in the geosynthetics of sections CS5-CS11 (R=20 mm).

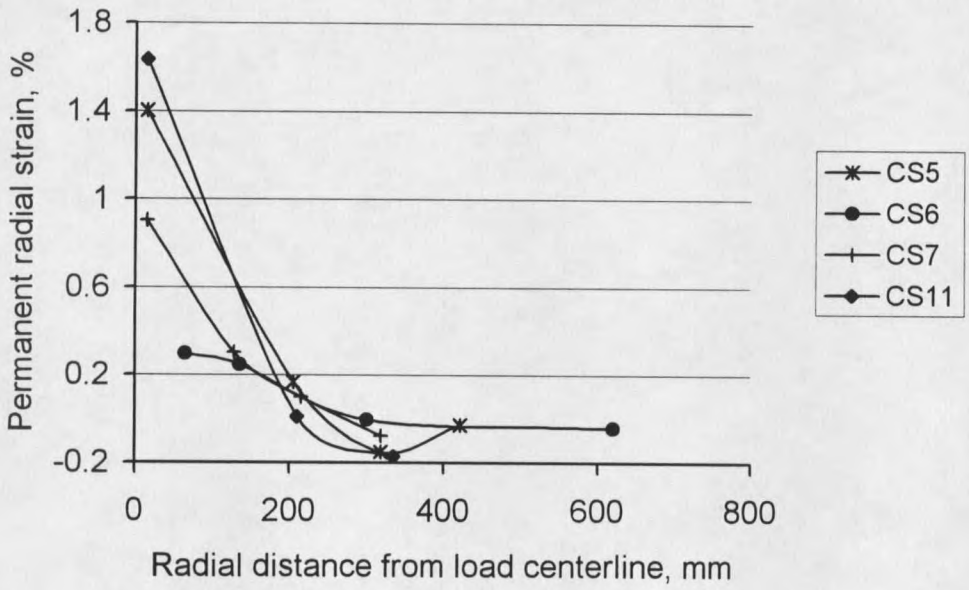


Figure 4.24 Permanent radial strain in the geosynthetic (M) versus radial distance of sections CS5-CS11 at cycle 7500.

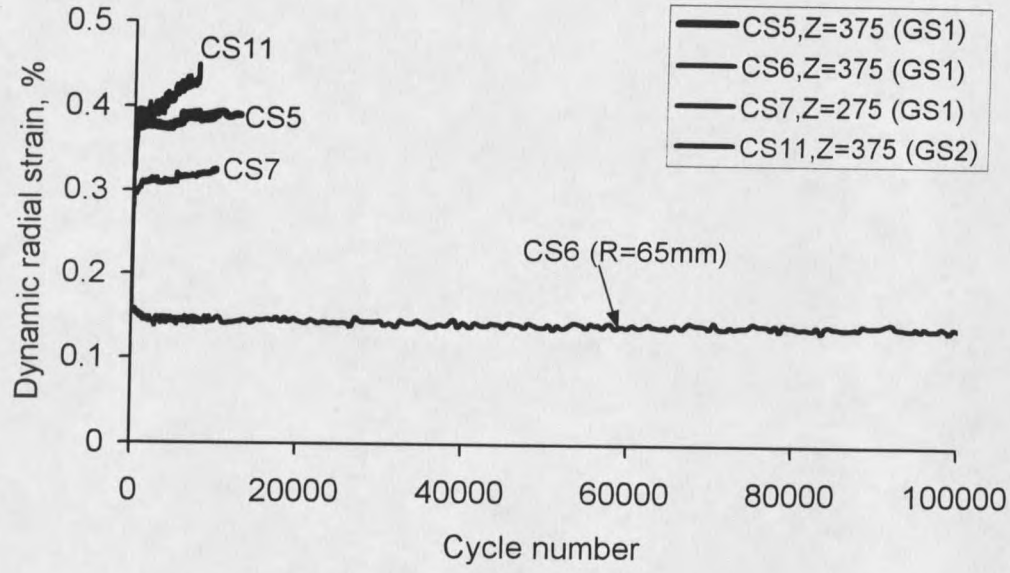


Figure 4.25 Dynamic radial strain (M) in the geosynthetics of sections CS5-CS11 (R=15 mm).

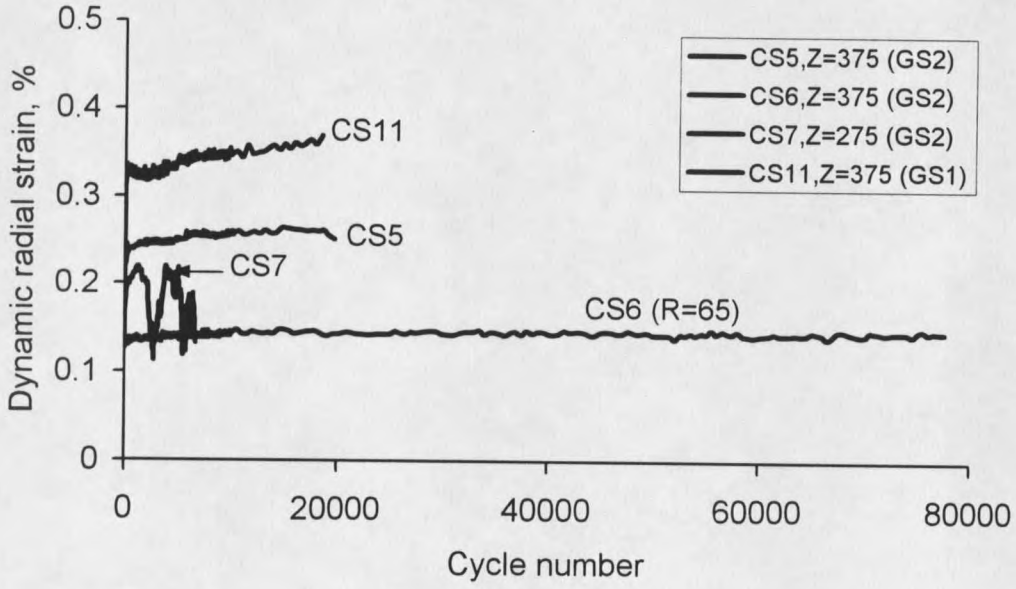


Figure 4.26 Dynamic radial strain (XM) in the geosynthetics of sections CS5-CS11 (R=20 mm).

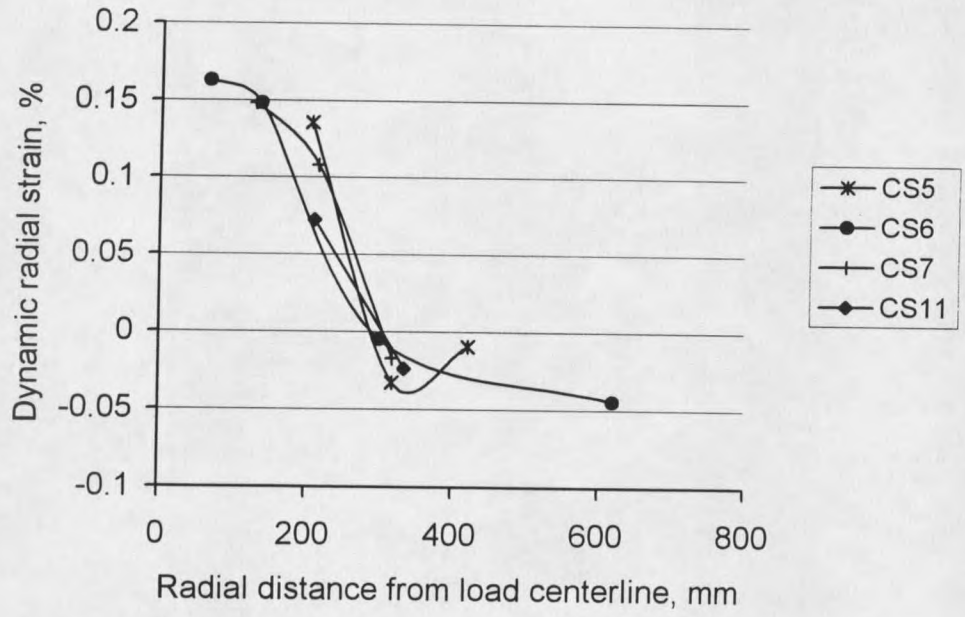


Figure 4.27 Dynamic radial strain in the geosynthetic (M) versus radial distance of sections CS5-CS11 at cycle 1.

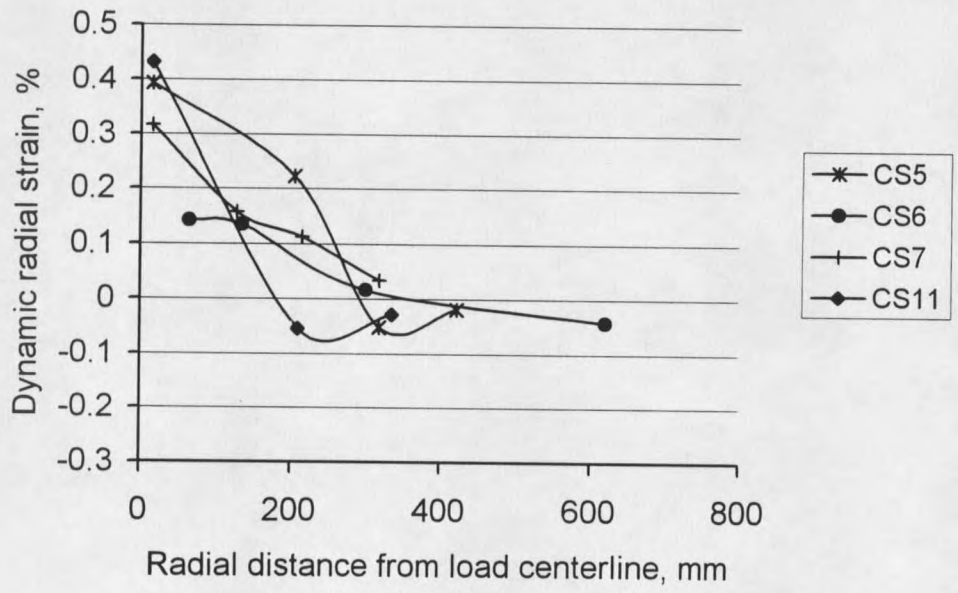


Figure 4.28 Dynamic radial strain in the geosynthetic (M) versus radial distance of sections CS5-CS11 at cycle 7500.

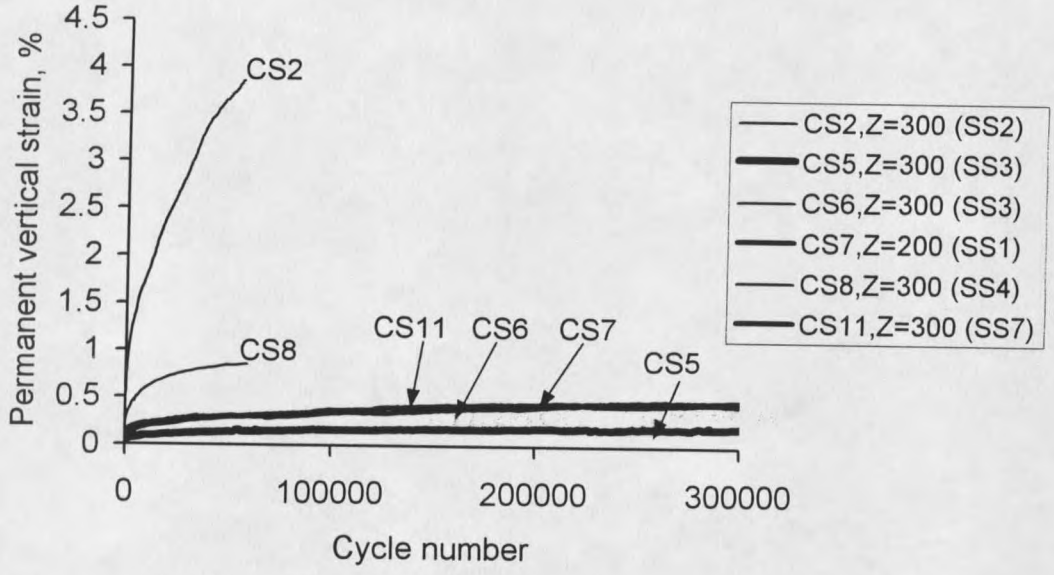


Figure 4.29 Permanent vertical strain versus cycle number in the base beneath the load centerline (R=65mm) (CS2-CS11).

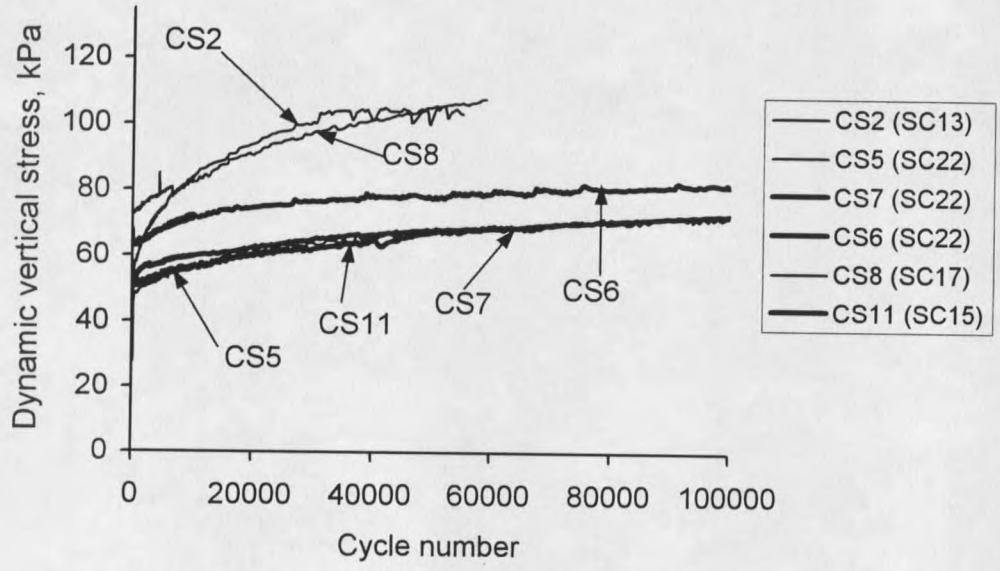


Figure 4.30 Dynamic vertical stress versus cycle number in the subgrade of sections CS2-CS11 (R=0, Z=450 mm).

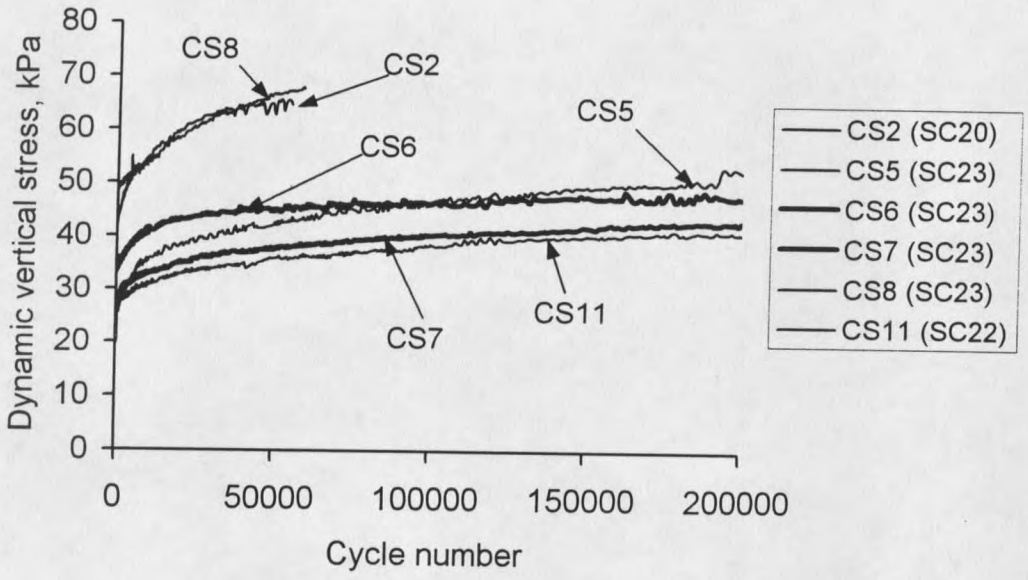


Figure 4.31 Dynamic vertical stress versus cycle number in the subgrade of sections CS2-CS11 (R=0, Z=625 mm).

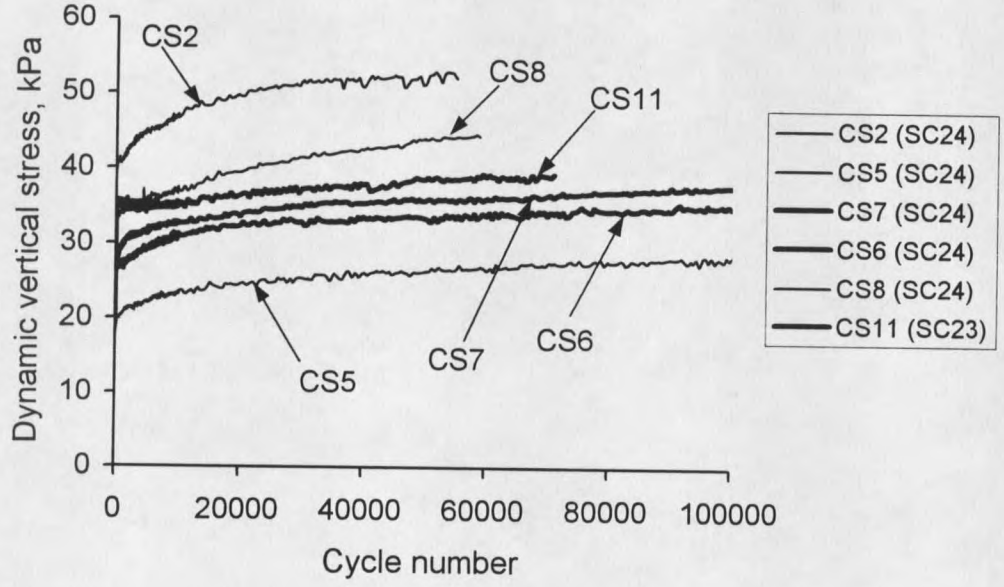


Figure 4.32 Dynamic vertical stress versus cycle number in the subgrade of sections CS2-CS11 (R=0, Z=775 mm).

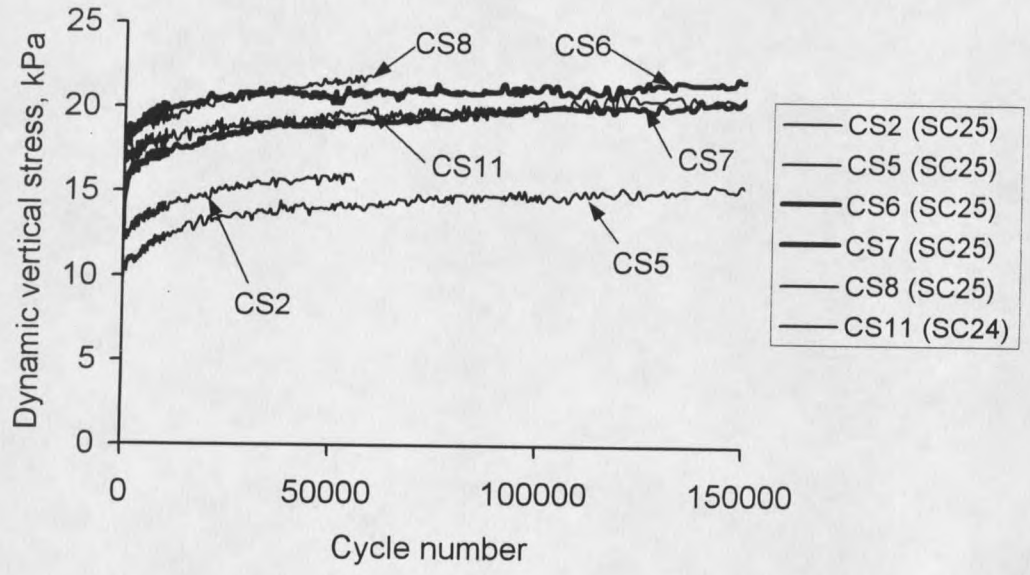


Figure 4.33 Dynamic vertical stress versus cycle number in the subgrade of sections CS2-CS11 (R=0, Z=1075 mm).

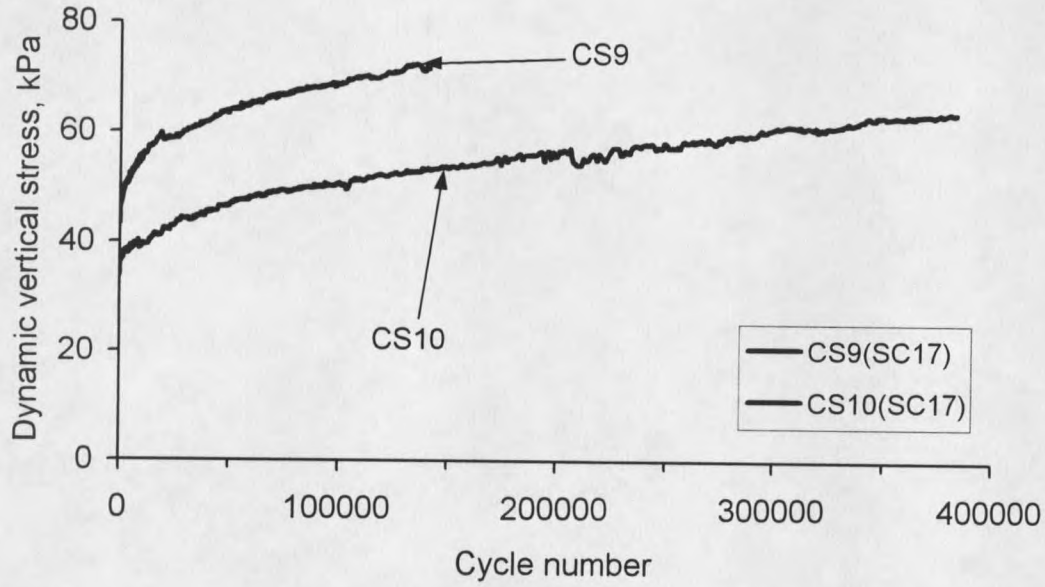


Figure 4.34 Dynamic vertical stress versus cycle number in the subgrade of sections CS9-CS10 (R=200, Z=525mm).

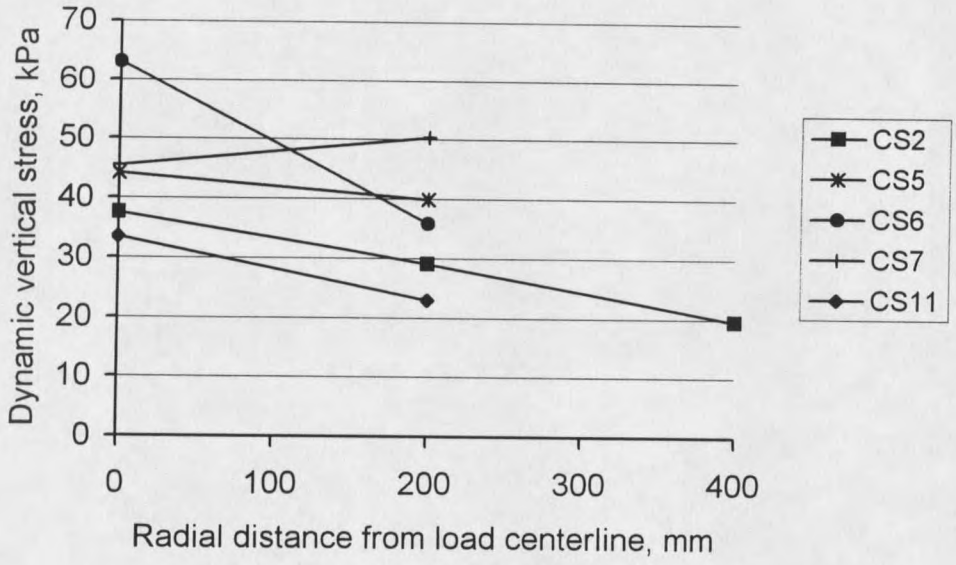


Figure 4.35 Dynamic vertical stress in the subgrade versus radial distance of sections CS2-CS11 at cycle 1.

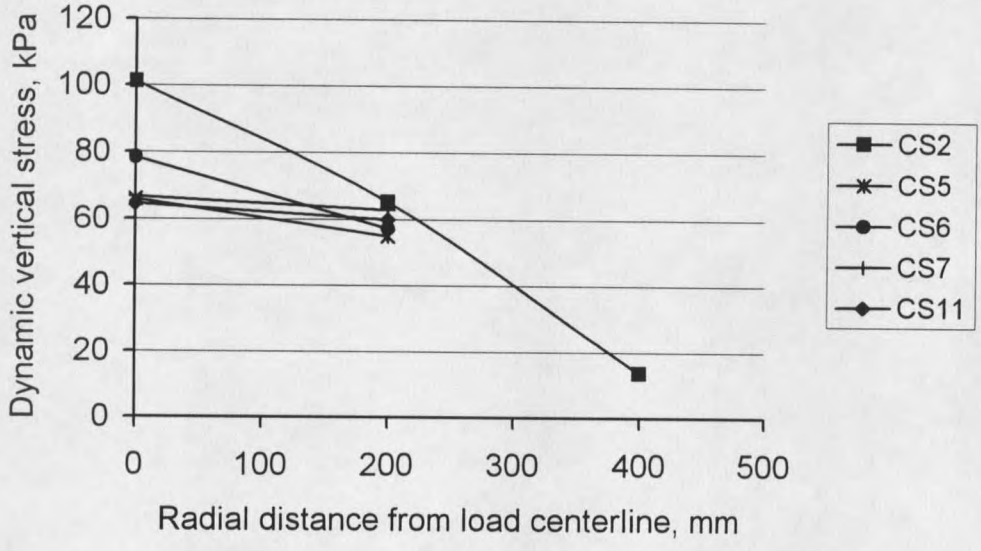


Figure 4.36 Dynamic vertical stress in the subgrade versus radial distance of sections CS2-CS11 at cycle 40000.

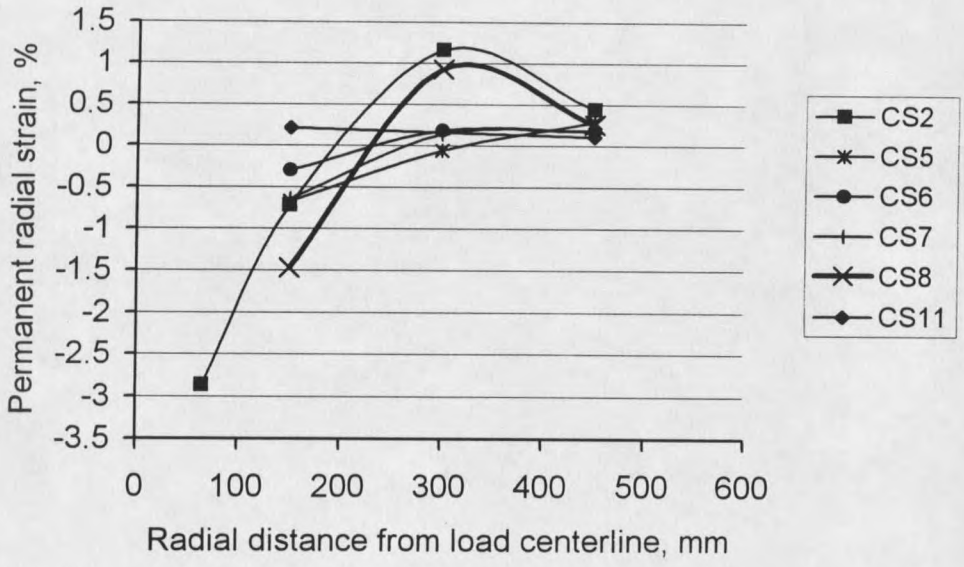


Figure 4.37 Permanent radial strain in the subgrade versus radial distance of sections CS2-CS11 at cycle 40000.

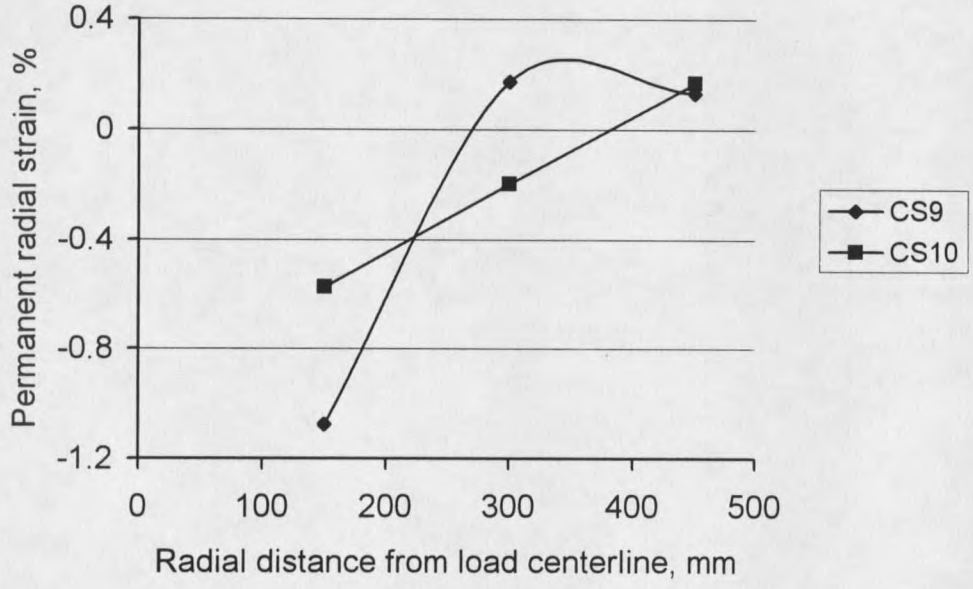


Figure 4.38 Permanent radial strain versus radial distance in the subgrade of sections CS9-CS10 at cycle 125000 (Z=490 mm).

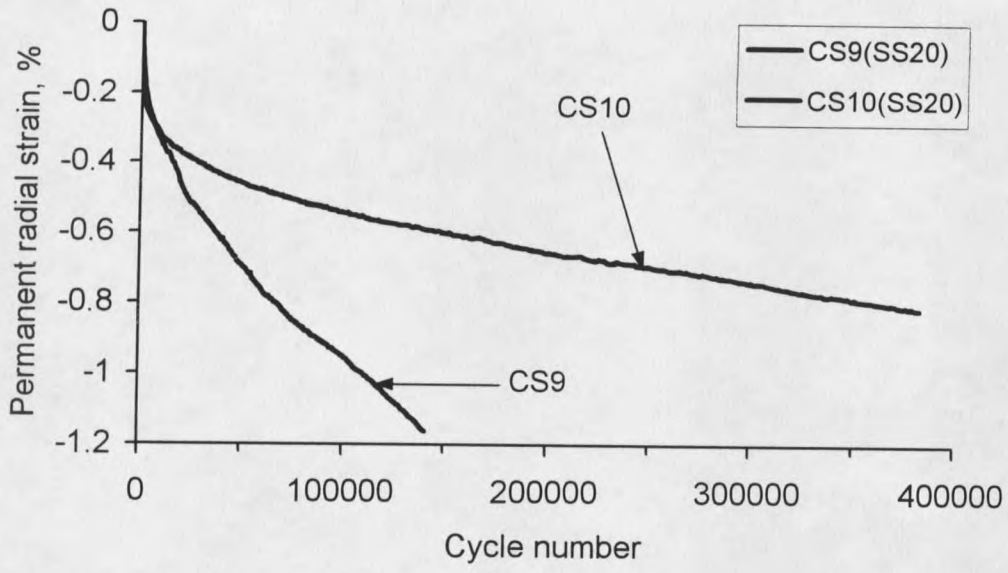


Figure 4.39 Permanent radial strain versus cycle number in the subgrade of sections CS9-CS10 (R=150mm, Z=490mm).

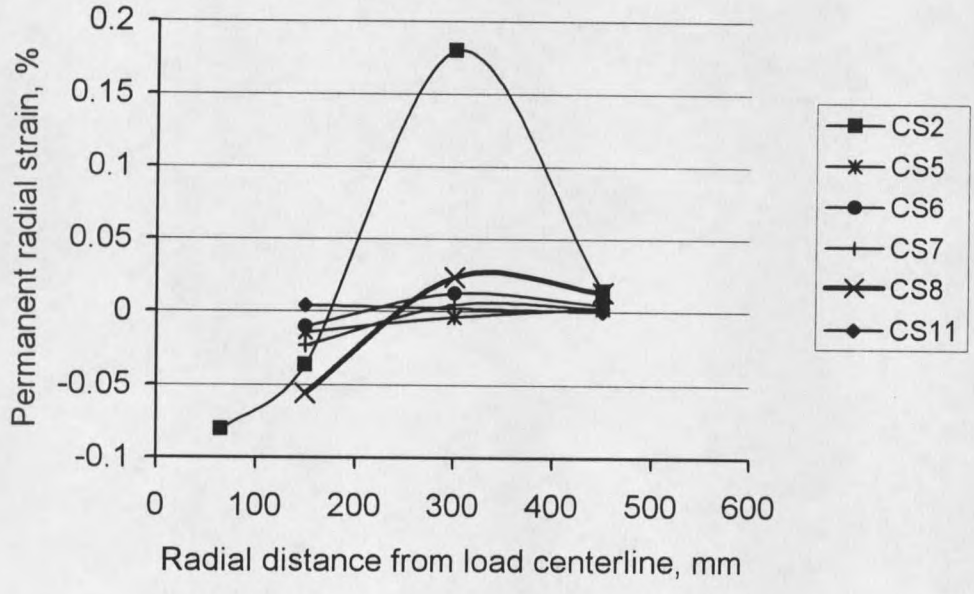


Figure 4.40 Permanent radial strain in the subgrade versus radial distance of sections CS2-CS11 at cycle 1.

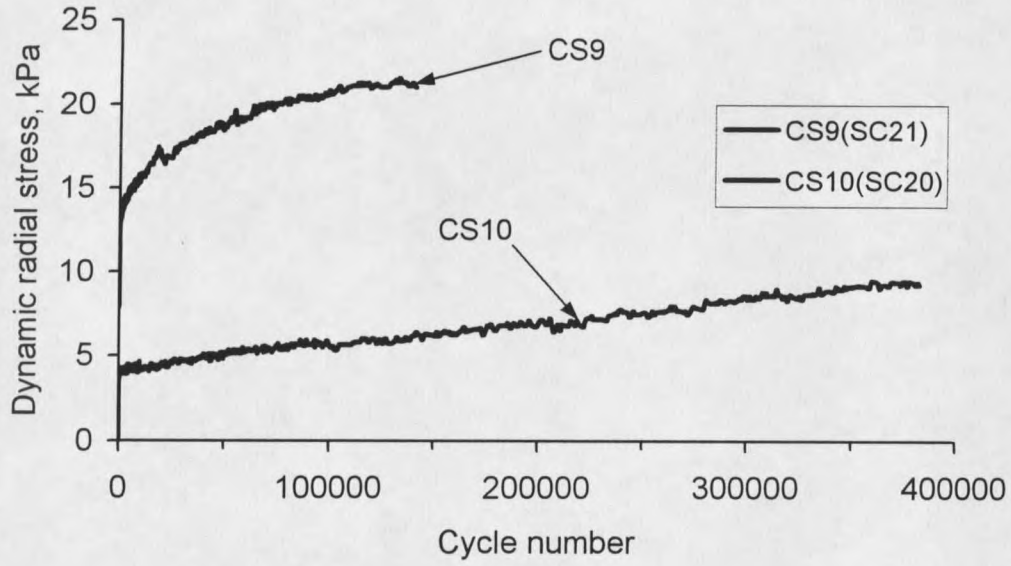


Figure 4.41 Dynamic radial stress versus cycle number in the subgrade of sections CS9-CS10 (R=250, Z=525mm).

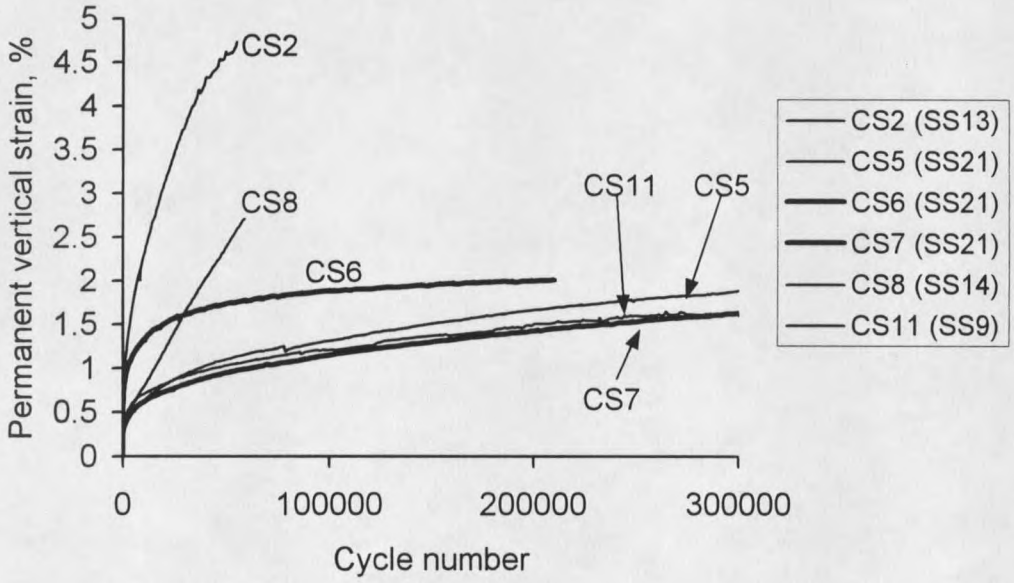


Figure 4.42 Permanent vertical strain versus cycle number in the subgrade of sections CS2-CS11 (R=65, Z=450 mm).

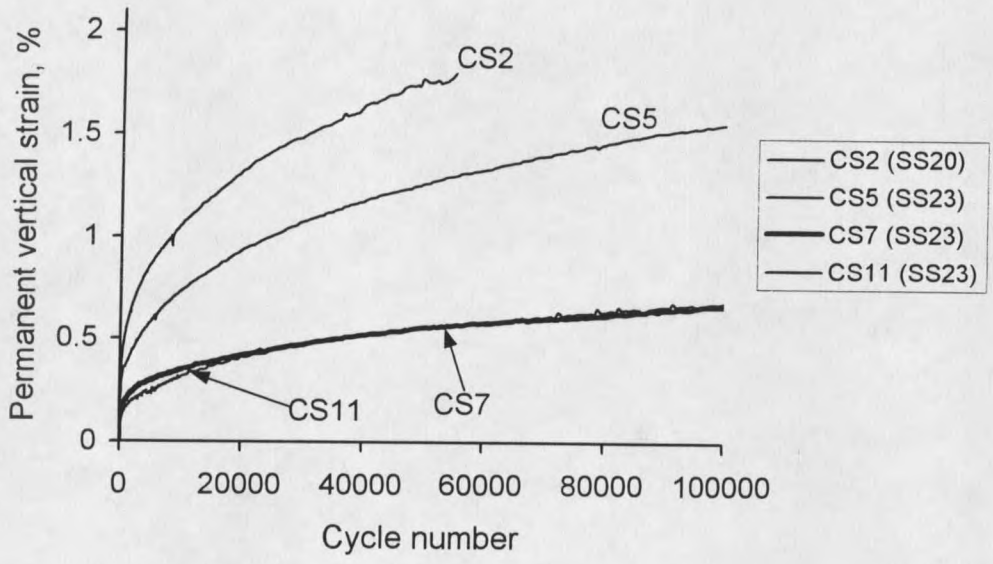


Figure 4.43 Permanent vertical strain versus cycle number in the subgrade of sections CS2-CS11 (R=65, Z=625 mm).

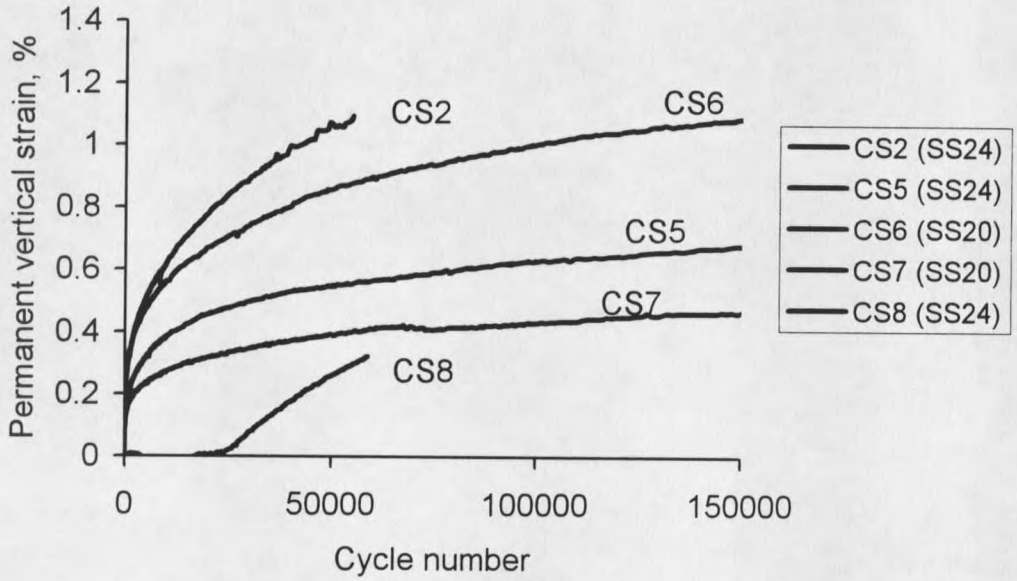


Figure 4.44 Permanent vertical strain versus cycle number in the subgrade of sections CS2-CS11 (R=65, Z=775 mm).

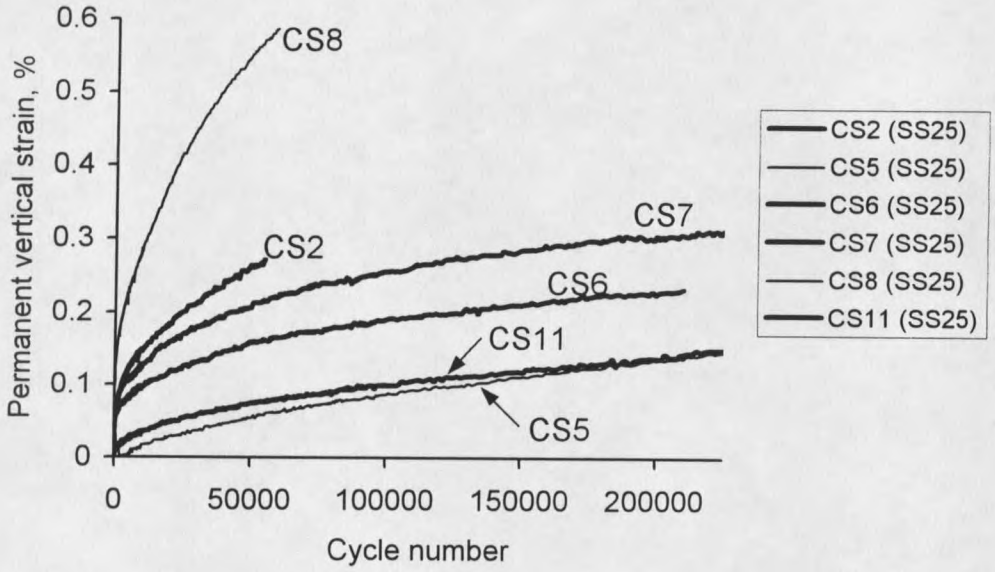


Figure 4.45 Permanent vertical strain versus cycle number in the subgrade of sections CS2-CS11 (R=65, Z=1075 mm).

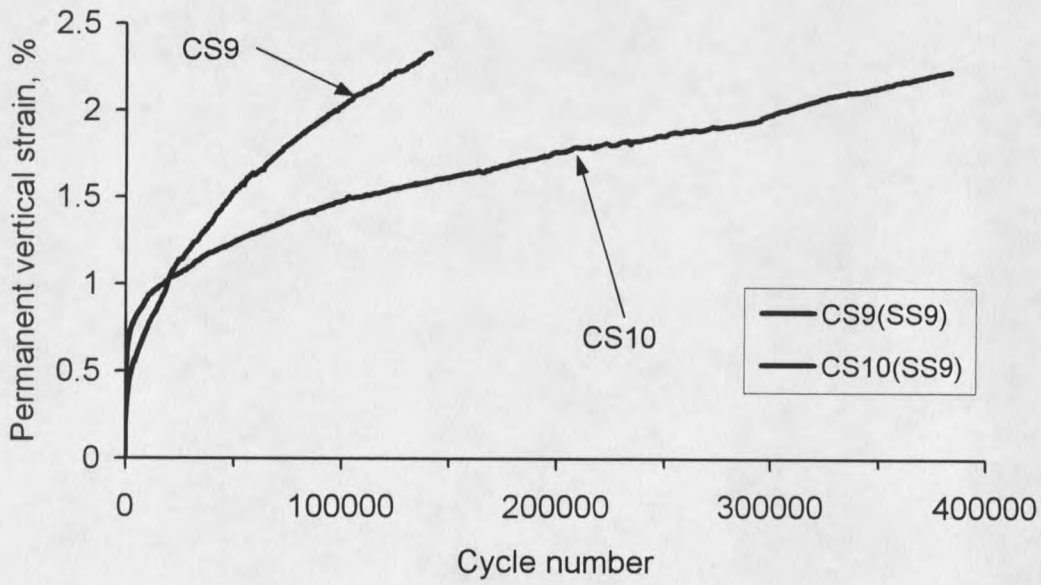


Figure 4.46 Permanent vertical strain versus cycle number in the subgrade of sections CS9-CS10 (R=65mm, Z=525mm).

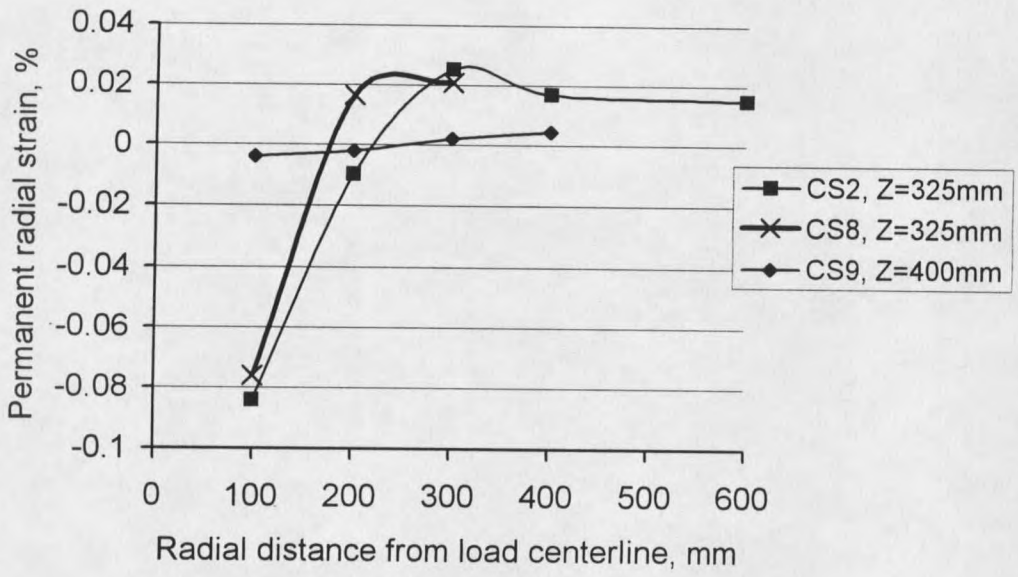


Figure 4.47 Permanent radial strain in the base versus radial distance of sections CS2, CS8, and CS9 at cycle 1.

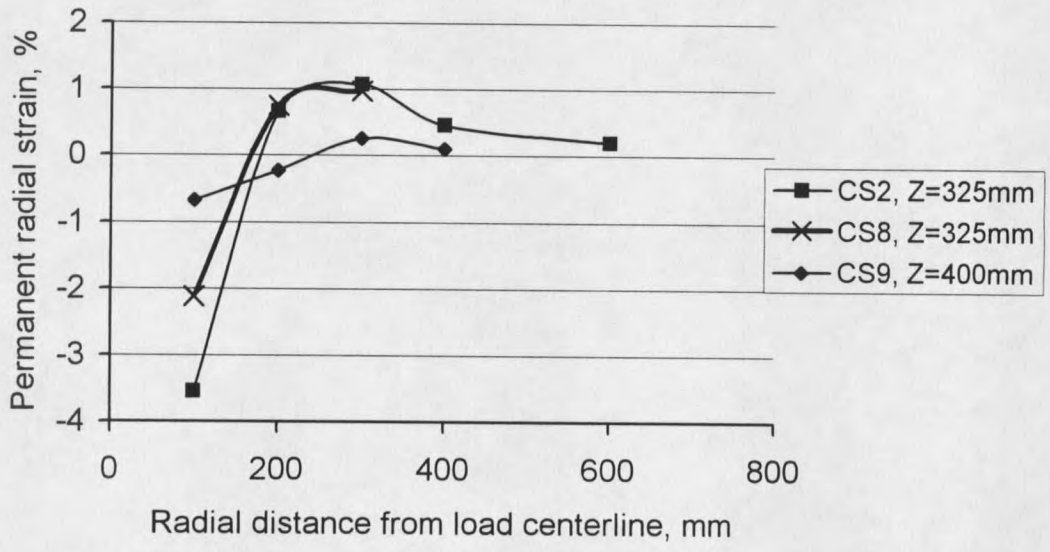


Figure 4.48 Permanent radial strain in the base versus radial distance of sections CS2, CS8, and CS9 at cycle 40000.

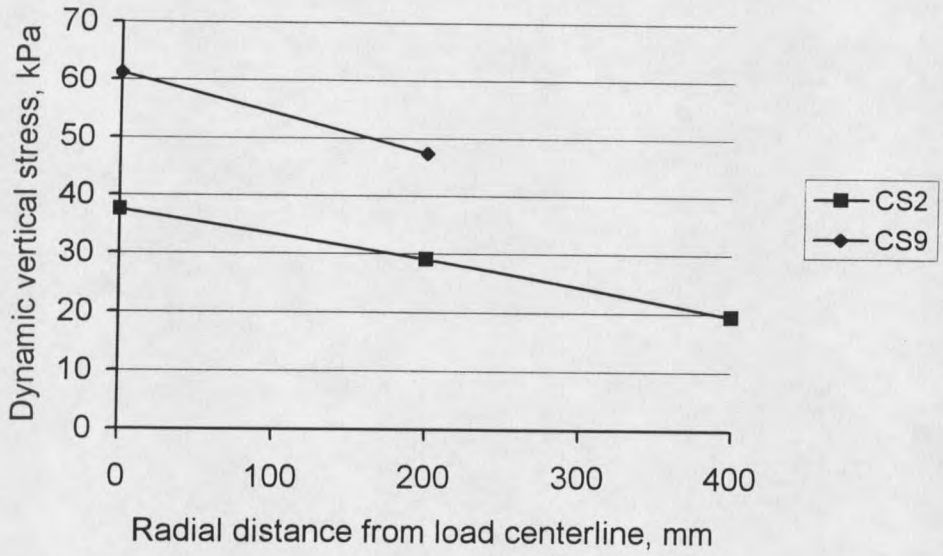


Figure 4.49 Dynamic vertical stress in the subgrade versus radial distance of sections CS2 and CS9 at cycle 1.

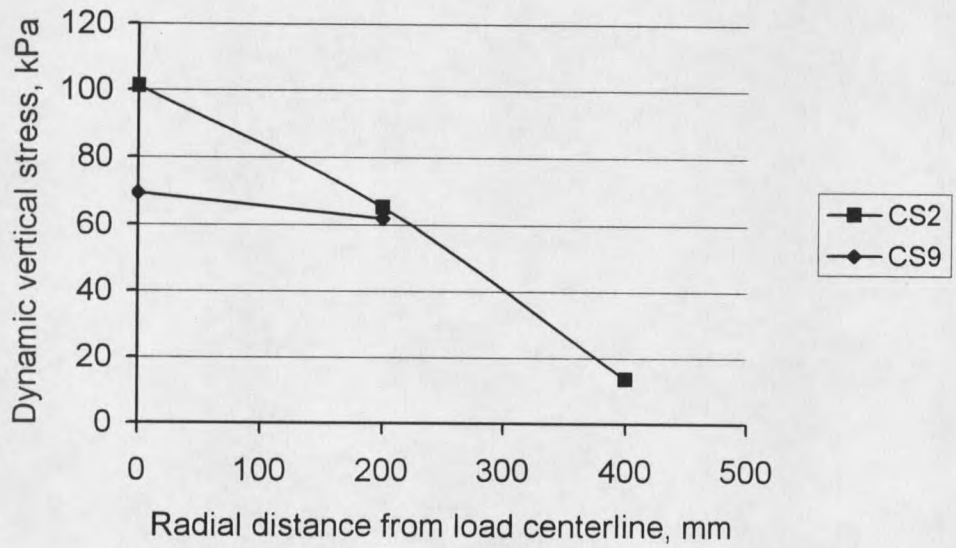


Figure 4.50 Dynamic vertical stress in the subgrade versus radial distance of sections CS2 and CS9 at cycle 40000.

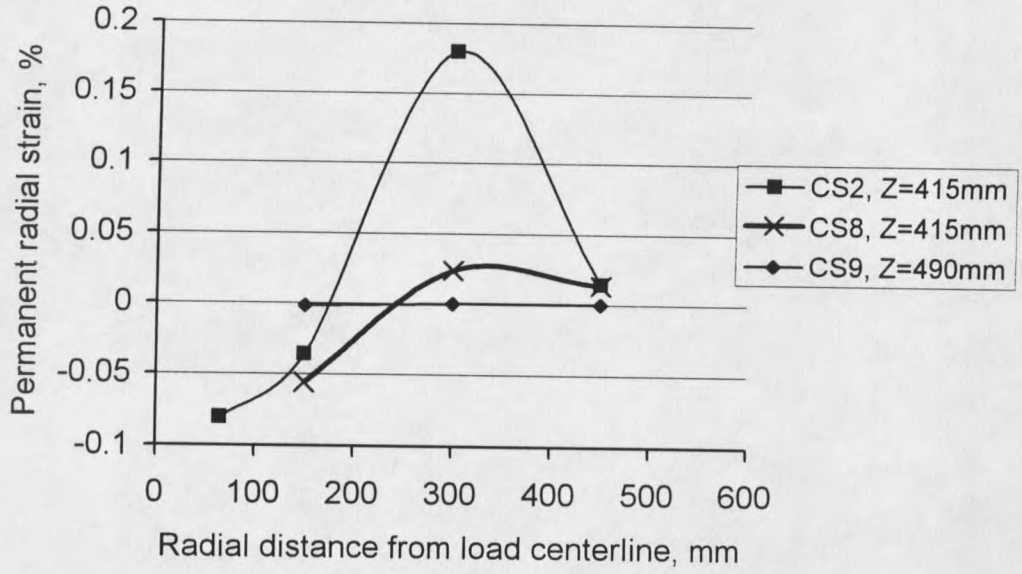


Figure 4.51 Permanent radial strain in the subgrade versus radial distance of sections CS2, CS8, and CS9 at cycle 1.

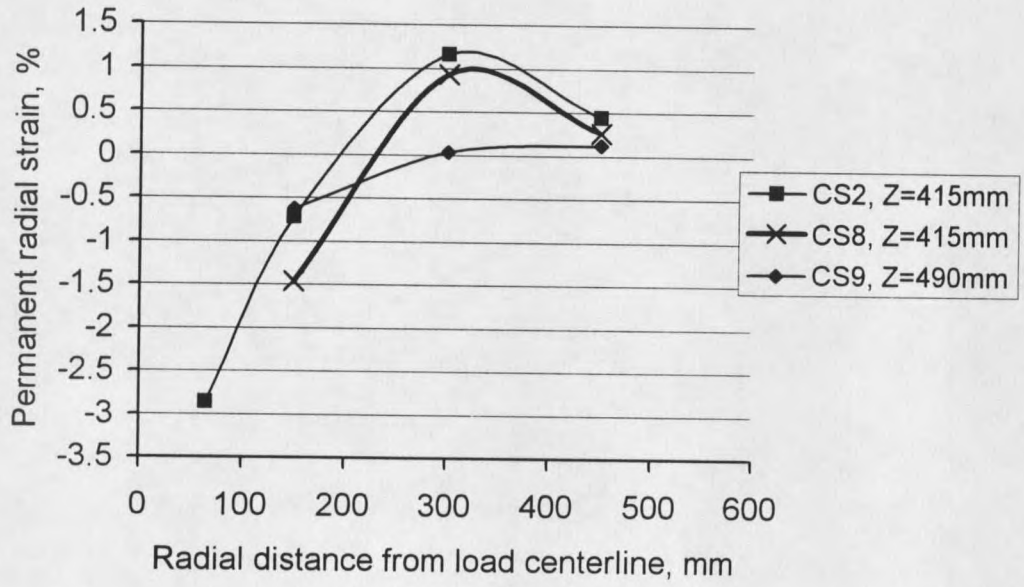


Figure 4.52 Permanent radial strain in the subgrade versus radial distance of sections CS2, CS8, and CS9 at cycle 40000.

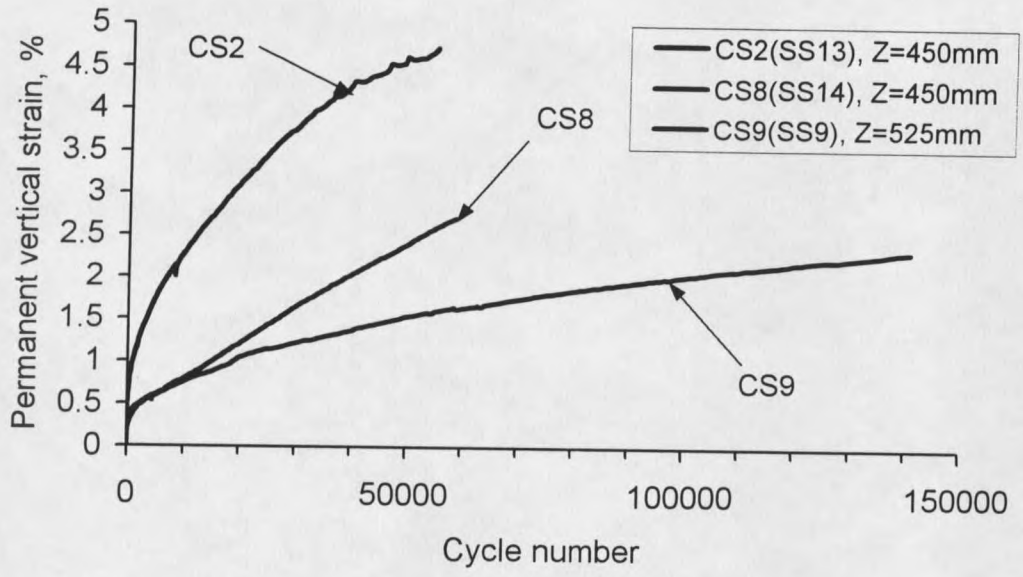


Figure 4.53 Permanent vertical strain versus cycle number in the subgrade of sections CS2, CS8, and CS9 (R=65mm).

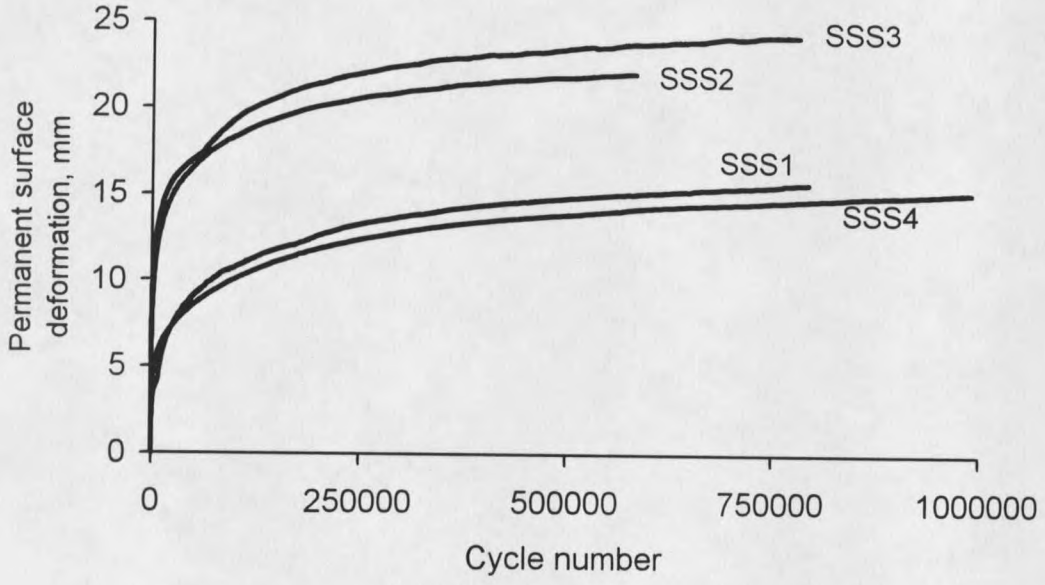


Figure 4.54 Permanent surface deformation versus cycle number for sections SSS1-4.

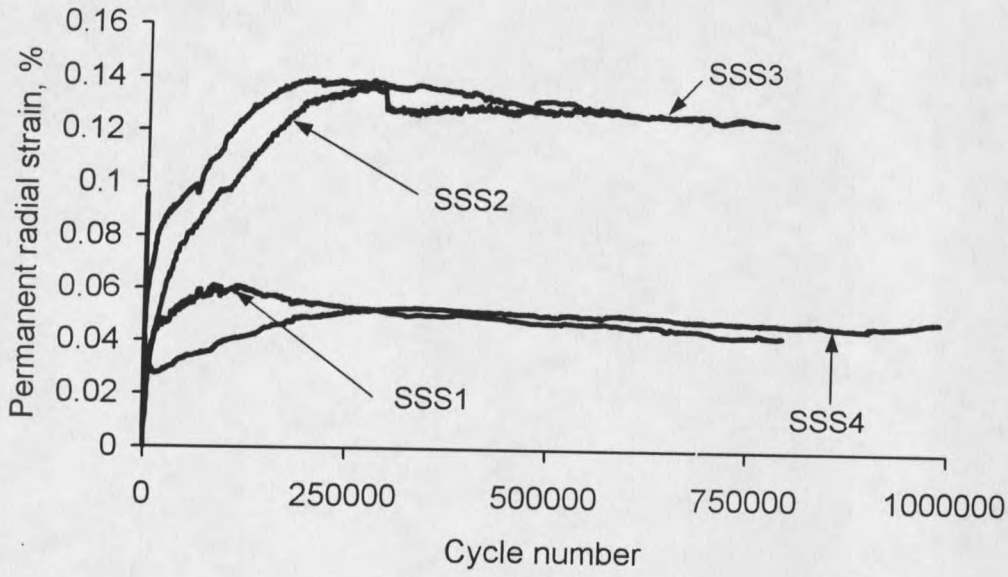


Figure 4.55 Permanent radial strain vs. cycle in the bottom of asphalt layer at R=0 (SSS1-4).

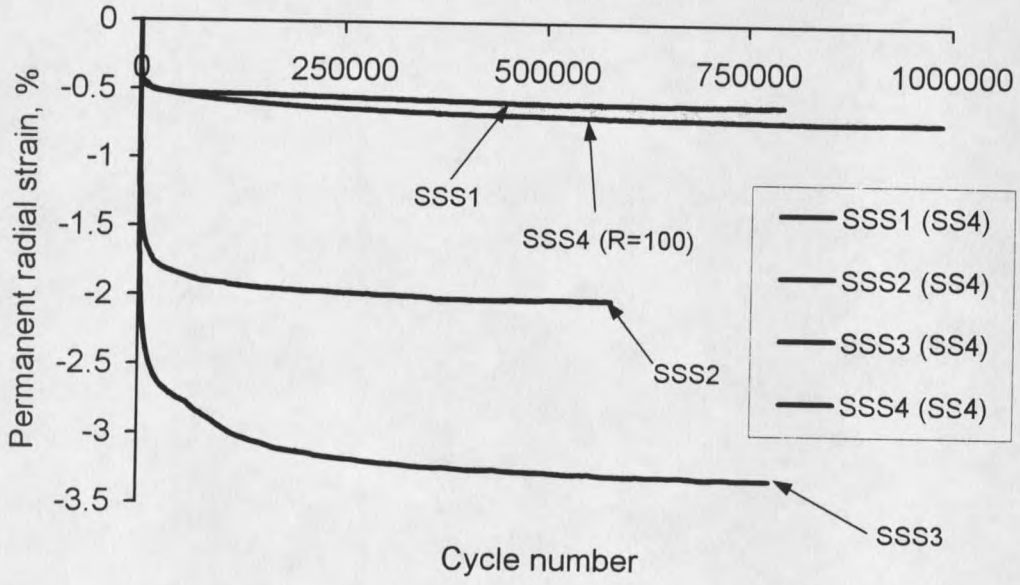


Figure 4.56 Permanent radial strain in the base (R=150mm, Z=215mm) (SSS1-4).

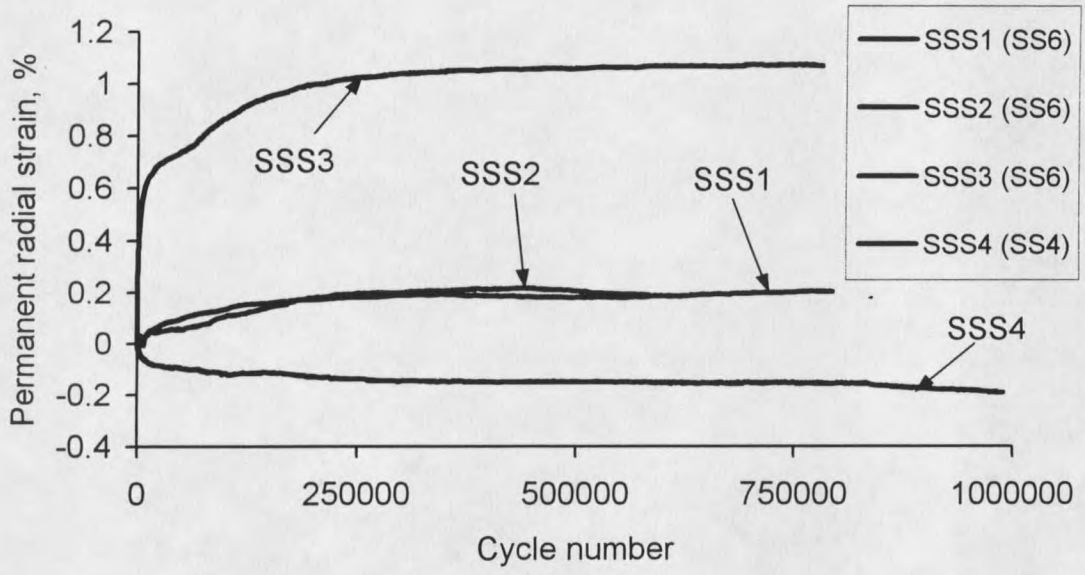


Figure 4.57 Permanent radial strain in the base (R=300mm, Z=215mm) (SSS1-4).

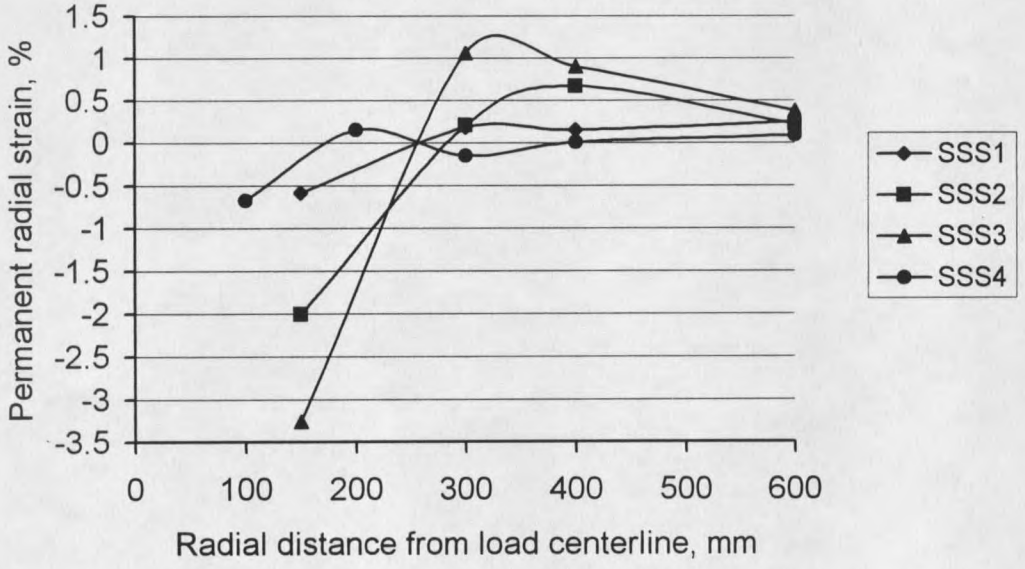


Figure 4.58 Permanent radial strain in the base versus radial distance at cycle 500000 (Z=160 mm) (SSS1-4).

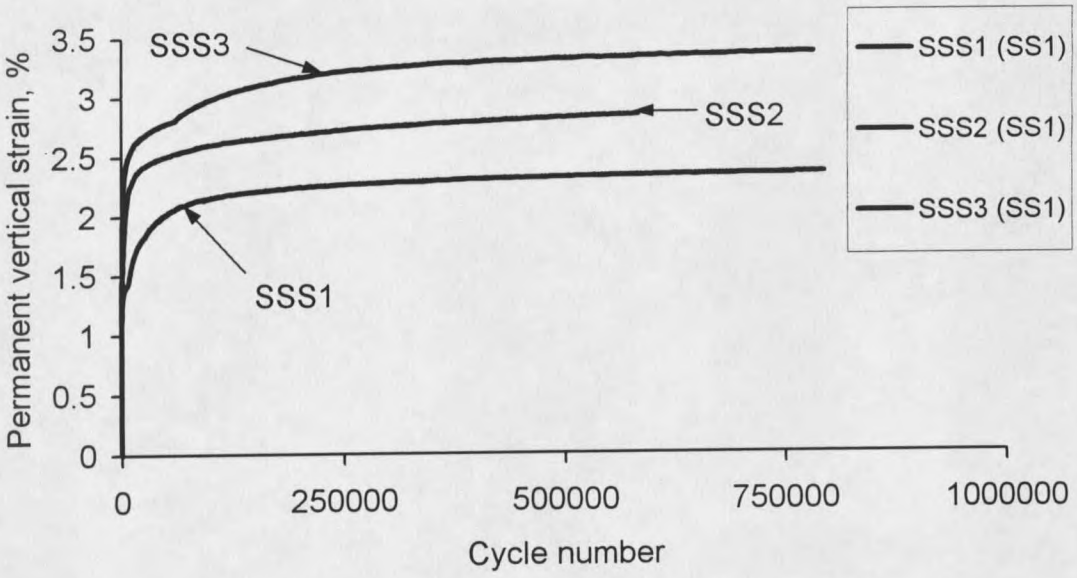


Figure 4.59 Permanent vertical strain versus cycle number in the base beneath the load centerline (R=60 mm) (Z= 160 mm) (SSS1-4).

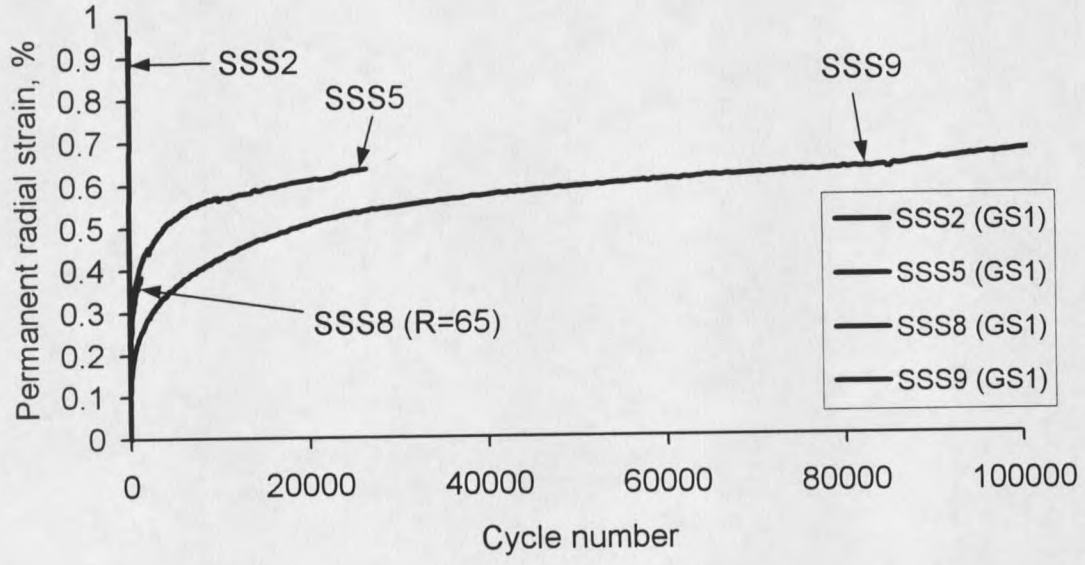


Figure 4.60 Permanent radial strain (M) in the geosynthetics (R=15 mm).

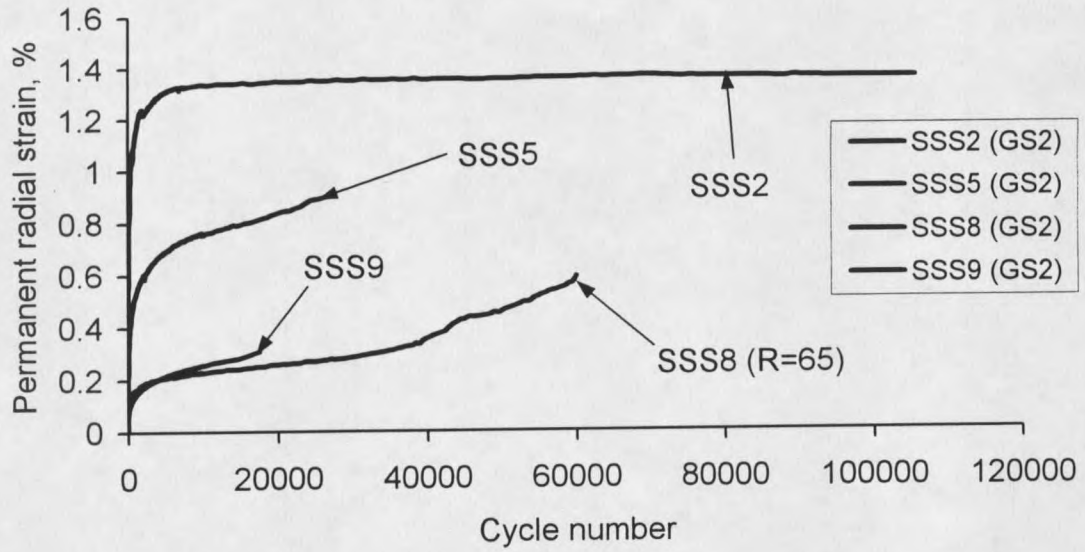


Figure 4.61 Permanent radial strain (XM) in the geosynthetics (R=23 mm).

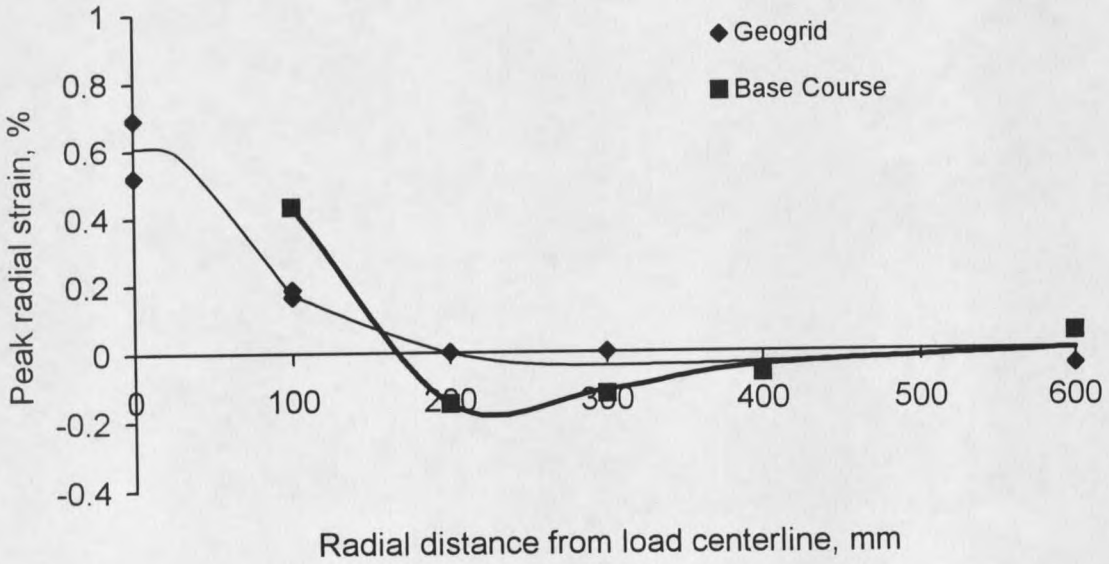


Figure 4.62 Distribution of peak radial strain in the geogrid and base course aggregate in section SSS5 at 5000 load cycles.

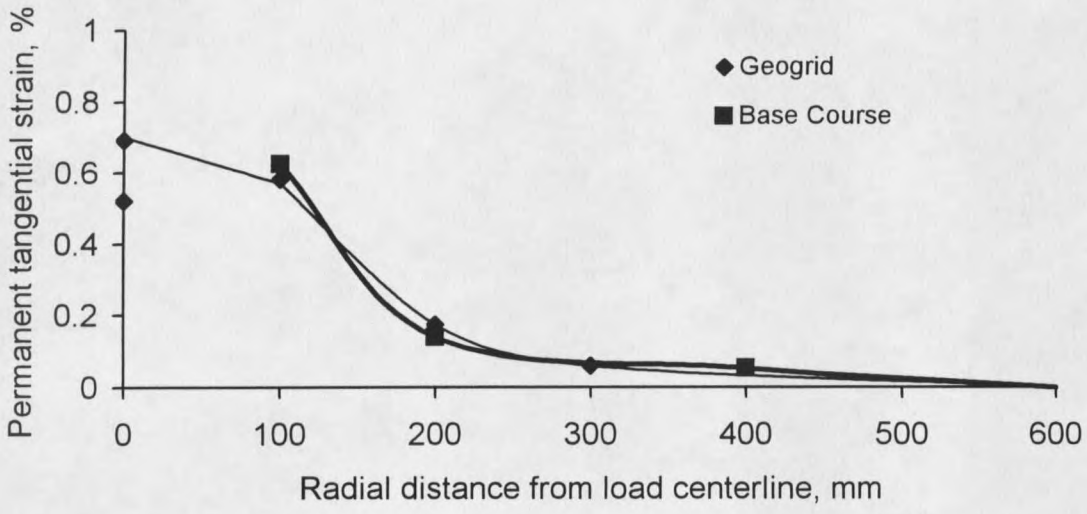


Figure 4.63 Distribution of permanent tangential strain in the geogrid and base course aggregate in section SSS5 at 5000 load cycles.

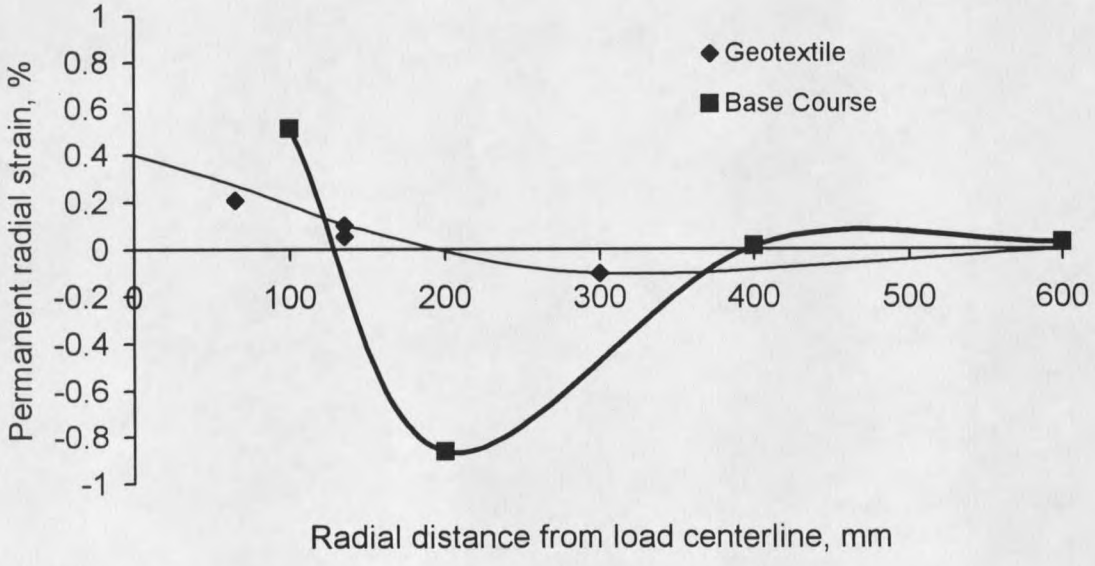


Figure 4.64 Distribution of permanent radial strain in the geotextile and base course aggregate in section SSS8 at 5000 load cycles.

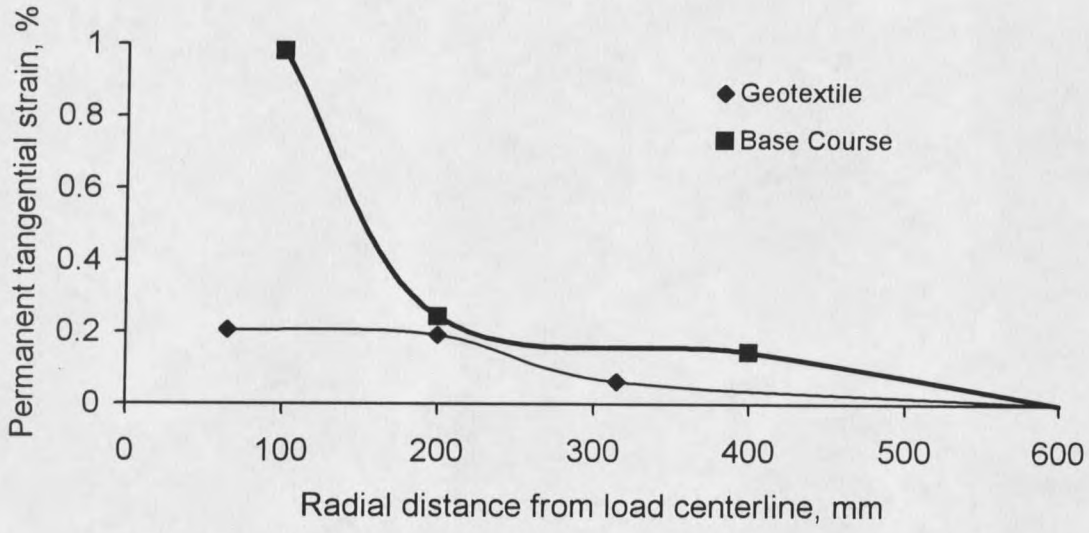


Figure 4.65 Distribution of permanent tangential strain in the geotextile and base course aggregate in section SSS8 at 5000 load cycles.

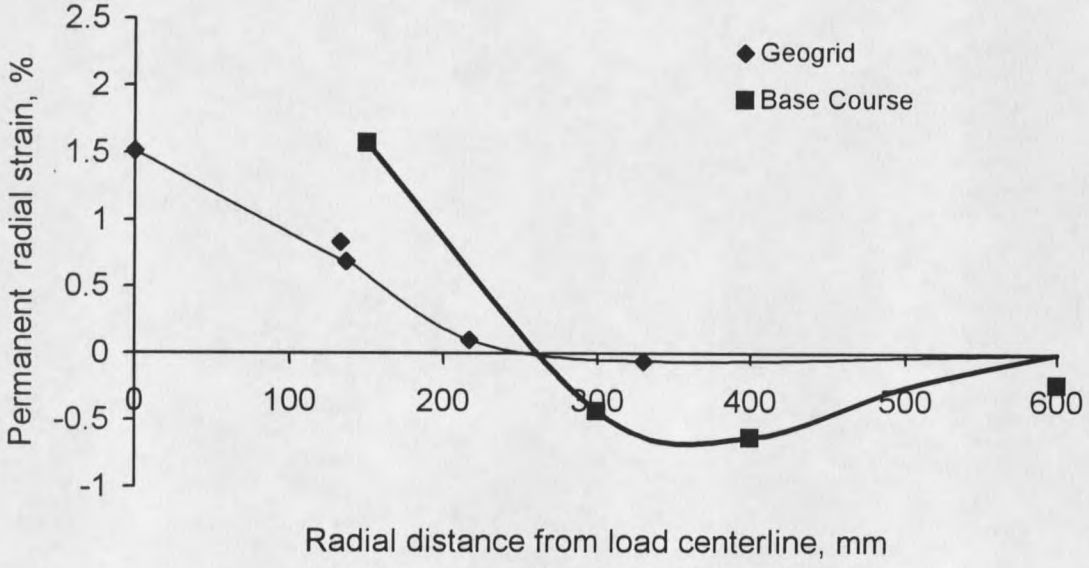


Figure 4.66 Distribution of peak radial strain in the geogrid and base course aggregate in section SSS2 at 5000 load cycles.

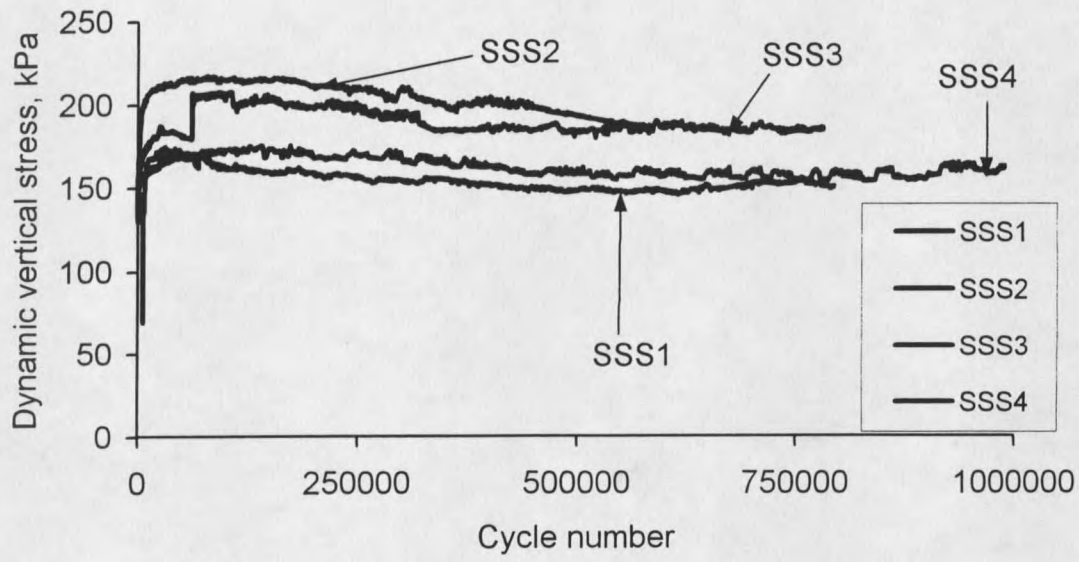


Figure 4.67 Dynamic vertical stress versus cycle number in the subgrade (R=0, Z= 350mm) (SSS1-4).

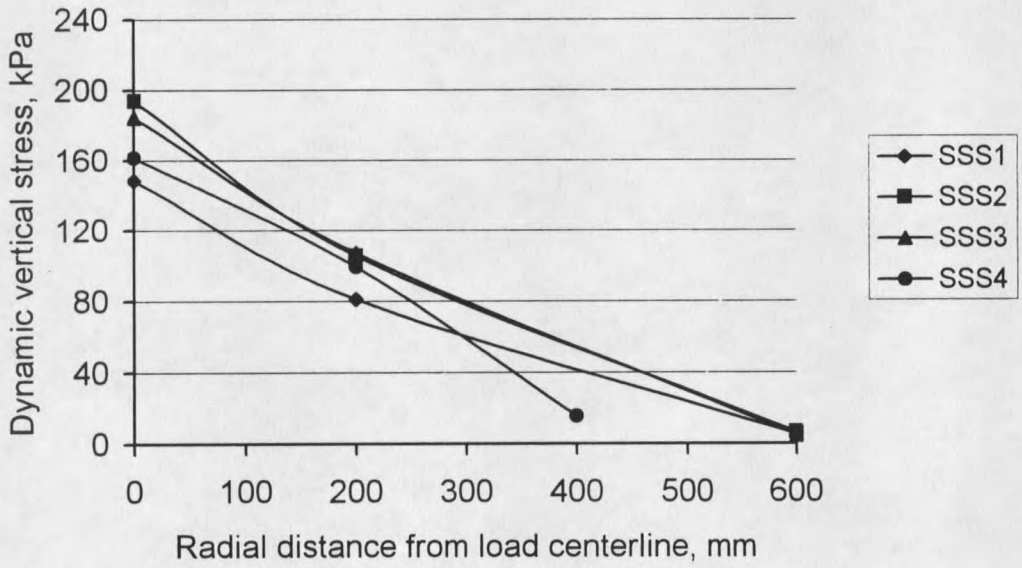


Figure 4.68 Dynamic vertical stress versus radial distance in the subgrade at cycle 500000 (Z=350 mm) (SSS1-4).

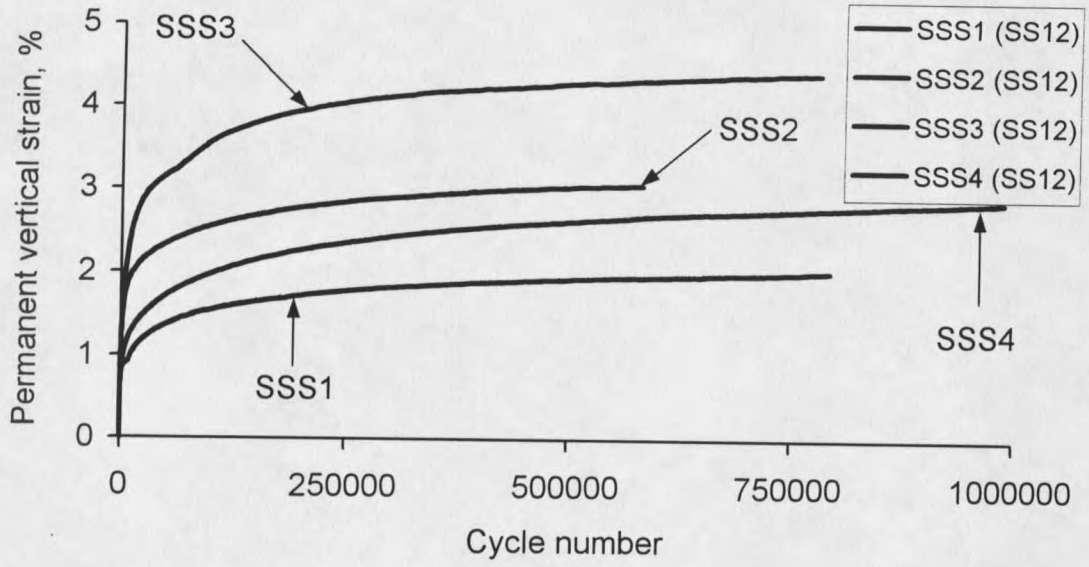


Figure 4.69 Permanent vertical strain versus cycle number in the subgrade (R=60 mm) (Z=350 mm) (SSS1-4).

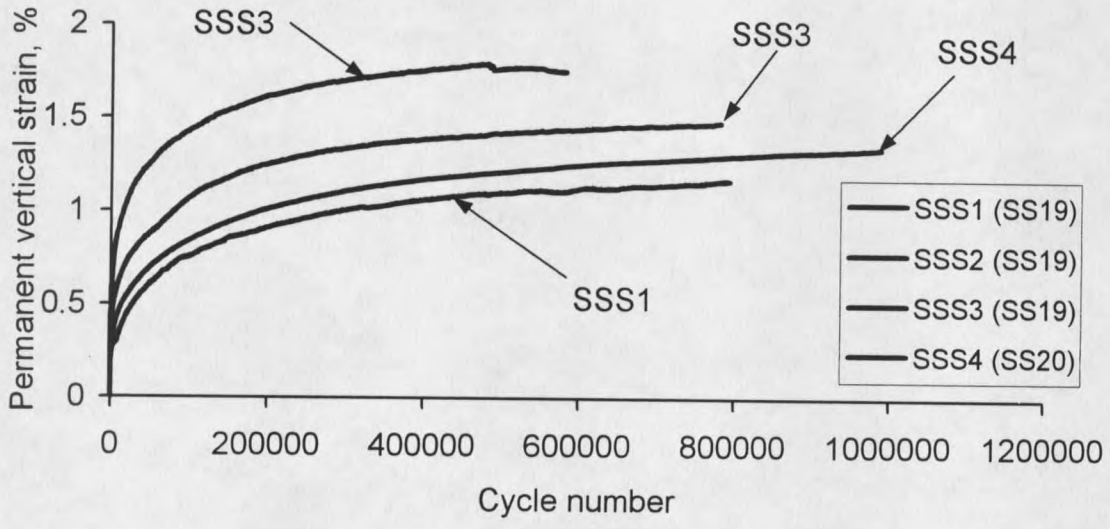


Figure 4.70 Permanent vertical strain versus cycle number in the subgrade (R=60 mm) (Z=575 mm) (SSS1-4).

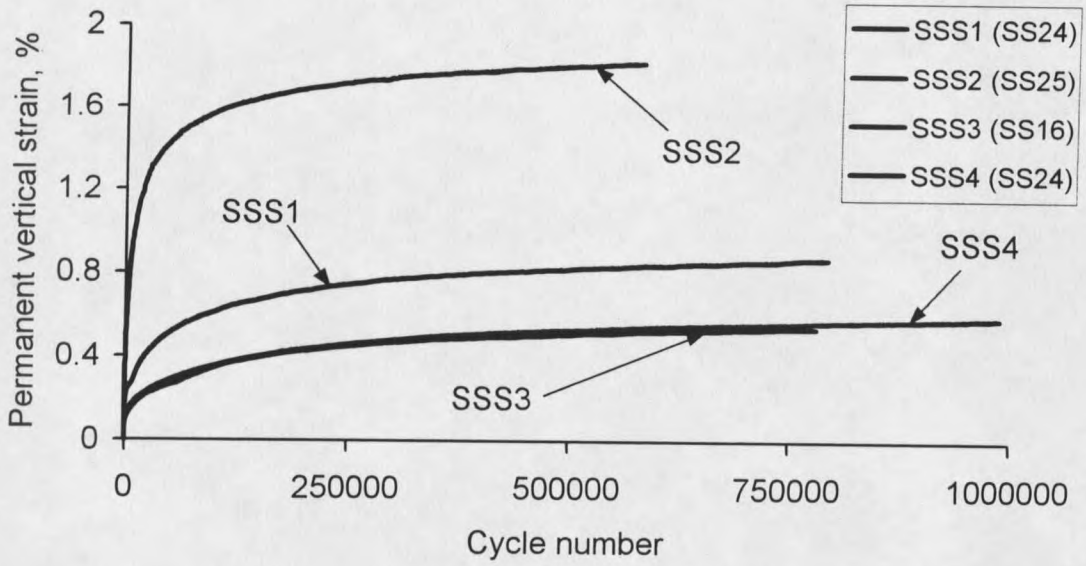


Figure 4.71 Permanent vertical strain versus cycle number in the subgrade (R=60 mm) (Z=825 mm) (SSS1-4).

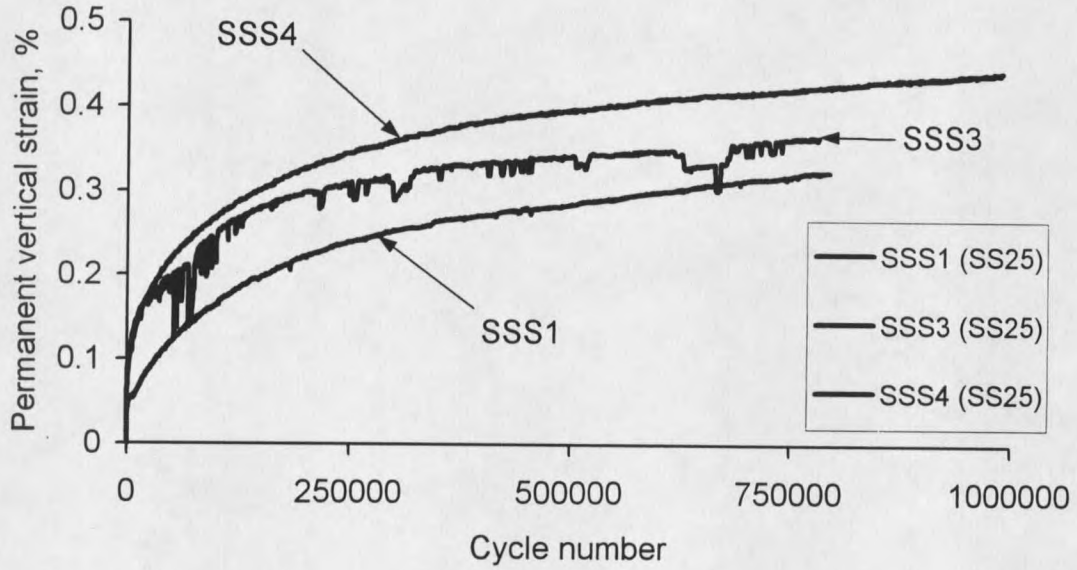


Figure 4.72 Permanent vertical strain versus cycle number in the subgrade (R=60 mm) (Z=1075 mm) (SSS1-4).

CHAPTER FIVE

COMPARISON OF SINGLE-PULSE TEST RESULTS TO LINEAR ELASTIC THEORY

Introduction

This chapter provides comparisons between the Preliminary Clay Subgrade (PCS1) test results and linear elastic theory, using the computer program KENLAYER. These comparisons have significance related to the mechanistic-empirical approach to design. A mechanistic-empirical design approach for pavements involves the combination of stress/strain analysis with empirical rut depth predictions or failure criteria. It is noted that this chapter does not provide any evaluation of reinforcement through modeling.

Additionally, several empirical models defining subgrade failure by rutting are used in conjunction with Sections CS2 and CS8 (unreinforced control sections), to predict the number of cycles to a prescribed failure condition. This section will explain how well empirical failure criteria predict failure for these unreinforced test sections.

Third, an empirical model is used to predict vertical plastic strain accumulation in the subgrade and is contrasted to actual vertical strain development in the test section CS2. Back-calculated model parameters from this research are compared to those found in the literature. Finally, comments are made to determine the adequacy of stress, strain,

and rut predictions for unreinforced experimental test sections using a mechanistic-empirical design approach.

KENLAYER Computer Program

The backbone of the model is a solution for an elastic multi-layer system under a uniformly loaded circular area. This loading condition was chosen as it is similar to the loading found in all experimental test sections, in which loading was provided through a 305 mm diameter plate as discussed in Chapter 3. The model can provide results for up to 19 different layers and for 10 different radial coordinates. Model outputs include vertical displacements, radial displacements, vertical stress, radial stress, vertical strain, radial strain, and shear strain. Assumptions of the model, as it was used in this research, include: linear elastic material behavior, a constant elastic modulus, and pavement layers that are fully bonded. When layers are fully bonded, vertical stress, shear stress, vertical and radial displacements, are transmitted between layers without interruption from the interface. An additional assumption is that the layers are infinitely large in horizontal extent, as opposed to the finite 2m by 2m plan area of the experimental test box.

Model Geometry and Determination of Pavement Layer Elastic Moduli

Model geometry was chosen to match test section layer thicknesses. The test sections PCS1, CS2, and CS8 included three layers: the AC, the base course, and the

subgrade. The KENLAYER model incorporated four layers, which included an additional infinitely thick layer of concrete below the subgrade, to mimic the concrete present below the experimental test box. KENLAYER assumes that the last layer input into the model is infinite in thickness. Output from the model was calculated at depths where instrumentation was present. Model geometry is shown in Figure 5.1.

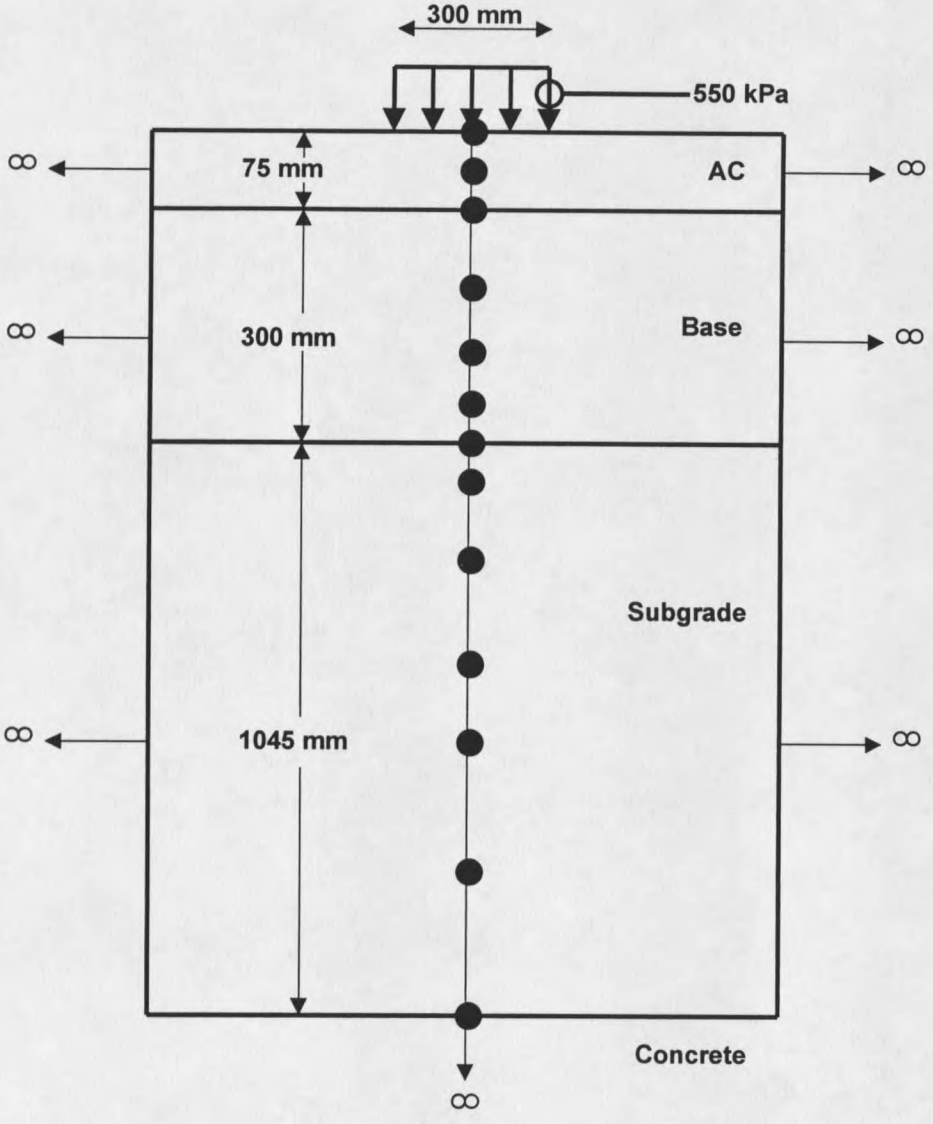


Figure 5.1. Model geometry illustrating response levels corresponding to instrument depths.

Loading was specified in KENLAYER as a 550 kPa pressure applied over a circular area. The radius of the circular area was specified as 150 mm.

Layer properties, which included elastic moduli and Poisson's ratio, were obtained in a manner designed to be similar to how a pavement engineer would obtain the aforementioned properties. Thus, elaborate material testing regimes were not implemented.

The elastic modulus for the AC layer was determined through the Shell nomographs (Huang, 1993) utilizing data from standard penetration tests (ASTM D-5) performed on the PG 58-28 asphalt binder. Tests yielded a penetration of 53 at 4° C, and 102 at 25° C. The calculated penetration index (PI) was 7.65 (Huang, 1993). Stiffness of the binder was estimated from Figure 7.20 (Huang, 1993) assuming asphalt cement percent by volume of 15.1% and percent aggregate by volume of 79.9%. An average bulk density of 22.8 kN/m^3 for the mix was used in determining asphalt cement and aggregate volume percentages. An average asphalt binder content of 6.5% by weight and an air voids content of 4.9% by volume was assumed in determining bulk density. Additionally, a specific gravity of the binder of 1.0 was assumed. A loading rate of 1 Hz was assumed, because this value matched the loading rate on the test sections. This approach is taking into account the viscoelastic properties of the AC by specifying an elastic modulus at a frequency of loading. Figure 7.20 (Huang, 1993) yielded an asphalt binder stiffness of 10^4 kPa. Knowing the mixture proportions, and the asphalt binder

stiffness, Figure 7.19 (Huang, 1993) yielded an asphalt concrete mix stiffness of 1.3 x 10^6 kPa (190,000 psi).

The base course modulus was estimated using the AASHTO Design of Pavement Structures (AASHTO, 1993) which referenced NCHRP 128 (NCHRP, 1972). This NCHRP report provides correlations between CBR and elastic modulus. Field CBR was estimated from experimental DCP results using the correlations provided by Mn Road (1993). These correlations yielded a field CBR of approximately 40%. A modulus of 117,300 kPa (17,000 psi) was then estimated from the "subbase" graph, found in both the NCHRP report and the AASHTO design guide. The gradation for the base course used in the experimental test section plotted between the "subbase" and "base" gradations for the AASHO Road tests, which were the basis of the NCHRP correlations. Furthermore, the AASHO "base" had a CBR greater than 75%, and the "subbase", a CBR less than 60%. Thus, it was decided that the experimental test section base course more closely resembled the "subbase" in the AASHO tests.

The subgrade elastic modulus was estimated through a common correlation between CBR and resilient modulus. Modulus was estimated as 1500 times the CBR in percent (Huang, 1993). Laboratory CBR tests discussed in Chapter 3 yielded a CBR of 1.5 %, corresponding to the in-situ water content of approximately 45% in the test sections. Thus, a resilient modulus of 15,500 kPa (2250 psi) was estimated. The calculated modulus was similar to a 16,600 kPa (2400 psi) modulus obtained from NCHRP 128 (1972) for soaked samples of similar clay samples.

A concrete modulus below the test section of 3.8 x 10^7 kPa (5.5 x 10^6 psi) was estimated from Table 18.2 in Mindess (1981).

Poisson ratios for the four layer materials were estimated from various sources. The AC, base course, and subgrade poisson ratios were obtained from Table 7.5.3 (Huang, 1993). The portland cement concrete ratio was obtained from Mindess, (1981). Table 5.1 gives a summary of the layer thickness, elastic moduli, and Poisson ratios used for modeling purposes.

Table 5.1. Summary of model input parameters.

Material	Elastic Modulus (kPa)	Poisson Ratio	Thickness (m)
AC	1.31 x 10^6	0.40	0.075
Base	1.17 x 10^5	0.35	0.300
Subgrade	1.52 x 10^4	0.45	1.045
Concrete	3.79 x 10^7	0.25	infinite

Comparison of Model Output to Section PCS1

As discussed in Chapter 3, responses of stress, strain, and surface deflection (rut), versus radial distance from the load were generated from the PCS1 test section. In this chapter, these plots are compared with those generated from the linear elastic program KENLAYER. All plots comparing linear elastic model results to test section results are included at the end of this chapter.

Data from PCS1 was formatted such that an instrument response was plotted versus radial distance from the load, as the load was placed at different locations across

the section. Load movement was discussed in detail in Chapter 3. For each instrument, a minimum of three data points was generated at each radial distance. Each data point corresponded to an application of the load at the particular radial distance. Some instruments had up to six data points at a given radial distance. Six data points were possible when the instrument was located near the center of the test box. Due to the instrument location, it was possible to generate data on either side of the instrument at the same radial distance. Other instruments located closer to the wall did not have as many data points because the load could not be applied on both sides.

Data was compiled for all of the instruments and the response points were averaged (whether three or six points) at each radial distance for each instrument. A curve was drawn through the average response at each distance, and these data were compared to KENLAYER model results. These curves are presented in Figures 5.2-5.28 at the end of the chapter. A discussion of surface deflection, strain in the AC layer, stress in the base and subgrade, and base and subgrade strains is now presented for the PCS1 section and the model results. In all figures, the instrument name and depth is given for the experimental results.

Surface Deflections/AC Strain

The surface deflection predictions of the model are shown with experimental results in Figure 5.2. Actual data points are shown along with the "average" response for the experimental results. The load was applied in the center of the box (location 8), as well as applications 200 mm from the center (locations 6,10) and 400 mm from the center

(locations 4,12). It is noticed that the responses plotted from locations 200 mm and 400 mm from the center matched the responses when the load was placed in the center (location 8). Additionally, loads applied first (locations 4,6) matched those applied later (locations 8,10,12), illustrating that the pavement did not stiffen. In other words, the first few load applications did not influence the elastic response of subsequent load applications.

Figure 5.2 illustrates that model predictions for surface deformation are significantly less than the experimental results. Figure 5.2 and all remaining figures for this chapter are contained at the end of the chapter. Additionally, the shape of the deflection "bowl" is much steeper for the experimental results. Reasons for both of these trends may be derived from actual material parameters differing from those in the model, but most importantly differences in boundary conditions. The model assumes infinite layer extents to those finite extents in the test box. This "half-space" assumption may result in the model being "stiffer" than the test section. The experimental section may have upward movement of the AC layer at the wall/AC interface, which could result in a steeper deflection bowl. The existence of boundary condition effects discussed previously was disproved however, through identical runs with the commercial ABAQUS (Hibbitt, Karlsson & Sorensen, Inc., 1998) finite element code. The model runs in ABAQUS freed the AC layer from the wall conditions allowing movement in two directions. Resulting surface deformations matched those of the KENLAYER program. Thus, boundary condition differences are not the major cause of the significant underpredictions of surface deflection of the linear elastic model.

AC strain is presented in Figure 5.3. The model underpredicts tensile strain beneath the load area (up to 150 mm radial distance) and beyond. The trend of tensile strain directly beneath the load application and compression at larger radial distances is predicted well by the model.

Stress Predictions

Stress comparisons between model predictions and experimental results are provided in Figures 5.4-5.14. It is noted that the model predicts significant tensile stresses in the base beneath the load application. This prediction invalidates the concept that granular soil materials cannot support tension and is a shortcoming of the elastic model. If these tensile stresses were transferred through the use of a plasticity or "failure" model in a downward and outward manner through the section, higher stress/strain may have been applied to the subgrade resulting in increased deformation. Thus, the inadequacies of correctly predicting soil behavior in tension may be the main reason why the linear elastic model significantly underpredicts surface deformation of the control section. Additionally, higher vertical strains may have been exhibited by the base layer due to the loss of strength in the radial direction, adding to additional deformation.

Vertical stresses were underpredicted by the model (Figure 5.7) in the base layer. This may be due to invalid predictions of tensile stresses in the base or boundary conditions mentioned previously. In general, the trend of decreasing vertical stress with increasing radial distance, was exhibited by the model and the experimental results.

Stress in the subgrade (Figures 5.8-5.14) was drastically underpredicted by the model. The underpredictions may be due to problems associated with model assumptions predicting tensile stresses in the base layer. Tensile predictions may "stiffen" the base compared to a case where the soil could not support tension, and result in smaller stresses being applied to the subgrade. It is noted that in cases where two instruments were present in the same layer, that in general, the two instruments provided similar responses of stress (Figures 5.8-5.10, 5.13).

Strain Predictions

Experimental results in Figures 5.15-5.17 show large tensile regions of radial and tangential strains. These results are underpredicted by the model. The development of significant tensile radial and tangential strains in the base signifies material is moving outward from the loaded area. This outward material movement not predicted by the model may be a reason for underprediction of total surface deflection.

Vertical strain in the base and subgrade layers is again underpredicted by the model (Figures 5.18, 5.21, 5.24). Of interest, the vertical strain in the top of the subgrade at a depth of 450 mm (Figure 5.21) is underpredicted beneath the load center by a factor of approximately four. Assuming that a significant portion of the total rut depth is derived from the top of the subgrade, this underprediction is significant with respect to total surface deformation. Again, reasons for small vertical strain predicted by the model may include the development of significant tensile stress in the base layer beneath the load. Again, these predictions by the model of tensile stress may lead to a less critical

state of stress and strain in the top of the subgrade, reducing the total rut development predicted by the linear elastic model.

Stress and Strain Beneath Load Centerline

Plots were generated to illustrate stress and strain distributions with increasing depth in the test section. These plots (Figures 5.25-5.28) were generated directly beneath the load centerline. Vertical stress throughout the depth of the section was underpredicted by the model. Areas significantly underpredicted are in the base (Z=300 mm) and in the top of the subgrade (Z=450 mm). Radial stress predictions in Figure 5.26 show that the model and experimental results exhibit virtually no radial stress in both the base and subgrade layers. It is noted that the model predicted unusually large radial stresses in the AC layer, as shown in Figure 5.26.

Radial strain trends were illustrated well with the model results directly beneath the load. Figure 5.27 shows that the maximum radial strain in the model and the experimental results occurs at or near the base/subgrade interface (Z=375 mm). Although the model underpredicted the magnitude of the strains, the importance of reinforcement placement near areas of high radial strain in the base is illustrated. This may be a reason to use a linear elastic model to determine reinforcement placement within an experimental section or in a road, when trying to utilize the lateral restraint function discussed in Chapter 4. Vertical strains were underpredicted by a factor of 4-5 as shown in Figure 5.28. Interestingly, the highest vertical strains were recorded in the top of the subgrade (Z=450-625 mm).

Subgrade Strain Criterion Analysis

This section will describe how a mechanistic-empirical design approach describes section behavior and provides failure criteria. Subgrade strain criteria have been developed to aid pavement engineers in providing a thickness design that would service anticipated traffic loads without allowing a prescribed rut depth. Essentially, the basis of the analysis relies on limiting vertical strain development in the top of the subgrade so that permanent rut depth progression is limited. Several empirical relations have been developed (Asphalt Institute, 1991; U.K. Transport & Road Research Laboratory, in Huang, 1993; and Shell, 1985) which relate the vertical strain experienced by the top of the subgrade, from the first cycle of load to a corresponding number of cycles to failure (N_f). The number of cycles to failure (N_f) utilizes a prescribed surface rut depth, for which the relations were developed. These empirical relations assume that the asphalt and base layers do not contribute to rutting. Several other relations exist (i.e. Belgian Road Research Center), but were not used in this comparison to the experimental test sections because of difficulty in interpreting the failure criteria (rut depth) used in these relations. Reiterrating, in the subgrade strain method, it is assumed that if the subgrade compressive strain is controlled, reasonable surface depths will not be exceeded. A general relation between the number of cycles to failure and the first cycle (elastic) strain is given as (Huang, 1993):

$$N_f = x\,(\varepsilon_c)^{-y} \qquad (5.1)$$

Where:

N_f = the allowable number of load repetitions to limit permanent deformation at a prescribed rut depth considered failure

ε_c = the compressive strain on the top of the subgrade

x = constant determined from road test

y = constant determined from road test

The number of cycles for a prescribed failure (rut depth), were calculated using the Asphalt Institute, the U.K. Transport & Road Research Laboratory, and the Shell Oil Co. relations, in combination with the vertical compressive strain at the top of the subgrade layer obtained from KENLAYER results. The cycles to failure from the empirical relations were then compared to the actual cycle numbers in the experimental test sections (control sections CS2 & CS8) at the same rut depth criteria. Model constants "x" and "y" from various agencies are summarized in Table 5.2. The results comparing the number of cycles to failure predicted by the empirical relations to the number of cycles at "failure" for the test sections CS2 and CS8 are presented in Table 5.3.

Table 5.2. Empirical constants "x" and "y" and rut depth proposed by various agencies.

Agency	x	y	Rut Depth (mm)
Asphalt Institute	1.365×10^{-9}	4.477	12.7
Shell (85% reliability)	1.94×10^{-7}	4.0	20
U.K. Transport & Road Research Laboratory (85% reliability)	6.18×10^{-7}	3.95	10.2
Belgian Road Research Center	3.05×10^{-9}	4.35	N/A

N/A = Not Available

Table 5.3. Comparison of empirical failure models (rutting) to CS2 and CS8.

Agency / Rut Depth	Cycles to Failure (N_f)	CS2	CS8
Asphalt Institute / 12.7 mm	2650	5400	2800
U.K. Transport & Road Research Laboratory / 10.2 mm	4292	2600	800
Shell Oil Co. / 20 mm	18,480	20,500	18,500

As shown in the Table 5.3, it is apparent that the Asphalt Institute strain criteria conservatively predicts the number of cycles to failure for both CS2 and CS8. The U.K. Transport & Road Research Laboratory formula over predicts the cycles to failure. Reasons for the overprediction may include a limited number of test sections or materials which did not behave similar to the materials used in the experimental test sections, or that small failure criterion were difficult to predict. The Shell Oil Co. criterion also reasonably predicts rut failure for the two experimental sections, given a "rut failure" of 20 mm.

In a design mode, one could rearrange the strain relation shown in (5.1) and solve for the limiting subgrade compressive strain (ε_c), given a number of design ESALS or load cycles. Given the fact that the mechanistic-empirical design method has not been

used to a great extent in practice at this time, the application may be best suited as a check to common road design procedures such as the current AASHTO design method.

Rut Development Predictions Using Empirical Relations

This section uses empirical plastic strain accumulation relations to predict subgrade rutting as a function of load application number. Essentially, it was desired to predict section rut behavior based on the first cycle of permanent strain in the subgrade. The most commonly used model (Li, et al., 1996) is a power function of the following form:

$$\varepsilon_p = A(N)^b \qquad (5.2)$$

Where:

ε_p = cumulative plastic strain (%)

A = soil plastic strain after the first cycle of repeated loading

N = number of repeated load applications

b = material constant

The "A" coefficient is dependent on soil type, soil physical state, and the deviator stress. Deviator stress in this case is defined as the difference between the applied vertical stress and the horizontal stress at a given vertical depth. The constant "b" has been shown by several (Monismith et al. 1975; Knutson et al. 1977; Li et al. 1996) to be independent of soil physical state (i.e. soil moisture and dry density) for a given soil type.

Li et al. (1996) has also shown the parameter to be insensitive to changes in the deviator stress. Therefore, "b" only differs for different soil types.

As stated previously, "A" in relation (5.2) is a function of several variables. Li et al. (1996) studied the influence of soil type and soil physical state on the parameter "A". Li et al. (1996) used the soil static strength (unconfined compressive strength) to incorporate both water content and dry density as physical state characteristics. To define "A" as a function of both the deviator stress and the soil physical state, the author proposed the following relation for the parameter "A":

$$A = a(\sigma_d/\sigma_s)^m \qquad (5.3)$$

Where:

σ_d= deviator stress

σ_s = soil static strength (unconfined compressive strength)

a,m = material parameters determined through laboratory tests

Subsituting (5.3) into (5.1) yields:

$$\varepsilon_p = a(\sigma_d/\sigma_s)^m(N)^b \qquad (5.4)$$

The preceding relation (5.4) was used in this research to try and predict strain accumulation for section CS2. Data from CS8 (permanent vertical strain in the subgrade) was not used due to instrument problems. Deviator stress was estimated from

KENLAYER at various depths. Soil static strength (unconfined compressive strength) was estimated from consolidated undrained conventional triaxial compression (CU-CTC) tests performed on the clay subgrade material. Material parameters "a", "b", and "m" were estimated from an "average" CH clay from Table 2 in Li et al. (1996). When compared to section CS2, the empirical relation (5.4) using the assumed parameters from Li et al. (1996) greatly underpredicted plastic vertical strain accumulation in the subgrade by an order of magnitude. This may be due to the fact that the CH clay used in this study had a much higher water content (45%), than those listed in Table 2 from Li et al. (1996).

It was then decided to use equation 5.2 for simplification. "A" was determined from the first cycle plastic strain from four LVDT's (SS13,SS20,SS24,SS25) at several depths from experimental test section CS2. Relation 5.2 was applied to the cycle numbers in the test section and the best-fit "b" was found for each LVDT long-term behavior. Values of "b" of 0.34, 0.34, 0.32, and 0.32 were obtained by trial-and-error for the LVDT's respectively in order listed above. Most importantly, the values of "b" found for each layer of the subgrade were very similar. Additional validy between LVDT measurements of vertical strain in several layers is gained. Essentially, the "b" value should remain constant through the depth of the subgrade. If calculated "b" values differed significantly, confidence in the LVDT measurements of vertical strain would be lost. The parameter "b" for the clay subgrade was averaged from the four long-term strains to yield 0.323. Surprisingly, this value of "b was significantly higher than the values of "b" presented in Table 1 in Li et al. (1996). The highest value of "b" for a CH clay at a water content of approximately 30% was 0.26. A reason for the high "b" value

obtained from the test section may be from a difference in clay content of the soil used in this study as opposed to clays listed in Table 1 in Li et al. (1996). Knowing "A" and "b", permanent plastic strain was calculated for each LVDT at 55,000 total cycles of load, using relation (5.2).

To predict total section deformation at 55,000 cycles (assuming that only the subgrade contributes to surface deformation), each permanent strain was multiplied by an assumed thickness of subgrade equal to the distance between two adjacent LVDT's, resulting in four finite deformations for the subgrade. This calculation assumed a linear distribution of vertical strain between adjacent instruments. These deformations were then summed for the entire subgrade. Total deformation for the subgrade was estimated at 12.8 mm. Total permanent deformation for the test section CS2 for 55,000 cycles was approximately 27.8 mm. Thus, assuming that permanent subgrade deformation contributed solely to the permanent deformation of the section would be grossly underestimating rut depth.

It was decided to back-calculate material parameters "a" and "m" for the experimental test section to compare with results back-calculated in Table 1 (Li et al. 1996). The deviator stress was estimated using the KENLAYER computer program, as results for vertical and radial stress were not available from the test section data for the lower levels in the subgrade. "A" was used from the first cycle strains from the four LVDT's at different depths. Static soil strength (σ_s) was found from triaxial results described previously.

Four points were plotted corresponding to four values of "A" and (σ_d/σ_s) at each depth where an LVDT was located in the subgrade. A power function was fit to the experimental data and is shown in Figure 5.31. The parameters "a" and "m" were then found from the best-fit power relation. The experimentally determined parameters "b", "a", and "m" are shown along with back-calculated parameters taken from Table 2 (Li et al., 1996) in Table 5.4. According to Li et al. (1996), all three parameters generally increase with increasing clay content and soil plasticity. Values from the experimental work indicate that the three parameters lie in the upper range of those presented in Li et al. (1996), which is reasonable.

Table 5.4. Comparison of experimental plastic strain parameters to parameters from Li et al. (1996).

Model Parameters		Soil Classification				This Study
		ML	MH	CL	CH	
b	Average	0.10	0.13	0.16	0.18	0.32
b	Range	0.06-0.17	0.08-0.19	0.08-0.34	0.12-0.27	-
b	Observation number	6	4	13	7	-
a	Average	0.64	0.84	1.1	1.2	2.35
a	Range	-	-	0.3-3.5	0.82-1.5	-
a	Observation number	1	1	7	5	-
m	Average	1.7	2.0	2.0	2.4	2.12
m	Range	1.4-2.0	1.3-4.2	1.0-2.6	1.3-3.9	-
m	Observation number	3	4	10	7	-

If models were developed for plastic vertical strain development in the base, one could better estimate total section deformation using the subgrade deformation relations and the base relations. At this point empirical relations have not been developed for base

materials and higher order constitutive models must be used to predict base course behavior. Thus, linear elastic estimations which assume that deformations occur only in the subgrade are probably not conservative based on the analysis presented in this chapter.

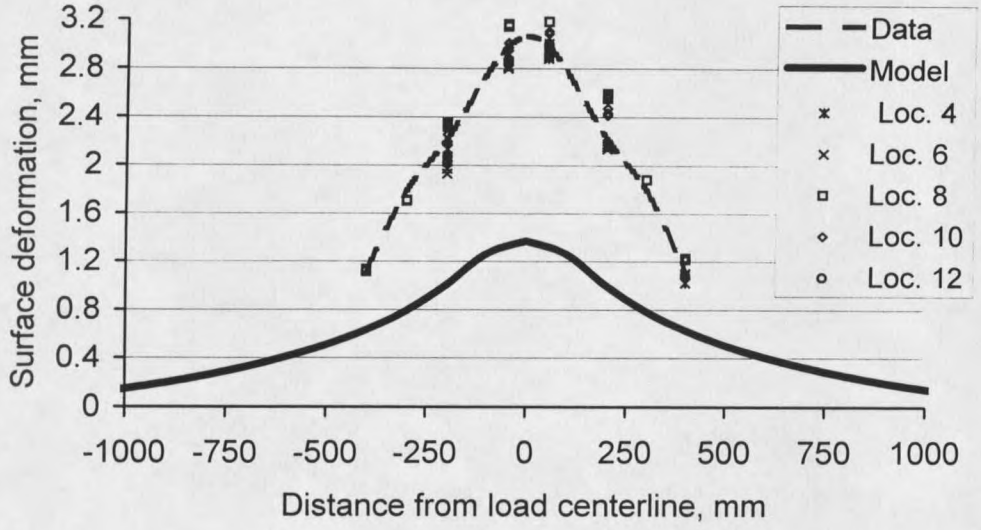


Figure 5.2. Peak elastic asphalt concrete surface deflection.

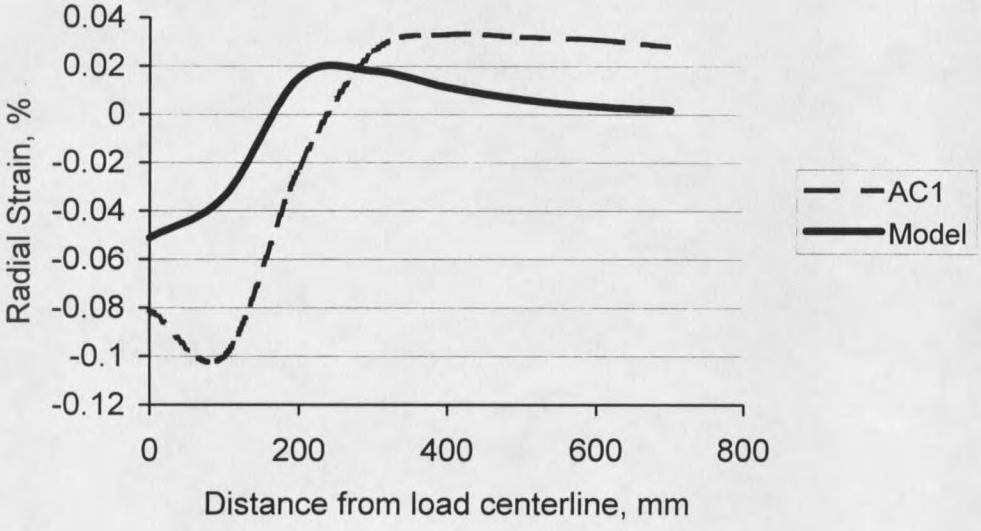


Figure 5.3. Peak elastic radial strain versus radial distance in the AC.
(Z=67 mm)

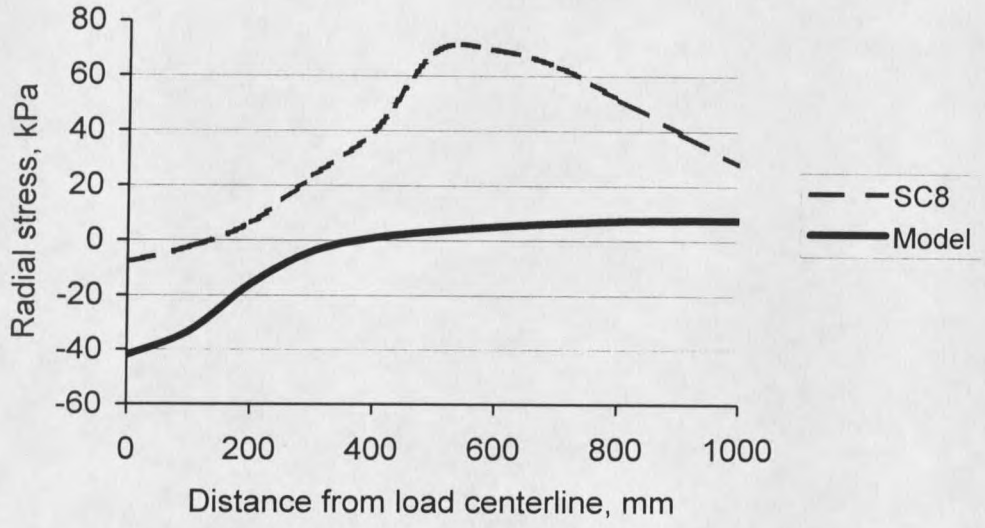


Figure 5.4 Peak elastic radial stress versus radial distance in the base. (Z=225 mm)

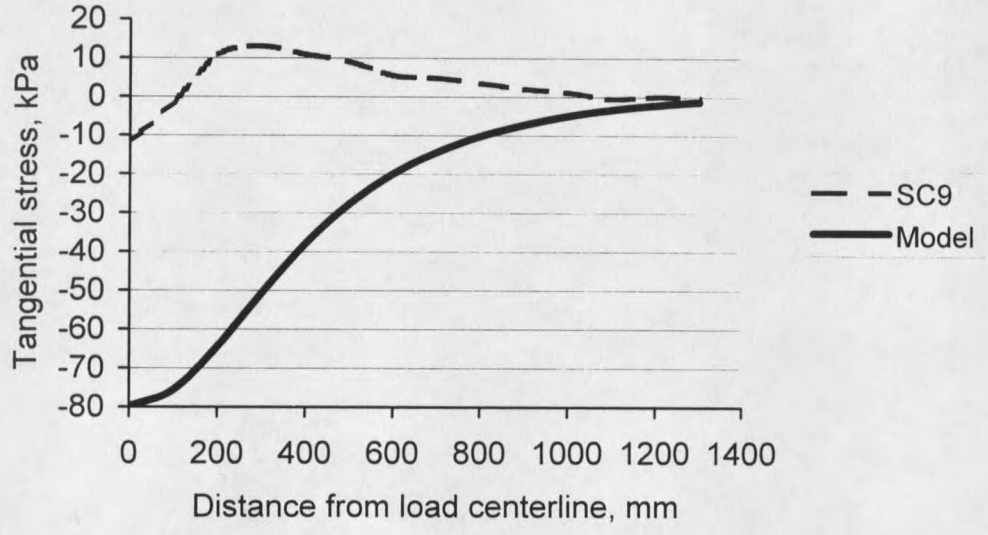


Figure 5.5. Peak elastic tangential stress versus radial distance in the base. (Z=300 mm)

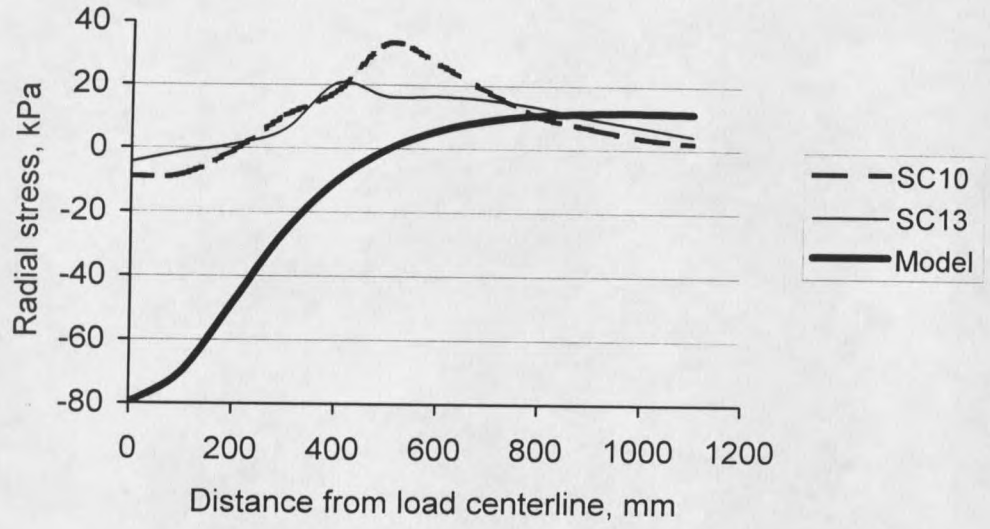


Figure 5.6. Peak elastic radial stress versus radial distance in the base. (Z=300 mm)

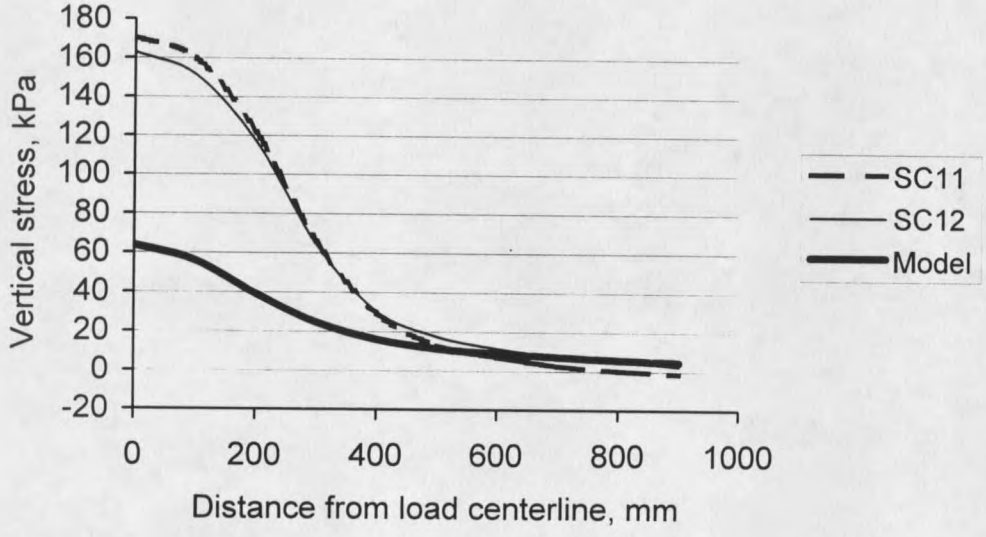


Figure 5.7. Peak elastic vertical stress versus radial distance in the base. (Z=300 mm)

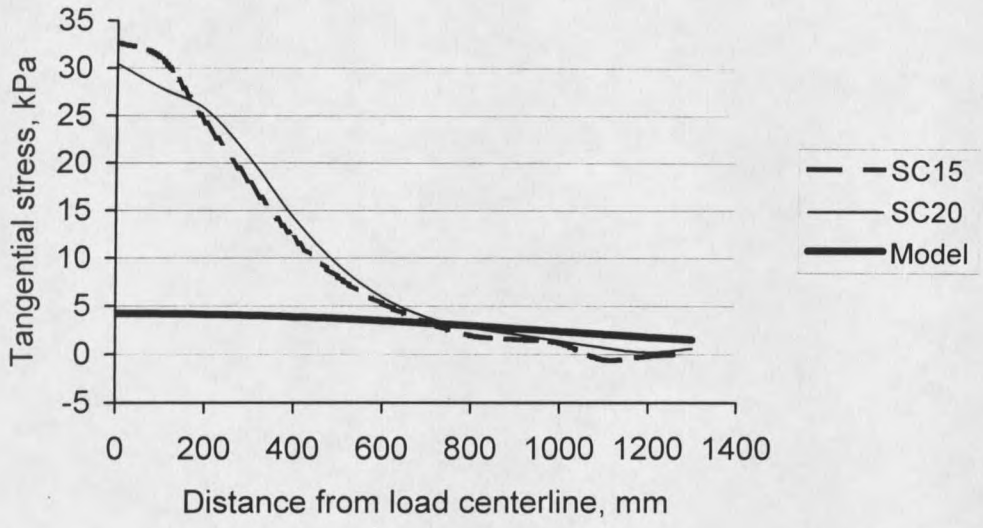


Figure 5.8. Peak elastic tangential stress versus distance in the subgrade. (Z=450 mm)

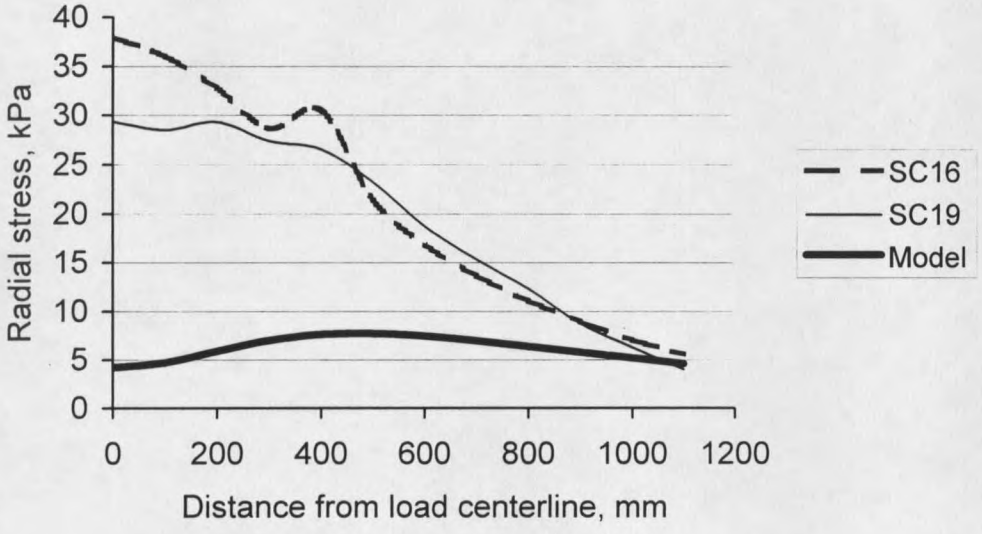


Figure 5.9. Peak elastic radial stress versus radial distance in the subgrade. (Z=450 mm)

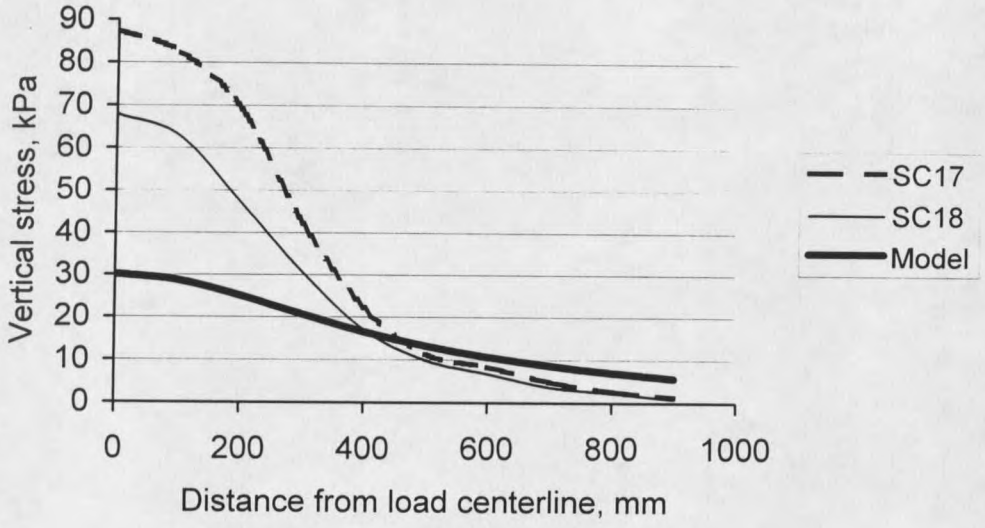


Figure 5.10. Peak elastic vertical stress versus radial distance in the subgrade. (Z=450 mm)

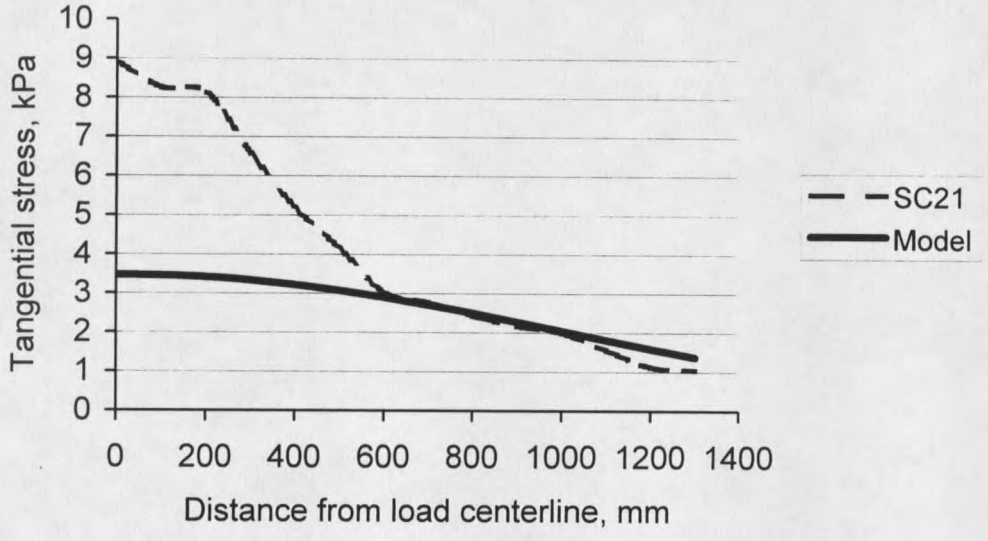


Figure 5.11. Peak tangential stress versus distance in the subgrade. (Z=675 mm)

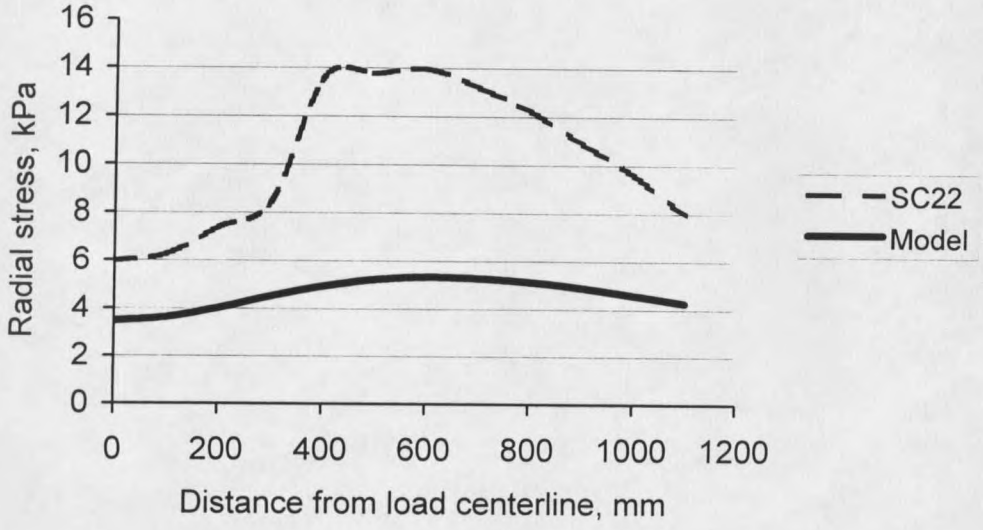


Figure 5.12. Peak elastic radial stress versus radial distance in the subgrade. (Z=675 mm)

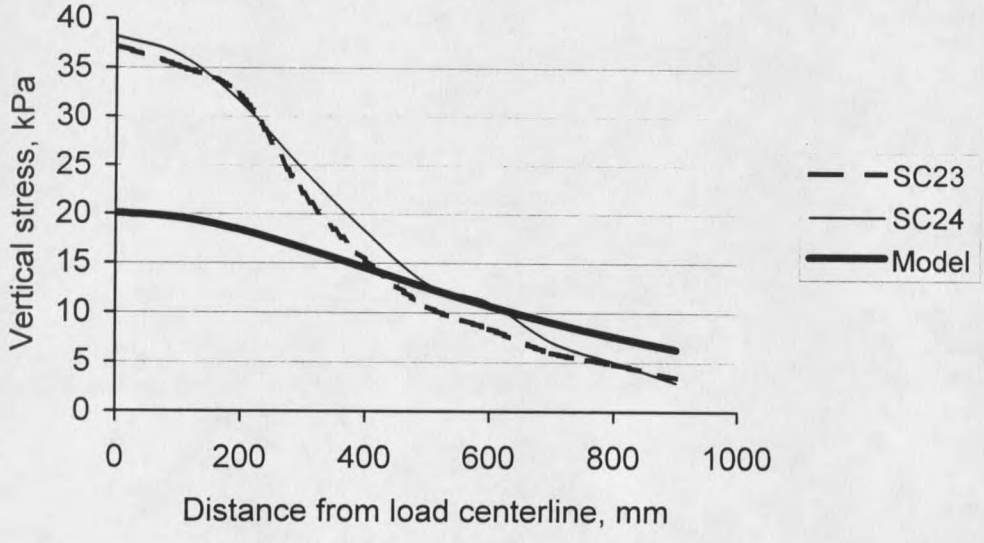


Figure 5.13. Peak elastic vertical stress versus radial distance in the subgrade. (Z=675 mm)

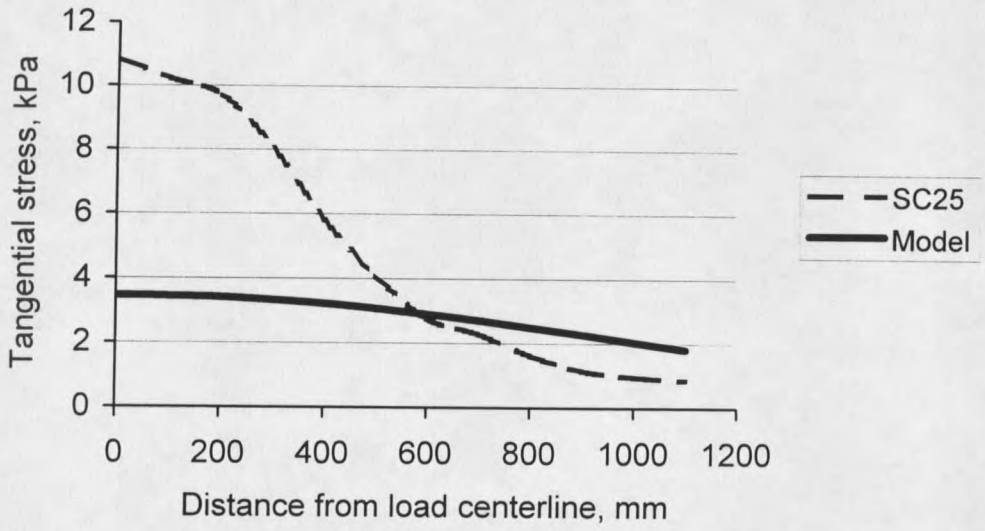


Figure 5.14. Peak elastic tangential stress versus distance in the subgrade. (Z=675 mm)

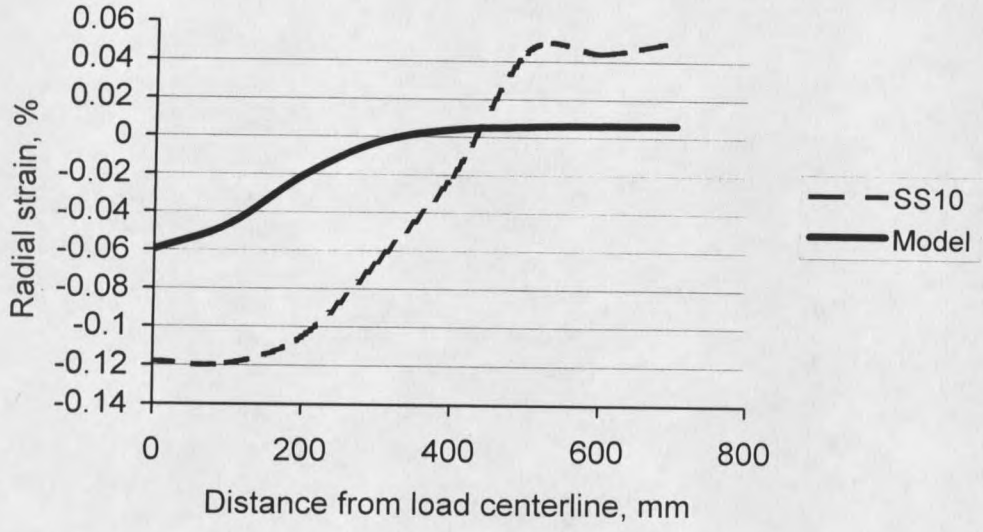


Figure 5.15. Peak elastic radial strain versus radial distance in the base. (Z=225 mm)

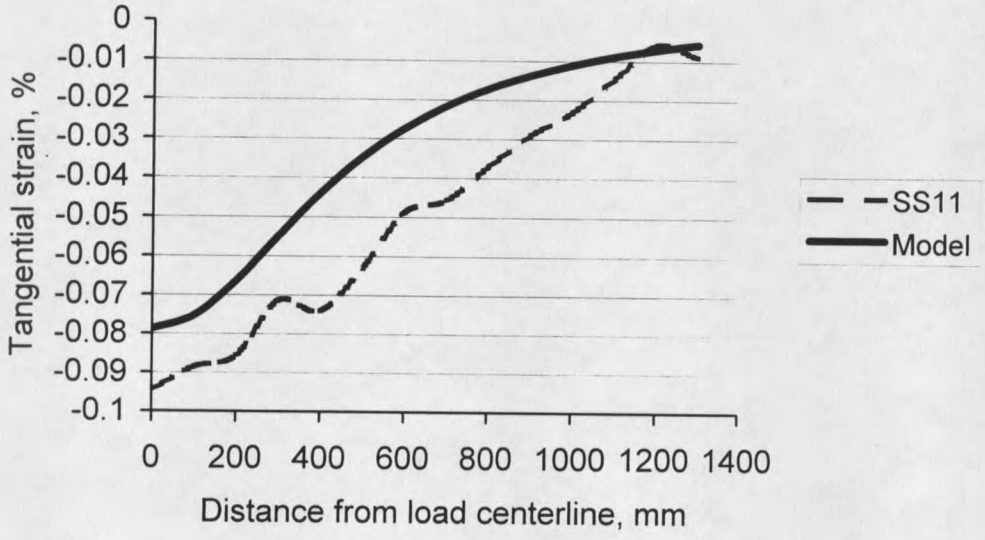


Figure 5.16. Peak elastic tangential strain versus radial distance in the base. (Z=355 mm)

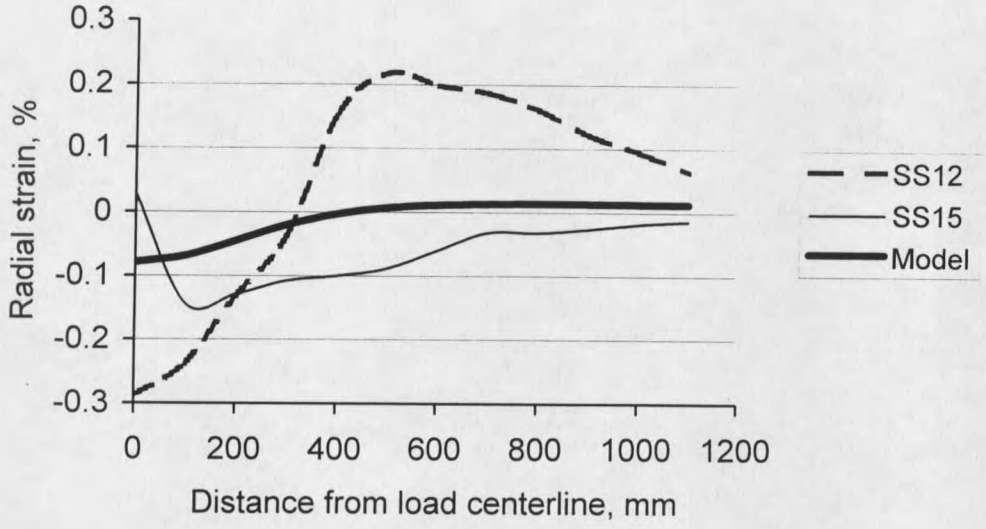


Figure 5.17. Peak elastic radial strain versus radial distance in the base. (Z=355 mm)

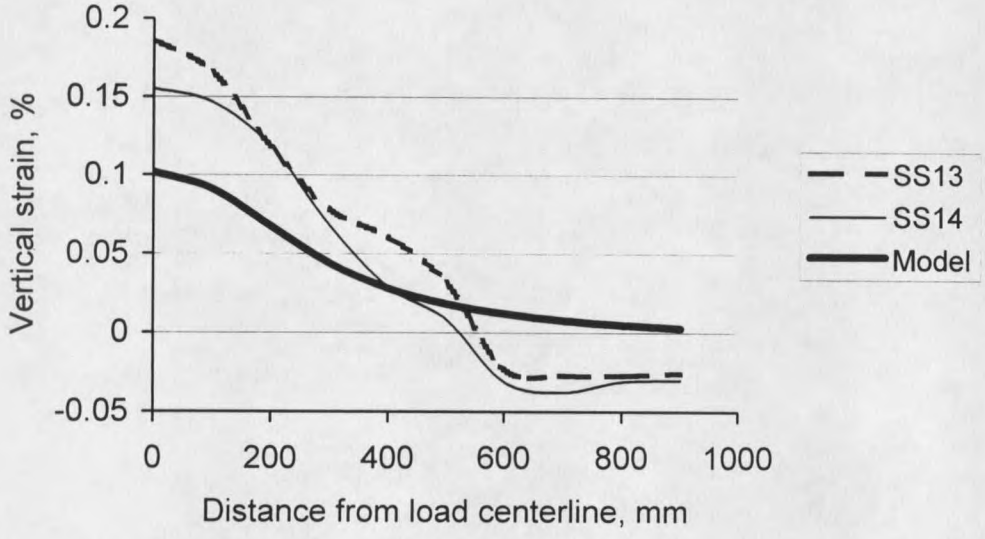


Figure 5.18. Peak elastic vertical strain versus radial distance in the base. (Z=300 mm)

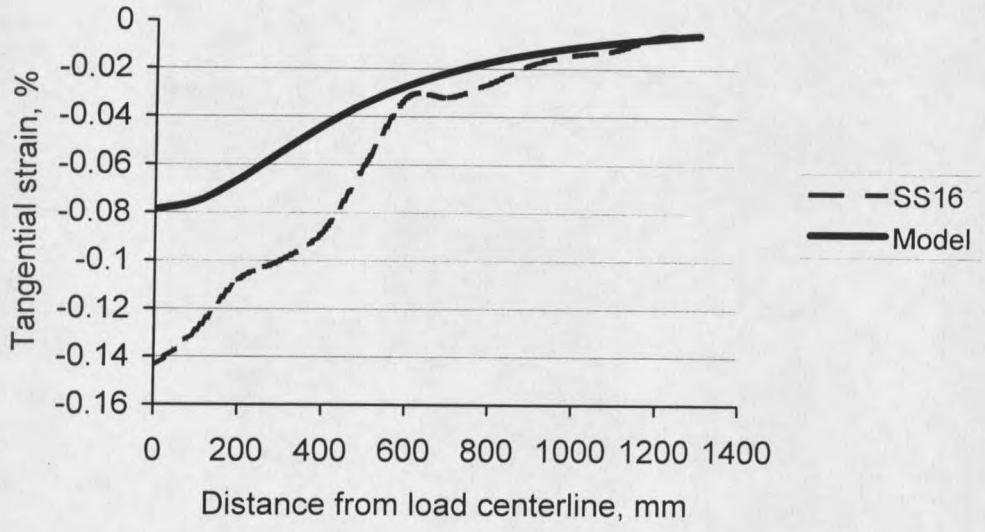


Figure 5.19. Peak elastic tangential strain versus radial distance in the base. (Z=355 mm)

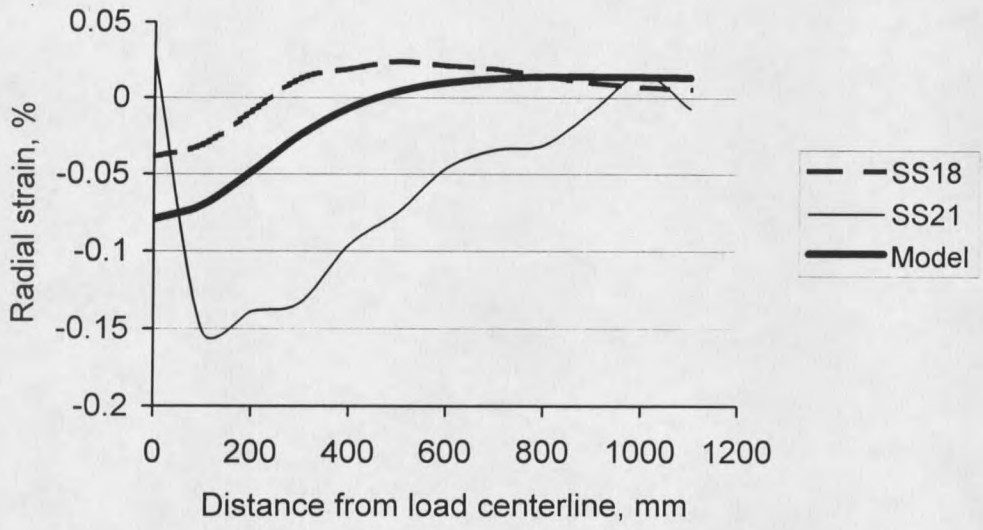


Figure 5.20. Peak elastic radial strain versus radial distance in the subgrade. (Z=415 mm)

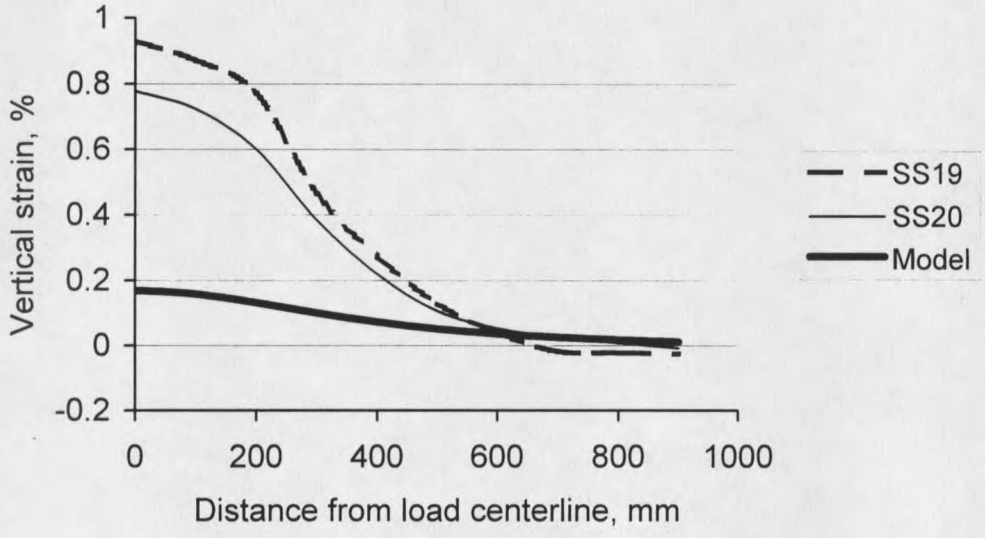


Figure 5.21. Peak elastic vertical strain versus radial distance in the subgrade. (Z=450 mm)

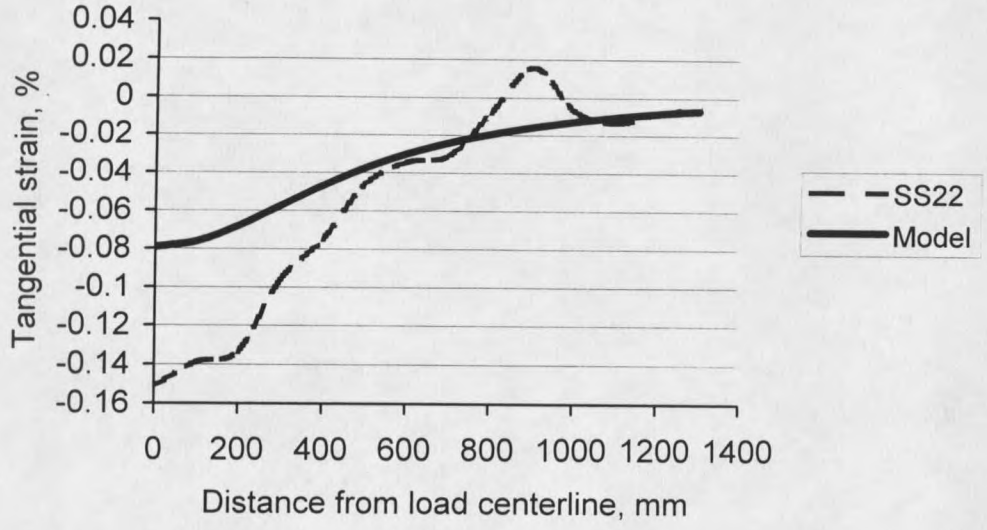


Figure 5.22. Peak elastic tangential strain versus distance in the subgrade. (Z=415 mm)

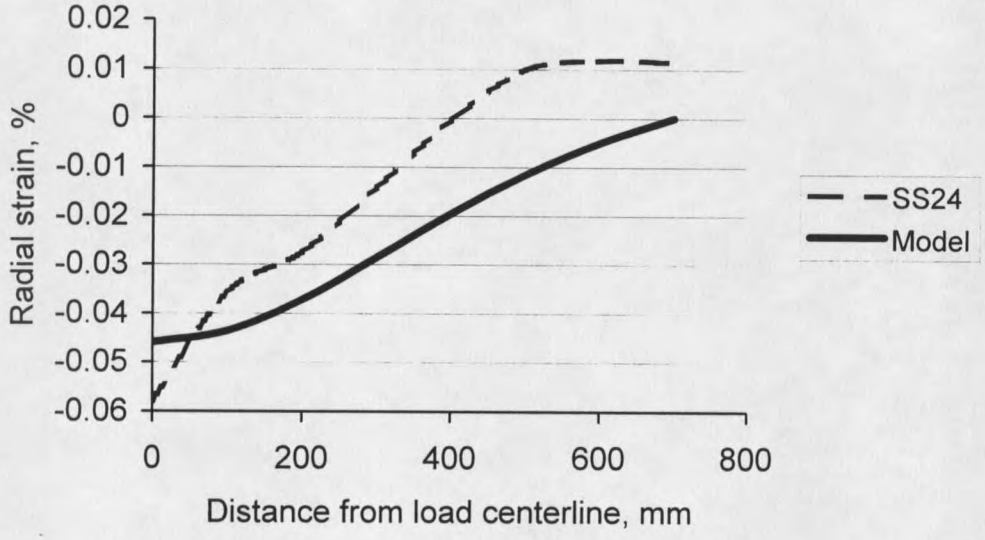


Figure 5.23. Peak elastic radial strain versus radial distance in the subgrade. (Z=675 mm)

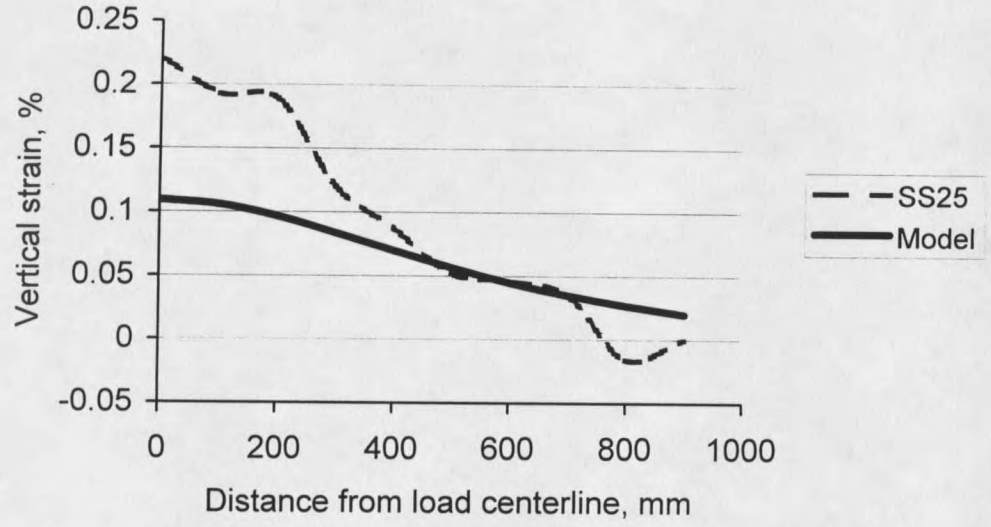


Figure 5.24. Peak elastic vertical strain versus radial distance in the subgrade. (Z=675 mm)

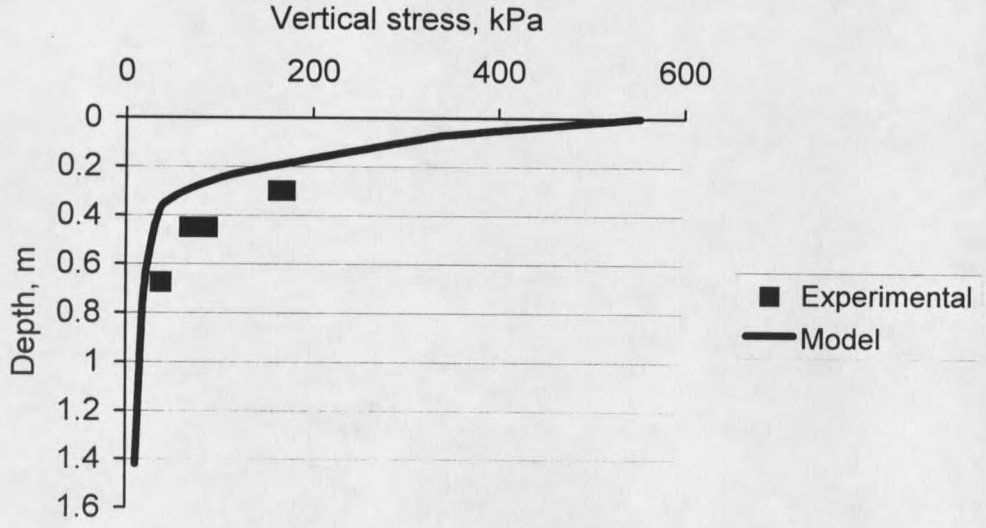


Figure 5.25. Peak elastic vertical stress versus depth at R=0 mm.

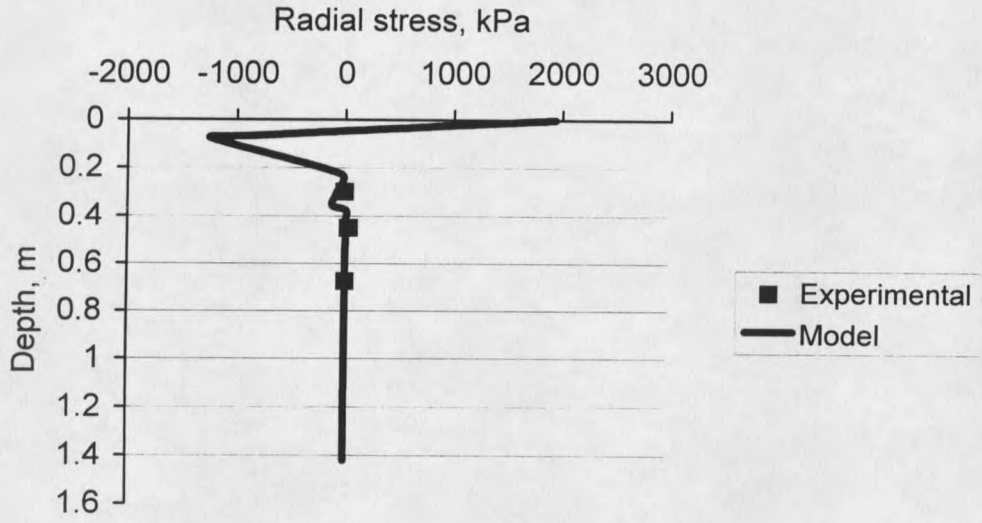


Figure 5.26. Peak elastic radial stress versus depth at R=0 mm.

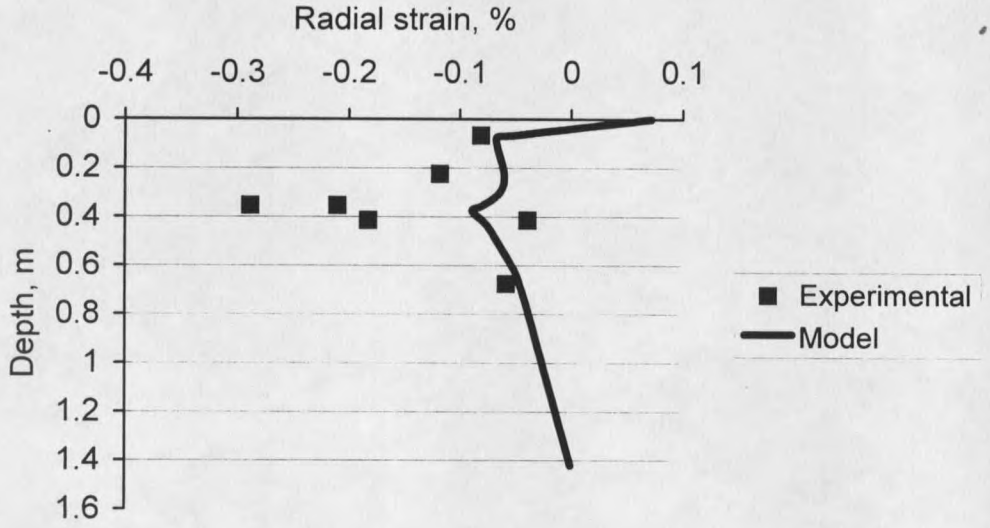


Figure 5.27. Peak elastic radial strain versus depth at R=0 mm.

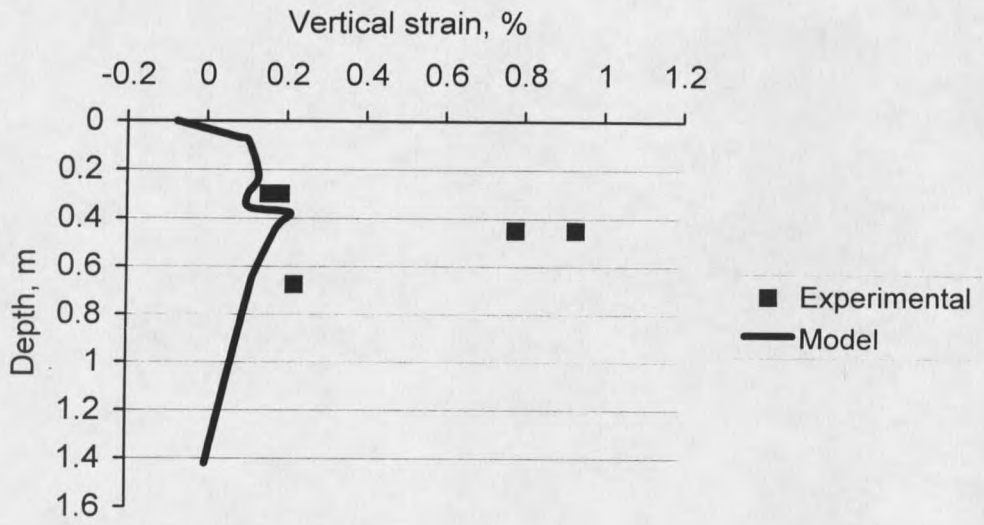


Figure 5.28. Peak elastic vertical strain versus depth at R=0 mm.

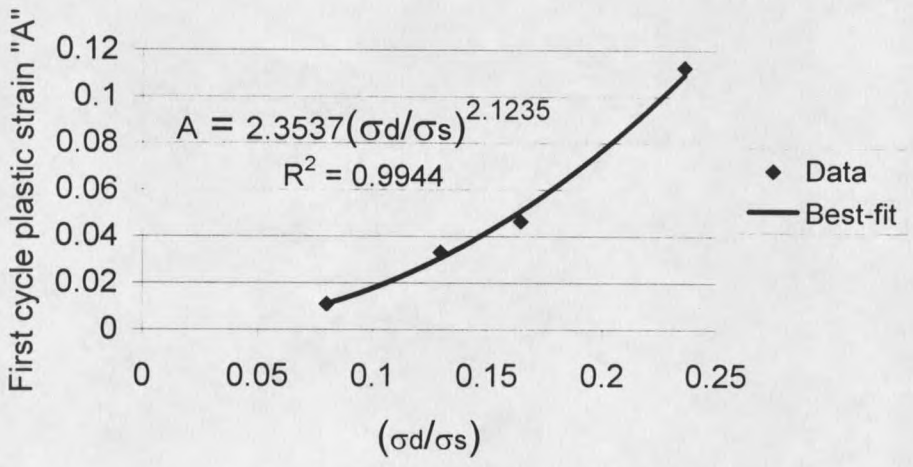


Figure 5.29. First cycle plastic strain parameter "A" as a function of the deviator stress/static stress ratio.

CHAPTER SIX

CONCLUSIONS AND RECOMMENDATIONS

Summary

A total of 21 laboratory-scale flexible pavements were constructed and cyclically loaded in a 2m x 2m x 1.5m concrete test box. Loading was supplied through a 305 mm diameter circular plate with a net 550 kPa pressure applied to the pavement surface. This load simulated one tire from equivalent standard axle load (ESAL). Control (unreinforced) and reinforced sections were constructed.

The objective of this study was to evaluate the effects of the addition of several different types of geosynthetics (one geotextile and two geogrids) to the base course layer as reinforcement. Primarily, this study concentrated on the effects of reinforcement on rutting behavior. Variables investigated throughout the experimental testing included subgrade type, geosynthetic type, base course thickness, and location of placement of the geosynthetics within a section. Two subgrades were used consisting of a silty-sand and a CH clay. The silty-sand exhibited high CBR values up to approximately 20, while the CH clay was tested at a CBR of 1.5. Geosynthetic types investigated in this research included an Amoco 2006 woven geotextile, a Tensar BX-1100 biaxial geogrid, and a

Tensar BX-1200 biaxial geogrid. These three materials were used to study differences in stiffness and soil/geosynthetic interaction, and their effects on reinforced pavement rutting performance. Base course thickness was varied to study the effects of additional base material on the overall rutting performance of a section. Additionally, base course additions were compared to similar geosynthetic reinforced sections to estimate the amount of base material that could be replaced by geosynthetic reinforcement to provide equal rutting performance. Geosynthetic reinforcement was installed at either the subgrade/base course interface, or was moved up into the base layer to study the effects on rutting due to reinforcement placement.

Measurements of surface deflection were made across the surface of the asphalt concrete to provide dynamic information and rutting comparisons between all sections. Additionally, approximately 90 instruments were installed in sections measuring soil stress and strain, strain in the geosynthetics, soil moisture, and soil temperature. Instruments were distributed throughout the depth of a section and were installed in lateral directions outward from the load centerline at each depth. This arrangement of instruments provided a clear understanding of stress/strain behavior in both control and reinforced sections.

Interpretations of the effects of reinforcement were made though analysis of soil stress and strain distributions in the base and subgrade layers, as well as the surface deflections of the asphalt concrete layer. Also integrated into this analysis were measurements of strain in the geosynthetics. Beneficial effects of reinforcement were described by the shear resisting interface mechanism, which is summarized below. It was

demonstrated that this reinforcement mechanism reduces rutting in both the base course and the subgrade layers by providing shear resistance to the soil. Several other beneficial mechanisms/effects were shown to affect permanent rut development and are also summarized below.

As a separate component of this research, a linear layered-elastic model called KENLAYER was used to predict the stress/strain response of an unreinforced control section with a clay subgrade. This model was used to discover weaknesses in modeling methodologies, which existed in predicting overall pavement behavior from linear elastic theory. These weaknesses will facilitate the development of a finite element model, which is extension to this study. Additionally, several empirical performance models that describe primarily cumulative plastic deformation of the subgrade were compared with the behavior of the unreinforced control section. Empirical parameters describing cumulative plastic deformation of the subgrade soil were back-calculated and compared with parameters from the literature.

Shear Resisting Interface Mechanism

This section concludes the experimental findings supporting the shear resisting interface mechanism and its associated effects. The shear resisting mechanism has been shown to reduce pavement rut development immediately within the first several cycles of load, without requiring excessive deformations in order to function. Adding geosynthetic

reinforcement to the base layer was found to provide the following beneficial effects in terms of total rut development minimization:

- Lateral strain was significantly reduced in the base layer in reinforced sections from the lateral restraint provided by the geosynthetics, that provided a basis for other mechanisms/effects described hereafter.
- Vertical strain in the base layer was reduced in part by the lateral restraint provided by the geosynthetic. Theoretically, the reduction in vertical strain in the base results from an increase in the mean stress of the layer as well as a reduction in lateral aggregate movement from the lateral restraint mechanism. An increase in mean stress in the base layer could not be shown from experimental data. Two reasons may account for the lack of characterization of this effect: 1) An increase in mean stress may have occurred for a relatively thin layer of the base which made measurement of stress difficult due to the size of the instrument, and 2) Stress cells may have not been located in areas where mean stress did increase.
- An improved vertical stress distribution resulting from reinforcement of the base layer provided a less severe state of stress on the top of the subgrade, which reduced rutting potential.
- A reduction of lateral spreading in the subgrade was exhibited by reinforced sections, due to lateral restraint of the base aggregate and the resistance of shear provided by the geosynthetic.

- A significant reduction of the vertical strain in the subgrade was shown in reinforced sections resulting from a combination of the effects shown above.

From the aforementioned beneficial effects of the shear resisting interface mechanism, one would expect significant quantitative increases in performance due to the addition of reinforcement. As expected, rut development was greatly reduced for a clay subgrade with a CBR of 1.5, through the inclusion of several geosynthetic materials as reinforcement. The reinforced sections with a 300 mm base exhibited the following peak traffic benefit ratios (TBR's), defined as the ratio of the number of load cycles of a reinforced section to an identical unreinforced section necessary to achieve a particular rut depth:

- 8 for the AMOCO 2006 geotextile
- 18 for the BX-1100 geogrid
- 42 for the BX-1200 geogrid
- 56 for the BX-1100 geogrid placed up in the base layer
- 14 for the BX-1100 geogrid used with a 375 mm thick base

Unfortunately in the case of the reinforced clay subgrade sections, no single instrument measure stood out as a distinct predictive indicator of performance between different types of reinforcement. Rather, several measures of stress and strain were needed to distinguish benefits of different types of reinforcement.

For the clay subgrade sections, all geosynthetics used to reinforce a 300 mm thick base improved rutting performance better than the addition of an additional 75 mm of base aggregate. Reiterating, all geosynthetic reinforced sections with a 300 mm thick base performed better than a control section with a total base thickness of 375 mm base. Thus, it is concluded for the subgrade conditions evaluated, that reinforcement provided more benefit in terms of performance than the addition of 75 mm of base. As discussed in the introductory chapter, the reduction of base aggregate required in a suitable pavement design through the addition of a geosynthetic as reinforcement has been proven to be viable in providing equal performance. Economic considerations of base thickness reductions are discussed in the "Recommendations for Further Research" section of this chapter.

Geogrid stiffness was an influential variable in this study. Section CS5 that had a stiffer BX-1200 geogrid was shown to have performed significantly better in terms of permanent rut development than a less-stiff BX-1100 geogrid when both were placed at the base/subgrade interface. Traffic benefit ratios from the two sections were 42 and 18, for the BX-1200 and BX-1100 geogrids respectively.

Placement position of reinforcement within the base layer was also shown to be influential in the development of permanent rut in the test sections. Placing a BX-1100 geogrid up 100 mm into a 300 mm thick resulted in a peak TBR of approximately 56, compared with a TBR of 18 for the same geogrid placed at the base/subgrade interface. It is also noted that the BX-1100 geogrid placed at the base/subgrade interface of a 375 total thickness of base resulted in a peak TBR of approximately 14. Thus it was inferred

that placement of the geogrid higher up in the 375 mm thick base course would have improved rutting performance. It was discussed previously that moving the reinforcement up into the base would improve performance for thicker base course sections, which would reduce the lateral movement of the aggregate.

Reinforcement mechanisms were shown to be functioning in the stiffer silty-sand subgrade sections, but did not have a profound impact on surface rutting behavior. Most likely, the subgrade was too stiff to be amenable to reinforcement benefits.

Modeling Developments

This research has shown that advanced modeling techniques are needed to accurately predict the behavior of pavements composed of a granular base course material over a soft clay subgrade. A layered linear elastic model was shown to provide significant underpredictions of rut depth. These modeling efforts must be able to predict the loss of support for granular materials placed in tension and the soil/geosynthetic interaction in order to accurately describe overall rut development for both control sections and reinforced sections. Development of plastic strain in both the soil near the geosynthetic and in the geosynthetic itself must be accurately quantified due to the significance of this behavior on overall rut development of the pavement system. Additionally, both stress and cycle-dependent responses of the granular base and the clay subgrade must be accounted for in any modeling attempts.

Recommendations for Further Research

Several recommendations are made for further research in this area:

- Perform region-specific economic analyses incorporating geosynthetic costs, associated base aggregate costs, and construction costs to determine viability of geosynthetic reinforcement technology.
- Build and load additional test sections investigating the following variables in order to further quantify the benefits of geosynthetic reinforcement:
    - Base thickness variations
    - Reinforcement placement within the base layer
    - Additional subgrade materials
- Perform comparisons of current AASHTO design methods and data from this research to determine the relationship between the TBR and base course aggregate savings. This analysis would provide an accurate determination of pavement performance benefits resulting from geosynthetic reinforcement. Analysis of this type would also further develop economic implications of this technology.

BIBLIOGRAPHY

Al-Qadi, I.L., Brandon, T.L. and Bhutta, A., 1997, "Geosynthetic Stabilized Flexible Pavements", *Proceedings of the Conference Geosynthetics '97*, Long Beach, California, USA, March, Vol. 2, pp. 647-662.

Al-Qadi, I.L., Brandon, T.L., Valentine, R.J., Lacina, B.A. and Smith, T.E., 1994, "Laboratory Evaluation of Geosynthetic Reinforced Pavement Sections", In *Transportation Research Record 1439*, TRB, National Research Council, Washington DC., pp. 25-31.

American Association of State Highway and Transportation Officials (AASHTO), 1993, *AASHTO Guide for Design of Pavement Structures*, Washington, DC, USA.

American Association of State Highway and Transportation Officials (AASHTO), 1981, *AASHTO Guide for Design of Pavement Structures*, Washington, DC, USA.

Anderson, P. and Killeavy, M., 1989, "Geotextiles and Geogrids: Cost Effective Alternate Materials for Pavement Design and Construction", *Proceedings of the Conference Geosynthetics '89* , San Diego, CA, USA, pp. 353-360.

Appea, A.K., Al-Qadi, I.L., Bhutta, S.A., and Coree B.J., "Quantitative Assessment of Transition Layer in Flexible Pavements", Preprint Paper 980994. *Transportation Research Board 77th Annual Meeting*, January 1998, Washington, D.C.

Askegaard, V. Brink, A., and Ullidtz, P., "Pressure Cell Calibration Tests", Preprint Paper 970158. *Transportation Research Board 76th Annual Meeting*, January 1997, Washington, D.C.

Barker, W.R., 1987, "Open-Graded Bases for Airfield Pavements", Technical Report GL-87-16, USAE Waterways Experiment Station, Vicksburg, Mississippi, USA, 76 p.

Barksdale, R. D., Brown, S. F. and Chan, F., 1989, *"Potential Benefits of Geosynthetics in Flexible Pavement Systems"*, National Cooperative Highway Research Program Report No. 315 , Transportation Research Board, National Research Council, Washington DC.

Bender, D.A. and Barenberg, E.J., (1978), "Design and Behavior of Soil-Fabric-Aggregate Systems", In *Transportation Research Record 671*, TRB, National Research Council, Washington, DC, USA, pp. 64-75.

Bhutta, S.A., Al-Qadi I.L., and Brandon, T.L., "In-Situ Measurements of Flexible Pavement's Response to Vehicular Loading", Preprint Paper 980993. *Transportation Research Board 77th Annual Meeting*, January 1998, Washington, D.C.

Brandon, T.L., Al-Qadi, I.L., Lacina, B.A. and Bhutta, S.A., 1996, "Construction and Instrumentation of Geosynthetically Stabilized Secondary Road Test Sections", In *Transportation Research Record 1534*, TRB, National Research Council, Washington, DC, USA, pp. 50-57.

Brown, S.F. and Brunton, J.M., "Improvements to Pavement Subgrade Strain Criterion", *ASCE Journal of Transportation Engineering* Vol. 110, No. 6, November 1984. Pp 551-567.

Brown, S.F., "Soil Mechanics in Pavement Engineering", 1996, *Geotechnique* Vol. 46 No. 3, pp. 383-426.

Brown, S.F., Jones, C.P.D. and Brodrick, B.V., 1982, "Use of Non-Woven Fabrics in Permanent Road Pavements", *Proceedings of the Institution of Civil Engineers*, London, Part 2, Vol.73, pp. 541-563.

Brown, S.F., Jones, C.P.D. and Brodrick, B.V., 1983, "Discussion of Paper: Use of Non-Woven Fabrics in Permanent Road Pavements", *Proceedings of the Institution of Civil Engineers*, London, Part 2, Vol.75, pp. 343-358.

Burd, H.J. and Brocklehurst, C.J., 1990, "Finite Element Studies of the Mechanics of Reinforced Unpaved Roads", *Proceedings of the 4th International Conference on Geotextiles, Geomembranes and Related Products*, The Hauge, Netherlands, pp. 217-221.

Burd, H.J. and Brocklehurst, C.J., 1992, "Parametric Studies of a Soil Reinforcement Problem Using Finite Element Analysis", *Proceedings of the Conference on Computer Methods and Advances in Geomechanics*, Balkema, pp. 1783-1788.

Cancelli, A., Montanelli, F., Rimoldi, P. and Zhao, A., 1996, "Full Scale Laboratory Testing on Geosynthetics Reinforced Paved Roads", *Proceedings of the International Symposium on Earth Reinforcement*, Fukuoka/Kyushu, Japan, November, Balkema, pp. 573-578.

Carroll, R.G. Jr., Walls, J.C. and Haas, R., 1987, "Granular Base Reinforcement of Flexible Pavements Using Geogrids", *Proceedings of the Conference Geosynthetics '87*, New Orleans, U.S.A., pp.46-57.

Chan, F.W.K., 1990, *"Permanent Deformation Resistance of Granular Layers in Pavements"*, Ph.D. Thesis, University of Nottingham, 146p.

Christopher, B.R. and Holtz, R.G., 1985, *"Geotextile Engineering Manual"*, U.S. Department of Transportation, Federal Highway Administration, FHWA-TS-86/203, Washington DC, USA, 1044p.

Collin, J. G., Kinney, T. C. and Fu, X., 1996, "Full Scale Highway Load Test of Flexible Pavement Systems With Geogrid Reinforced Base Courses" *Geosynthetics Intentional*, Vol. 3, No. 4, pp. 537-549.

Davies, M.C.R. and Bridle, R.J., 1990, "Predicting the Permanent Deformation of Reinforced Flexible Pavement Subject to Repeated Loading," *Proceedings of the International Reinforced Soil Conference, Performance of Reinforced Soil Structures*, Glasgow, UK, A. McGown, K.C. Yeo and K.Z. Andrawes, eds., British Geotechnical Society, Thomas Telford, London, pp. 421 - 425, UK.

Dondi, G., 1994, "Three-Dimensional Finite Element Analysis of a Reinforced Paved Road", *Proceedings of the Fifth International Conference on Geotextiles, Geomembranes and Related Products*, Singapore, pp. 95-100.

Douglas, R.A., 1993, "Stiffnesses of Geosynthetic Built Unpaved Road Structures: Experimental Programme, Analysis and Results," *Proceedings of the Conference Geosynthetics '93*, Vancouver, pp. 21-34.

Federal Highway Administration, *"Instrumentation for Flexible Pavements"*, August 1989, Publication No. FHWA-RD-89-084.

Giroud, J. P. and Noiray, L. 1981, "Geotextile Reinforced Unpaved Road Design" *Journal of the Geotechnical Engineering Division*, ASCE, Vol. 107, No GT9, pp. 1233-1254.

Haas R., Wall, J., and Carroll, R.G., 1988, "Geogrid Reinforcement of Granular Bases in Flexible Pavements," In *Transportation Research Record 1188*, TRB, National Research Council, Washington DC, USA, pp. 19 - 27.

Halliday, A.R. and Potter, J.F., 1984, *"The Performance of a Flexible Pavement Constructed on a Strong Fabric"*, Transport and Road Research Laboratory, Report 1123, Crowthorne, Berkshire, 15 p.

Hayden, S.A. and Dunn, P.A. Jr., 1996, "The Use of Geosynthetics with Reinforcement, Separation and Drainage Applications For Highway Reconstruction Along a 1.9 Mile Portion of Route 1A in the Towns of Frankfort and Winterport", A Proposal Submitted to the Maine Department of Transportation, 15 p.

Hibbitt, Karlsson, and Sorenson, Inc. *ABAQUS Finite Element Program*, 1998.

Highway Research Board, 1962, *'The AASHO Road Test, Report 2: Materials and Construction"*. National Academy of Sciences, Washington D.C.

Highway Research Board, 1962, *'The AASHO Road Test, Report 7: Summary Report. National Academy of Sciences"*, Washington D.C.

Highway Research Board, 1962, *'The AASHO Road Test: History and Description of Project"*. National Academy of Sciences, Washington D.C.

Holtz, R.D., Christopher, B. R. and Berg, R.R., 1995, "Geosynthetic Design and Construction Guidelines", U.S. Department of Transportation, Federal Highway Administration, FHWA-A-HI-95, National Highway Institute Course No. 13213, Washington DC, USA, 396p.

Holtz, R.D., Christopher, B.R., and Berg, R.R., "Geosynthetic Design and Construction Guidelines" FHWA Publication No. HI-95-038. May 1995. 395 p.

Houlsby, G.T. and Jewell, R.A., 1990, "Design of Reinforced Unpaved Roads for small Rut Depths" *Proceedings of the 4th International Conference on Geotextiles, Geomembranes and Related Products*, Vol. 1, pp. 171-176.

Huang, Y.H., 1993, *Pavement Analysis and Design*, Prentice Hall, Englewood Cliffs, New Jersey, USA, 805 p.

Jewell, R.A., Soil Reinforcement with Geotextiles. *Construction Industry Research and Information Association Special Publication 123*. 1996. London. 332 p.

Jones, C.J., *Earth Reinforcement and Soil Structures*, 1996: American Society of Civil Engineers, New York. 379p.

Kennepohl, G., 1993, "New Initiative-Geogrid Pavement Reinforcement", R & D Reports, Ontario Ministry of Transportation, Vol. 5, No. 2, pg. 2.

Kennepohl, G., Kamel, N., Walls, J. and Haas, R., 1985, "Geogrid Reinforcement of Flexible Pavements: Design Basis and Field Trials", *Proceedings of the Association of Asphalt Paving Technologists*, San Antonio, Texas, February, Vol. 54, pp.45-70.

Kinney, T.C., Stone, D.K., and Schuler, J., "Using Geogrids for Base Reinforcement as Measured by a Falling Weight Deflectometer in a Full-Scale Laboratory Study", Preprint Paper 981471. *Transportation Research Board 77th Annual Meeting*, January 1998, Washington, D.C.

Koerner, R.M., *Designing with Geosynthetics.* Prentice Hall New Jersey, 1994 3rd Edition, 783 p.

Li, Dingqing., Selig, E.T., "Cumulative Plastic Deformation for Fine-Grained Subgrade Soils", *ASCE Journal of Geotechnical Engineering,* December, 1996 pp. 1006-1013 Vol. 122, No. 12.

Liu, X., Scarpas, A. Blaauwendraad, J., and Genske, D.D., "Geogrid Reinforcing of Recycled Aggregate Materials for Road Construction: A Finite Element Investigation", Preprint Paper 981343. *Transportation Research Board 77th Annual Meeting*, January 1998, Washington, D.C.

Miura, N., Sakai, A., Taesiri, Y., Yamanouchi, T. and Yasuhara, K., 1990, "Polymer Grid Reinforced Pavement on Soft Clay Grounds", *Geotextiles and Geomembranes*, Vol. 9, pp. 99-123.

Moghaddas-Nejad, F. and Small, J.C., 1996, "Effect of Geogrid Reinforcement in Model Track Tests on Pavements", *Journal of Transportation Engineering*, ASCE, Vol. 122, No. 6, pp. 468-474.

Monismith, C.L., Ogawa, N., and Freeme, C.R. "Permanent Deformation Characteristics of Subgrade Soils Due to Repeated Loading." *Transportation Research Record,* No. 537, Transportation Research Board, Washington, D.C., 1975, pp. 1-17.

Montanelli, F., Zhao, A. and Rimoldi, P., 1997, "Geosynthetic-Reinforced Pavement System: Testing and Design", *Proceedings of the Conference Geosynthetics '97*, Long Beach, California, U.S.A., Vol. 2, pp. 619-632.

Office of Minnestota Road Research (Mn Road), *"User Guide to the Dynamic Cone Penetrometer"*, Minnesota Department of Transportation, 1993.

Oglesby, J.W., Mahmoodzadegan, B., and Griffin, P.M. "Evaluation of Methods and Materials Used to Attach Strain Gages to Polymer Grids for High Strain Conditions", Louisiana Transportation Research Center FHWA/LA-92/265 December, 1992, 54 p.

Penner, R., 1985, *Geogrid Reinforcement of the Granular Base Layer in Conventional Three-Layer Pavement Sections*, M.S. Thesis, University of Waterloo, August, 130p.

Penner, R., Haas, R., Walls, J. and Kennepohl, G., 1985, "Geogrid Reinforcement of Granular Bases", Paper Presented at the *Roads and Transportation Association of Canada Annual Conference*, Vancouver, Canada, September.

Perkins, K.E., and Brandon, T.L., "Performance of Soil-Geotextile Systems in Dynamic Loading Tests", Preprint Paper 980992. *Transportation Research Board 77th Annual Meeting*, January 1998, Washington, D.C.

Perkins, S.W. and Ismeik, M., 1997, "A Synthesis and Evaluation of Geosynthetic Reinforced Base Layers in Flexible Pavements: Part I", *Geosynthetics International*, Vol. 4, No. 6, pp. 549-604.

Perkins, S.W. and Ismeik, M., 1997, "A Synthesis and Evaluation of Geosynthetic Reinforced Base Layers in Flexible Pavements: Part II", *Geosynthetics International*, Vol. 4, pp. 549-604

Perkins, S.W., Ismeik, M., and Fogelsong, M.L., "Mechanical Response of a Geosynthetic-Reinforced Pavement System to Cyclic Loading" In *Proceedings of the Fifth International Conference on the Bearing Capacity of Roads and Airfields*, Norwegian University of Science and Technology Trondheim, Norway, July 1998, pp. 1503-1512.

Perkins, S.W., Ismeik, M., Fogelsong, M.L., Wang, Y. and Cuelho, E.V., 1998, "Geosynthetic-Reinforced Pavements: Overview and Preliminary Results", In *The Sixth International Conference on Geosynthetics*, March, Atlanta, Georgia, U.S.A.

Pidwerbesky, B.D., "Strain Response and Performance of Subgrades and Flexible Pavements Under Various Loading Conditions", in *Transportation Research Board Record 1482*, pp 87-93., 1995.

Ruddock, E.C., Potter, J.F. and McAvoy, A.R., 1982, "A Full-Scale Experiment on Granular and Bituminous Road Pavements Laid on Fabrics", *Proceedings of the Second International Conference on Geotextiles*, Las Vegas, Nevada, USA, Vol.2, pp. 365-370.

Sellmeijer, J.B., 1990, "Design of Geotextile Reinforced Paved Roads and Parking Areas", *Proceedings of the Conference Geotextiles, Geomembranes and Related Products*, Balkema, Rotterdam, pp.177-182.

Shahu, J.T., Yudhbir, and Rao, N.S., Discussion of "Cumulative Plastic Deformation for Fine-Grained Subgrade Soils", *ASCE Journal of Geotechnical Engineering*, November, 1998, pp. 1153-1154.

Smith, T.E., Brandon, T.L., Al-Qadi, I.L., Lacina, B.A., Bhutta, S.A. and Hoffman, S.E., 1995, *Laboratory Behavior of Geogrid and Geotextile Reinforced Flexible Pavements*, Final Report Submitted to Atlantic Construction Fabrics, Inc. Amoco Fibers and Fabrics Company and the Virginia Center for Innovative Technology, February, Virginia Polytechnic Institute and State University, Department of Civil Engineering, Blacksburg, Virginia, USA, 94p.

Steward, J.E., Williamson, R. and Mohney, J., 1977, "Guidelines for use of Fabrics in Construction and Maintenance of Low-Volume Roads", USDA, Forest Service report PB-276 972, Portland, Oregon, 172p.

Van Til, C.J., McCullough, B.F., Vallerga, B.A., and Hicks, R.G., "Evaluation of AASHO Interim Guides for Design of Pavement Structures", *National Cooperative Highway Research Program Report 128*. Highway Research Board, 1972.

Wathugala, G.W. and Desai, C.S., 1993, "Constitutive Model for Cyclic Behavior of Clay I: Theory", *Journal of Geotechnical Engineering*, ASCE, Bol. 119, No. 4, pp.714-729.

Wathugala, G.W., Huang, B. and Pal, S., 1996, "Numerical Simulation of Geosynthetic Reinforced Flexible Pavement", In *Transportation Research Record 1534*, TRB, National Research Council, Washington, DC, USA, pp. 58-65.

Webster, S. L., 1993, *"Geogrid Reinforced Base Courses For Flexible Pavements For Light Aircraft, Test Section Construction, Behavior Under Traffic, Laboratory Tests, and Design Criteria"*, Technical Report GL-93-6, USAE Waterways Experiment Station, Vicksburg, Mississippi, USA, 86 p.

APPENDIX A

INSTRUMENT LOCATION TABLES

Table A1. Sensor locations for test section SSS1.

Sensor	Name	Pavement Layer	Orientation	Actual Location (mm)		
				x	y	z
Load Cell	LC	Surface	Vertical	0	0	0
Surface Deform. (LVDT)	SD1	Surface	Vertical	400	0	0
	SD2	Surface	Vertical	270	0	0
	SD3	Surface	Vertical	170	0	0
	SD4	Surface	Vertical	50	0	0
	SD5	Surface	Vertical	-50	0	0
	SD6	Surface	Vertical	-170	0	0
	SD7	Surface	Vertical	-270	0	0
	SD8	Surface	Vertical	-400	0	0
Stress Cell	SC1	Base	Vertical	0	0	175
	SC2	Base	Vertical	148	145	175
	SC3	Base	Vertical	284	285	175
	SC4	Base	Radial	-157	5	161
	SC5	Base	Radial	315	0	158
	SC6	Base	Radial	-300	7	158
	SC7	Base	Radial	280	-283	158
	SC8	Base	Radial	610	20	158
	SC9	Base	Tangential	-71	70	158
	SC10	Base	Tangential	140	-143	167
	SC11	Base	Tangential	289	289	158
	SC12	Subgrade - 1	Vertical	3	0	350
	SC13	Subgrade - 1	Vertical	145	147	350
	SC14	Subgrade - 1	Vertical	-425	-430	350
	SC15	Subgrade - 1	Radial	-210	4	350
	SC16	Subgrade - 1	Radial	453	5	350
	SC17	Subgrade - 1	Tangential	0	147	350
	SC18	Subgrade - 1	Tangential	295	-5	350
	SC19	Subgrade - 2	Vertical	0	0	575
	SC20	Subgrade - 2	Vertical	210	210	581
	SC21	Subgrade - 2	Vertical	-566	-566	575
	SC22	Subgrade - 2	Radial	-340	0	578
	SC23	Subgrade - 2	Tangential	0	210	578
	SC24	Subgrade - 3	Vertical	0	-15	825
	SC25	Subgrade - 4	Vertical	0	0	1075
AC Strain Gages	AC1	AC	Horizontal	0	0	67
	AC2	AC	Radial	152	0	67
	AC3	AC	Tangential	0	150	67
	AC4	AC	Tangential	-300	0	67

Table A1. Continued.

Soil Strain (LVDT)	SS1	Base	Vertical	-45	-45	161
	SS2	Base	Vertical	-143	-141	160
	SS3	Base	Vertical	0	400	160
	SS4	Base	Radial	0	-160	215
	SS6	Base	Radial	-212	-212	215
	SS7	Base	Radial	0	-410	215
	SS8	Base	Radial	-600	0	215
	SS9	Base	Tangential	74	74	215
	SS10	Base	Tangential	200	0	215
	SS11	Base	Tangential	-281	-284	215
	SS12	Subgrade - 1	Vertical	-50	-50	350
	SS13	Subgrade - 1	Vertical	-145	-141	354
	SS14	Subgrade - 1	Vertical	415	430	351
	SS15	Subgrade - 1	Radial	0	-212	310
	SS16	Subgrade - 1	Radial	0	-450	310
	SS17	Subgrade - 1	Tangential	150	0	307
	SS18	Subgrade - 1	Tangential	0	300	311
	SS19	Subgrade - 2	Vertical	-36	-48	562
	SS20	Subgrade - 2	Vertical	-209	-210	568
	SS21	Subgrade - 2	Vertical	543	553	574
	SS22	Subgrade - 2	Radial	0	-350	574
	SS24	Subgrade - 3	Vertical	-50	-50	825
	SS25	Subgrade - 4	Vertical	-45	-45	1075
TDR Probes	MC1	Subgrade 2-3	Radial	0	-550	670
	MC2	Subgrade 3-4	Radial	0	550	920
Temp. Probes	TP1	Base	NA	300	560	190
	TP2	Base	NA	300	-100	190
	TP3	Base	NA	-150	-400	190
	TP4	Base	NA	-210	100	190
	TP5	Subgrade 1-2	NA	300	100	425
	TP6	Subgrade 1-2	NA	70	-70	425
	TP7	Subgrade 1-2	NA	-200	-400	425
	TP8	Subgrade 1-2	NA	-150	150	425
	TP9	Subgrade-3	NA	-70	50	825
	TP10	Subgrade-4	NA	-70	50	1075

Table A2. Sensor locations for test section SSS2.

Sensor	Name	Pavement Layer	Orientation	Actual Location (mm)		
				x	y	z
Load Cell	LC	Surface	Vertical	0	0	0
Surface Deform. (LVDT)	SD1	Surface	Vertical	400	0	0
	SD2	Surface	Vertical	270	0	0
	SD3	Surface	Vertical	170	0	0
	SD4	Surface	Vertical	50	0	0
	SD5	Surface	Vertical	-50	0	0
	SD6	Surface	Vertical	-170	0	0
	SD7	Surface	Vertical	-270	0	0
	SD8	Surface	Vertical	-400	0	0
Stress Cell	SC1	Base	Vertical	0	0	160
	SC2	Base	Vertical	143	148	160
	SC3	Base	Vertical	280	283	160
	SC4	Base	Radial	-152	-2	160
	SC5	Base	Radial	304	4	160
	SC6	Base	Radial	-298	0	160
	SC7	Base	Radial	285	-286	160
	SC8	Base	Radial	603	0	160
	SC9	Base	Tangential	-70	70	160
	SC10	Base	Tangential	138	-145	160
	SC11	Base	Tangential	-280	285	160
	SC12	Subgrade - 1	Vertical	0	0	350
	SC13	Subgrade - 1	Vertical	140	145	350
	SC14	Subgrade - 1	Vertical	-420	-425	350
	SC15	Subgrade - 1	Radial	-204	0	350
	SC16	Subgrade - 1	Radial	450	0	350
	SC17	Subgrade - 1	Tangential	2	153	350
	SC18	Subgrade - 1	Tangential	302	4	350
	SC19	Subgrade - 2	Vertical	0	0	575
	SC20	Subgrade - 2	Vertical	215	209	575
	SC21	Subgrade - 2	Vertical	-560	-562	575
	SC22	Subgrade - 2	Radial	-352	0	575
	SC23	Subgrade - 2	Tangential	3	205	575
	SC24	Subgrade - 3	Vertical	0	5	825
	SC25	Subgrade - 4	Vertical	0	0	1075
AC Strain Gages	AC1	AC	Horizontal	0	0	67
	AC2	AC	Radial	217	0	67
	AC3	AC	Tangential	0	150	67
	AC4	AC	Tangential	-300	0	67
Geosyn. Strain	GS1	Geogrid	Radial-M	15	0	160
	GS2	Geogrid	Radial-T	0	20	160
	GS3	Geogrid	Tangential-M	15	-117	160

Table A2. Continued.

Geosyn. Strain	GS4	Geogrid	Radial-M	133	0	160
	GS5	Geogrid	Tangential-T	-117	20	160
	GS6	Geogrid	Radial-T	0	137	160
	GS7	Geogrid	Radial-M	-217	0	160
	GS8	Geogrid	Tangential-T	207	-20	160
	GS9	Geogrid	Tangential-M	-15	313	160
	GS10	Geogrid	Radial-T	0	-330	160
	GS11	Geogrid	Tangential-T	-622	20	160
	GS12	Geogrid	Radial-M	620	0	160
Soil Strain (LVDT)	SS1	Base	Vertical	-45	-45	160
	SS2	Base	Vertical	-146	-142	160
	SS3	Base	Vertical	0	400	160
	SS4	Base	Radial	0	-162	215
	SS5	Base	Radial	-2	303	215
	SS6	Base	Radial	-212	-212	215
	SS7	Base	Radial	0	-405	215
	SS8	Base	Radial	-595	0	215
	SS9	Base	Tangential	73	74	215
	SS10	Base	Tangential	204	0	215
	SS11	Base	Tangential	-283	-284	215
	SS12	Subgrade - 1	Vertical	-45	-45	350
	SS13	Subgrade - 1	Vertical	-142	-144	350
	SS14	Subgrade - 1	Vertical	420	425	350
	SS15	Subgrade - 1	Radial	0	-200	315
	SS16	Subgrade - 1	Radial	0	-453	315
	SS17	Subgrade - 1	Tangential	150	2	315
	SS18	Subgrade - 1	Tangential	0	302	315
	SS19	Subgrade - 2	Vertical	-45	-45	575
	SS20	Subgrade - 2	Vertical	-212	-213	575
	SS21	Subgrade - 2	Vertical	560	562	575
	SS22	Subgrade - 2	Radial	0	-350	575
	SS23	Subgrade - 2	Tangential	202	2	575
	SS25	Subgrade - 3	Vertical	-45	-45	825
	SS24	Subgrade - 4	Vertical	-45	-45	1075
TDR Probes	MC1	Subgrade 2-3	Radial	0	-550	670
	MC2	Subgrade 3-4	Radial	0	550	920
Temp. Probes	TP1	Base	NA	300	560	190
	TP2	Base	NA	300	-100	190
	TP3	Base	NA	-150	-400	190
	TP4	Base	NA	-210	100	190
	TP5	Subgrade 1-2	NA	300	100	425
	TP6	Subgrade 1-2	NA	70	-70	425
	TP7	Subgrade 1-2	NA	-200	-400	425
	TP8	Subgrade 1-2	NA	-150	150	425
	TP9	Subgrade-3	NA	-70	50	825
	TP10	Subgrade-4	NA	-70	50	1075

Table A3. Sensor locations for test section SSS3.

Sensor	Name	Pavement Layer	Orientation	Actual Location (mm)		
				x	y	z
Load Cell	LC	Surface	Vertical	0	0	0
Surface Deform. (LVDT)	SD1	Surface	Vertical	400	0	0
	SD2	Surface	Vertical	270	0	0
	SD3	Surface	Vertical	170	0	0
	SD4	Surface	Vertical	50	0	0
	SD5	Surface	Vertical	-50	0	0
	SD6	Surface	Vertical	-170	0	0
	SD7	Surface	Vertical	-270	0	0
	SD8	Surface	Vertical	-400	0	0
Stress Cell	SC1	Base	Vertical	0	0	160
	SC2	Base	Vertical	142	143	160
	SC3	Base	Vertical	283	283	160
	SC4	Base	Radial	-154	0	160
	SC5	Base	Radial	305	-2	160
	SC6	Base	Radial	-300	4	160
	SC7	Base	Radial	280	-281	160
	SC8	Base	Radial	605	0	160
	SC9	Base	Tangential	-71	70	160
	SC10	Base	Tangential	141	-145	160
	SC11	Base	Tangential	-284	285	160
	SC12	Subgrade - 1	Vertical	0	0	350
	SC13	Subgrade - 1	Vertical	142	140	350
	SC14	Subgrade - 1	Vertical	-427	-422	350
	SC15	Subgrade - 1	Radial	-205	-3	350
	SC16	Subgrade - 1	Radial	450	2	350
	SC17	Subgrade - 1	Tangential	0	150	350
	SC18	Subgrade - 1	Tangential	300	5	350
	SC19	Subgrade - 2	Vertical	0	2	575
	SC20	Subgrade - 2	Vertical	212	210	575
	SC21	Subgrade - 2	Vertical	-566	-566	575
	SC22	Subgrade - 2	Radial	-346	3	575
	SC23	Subgrade - 2	Tangential	0	205	575
	SC24	Subgrade - 3	Vertical	0	5	825
	SC25	Subgrade - 4	Vertical	0	0	1075
AC Strain Gages	AC1	AC	Horizontal	0	0	67
	AC2	AC	Radial	217	0	67
	AC3	AC	Tangential	0	150	67
	AC4	AC	Tangential	-300	0	67
Geosyn. Strain	GS1	Geotextile	Radial-M	-65	0	160
	GS2	Geotextile	Radial-T	0	-65	160
	GS3	Geotextile	Tangential-M	0	-200	160

Table A3. Continued.

Geosyn Strain	GS4	Geotextile	Radial-M	135	0	160
	GS5	Geotextile	Tangential-T	-200	0	160
	GS6	Geotextile	Radial-T	0	135	160
	GS7	Geotextile	Radial-M	-300	0	160
	GS8	Geotextile	Tangential-T	270	0	160
	GS9	Geotextile	Tangential-M	0	315	160
	GS10	Geotextile	Radial-T	0	-330	160
	GS11	Geotextile	Tangential-T	-620	0	160
	GS12	Geotextile	Radial-M	620	0	160
Soil Strain (LVDT)	SS1	Base	Vertical	-45	-45	160
	SS2	Base	Vertical	-140	-143	160
	SS3	Base	Vertical	-2	398	160
	SS4	Base	Radial	0	-154	215
	SS5	Base	Radial	1	297	215
	SS6	Base	Radial	-212	-214	215
	SS7	Base	Radial	3	-402	215
	SS8	Base	Radial	-603	2	215
	SS9	Base	Tangential	70	73	215
	SS10	Base	Tangential	200	0	215
	SS11	Base	Tangential	-286	-280	215
	SS12	Subgrade - 1	Vertical	-45	-45	350
	SS13	Subgrade - 1	Vertical	-143	-140	350
	SS14	Subgrade - 1	Vertical	423	428	350
	SS15	Subgrade - 1	Radial	0	-202	315
	SS5	Subgrade - 1	Radial	3	-454	315
	SS17	Subgrade - 1	Tangential	147	0	315
	SS18	Subgrade - 1	Tangential	5	303	315
	SS19	Subgrade - 2	Vertical	-45	-45	575
	SS20	Subgrade - 2	Vertical	-210	-209	575
	SS21	Subgrade - 2	Vertical	560	560	575
	SS22	Subgrade - 2	Radial	0	-345	575
	SS16	Subgrade - 3	Vertical	-45	-45	825
	SS25	Subgrade - 4	Vertical	-45	-45	1075
TDR Probes	MC1	Subgrade 2-3	Radial	0	-550	670
	MC2	Subgrade 3-4	Radial	0	550	920
Temp. Probes	TP1	Base	NA	300	560	190
	TP2	Base	NA	300	-100	190
	TP3	Base	NA	-150	-400	190
	TP4	Base	NA	-210	100	190
	TP5	Subgrade 1-2	NA	300	100	425
	TP6	Subgrade 1-2	NA	70	-70	425
	TP7	Subgrade 1-2	NA	-200	-400	425
	TP8	Subgrade 1-2	NA	-150	150	425
	TP9	Subgrade-3	NA	-70	50	825
	TP10	Subgrade-4	NA	-70	50	1075

Table A4. Sensor locations for test section SSS4.

Sensor	Name	Pavement Layer	Orientation	Actual Location (mm)		
				x	y	z
Load Cell	LC	Surface	Vertical	0	0	0
Surface Deform. (LVDT)	SD1	Surface	Vertical	400	0	0
	SD2	Surface	Vertical	270	0	0
	SD3	Surface	Vertical	170	0	0
	SD4	Surface	Vertical	50	0	0
	SD5	Surface	Vertical	-50	0	0
	SD6	Surface	Vertical	-170	0	0
	SD7	Surface	Vertical	-270	0	0
	SD8	Surface	Vertical	-400	0	0
Stress Cell	SC1	Base	Vertical	0	0	160
	SC2	Base	Vertical	107	107	160
	SC3	Base	Vertical	210	212	160
	SC4	Base	Radial	0	-103	160
	SC5	Base	Radial	-197	0	160
	SC6	Base	Radial	298	0	160
	SC7	Base	Radial	282	-282	160
	SC8	Base	Radial	604	0	160
	SC9	Base	Tangential	-70	70	160
	SC10	Base	Tangential	-140	-142	160
	SC11	Base	Tangential	-280	282	160
	SC12	Subgrade - 1	Vertical	0	0	350
	SC13	Subgrade - 1	Vertical	143	140	350
	SC14	Subgrade - 1	Vertical	-280	-284	350
	SC15	Subgrade - 1	Radial	-145	2	350
	SC16	Subgrade - 1	Radial	0	-298	350
	SC17	Subgrade - 1	Radial	451	-2	350
	SC18	Subgrade - 1	Tangential	-3	152	350
	SC19	Subgrade - 2	Tangential	297	0	575
	SC20	Subgrade - 2	Vertical	0	0	575
	SC21	Subgrade - 2	Vertical	210	215	575
	SC22	Subgrade - 2	Radial	-348	3	575
	SC23	Subgrade - 2	Tangential	2	202	575
	SC24	Subgrade - 3	Vertical	0	0	825
	SC25	Subgrade - 4	Vertical	0	0	1075
AC Strain Gages	AC1	AC	Center	0	0	67
	AC2	AC	Radial	219	0	67
	AC3	AC	Tangential	0	152	67
	AC4	AC	Tangential	-300	0	67

Table A4. Continued.

Soil Strain (LVDT)	SS1	Base	Vertical	-45	-45	160
	SS2	Base	Vertical	-109	-110	160
	SS3	Base	Vertical	0	-300	160
	SS4	Base	Radial	70	-72	215
	SS5	Base	Radial	0	203	215
	SS6	Base	Radial	-210	-210	215
	SS7	Base	Radial	0	-404	215
	SS8	Base	Radial	-604	0	215
	SS9	Base	Tangential	70	72	215
	SS10	Base	Tangential	203	0	215
	SS11	Base	Tangential	-280	-279	215
	SS12	Subgrade - 1	Vertical	-45	-45	350
	SS13	Subgrade - 1	Vertical	-140	-141	350
	SS14	Subgrade - 1	Vertical	280	282	350
	SS15	Subgrade - 1	Radial	-4	-148	315
	SS16	Subgrade - 1	Radial	-298	5	315
	SS17	Subgrade - 1	Radial	-3	-454	315
	SS18	Subgrade - 1	Tangential	152	0	315
	SS19	Subgrade - 2	Tangential	0	304	575
	SS20	Subgrade - 2	Vertical	-45	-45	575
	SS21	Subgrade - 2	Vertical	-210	-213	575
	SS22	Subgrade - 2	Radial	-3	-350	575
	SS23	Subgrade - 2	Tangential	201	-2	575
	SS24	Subgrade - 3	Vertical	-45	-45	825
	SS25	Subgrade - 4	Vertical	-45	-45	1075
TDR Probes	MC1	Subgrade 2-3	Radial	0	-550	675
	MC2	Subgrade 3-4	Radial	0	550	925
Temp. Probes	TP1	Base	NA	180	350	190
	TP2	Base	NA	210	-300	190
	TP3	Base	NA	-150	-420	190
	TP4	Base	NA	-350	220	190
	TP5	Subgrade 1-2	NA	300	100	425
	TP6	Subgrade 1-2	NA	70	-70	425
	TP7	Subgrade 1-2	NA	-200	-400	425
	TP8	Subgrade 1-2	NA	-150	150	425
	TP9	Subgrade-3	NA	-70	50	825
	TP10	Subgrade-4	NA	-70	50	1075

Table A5. Sensor locations for test section SSS5.

Sensor	Name	Pavement Layer	Orientation	Actual Location (mm)		
				x	y	z
Load Cell	LC	Surface	Vertical	0	0	0
Surface Deform. (LVDT)	SD1	Surface	Vertical	400	0	0
	SD2	Surface	Vertical	270	0	0
	SD3	Surface	Vertical	170	0	0
	SD4	Surface	Vertical	50	0	0
	SD5	Surface	Vertical	-50	0	0
	SD6	Surface	Vertical	-170	0	0
	SD7	Surface	Vertical	-270	0	0
	SD8	Surface	Vertical	-400	0	0
Stress Cell	SC1	Base	Vertical	0	0	160
	SC2	Base	Vertical	106	110	160
	SC3	Base	Vertical	212	210	160
	SC4	Base	Radial	0	-98	160
	SC5	Base	Radial	-202	3	160
	SC6	Base	Radial	297	4	160
	SC7	Base	Radial	281	-280	160
	SC8	Base	Radial	599	0	160
	SC9	Base	Tangential	-72	72	160
	SC10	Base	Tangential	-139	-140	160
	SC11	Base	Tangential	-282	279	160
	SC12	Subgrade - 1	Vertical	0	0	350
	SC13	Subgrade - 1	Vertical	143	140	350
	SC14	Subgrade - 1	Vertical	-280	-284	350
	SC15	Subgrade - 1	Radial	-145	2	350
	SC16	Subgrade - 1	Radial	0	-298	350
	SC17	Subgrade - 1	Radial	451	-2	350
	SC18	Subgrade - 1	Tangential	-3	152	350
	SC19	Subgrade - 2	Tangential	297	0	575
	SC20	Subgrade - 2	Vertical	0	0	575
	SC21	Subgrade - 2	Vertical	210	215	575
	SC22	Subgrade - 2	Radial	-348	3	575
	SC23	Subgrade - 2	Tangential	2	202	575
	SC24	Subgrade - 3	Vertical	0	0	825
	SC25	Subgrade - 4	Vertical	0	0	1075
AC Strain Gages	AC1	AC	Center	0	0	67
	AC2	N/A				
	AC3	N/A				
Geosyn. Strain	GS1	Geogrid	Radial-M	15	0	275
	GS2	Geogrid	Radial-T	0	-20	275
	GS3	Geogrid	Tangential-M	15	-117	275
	GS4	Geogrid	Radial-M	127	0	275

Table A5. Continued.

Geosyn. Strain	GS5	Geogrid	Tangential-T	-111	22	275
	GS6	Geogrid	Radial-T	0	135	275
	GS7	Geogrid	Radial-M	-215	0	275
	GS8	Geogrid	Tangential-T	197	-20	275
	GS9	Geogrid	Tangential-M	-15	305	275
	GS10	Geogrid	Radial-T	0	-330	275
	GS11	Geogrid	Tangential-T	-613	20	275
	GS12	Geogrid	Radial-M	597	0	275
Soil Strain (LVDT)	SS1	Base	Vertical	-45	-45	160
	SS2	Base	Vertical	-107	-106	160
	SS3	Base	Vertical	0	-298	160
	SS4	Base	Radial	73	-75	215
	SS5	Base	Radial	0	206	215
	SS6	Base	Radial	-209	-210	215
	SS7	Base	Radial	0	-400	215
	SS8	Base	Radial	-600	3	215
	SS9	Base	Tangential	73	74	215
	SS10	Base	Tangential	201	-3	215
	SS11	Base	Tangential	-283	-284	215
	SS12	Subgrade - 1	Vertical	-45	-45	350
	SS13	Subgrade - 1	Vertical	-140	-141	350
	SS14	Subgrade - 1	Vertical	280	282	350
	SS15	Subgrade - 1	Radial	-4	-148	315
	SS16	Subgrade - 1	Radial	-298	5	315
	SS17	Subgrade - 1	Radial	-3	-454	315
	SS18	Subgrade - 1	Tangential	152	0	315
	SS19	Subgrade - 2	Tangential	0	304	575
	SS20	Subgrade - 2	Vertical	-45	-45	575
	SS21	Subgrade - 2	Vertical	-210	-213	575
	SS22	Subgrade - 2	Radial	-3	-350	575
	SS23	Subgrade - 2	Tangential	201	-2	575
	SS24	Subgrade - 3	Vertical	-45	-45	825
	SS25	Subgrade - 4	Vertical	-45	-45	1075
TDR Probes	MC1	Subgrade 2-3	Radial	0	-550	675
	MC2	Subgrade 3-4	Radial	0	550	925
Temp. Probes	TP1	Base	NA	180	350	190
	TP2	Base	NA	210	-300	190
	TP3	Base	NA	-150	-420	190
	TP4	Base	NA	-350	220	190
	TP5	Subgrade 1-2	NA	300	100	425
	TP6	Subgrade 1-2	NA	70	-70	425
	TP7	Subgrade 1-2	NA	-200	-400	425
	TP8	Subgrade 1-2	NA	-150	150	425
	TP9	Subgrade-3	NA	-70	50	825
	TP10	Subgrade-4	NA	-70	50	1075

Table A6. Sensor locations for test section SSS6.

Sensor	Name	Pavement Layer	Orientation	Actual Location (mm)		
				x	y	z
Load Cell	LC	Surface	Vertical	0	0	0
Surface Deform. (LVDT)	SD1	Surface	Vertical	400	0	0
	SD2	Surface	Vertical	270	0	0
	SD3	Surface	Vertical	170	0	0
	SD4	Surface	Vertical	50	0	0
	SD5	Surface	Vertical	-50	0	0
	SD6	Surface	Vertical	-170	0	0
	SD7	Surface	Vertical	-270	0	0
	SD8	Surface	Vertical	-400	0	0
Stress Cell	SC1	Base	Vertical	0	0	160
	SC2	Base	Vertical	105	105	160
	SC3	Base	Vertical	209	210	160
	SC4	Base	Radial	0	-100	160
	SC5	Base	Radial	-200	2	160
	SC6	Base	Radial	300	0	160
	SC7	Base	Radial	280	-280	160
	SC8	Base	Radial	602	0	160
	SC9	Base	Tangential	-68	68	160
	SC10	Base	Tangential	-137	-140	160
	SC11	Base	Tangential	-279	280	160
	SC12	Subgrade - 1	Vertical	0	0	350
	SC13	Subgrade - 1	Vertical	143	140	350
	SC14	Subgrade - 1	Vertical	-280	-284	350
	SC15	Subgrade - 1	Radial	-145	2	350
	SC16	Subgrade - 1	Radial	0	-298	350
	SC17	Subgrade - 1	Radial	451	-2	350
	SC18	Subgrade - 1	Tangential	-3	152	350
	SC19	Subgrade - 2	Tangential	297	0	575
	SC20	Subgrade - 2	Vertical	0	0	575
	SC21	Subgrade - 2	Vertical	210	215	575
	SC22	Subgrade - 2	Radial	-348	3	575
	SC23	Subgrade - 2	Tangential	2	202	575
	SC24	Subgrade - 3	Vertical	0	0	825
	SC25	Subgrade - 4	Vertical	0	0	1075
AC Strain Gages	AC1	AC	Center	0	0	67
	AC2	AC	Radial	219	0	67
	AC3	AC	Tangential	0	152	67
	AC4	AC	Tangential	-300	0	67

Table A6. Continued.

Soil Strain (LVDT)	SS1	Base	Vertical	-45	-45	160
	SS2	Base	Vertical	-105	-107	160
	SS3	Base	Vertical	3	-306	160
	SS4	Base	Radial	69	-72	215
	SS5	Base	Radial	0	198	215
	SS6	Base	Radial	-207	-209	215
	SS7	Base	Radial	4	-400	215
	SS8	Base	Radial	-600	0	215
	SS9	Base	Tangential	69	70	215
	SS10	Base	Tangential	199	3	215
	SS11	Base	Tangential	-280	-280	215
	SS12	Subgrade - 1	Vertical	-45	-45	350
	SS13	Subgrade - 1	Vertical	-140	-141	350
	SS14	Subgrade - 1	Vertical	280	282	350
	SS15	Subgrade - 1	Radial	-4	-148	315
	SS16	Subgrade - 1	Radial	-298	5	315
	SS17	Subgrade - 1	Radial	-3	-454	315
	SS18	Subgrade - 1	Tangential	152	0	315
	SS19	Subgrade - 2	Tangential	0	304	575
	SS20	Subgrade - 2	Vertical	-45	-45	575
	SS21	Subgrade - 2	Vertical	-210	-213	575
	SS22	Subgrade - 2	Radial	-3	-350	575
	SS23	Subgrade - 2	Tangential	201	-2	575
	SS24	Subgrade - 3	Vertical	-45	-45	825
	SS25	Subgrade - 4	Vertical	-45	-45	1075
TDR Probes	MC1	Subgrade 2-3	Radial	0	-550	675
	MC2	Subgrade 3-4	Radial	0	550	925
Temp. Probes	TP1	Base	NA	180	350	190
	TP2	Base	NA	210	-300	190
	TP3	Base	NA	-150	-420	190
	TP4	Base	NA	-350	220	190
	TP5	Subgrade 1-2	NA	300	100	425
	TP6	Subgrade 1-2	NA	70	-70	425
	TP7	Subgrade 1-2	NA	-200	-400	425
	TP8	Subgrade 1-2	NA	-150	150	425
	TP9	Subgrade-3	NA	-70	50	825
	TP10	Subgrade-4	NA	-70	50	1075

Table A7. Sensor locations for test section SSS7.

Sensor	Name	Pavement Layer	Orientation	Actual Location (mm)		
				x	y	z
Load Cell	LC	Surface	Vertical	0	0	0
Surface Deform. (LVDT)	SD1	Surface	Vertical	400	0	0
	SD2	Surface	Vertical	270	0	0
	SD3	Surface	Vertical	170	0	0
	SD4	Surface	Vertical	50	0	0
	SD5	Surface	Vertical	-50	0	0
	SD6	Surface	Vertical	-170	0	0
	SD7	Surface	Vertical	-270	0	0
	SD8	Surface	Vertical	-400	0	0
Stress Cell	SC1	Base	Vertical	0	0	160
	SC2	Base	Vertical	103	106	160
	SC3	Base	Vertical	212	210	160
	SC4	Base	Radial	0	-102	160
	SC5	Base	Radial	-204	0	160
	SC6	Base	Radial	297	0	160
	SC7	Base	Radial	284	-285	160
	SC8	Base	Radial	605	0	160
	SC9	Base	Tangential	-70	70	160
	SC10	Base	Tangential	-140	-140	160
	SC11	Base	Tangential	-280	280	160
	SC12	Subgrade - 1	Vertical	0	0	350
	SC13	Subgrade - 1	Vertical	143	140	350
	SC14	Subgrade - 1	Vertical	-280	-284	350
	SC15	Subgrade - 1	Radial	-145	2	350
	SC16	Subgrade - 1	Radial	0	-298	350
	SC17	Subgrade - 1	Radial	451	-2	350
	SC18	Subgrade - 1	Tangential	-3	152	350
	SC19	Subgrade - 2	Tangential	297	0	575
	SC20	Subgrade - 2	Vertical	0	0	575
	SC21	Subgrade - 2	Vertical	210	215	575
	SC22	Subgrade - 2	Radial	-348	3	575
	SC23	Subgrade - 2	Tangential	2	202	575
	SC24	Subgrade - 3	Vertical	0	0	825
	SC25	Subgrade - 4	Vertical	0	0	1075
AC Strain Gages	AC1	AC	Center	0	0	67
	AC2	AC	Radial	219	0	67
	AC3	AC	Tangential	0	152	67
	AC4	AC	Tangential	-300	0	67

Table A7. Continued.

Soil Strain (LVDT)	SS1	Base	Vertical	-45	-45	160
	SS2	Base	Vertical	-102	-106	160
	SS3	Base	Vertical	0	-300	160
	SS4	Base	Radial	72	-70	215
	SS5	Base	Radial	0	200	215
	SS6	Base	Radial	-210	-210	215
	SS7	Base	Radial	0	-395	215
	SS8	Base	Radial	-595	0	215
	SS9	Base	Tangential	70	70	215
	SS10	Base	Tangential	204	0	215
	SS11	Base	Tangential	-278	-284	215
	SS12	Subgrade - 1	Vertical	-45	-45	350
	SS13	Subgrade - 1	Vertical	-140	-141	350
	SS14	Subgrade - 1	Vertical	280	282	350
	SS15	Subgrade - 1	Radial	-4	-148	315
	SS16	Subgrade - 1	Radial	-298	5	315
	SS17	Subgrade - 1	Radial	-3	-454	315
	SS18	Subgrade - 1	Tangential	152	0	315
	SS19	Subgrade - 2	Tangential	0	304	575
	SS20	Subgrade - 2	Vertical	-45	-45	575
	SS21	Subgrade - 2	Vertical	-210	-213	575
	SS22	Subgrade - 2	Radial	-3	-350	575
	SS23	Subgrade - 2	Tangential	201	-2	575
	SS24	Subgrade - 3	Vertical	-45	-45	825
	SS25	Subgrade - 4	Vertical	-45	-45	1075
TDR Probes	MC1	Subgrade 2-3	Radial	0	-550	675
	MC2	Subgrade 3-4	Radial	0	550	925
Temp. Probes	TP1	Base	NA	180	350	190
	TP2	Base	NA	210	-300	190
	TP3	Base	NA	-150	-420	190
	TP4	Base	NA	-350	220	190
	TP5	Subgrade 1-2	NA	300	100	425
	TP6	Subgrade 1-2	NA	70	-70	425
	TP7	Subgrade 1-2	NA	-200	-400	425
	TP8	Subgrade 1-2	NA	-150	150	425
	TP9	Subgrade-3	NA	-70	50	825
	TP10	Subgrade-4	NA	-70	50	1075

Table A8. Sensor locations for test section SSS8.

Sensor	Name	Pavement Layer	Orientation	Actual Location (mm)		
				x	y	z
Load Cell	LC	Surface	Vertical	0	0	0
Surface Deform. (LVDT)	SD1	Surface	Vertical	400	0	0
	SD2	Surface	Vertical	270	0	0
	SD3	Surface	Vertical	170	0	0
	SD4	Surface	Vertical	50	0	0
	SD5	Surface	Vertical	-50	0	0
	SD6	Surface	Vertical	-170	0	0
	SD7	Surface	Vertical	-270	0	0
	SD8	Surface	Vertical	-400	0	0
Stress Cell	SC1	Base	Vertical	0	0	160
	SC2	Base	Vertical	108	105	160
	SC3	Base	Vertical	215	215	160
	SC4	Base	Radial	0	-104	160
	SC5	Base	Radial	-198	0	160
	SC6	Base	Radial	304	0	160
	SC7	Base	Radial	284	-284	160
	SC8	Base	Radial	595	0	160
	SC9	Base	Tangential	-73	70	160
	SC10	Base	Tangential	-142	-141	160
	SC11	Base	Tangential	-285	283	160
	SC12	Subgrade - 1	Vertical	0	0	350
	SC13	Subgrade - 1	Vertical	143	140	350
	SC14	Subgrade - 1	Vertical	-280	-284	350
	SC15	Subgrade - 1	Radial	-145	2	350
	SC16	Subgrade - 1	Radial	0	-298	350
	SC17	Subgrade - 1	Radial	451	-2	350
	SC18	Subgrade - 1	Tangential	-3	152	350
	SC19	Subgrade - 2	Tangential	297	0	575
	SC20	Subgrade - 2	Vertical	0	0	575
	SC21	Subgrade - 2	Vertical	210	215	575
	SC22	Subgrade - 2	Radial	-348	3	575
	SC23	Subgrade - 2	Tangential	2	202	575
	SC24	Subgrade - 3	Vertical	0	0	825
	SC25	Subgrade - 4	Vertical	0	0	1075
AC Strain Gages	AC1	AC	Center	0	0	67
	AC2	AC	Radial	219	0	67
	AC3	AC	Tangential	0	152	67
	AC4	AC	Tangential	-300	0	67

Table A8. Continued.

Geosyn. Strain	GS1	Geotextile	Radial-M	-65	0	275
	GS2	Geotextile	Radial-T	0	-65	275
	GS3	Geotextile	Tangential-M	0	-200	275
	GS4	Geotextile	Radial-M	135	0	275
	GS6	Geotextile	Radial-T	0	135	275
	GS7	Geotextile	Radial-M	-300	0	275
	GS9	Geotextile	Tangential-M	0	315	275
	GS11	Geotextile	Tangential-T	-620	0	275
Soil Strain (LVDT)	SS1	Base	Vertical	-45	-45	160
	SS2	Base	Vertical	-108	-108	160
	SS3	Base	Vertical	0	-305	160
	SS4	Base	Radial	70	-70	215
	SS5	Base	Radial	0	200	215
	SS6	Base	Radial	-215	-212	215
	SS7	Base	Radial	2	-405	215
	SS8	Base	Radial	-605	0	215
	SS9	Base	Tangential	71	71	215
	SS10	Base	Tangential	200	0	215
	SS11	Base	Tangential	-285	-285	215
	SS12	Subgrade - 1	Vertical	-45	-45	350
	SS13	Subgrade - 1	Vertical	-140	-141	350
	SS14	Subgrade - 1	Vertical	280	282	350
	SS15	Subgrade - 1	Radial	-4	-148	315
	SS16	Subgrade - 1	Radial	-298	5	315
	SS17	Subgrade - 1	Radial	-3	-454	315
	SS18	Subgrade - 1	Tangential	152	0	315
	SS19	Subgrade - 2	Tangential	0	304	575
	SS20	Subgrade - 2	Vertical	-45	-45	575
	SS21	Subgrade - 2	Vertical	-210	-213	575
	SS22	Subgrade - 2	Radial	-3	-350	575
	SS23	Subgrade - 2	Tangential	201	-2	575
	SS24	Subgrade - 3	Vertical	-45	-45	825
	SS25	Subgrade - 4	Vertical	-45	-45	1075
TDR Probes	MC1	Subgrade 2-3	Radial	0	-550	675
	MC2	Subgrade 3-4	Radial	0	550	925
Temp. Probes	TP1	Base	NA	180	350	190
	TP2	Base	NA	210	-300	190
	TP3	Base	NA	-150	-420	190
	TP4	Base	NA	-350	220	190
	TP5	Subgrade 1-2	NA	300	100	425
	TP6	Subgrade 1-2	NA	70	-70	425
	TP7	Subgrade 1-2	NA	-200	-400	425
	TP8	Subgrade 1-2	NA	-150	150	425
	TP9	Subgrade-3	NA	-70	50	825
	TP10	Subgrade-4	NA	-70	50	1075

Table A9. Sensor locations for test section SSS9.

Sensor	Name	Pavement Layer	Orientation	Actual Location (mm)		
				x	y	z
Load Cell	LC	Surface	Vertical	0	0	0
Surface Deform. (LVDT)	SD1	Surface	Vertical	400	0	0
	SD2	Surface	Vertical	270	0	0
	SD3	Surface	Vertical	170	0	0
	SD4	Surface	Vertical	50	0	0
	SD5	Surface	Vertical	-50	0	0
	SD6	Surface	Vertical	-170	0	0
	SD7	Surface	Vertical	-270	0	0
	SD8	Surface	Vertical	-400	0	0
Stress Cell	SC1	Base	Vertical	0	0	160
	SC2	Base	Vertical	105	105	160
	SC3	Base	Vertical	210	212	160
	SC4	Base	Radial	0	-100	160
	SC5	Base	Radial	-204	0	160
	SC6	Base	Radial	300	0	160
	SC7	Base	Radial	283	-283	160
	SC8	Base	Radial	605	0	160
	SC9	Base	Tangential	-70	72	160
	SC10	Base	Tangential	-140	-140	160
	SC11	Base	Tangential	-280	284	160
	SC12	Subgrade - 1	Vertical	0	0	350
	SC13	Subgrade - 1	Vertical	143	140	350
	SC14	Subgrade - 1	Vertical	-280	-284	350
	SC15	Subgrade - 1	Radial	-145	2	350
	SC16	Subgrade - 1	Radial	0	-298	350
	SC17	Subgrade - 1	Radial	451	-2	350
	SC18	Subgrade - 1	Tangential	-3	152	350
	SC19	Subgrade - 2	Tangential	297	0	575
	SC20	Subgrade - 2	Vertical	0	0	575
	SC21	Subgrade - 2	Vertical	210	215	575
	SC22	Subgrade - 2	Radial	-348	3	575
	SC23	Subgrade - 2	Tangential	2	202	575
	SC24	Subgrade - 3	Vertical	0	0	825
	SC25	Subgrade - 4	Vertical	0	0	1075
AC Strain Gages	AC1	AC	Center	0	0	67
	AC2	AC	Radial	219	0	67
	AC3	AC	Tangential	0	152	67
	AC4	AC	Tangential	-300	0	67

Table A9. Continued.

Geosyn. Strain	GS1	Geogrid	Radial-M	15	0	275
	GS2	Geogrid	Radial-T	0	23	275
	GS3	Geogrid	Tangential-M	15	-119	275
	GS4	Geogrid	Radial-M	130	0	275
	GS5	Geogrid	Tangential-T	-113	22	275
	GS6	Geogrid	Radial-T	0	139	275
	GS7	Geogrid	Radial-M	-223	0	275
	GS8	Geogrid	Tangential-T	170	-24	275
	GS9	Geogrid	Tangential-M	-16	315	275
	GS10	Geogrid	Radial-T	0	-332	275
	GS11	Geogrid	Tangential-T	-612	23	275
	GS12	Geogrid	Radial-M	605	0	275
Soil Strain (LVDT)	SS1	Base	Vertical	-45	-45	160
	SS2	Base	Vertical	-109	-105	160
	SS3	Base	Vertical	2	-305	160
	SS4	Base	Radial	70	-70	215
	SS5	Base	Radial	0	200	215
	SS6	Base	Radial	-212	-215	215
	SS7	Base	Radial	5	-400	215
	SS8	Base	Radial	-605	0	215
	SS9	Base	Tangential	72	72	215
	SS10	Base	Tangential	200	0	215
	SS11	Base	Tangential	-280	-280	215
	SS12	Subgrade - 1	Vertical	-45	-45	350
	SS13	Subgrade - 1	Vertical	-140	-141	350
	SS14	Subgrade - 1	Vertical	280	282	350
	SS15	Subgrade - 1	Radial	-4	-148	315
	SS16	Subgrade - 1	Radial	-298	5	315
	SS17	Subgrade - 1	Radial	-3	-454	315
	SS18	Subgrade - 1	Tangential	152	0	315
	SS19	Subgrade - 2	Tangential	0	304	575
	SS20	Subgrade - 2	Vertical	-45	-45	575
	SS21	Subgrade - 2	Vertical	-210	-213	575
	SS22	Subgrade - 2	Radial	-3	-350	575
	SS23	Subgrade - 2	Tangential	201	-2	575
	SS24	Subgrade - 3	Vertical	-45	-45	825
	SS25	Subgrade - 4	Vertical	-45	-45	1075
TDR Probes	MC1	Subgrade 2-3	Radial	0	-550	675
	MC2	Subgrade 3-4	Radial	0	550	925
Temp. Probes	TP1	Base	NA	180	350	190
	TP2	Base	NA	210	-300	190
	TP3	Base	NA	-150	-420	190
	TP4	Base	NA	-350	220	190
	TP6	Subgrade 1-2	NA	70	-70	425
	TP7	Subgrade 1-2	NA	-200	-400	425
	TP8	Subgrade 1-2	NA	-150	150	425
	TP9	Subgrade-3	NA	-70	50	825
	TP10	Subgrade-4	NA	-70	50	1075

Table A10. Sensor locations for test section PCS1.

Sensor	Name	Channel Number	Pavement Layer	Orientation	Actual Location (mm)		
					x	y	z
Load Cell	LC	1	Surface	Vertical	0	0	0
Surface Deformation (LVDT)	SD1	2	Surface	Vertical	400	0	0
	SD2	3	Surface	Vertical	270	0	0
	SD3	4	Surface	Vertical	170	0	0
	SD4	5	Surface	Vertical	50	0	0
	SD5	6	Surface	Vertical	-50	0	0
	SD6	7	Surface	Vertical	-170	0	0
	SD7	8	Surface	Vertical	-270	0	0
	SD8	9	Surface	Vertical	-400	0	0
Stress Cell	SC8	17	Base -1	Radial	0	-300	225
	SC9	18	Base - 2	Tangential	600	0	300
	SC10	19	Base - 2	Radial	400	0	300
	SC11	20	Base - 2	Vertical	200	0	300
	SC12	21	Base - 2	Vertical	-200	0	300
	SC13	22	Base - 2	Radial	-400	0	300
	SC14	23	Base - 2	Tangential	-600	0	300
	SC15	24	Subgrade - 2	Tangential	600	0	450
	SC16	25	Subgrade - 2	Radial	400	0	450
	SC17	26	Subgrade - 2	Vertical	200	0	450
	SC18	27	Subgrade - 2	Vertical	-200	0	450
	SC19	28	Subgrade - 2	Radial	-400	0	450
	SC20	29	Subgrade - 2	Tangential	-600	0	450
	SC21	30	Subgrade - 3	Tangential	600	0	675
	SC22	31	Subgrade - 3	Radial	400	0	675
	SC23	32	Subgrade - 3	Vertical	200	0	675
	SC24	33	Subgrade - 3	Vertical	-200	0	675
	SC25	34	Subgrade - 3	Tangential	-400	0	675
AC Strain Gages	AC1	35	AC	Center	0	0	67
	AC2	36	AC				
	AC3	37	AC				
	AC4	38	AC				
Soil Strain (LVDT)	SS10	64	Base - 1	Center	0	0	225
	SS11	65	Base - 3	Tangential	0	600	355
	SS12	66	Base - 3	Radial	0	400	355
	SS13	67	Base - 2	Vertical	0	200	300
	SS14	68	Base - 2	Vertical	0	-200	300
	SS15	69	Base - 3	Radial	0	-400	355
	SS16	70	Base - 3	Tangential	0	-600	355
	SS17	71	Subgrade - 1	Tangential	0	600	415
	SS18	72	Subgrade - 1	Radial	0	400	415
	SS19	73	Subgrade - 2	Vertical	0	200	450
	SS20	74	Subgrade - 2	Vertical	0	-200	450
	SS21	75	Subgrade - 1	Radial	0	-400	415

Table A10. Continued.

	SS22	76	Subgrade - 1	Tangential	0	-600	415
	SS23	77	Subgrade - 3	Vertical	0	200	675
	SS24	78	Subgrade - 3	Center	0	0	675
	SS25	79	Subgrade - 3	Vertical	0	-200	675

Table A11. Sensor locations for test section CS1.

Sensor	Name	Channel Number	Pavement Layer	Orientation	Actual Location (mm)		
					x	y	z
Load Cell	LC	0	Surface	Vertical	0	0	0
Surface Deformation (LVDT)	SD1	1	Surface	Vertical	400	0	0
	SD2	2	Surface	Vertical	270	0	0
	SD3	3	Surface	Vertical	170	0	0
	SD4	4	Surface	Vertical	50	0	0
	SD5	5	Surface	Vertical	-50	0	0
	SD6	6	Surface	Vertical	-170	0	0
	SD7	7	Surface	Vertical	-270	0	0
	SD8	8	Surface	Vertical	-400	0	0
Stress Cell	SC1	9	Base -1	Radial	-150	0	225
	SC2	10	Base - 2	Vertical	0	0	300
	SC3	11	Base - 2	Vertical	0	297	300
	SC4	12	Base - 2	Vertical	107	107	300
	SC5	13	Base - 2	Radial	-401	0	300
	SC6	14	Base - 2	Radial	-70	70	300
	SC7	15	Base - 2	Radial	140	-141	300
	SC8	16	Base - 2	Radial	0	-300	300
	SC9	17	Base - 2	Radial	0	-604	300
	SC10	18	Base - 2	Tangential	-100	0	300
	SC11	19	Base - 2	Tangential	0	200	300
	SC12	20	Base - 2	Tangential	-280	-280	300
	SC13	21	Subgrade - 1	Vertical	0	0	450
	SC14	22	Subgrade - 1	Vertical	0	-402	450
	SC15	23	Subgrade - 1	Vertical	200	0	450
	SC16	24	Subgrade - 1	Radial	-649	0	450
	SC17	25	Subgrade - 1	Radial	0	148	450
	SC18	26	Subgrade - 1	Radial	0	253	450
	SC19	27	Subgrade - 1	Radial	-315	317	450
	SC20	28	Subgrade - 2	Vertical	0	0	625
	SC21	29	Subgrade - 2	Vertical	-297	0	625
	SC22	30	Subgrade - 2	Radial	0	153	625
	SC23	31	Subgrade - 2	Radial	0	-600	625
	SC24	32	Subgrade - 3	Vertical	0	0	775
	SC25	33	Subgrade - 4	Vertical	0	0	1075
AC Strain Gages	AC1	34	AC	Radial	-150	0	67
		35					
		36					
		37					
Geosynthetic Strain	GS1	42	Geogrid	Radial-M	15	0	375
	GS2	43	Geogrid	Radial-T	0	23	375
	GS3	44	Geogrid	Tangential-M	15	-120	375
	GS4	45	Geogrid	Radial-M	126	0	375

Table A11. Continued.

	GS5	46	Geogrid	Tangential-T	-114	23	375
	GS6	47	Geogrid	Radial-T	0	140	375
	GS7	48	Geogrid	Radial-M	-215	0	375
	GS8	49	Geogrid	Tangential-T	198	-23	375
	GS9	50	Geogrid	Tangential-M	-15	315	375
	GS10	51	Geogrid	Radial-T	0	-293	375
	GS11	52	Geogrid	Tangential-T	-592	23	375
	GS12	53	Geogrid	Radial-M	605	0	375
Soil Strain (LVDT)	SS1	54	Base -1	Center -x-	0	0	225
	SS2	55	Base - 2	Vertical	0	64	300
	SS3	56	Base - 2	Vertical	-211	-212	300
	SS4	57	Base - 2	Vertical	0	-149	300
	SS5	58	Base - 2	Radial	0	395	325
	SS6	59	Base - 2	Radial	-69	-70	325
	SS7	60	Base - 2	Radial	-202	0	325
	SS8	61	Base - 2	Radial	212	212	325
	SS9	62	Base - 2	Radial	-600	0	325
	SS10	63	Base - 2	Tangential	101	0	325
	SS11	64	Base - 2	Tangential	200	0	325
	SS12	65	Base - 2	Tangential	0	-401	325
	SS14	66	Subgrade - 1	Vertical	-65	0	450
	SS13	67	Subgrade - 1	Vertical	0	401	450
	SS15	68	Subgrade - 1	Vertical	-199	0	450
	SS16	69	Subgrade - 1	Radial	65	0	415
	SS17	70	Subgrade - 1	Radial	0	-150	415
	SS18	71	Subgrade - 1	Radial	0	-300	415
	SS19	72	Subgrade - 1	Radial	-448	0	415
	SS20	73	Subgrade - 2	Vertical	65	0	625
	SS21	74	Subgrade - 2	Vertical	0	301	625
	SS22	75	Subgrade - 2	Radial	0	-151	625
	SS23	76	Subgrade - 2	Radial	0	-352	625
	SS24	77	Subgrade - 3	Vertical	0	65	775
	SS25	78	Subgrade - 4	Vertical	0	65	1075
Temperature Probes	TP1	3	Base -1		0	100	225
	TP4	6	Base -2		-300	0	300
	TP6	8	Base - 2		0	-500	300
	TP7	9	Subgrade 1		-300	0	450
	TP8	10	Subgrade 2		0	300	625
	TP9	11	Subgrade-3		0	-100	775
	TP10	12	Subgrade-4		0	-100	1075

Table A12. Sensor locations for test section CS2.

Sensor	Name	Channel Number	Pavement Layer	Orientation	Actual Location (mm)		
					x	y	z
Load Cell	LC	0	Surface	Vertical	0	0	0
Surface Deformation (LVDT)	SD1	1	Surface	Vertical	400	0	0
	SD2	2	Surface	Vertical	270	0	0
	SD3	3	Surface	Vertical	170	0	0
	SD4	4	Surface	Vertical	50	0	0
	SD5	5	Surface	Vertical	-50	0	0
	SD6	6	Surface	Vertical	-170	0	0
	SD7	7	Surface	Vertical	-270	0	0
	SD8	8	Surface	Vertical	-400	0	0
Stress Cell	SC1	9	Base -1	Radial	-151	0	225
	SC2	10	Base - 2	Vertical	0	0	300
	SC9	11	Base - 2	Vertical	0	300	300
	SC4	12	Base - 2	Vertical	106	107	300
	SC5	13	Base - 2	Radial	-340	0	300
	SC6	14	Base - 2	Radial	-71	71	300
	SC7	15	Base - 2	Radial	145	-141	300
	SC8	16	Base - 2	Radial	0	-300	300
	SC3	17	Base - 2	Radial	0	-600	300
	SC10	18	Base - 2	Tangential	-100	0	300
	SC11	19	Base - 2	Tangential	0	205	300
	SC12	20	Base - 2	Tangential	-283	-283	300
	SC13	21	Subgrade - 1	Vertical	0	0	450
	SC14	22	Subgrade - 1	Vertical	0	-401	450
	SC15	23	Subgrade - 1	Vertical	200	0	450
	SC16	24	Subgrade - 1	Radial	-649	0	450
	SC17	25	Subgrade - 1	Radial	0	150	450
	SC18	26	Subgrade - 1	Radial	0	252	450
	SC19	27	Subgrade - 1	Radial	-318	319	450
	SC20	28	Subgrade - 2	Vertical	0	-1	625
	SC21	29	Subgrade - 2	Vertical	-295	0	625
	SC22	30	Subgrade - 2	Radial	0	150	625
	SC23	31	Subgrade - 2	Radial	0	-600	625
	SC24	32	Subgrade - 3	Vertical	0	0	775
	SC25	33	Subgrade - 4	Vertical	0	0	1075
AC Strain Gages	AC1	34	AC	Radial	-150	0	67
		35					
		36					
		37					
Soil Strain (LVDT)	SS1	54	Base -1	Center -x-	0	0	225
	SS2	55	Base - 2	Vertical	0	66	300
	SS3	56	Base - 2	Vertical	-212	212	300
	SS4	57	Base - 2	Vertical	0	-150	300

Table A12. Continued.

	SS10	58	Base - 2	Radial	0	400	325
	SS6	59	Base - 2	Radial	-71	-72	325
	SS7	60	Base - 2	Radial	-200	0	325
	SS8	61	Base - 2	Radial	212	212	325
	SS9	62	Base - 2	Radial	-600	0	325
	SS5	63	Base - 2	Tangential	99	0	325
	SS11	64	Base - 2	Tangential	200	0	325
	SS12	65	Base - 2	Tangential	0	-401	325
	SS13	66	Subgrade - 1	Vertical	-65	0	450
	SS14	67	Subgrade - 1	Vertical	1	450	450
	SS15	68	Subgrade - 1	Vertical	-200	0	450
	SS16	69	Subgrade - 1	Radial	65	0	415
	SS17	70	Subgrade - 1	Radial	0	-150	415
	SS18	71	Subgrade - 1	Radial	0	-300	415
	SS19	72	Subgrade - 1	Radial	-450	0	415
	SS20	73	Subgrade - 2	Vertical	65	0	625
	SS21	74	Subgrade - 2	Vertical	0	297	625
	SS22	75	Subgrade - 2	Radial	0	-155	625
	SS23	76	Subgrade - 2	Radial	0	-355	625
	SS24	77	Subgrade - 3	Vertical	0	65	775
	SS25	78	Subgrade - 4	Vertical	0	60	1075
Temperature Probes	TP1	3	Base -1		0	100	225
	TP4	6	Base -2		-300	0	300
	TP6	8	Base - 2		0	-500	300
	TP7	9	Subgrade 1		-300	0	450
	TP8	10	Subgrade 2		0	300	625
	TP9	11	Subgrade-3		0	-100	775
	TP10	12	Subgrade-4		0	-100	1075

Table A13. Sensor locations for test section CS3.

Sensor	Name	Channel Number	Pavement Layer	Orientation	Actual Location (mm)		
					x	y	z
Load Cell	LC	0	Surface	Vertical	0	0	0
Surface Deformation (LVDT)	SD1	1	Surface	Vertical	400	0	0
	SD2	2	Surface	Vertical	270	0	0
	SD3	3	Surface	Vertical	170	0	0
	SD4	4	Surface	Vertical	50	0	0
	SD5	5	Surface	Vertical	-50	0	0
	SD6	6	Surface	Vertical	-170	0	0
	SD7	7	Surface	Vertical	-270	0	0
	SD8	8	Surface	Vertical	-400	0	0
Stress Cell	SC1	9	Base -1	Vertical	0	0	200
	SC2	10	Base - 2	Vertical	0	0	325
	SC18	26	Base -1	Radial	0	100	225
	SC20	28	Base - 2	Radial	0	100	325
	SC21	29	Subgrade - 1	Vertical	0	0	450
	SC22	30	Subgrade - 2	Vertical	0	0	625
	SC24	32	Subgrade - 3	Vertical	0	0	775
	SC25	33	Subgrade - 4	Vertical	0	0	1075
Geosynthetic Strain	GS1	42	Geogrid	Radial-M	-15	0	275
	GS2	43	Geogrid	Radial-T	0	-21	275
	GS3	44	Geogrid	Radial-M	128	0	275
	GS4	45	Geogrid	Radial-T	0	-142	275
Soil Strain (LVDT)	SS14	66	Base -1	Radial	130	0	200
	SS17	70	Base -1	Vertical	0	-65	200
	SS19	72	Base - 2	Vertical	-65	0	325
	SS20	73	Base - 2	Radial	0	-140	325
	SS21	74	Subgrade - 1	Vertical	-65	0	450
	SS22	75	Subgrade - 2	Vertical	-65	0	625
	SS24	77	Subgrade - 3	Vertical	-65	0	775
	SS25	78	Subgrade - 4	Vertical	-65	0	1075

Table A14. Sensor locations for test section CS5.

Sensor	Name	Channel Number	Pavement Layer	Orientation	Actual Location (mm)		
					x	y	z
Load Cell	LC	0	Surface	Vertical	0	0	0
Surface Deformation (LVDT)	SD1	1	Surface	Vertical	400	0	0
	SD2	2	Surface	Vertical	270	0	0
	SD3	3	Surface	Vertical	170	0	0
	SD4	4	Surface	Vertical	50	0	0
	SD5	5	Surface	Vertical	-50	0	0
	SD6	6	Surface	Vertical	-170	0	0
	SD7	7	Surface	Vertical	-270	0	0
	SD8	8	Surface	Vertical	-400	0	0
Stress	SC1		Base -1	Radial	0	150	225
	SC2		Base - 2	Vertical	0	0	300
	SC7		Base - 2	Vertical	106	106	300
	SC5		Base - 2	Vertical	0	300	300
	SC11		Base - 2	Radial	141	-141	300
	SC12		Base - 2	Radial	0	-300	300
	SC9		Base - 2	Radial	-400	0	300
	SC13		Base - 2	Radial	0	-600	300
	SC22		Subgrade - 1	Vertical	0	0	450
	SC17		Subgrade - 1	Vertical	200	0	450
	SC19		Subgrade - 1	Radial	-106	106	450
	SC15		Subgrade - 1	Radial	106	106	450
	SC20		Subgrade - 1	Radial	0	250	450
	SC18		Subgrade - 1	Radial	0	400	450
	SC23		Subgrade - 2	Vertical	0	0	625
	SC24		Subgrade - 3	Vertical	0	0	775
	SC25		Subgrade - 4	Vertical	0	0	1075
AC Strain Gages	AC1	34	AC	Radial	-150	0	67
		36					
		37					
Geosynthetic Strain	GS1	42	Geogrid	Radial-M	15	0	375
	GS2	43	Geogrid	Radial-T	0	20	375
	GS3	44	Geogrid	Radial-M	-318	0	375
	GS4	45	Geogrid	Radial-M	122	0	375
	GS5	46	Geogrid	Radial-M	422	0	375
	GS6	47	Geogrid	Radial-T	0	137	375
	GS7	48	Geogrid	Radial-M	-205	0	375
Soil Strain	SS1		Base –1	Center -x-	0	0	225
	SS2		Base –1	Radial	0	-150	225
	SS3		Base – 2	Vertical	0	65	300
	SS15		Base – 2	Vertical	0	-150	300
	SS4		Base – 2	Vertical	-212	212	300
	SS8		Base – 2	Radial	-71	-71	325

Table A14. Continued.

	SS9		Base – 2	Radial	-200	0	325
	SS11		Base – 2	Radial	212	212	325
	SS7		Base – 2	Radial	0	400	325
	SS13		Base – 2	Tangential	100	0	325
	SS5		Base – 2	Tangential	0	200	325
	SS21		Subgrade - 1	Vertical	-65	0	450
	SS17		Subgrade - 1	Vertical	-200	0	450
	SS14		Subgrade - 1	Vertical	0	-300	450
	SS12		Subgrade - 1	Vertical	283	283	450
	SS16		Subgrade - 1	Radial	-106	-106	415
	SS22		Subgrade - 1	Radial	212	-212	415
	SS19		Subgrade - 1	Radial	-318	318	415
	SS23		Subgrade - 2	Vertical	-65	0	625
	SS24		Subgrade - 3	Vertical	-65	0	775
	SS25		Subgrade - 4	Vertical	-65	0	1075

Table A15. Sensor locations for test section CS6.

Sensor	Name	Channel Number	Pavement Layer	Orientation	Actual Location (mm)		
					x	y	z
Load Cell	LC	0	Surface	Vertical	0	0	0
Surface Deformation (LVDT)	SD1	1	Surface	Vertical	400	0	0
	SD2	2	Surface	Vertical	270	0	0
	SD3	3	Surface	Vertical	170	0	0
	SD4	4	Surface	Vertical	50	0	0
	SD5	5	Surface	Vertical	-50	0	0
	SD6	6	Surface	Vertical	-170	0	0
	SD7	7	Surface	Vertical	-270	0	0
	SD8	8	Surface	Vertical	-400	0	0
Stress	SC2	9	Base -1	Radial	0	150	225
	SC1	10	Base - 2	Vertical	30	0	300
	SC5	13	Base - 2	Vertical	0	300	300
	SC14	15	Base - 2	Vertical	106	106	300
	SC16	17	Base - 2	Radial	-400	0	300
	SC11	19	Base - 2	Radial	141	-141	300
	SC21	20	Base - 2	Radial	0	-300	300
	SC13	21	Base - 2	Radial	0	-600	300
	SC15	23	Subgrade - 1	Radial	106	106	450
	SC18	26	Subgrade - 1	Radial	0	400	450
	SC17	28	Subgrade - 1	Radial	0	260	450
	SC20	25	Subgrade - 1	Vertical	200	0	450
	SC22	30	Subgrade - 1	Vertical	0	0	450
	SC23	31	Subgrade - 2	Vertical	0	0	625
	SC24	32	Subgrade - 3	Vertical	0	0	775
	SC25	33	Subgrade - 4	Vertical	0	0	1075
AC Strain Gages	AC1	34	AC	Radial	-150	0	67
		35					
		36					
Geosynthetic Strain	GS1	42	Geotextile	Radial-M	0	-65	375
	GS2	43	Geotextile	Radial-T	-65	0	375
	GS3	44	Geotextile	Tangential-M	0	-200	375
	GS4	45	Geotextile	Radial-M	135	0	375
	GS5	46	Geotextile	Tangential-T	-200	0	375
	GS6	47	Geotextile	Radial-T	0	135	375
	GS7	48	Geotextile	Radial-M	-300	0	375
	GS8	49	Geotextile	Tangential-T	270	0	375
	GS9	50	Geotextile	Tangential-M	0	315	375
	GS10	51	Geotextile	Radial-T	0	-330	375
	GS12	53	Geotextile	Radial-M	620	0	375
Soil Strain	SS1	54	Base –1	Center -x-	0	0	225
	SS2	55	Base –1	Radial	0	-150	225
	SS15	68	Base – 2	Vertical	0	-150	300

Table A15. Continued.

	SS3	56	Base – 2	Vertical	0	65	300
	SS4	57	Base – 2	Vertical	-212	212	300
	SS10	58	Base – 2	Tangential	0	200	325
	SS7	60	Base – 2	Radial	0	400	325
	SS8	61	Base – 2	Radial	-71	-71	325
	SS9	62	Base – 2	Radial	-200	0	325
	SS11	64	Base – 2	Radial	212	212	325
	SS18	66	Base – 2	Tangential	100	0	325
	SS16	69	Subgrade - 1	Radial	-106	-106	415
	SS19	72	Subgrade - 1	Radial	-318	318	415
	SS22	75	Subgrade - 1	Radial	212	-212	415
	SS12	65	Subgrade - 1	Vertical	-283	-283	450
	SS14	67	Subgrade - 1	Vertical	-10	-305	450
	SS17	70	Subgrade - 1	Vertical	-200	0	450
	SS21	74	Subgrade - 1	Vertical	-65	0	450
	SS23	76	Subgrade - 2	Vertical	-65	0	625
	SS20	77	Subgrade - 3	Vertical	-65	0	775
	SS25	78	Subgrade - 4	Vertical	-65	0	1075

Table A16. Sensor locations for test section CS7.

Sensor	Name	Channel Number	Pavement Layer	Orientation	Actual Location (mm)		
					x	y	z
Load Cell	LC	0	Surface	Vertical	0	0	0
Surface Deformation (LVDT)	SD1	1	Surface	Vertical	400	0	0
	SD2	2	Surface	Vertical	270	0	0
	SD3	3	Surface	Vertical	170	0	0
	SD4	4	Surface	Vertical	50	0	0
	SD5	5	Surface	Vertical	-50	0	0
	SD6	6	Surface	Vertical	-170	0	0
	SD7	7	Surface	Vertical	-270	0	0
	SD8	8	Surface	Vertical	-400	0	0
Stress Cell	SC1		Base -1	Vertical	0	0	200
	SC11		Base - 1	Vertical	150	0	200
	SC6		Base - 1	Radial	141	141	200
	SC2		Base - 1	Radial	-400	0	200
	SC13		Base - 2	Vertical	0	0	325
	SC16		Base - 2	Vertical	150	0	325
	SC14		Base - 2	Radial	141	141	325
	SC15		Base - 2	Radial	-400	0	325
	SC22		Subgrade - 1	Vertical	0	0	450
	SC21		Subgrade - 1	Vertical	200	0	450
	SC17		Subgrade - 1	Radial	106	106	450
	SC20		Subgrade - 1	Radial	0	250	450
	SC18		Subgrade - 1	Radial	0	400	450
	SC23		Subgrade - 2	Vertical	0	0	625
	SC24		Subgrade - 3	Vertical	0	0	775
	SC25		Subgrade - 4	Vertical	0	0	1075
AC Strain Gages	AC1	34	AC	Radial	-150	0	67
		35					
		36					
Geosynthetic Strain	GS1	42	Geogrid	Radial-M	-15	0	275
	GS2	43	Geogrid	Radial-T	0	-21	275
	GS3	44	Geogrid	Radial-M	128	0	275
	GS4	45	Geogrid	Radial-T	0	-142	275
	GS5	46	Geogrid	Radial-M	-215	0	275
	GS6	47	Geogrid	Radial-M	318	0	275
	GS7	48	Geogrid	Radial-T	0	420	275
Soil Strain (LVDT)	SS11		Base – 1	Vertical	0	65	200
	SS2		Base – 1	Vertical	0	-150	200
	SS3		Base – 1	Radial	-200	0	225
	SS10		Base – 1	Radial	-212	-212	225
	SS4		Base – 1	Radial	0	400	225
	SS8		Base – 2	Vertical	0	65	325
	SS9		Base – 2	Vertical	15	-140	325

Table A16. Continued.

	SS5		Base – 2	Radial	-71	-71	325
	SS24		Base – 2	Radial	-200	0	325
	SS15		Base – 2	Radial	-212	212	325
	SS7		Base – 2	Radial	0	400	325
	SS21		Subgrade - 1	Vertical	-65	0	450
	SS17		Subgrade - 1	Vertical	-200	0	450
	SS14		Subgrade - 1	Vertical	0	-300	450
	SS12		Subgrade - 1	Vertical	-283	-283	450
	SS16		Subgrade - 1	Radial	-106	-106	415
	SS19		Subgrade - 1	Radial	-318	318	415
	SS22		Subgrade - 1	Radial	212	-212	415
	SS23		Subgrade - 2	Vertical	-60	0	625
	SS20		Subgrade - 3	Vertical	-65	0	775
	SS25		Subgrade - 4	Vertical	-65	0	1075

Table A17. Sensor locations for test section CS8.

Sensor	Name	Channel Number	Pavement Layer	Orientation	Actual Location (mm)		
					x	y	z
Load Cell	LC	0	Surface	Vertical	0	0	0
Surface Deformation (LVDT)	SD1	1	Surface	Vertical	400	0	0
	SD2	2	Surface	Vertical	270	0	0
	SD3	3	Surface	Vertical	170	0	0
	SD4	4	Surface	Vertical	50	0	0
	SD5	5	Surface	Vertical	-50	0	0
	SD6	6	Surface	Vertical	-170	0	0
	SD7	7	Surface	Vertical	-270	0	0
	SD8	8	Surface	Vertical	-400	0	0
Stress	SC2		Base -1	Radial	0	150	225
	SC1		Base - 2	Vertical	0	0	300
	SC6		Base - 2	Vertical	106	106	300
	SC7		Base - 2	Vertical	0	300	300
	SC13		Base - 2	Radial	141	-141	300
	SC14		Base - 2	Radial	0	-300	300
	SC15		Base - 2	Radial	-400	0	300
	SC16		Base - 2	Radial	0	-600	300
	SC17		Subgrade - 1	Vertical	0	0	450
	SC18		Subgrade - 1	Vertical	200	0	450
	SC20		Subgrade - 1	Radial	106	106	450
	SC21		Subgrade - 1	Radial	0	250	450
	SC22		Subgrade - 1	Radial	0	400	450
	SC23		Subgrade - 2	Vertical	0	0	625
	SC24		Subgrade - 3	Vertical	0	0	775
	SC25		Subgrade - 4	Vertical	0	0	1075
AC Strain Gages	AC1	34	AC	Radial	-150	0	67
		35					
		36					
Soil Strain	SS2		Base –1	Center -x-	0	0	225
	SS3		Base –1	Radial	0	-150	225
	SS4		Base – 2	Vertical	0	65	300
	SS7		Base – 2	Vertical	0	-150	300
	SS8		Base – 2	Vertical	-212	212	300
	SS9		Base – 2	Radial	-71	-71	325
	SS10		Base – 2	Radial	-200	0	325
	SS11		Base – 2	Radial	212	212	325
	SS12		Base – 2	Radial	0	400	325
	SS5		Base – 2	Tangential	100	0	325
	SS17		Base – 2	Tangential	0	200	325
	SS20		Subgrade - 1	Radial	-106	-106	415
	SS21		Subgrade - 1	Radial	212	-212	415
	SS23		Subgrade - 1	Radial	-318	318	415

Table A17. Continued.

	SS14		Subgrade - 1	Vertical	-65	0	450
	SS16		Subgrade - 1	Vertical	-200	0	450
	SS15		Subgrade - 1	Vertical	0	-300	450
	SS19		Subgrade - 1	Vertical	283	283	450
	SS22		Subgrade - 2	Vertical	-65	0	625
	SS24		Subgrade - 3	Vertical	-65	0	775
	SS25		Subgrade - 4	Vertical	-65	0	1075

Table A18. Sensor locations for test section CS9.

Sensor	Name	Channel Number	Pavement Layer	Orientation	Actual Location (mm)		
					x	y	z
Load Cell	LC	0	Surface	Vertical	0	0	0
Surface Deformation (LVDT)	SD1	1	Surface	Vertical	400	0	0
	SD2	2	Surface	Vertical	270	0	0
	SD3	3	Surface	Vertical	170	0	0
	SD4	4	Surface	Vertical	50	0	0
	SD5	5	Surface	Vertical	-50	0	0
	SD6	6	Surface	Vertical	-170	0	0
	SD7	7	Surface	Vertical	-270	0	0
	SD8	8	Surface	Vertical	-400	0	0
Stress Cell	SC4		Base -1	Radial	0	150	263
	SC1		Base -1	Vertical	0	0	263
	SC2		Base - 2	Vertical	0	0	375
	SC5		Base - 2	Vertical	106	106	375
	SC6		Base - 2	Vertical	0	300	375
	SC7		Base - 2	Radial	141	-141	375
	SC12		Base - 2	Radial	0	-300	375
	SC13		Base - 2	Radial	-400	0	375
	SC14		Base - 2	Radial	0	-600	375
	SC15		Subgrade - 1	Vertical	0	0	525
	SC17		Subgrade - 1	Vertical	200	0	525
	SC20		Subgrade - 1	Radial	106	106	525
	SC21		Subgrade - 1	Radial	0	250	525
	SC22		Subgrade - 1	Radial	0	400	525
	SC23		Subgrade - 2	Vertical	0	0	700
	SC24		Subgrade - 3	Vertical	0	0	850
	SC25		Subgrade - 4	Vertical	0	0	1150
AC Strain Gages	AC1	34	AC	Radial	-150	0	67
		35					
		36					
Soil Strain (LVDT)	SS2		Base –1	Radial	0	300	263
	SS3		Base –1	Radial	-150	0	263
	SS17		Base – 1	Vertical	65	0	263
	SS8		Base – 1	Vertical	0	-150	215
	SS4		Base – 2	Vertical	0	65	375
	SS7		Base – 2	Vertical	0	-150	375
	SS15		Base – 2	Vertical	-212	212	375
	SS12		Base – 2	Radial	-71	-71	400
	SS10		Base – 2	Radial	-200	0	400
	SS11		Base – 2	Radial	212	212	400
	SS14		Base – 2	Radial	0	400	400
	SS20		Subgrade - 1	Radial	-106	-106	490
	SS21		Subgrade - 1	Radial	212	-212	490

Table A18. Continued.

	SS5		Subgrade - 1	Radial	-318	318	490
	SS9		Subgrade - 1	Vertical	-65	0	525
	SS16		Subgrade - 1	Vertical	-200	0	525
	SS23		Subgrade - 1	Vertical	0	-300	525
	SS19		Subgrade - 1	Vertical	283	283	525
	SS22		Subgrade - 2	Vertical	-65	0	700
	SS24		Subgrade - 3	Vertical	-65	0	850
	SS25		Subgrade - 4	Vertical	-65	0	1150

Table A19. Sensor locations for test section CS10.

Sensor	Name	Channel Number	Pavement Layer	Orientation	Actual Location (mm)		
					x	y	z
Load Cell	LC	0	Surface	Vertical	0	0	0
Surface Deformation (LVDT)	SD1	1	Surface	Vertical	400	0	0
	SD2	2	Surface	Vertical	270	0	0
	SD3	3	Surface	Vertical	170	0	0
	SD4	4	Surface	Vertical	50	0	0
	SD5	5	Surface	Vertical	-50	0	0
	SD6	6	Surface	Vertical	-170	0	0
	SD7	7	Surface	Vertical	-270	0	0
	SD8	8	Surface	Vertical	-400	0	0
Stress Cell	SC4		Base -1	Radial	0	150	263
	SC1		Base -1	Vertical	0	0	263
	SC2		Base - 2	Vertical	0	0	375
	SC5		Base - 2	Vertical	106	106	375
	SC11		Base - 2	Vertical	0	300	375
	SC12		Base - 2	Radial	141	-141	375
	SC13		Base - 2	Radial	0	-300	375
	SC14		Base - 2	Radial	-400	0	375
	SC15		Base - 2	Radial	0	-600	375
	SC16		Subgrade - 1	Vertical	0	0	525
	SC17		Subgrade - 1	Vertical	200	0	525
	SC19		Subgrade - 1	Radial	106	106	525
	SC20		Subgrade - 1	Radial	0	250	525
	SC21		Subgrade - 1	Radial	0	400	525
	SC22		Subgrade - 2	Vertical	0	0	700
	SC23		Subgrade - 3	Vertical	0	0	850
	SC24		Subgrade - 4	Vertical	0	0	1150
AC Strain Gages	AC1	34	AC	Radial	-150	0	67
		35					
		36					
Geosynthetic Strain	GS1	42	Geogrid	Radial-T	0	20	450
	GS2	43	Geogrid	Radial-M	-15	0	450
	GS3	44	Geogrid	Radial-M	125	0	450
	GS4	45	Geogrid	Radial-T	0	135	450
	GS5	46	Geogrid	Radial-M	-210	0	450
	GS6	47	Geogrid	Radial-M	335	0	450
	GS7	48	Geogrid	Radial-T	0	-412	450
Soil Strain (LVDT)	SS2		Base –1	Radial	0	300	263
	SS3		Base –1	Radial	-150	0	263
	SS12		Base – 1	Vertical	65	0	263
	SS8		Base – 1	Vertical	0	-150	263
	SS14		Base – 2	Vertical	0	65	375
	SS7		Base – 2	Vertical	0	-150	375

Table A19. Continued.

	SS15		Base – 2	Vertical	-212	212	375
	SS4		Base – 2	Radial	-71	-71	400
	SS10		Base – 2	Radial	-200	0	400
	SS11		Base – 2	Radial	212	212	400
	SS17		Base – 2	Radial	0	400	400
	SS20		Subgrade - 1	Radial	-106	-106	490
	SS21		Subgrade - 1	Radial	212	-212	490
	SS5		Subgrade - 1	Radial	-318	318	490
	SS9		Subgrade - 1	Vertical	-65	0	525
	SS16		Subgrade - 1	Vertical	-200	0	525
	SS22		Subgrade - 1	Vertical	0	-300	525
	SS19		Subgrade - 1	Vertical	283	283	525
	SS23		Subgrade - 2	Vertical	-65	0	700
	SS24		Subgrade - 3	Vertical	-65	0	850
	SS25		Subgrade - 4	Vertical	-65	0	1150

Table A20. Sensor locations for test section CS11.

Sensor	Name	Channel Number	Pavement Layer	Orientation	Actual Location (mm)		
					x	y	z
Load Cell	LC	0	Surface	Vertical	0	0	0
Surface Deformation (LVDT)	SD1	1	Surface	Vertical	400	0	0
	SD2	2	Surface	Vertical	270	0	0
	SD3	3	Surface	Vertical	170	0	0
	SD4	4	Surface	Vertical	50	0	0
	SD5	5	Surface	Vertical	-50	0	0
	SD6	6	Surface	Vertical	-170	0	0
	SD7	7	Surface	Vertical	-270	0	0
	SD8	8	Surface	Vertical	-400	0	0
Stress	SC1		Base -1	Radial	0	150	225
	SC2		Base - 2	Vertical	0	0	300
	SC4		Base - 2	Vertical	106	106	300
	SC6		Base - 2	Vertical	0	300	300
	SC7		Base - 2	Radial	141	-141	300
	SC12		Base - 2	Radial	0	-300	300
	SC11		Base - 2	Radial	-400	0	300
	SC13		Base - 2	Radial	0	-600	300
	SC15		Subgrade - 1	Vertical	0	0	450
	SC17		Subgrade - 1	Vertical	200	0	450
	SC19		Subgrade - 1	Radial	106	106	450
	SC20		Subgrade - 1	Radial	0	250	450
	SC21		Subgrade - 1	Radial	0	400	450
	SC22		Subgrade - 2	Vertical	0	0	625
	SC23		Subgrade - 3	Vertical	0	0	775
	SC24		Subgrade - 4	Vertical	0	0	1075
AC Strain Gages	AC1	34	AC	Radial	-150	0	67
		35					
		36					
Geosynthetic Strain	GS1	42	Geogrid	Radial-T	0	20	375
	GS2	43	Geogrid	Radial-M	-15	0	375
	GS3	44	Geogrid	Radial-M	125	0	375
	GS4	45	Geogrid	Radial-T	0	-135	375
	GS5	46	Geogrid	Radial-M	-210	0	375
	GS6	47	Geogrid	Radial-M	335	0	375
	GS7	48	Geogrid	Radial-T	0	-412	375
Soil Strain	SS2		Base –1	Center -x-	0	0	225
	SS3		Base –1	Radial	0	-150	225
	SS7		Base – 2	Vertical	0	65	300
	SS8		Base – 2	Vertical	0	-150	300
	SS14		Base – 2	Vertical	-212	212	300
	SS4		Base – 2	Radial	-71	-71	325
	SS10		Base – 2	Radial	-200	0	325

Table A20. Continued.

	SS11		Base – 2	Radial	212	212	325
	SS17		Base – 2	Radial	0	400	325
	SS12		Base – 2	Tangential	100	0	325
	SS15		Base – 2	Tangential	0	200	325
	SS20		Subgrade - 1	Radial	-106	-106	415
	SS21		Subgrade - 1	Radial	212	-212	415
	SS5		Subgrade - 1	Radial	-318	318	415
	SS9		Subgrade - 1	Vertical	-65	0	450
	SS16		Subgrade - 1	Vertical	-200	0	450
	SS22		Subgrade - 1	Vertical	0	-300	450
	SS19		Subgrade - 1	Vertical	283	283	450
	SS23		Subgrade - 2	Vertical	-65	0	625
	SS24		Subgrade - 3	Vertical	-65	0	775
	SS25		Subgrade - 4	Vertical	-65	0	1075

MONTANA STATE UNIVERSITY - BOZEMAN
3 1762 10421222 8